Master Thesis

Detached Eddy Simulation applied to three-dimensional aerodynamic full car simulations in motorsport.

D.M.E. de Jong

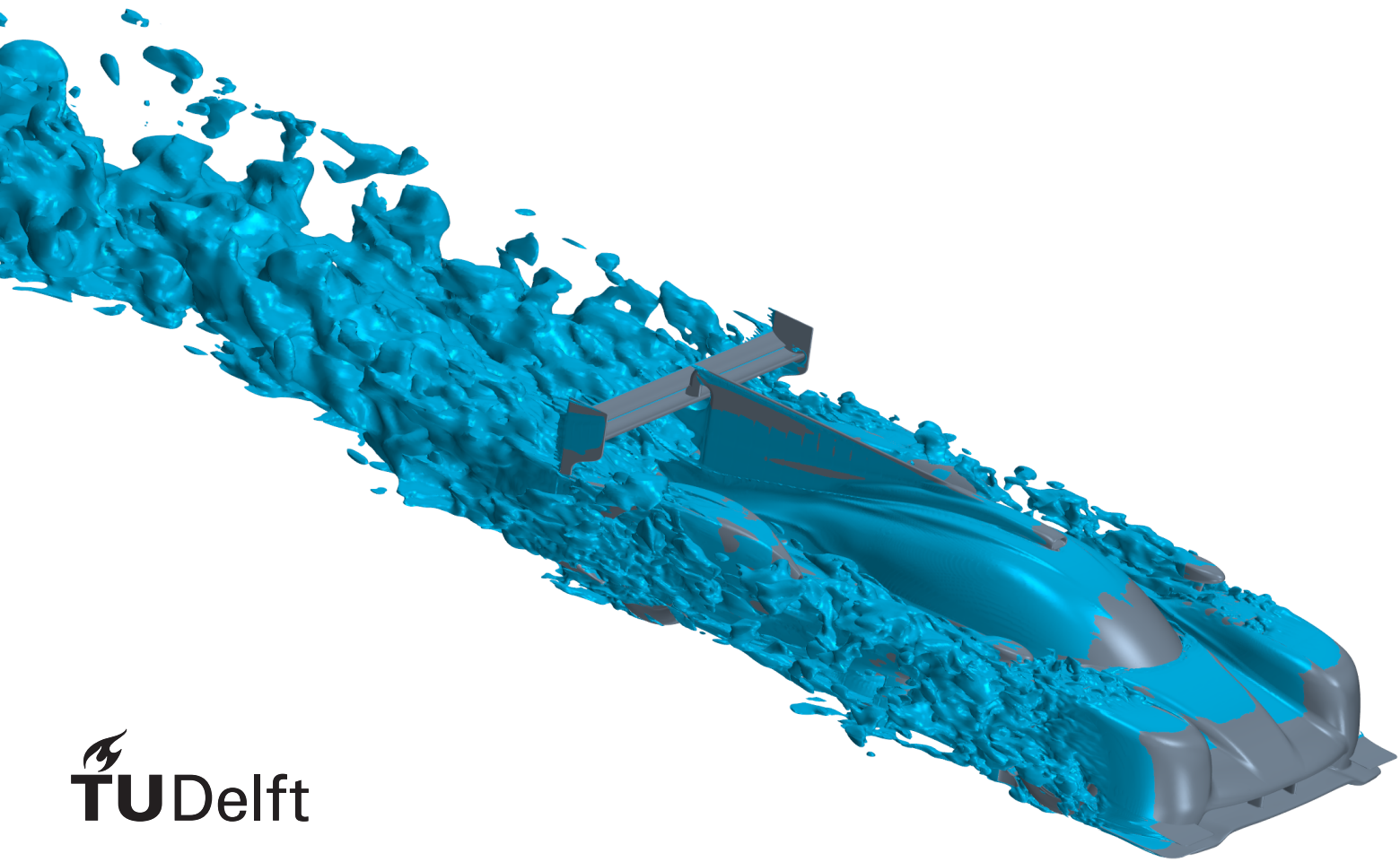

TU Delft

Master Thesis
Detached Eddy Simulation applied to three-dimensional aerodynamic full car simulations in motorsport.

by

D.M.E. de Jong

Student number: 4294580
Project duration: February 2019 – October 2019
Supervisors: Dr.techn. G.K. Dutzler, Porsche AG
Dr. Ir. A. van Zuijlen, TU Delft

This thesis is confidential and cannot be made public until November 2024.

TU Delft

Preface

My first word of thanks goes out to Dr.techn. Gerhard Dutzler, my supervisor at Porsche. During my eight months as his student he taught me many lessons about the interpretation of aerodynamic results and about motorsport aerodynamics in general. His expertise and meticulous way of working motivated me to get the most out of all steps of the process. This includes critically reassessing the methods used, as well as realistically thinking about potential improvements. Thank you for all of the feedback you have given me, for the detailed discussions about the results obtained and for all of your time and patience throughout the last couple of months.

Much appreciated was also the close involvement of my TU Delft supervisor, Dr.Ir. Alexander van Zuijlen. His guidance already started during my application at Porsche, reassuring me about a smooth cooperation between the TU Delft and Porsche. Our monthly meetings were a welcome reflection moment with refreshing insights. They were encouraging to explore certain topics more thoroughly and helped me to keep seeing the project from an aerospace point of view in addition to the automotive perspective at the company. Finally, the elaborate feedback on the draft report helped me to get translate my newly obtained insights into Detached Eddy Simulation into this final report.

Finally, this report could not have been written without Dr. Christos Pashias, who welcomed me in his team at the Aerodynamic Prototype Development department at Porsche Motorsport. He provided me with the opportunity to do my thesis at Porsche and to learn not only about aerodynamics but also about working in a team setting at a large company. Working in his team and experiencing the cooperation between the different roles in that team has enriched my master thesis and is therefore greatly appreciated.

D.M.E. de Jong
Weissach, October 2019

Contents

Summary

The main purpose of this report is to explore the possibility to use the Detached Eddy Simulation (DES) method as an aerodynamic simulation method in motorsport aerodynamics. To achieve this purpose, the DES method is explored first in theory, then in an airfoil model study and then in several full car cases. Together, these parts illustrate the added value for Porsche Motorsport to use Detached Eddy Simulation in their design process.

Detached Eddy Simulation is a Computational Fluid Dynamics (CFD) method aimed at simulating turbulent flows. It combines two other CFD methods, Large Eddy Simulation (LES) and the Reynolds-Averaged Navier-Stokes (RANS) equations. Large Eddy Simulation is an unsteady method that aims to resolve the turbulent flow structures with a high energy content and to model the small, low energy flow structures. It needs quite a fine mesh and small time step for this. This results in the high costs associated with the method, especially when simulating wall bounded flows. RANS on the other hand is a steady method that models the flow based on time averaging and poses less strict requirements on the mesh. The DES method tries to combine the low cost RANS method with the highly accurate LES method. It does so by using RANS where refining the mesh to allow for LES is too expensive, for example in the boundary layer. LES in turn is used where unsteady flow structures need to be captured and RANS is insufficient to represent the flow. Over time, different DES variants have been developed. The common principle distinguishing DES from other hybrid RANS-LES methods is to use a RANS model as a Subgrid-Scale model in the LES regions and as a full RANS model in the RANS regions. The switch between RANS and LES is based on the wall distance and the local grid size. Some DES variants use other factors as well to improve the performance of the method.

There are a number of different parameters which influence the accuracy of simulations using the Detached Eddy Simulation method. The DES method is quite sensitive to the mesh used. The mesh governs where LES and where RANS regions occur, but also governs how well the respective methods can be used in their designated regions. Other parameters that influence the accuracy are the time step, the turbulence model used within the DES formulation, the DES variant, the model coefficients and the inflow conditions. To assess the DES method in this report, comparisons are made with results obtained with the Realizable $k-\epsilon$ RANS model and wind tunnel data. The promise of the DES method is to capture more flow features compared to RANS and to correlate better with the wind tunnel data.

The ability of DES to do aerodynamic flow predictions is first investigated by various simulations of a high downforce rear wing and a NACA 0012 airfoil. Both airfoil models allow for a large number of simulations at a low cost, ensuring various factors of influence can be investigated. These simulations already indicate a number of the difficulties related to using the DES method, its inconsistencies included. A parameter change on a coarse mesh can have a very different influence than the same change on a finer mesh for example. This makes it difficult to specify a single set of recommended settings for rear wing simulations and for DES simulations in general. Also, the results for the rear wing are quite close to the expectations, while the NACA 0012 results do not fully agree with the wind tunnel data. Lower angles of attack are captured well, both in terms of lift coefficient and flow phenomena captured. This includes the prediction of the location of a laminar separation bubble and a small pressure side trailing edge separation. The actual separation point however, is not captured. Some first insights into the capabilities of the method are given however, like the ability to predict transition. Additionally, a number of lessons learned from the airfoil study are valuable for the full car and for future airfoil simulations. These are summarized in the considerations and recommendations, giving a set-up proposal and some guidelines for monitoring of the solution and possible errors. Included here is the initialization with RANS, careful design of the boundary layer mesh and monitoring through pressure taps. These considerations and recommendation are the starting point for the full car simulations discussed in the second part of the report.

The first car simulated is the GTE19, a grand tourer car designed for endurance racing and released in the summer of 2019. The set-up for the car simulations is based on the results obtained in the rear wing study together with recommendation from the STAR-CCM+ v11.02 user guide. The $k-\omega$ SST-IDDES formulation of the DES method is used and a number of variations in mesh, turbulent content and DES formulation are tested for the straight line case. Comparisons are done between RANS simulations, DES simulations on a

coarse mesh and DES simulations on a mesh designed specifically for the method. Transition is captured on both the front and rear wing for the finest mesh, outperforming the Realizable $k-\epsilon$ RANS model in this respect. Force data from two different wind tunnels, a 60% scale and a full scale one, indicates that the DES method in general predicts too much downforce produced by the floor. The balance between the front and rear downforce is quite good and within 5% of both sets of wind tunnel data. The drag prediction is very good and almost exactly in between the two sets of wind tunnel data. This is an important improvement compared to the RANS results as there the drag is always under predicted. The results for the cornering case of the same car are very similar.

The second car is the LMP1 car, a high endurance Le Mans prototype sports car. Porsche won the 24 hours of Le Mans three years in a row with this car, from 2015 to 2017. Two concepts for the 2015 car are investigated here, the S09 and the S15. PIV data of the LMP1 S09 is used to assess the ability of the DES method to capture vortices underneath the floor of the car, as well as their decay. The results indicate that the Realizable $k-\epsilon$ RANS model usually used by the team outperforms the DES method in this respect both in the straight line and the cornering case. The LMP1 S09 also indicates the ambiguity of the DES method. The transition on the rear wing can not be captured in this case and grid induced separation takes place. This is an issue related to the DES method in general, when the method tries to do an LES while the mesh is not fine enough to support it. A solution to this issue is to make the mesh less ambiguous, coarsen to obtain a RANS solution or refine to allow a proper LES.

Since only PIV data and no force data is available for the LMP1 S09, the LMP1 S15 car is used to assess the overall performance of the DES method on this car. The LMP1 S15 confirms the tendency of the DES method to over predict the downforce produced by the rear floor. To take it one step further, not only absolute forces but also force changes or deltas are computed. The delta is computed by looking at the difference in downforce and drag between two different designs or ride heights. In this case, two different ride heights are compared, resulting in a prediction of the force differences when changing the ride height. These predictions are very close to the wind tunnel predictions for a change in downforce. The DES is off less than 3% for downforce, drag and balance, while the RANS method has a difference up to %. This indicates that although the results indicate too much downforce, due to the consistency of this error the method is still good at predicting the impact of a ride height change.

Overall, contradicting conclusions can be drawn about the capabilities of Detached Eddy Simulation as a design tool. On the one hand, more flow phenomena can be captured, drag predictions are better and force changes due to a change in ride height are captured better than for the Realizable $k-\epsilon$ RANS method. On the other hand, the results are more ambiguous and sensitive to the local grid. The main recommendation is therefore to explore a few additional topics. Another airfoil study with a simpler separation can be done to assess the ability of DES to capture that. This can then be used to assess the settings needed for the DES method to perform well in other circumstances as well. For the full car, adjustments related to the inflow turbulence are expected to lead to potential improvements, because of the impact of this setting as shown in [14]. Also, costly potential improvements could be realised through the time step lowering the Courant Number as well as further mesh refinements. A prediction of the force change due to a design change should also be tested, since this is one of the primary aims of DES as a design tool. Finally, a comparison with LES results could provide more insight into the accuracy lost and the time and costs saved.

This thesis shows that Detached Eddy Simulation could be a valuable extension of the methods used to design for aerodynamic performance. A starting point and process have been put into place at Porsche motorsport allowing for the application and further exploration of the full potential of the method.

List of Symbols

Latin Symbols

C_{DES}	Model constant DES
d	Wall distance
$\tilde{d}$	DES length scale
f	Function
F_R	Resolution function
h_{max}	Maximum local grid spacing
k	Turbulent kinetic energy
k_c	Cut-off wave number
l	Characteristic length
p	Pressure
Re	Reynolds number
R_{ij}	Reynolds stresses
S_{ij}	Strain-rate tensor
t	Time
u_i, u_j, u_k	Cartesian velocity components
V	Volume
x_i, x_j, x_k	Cartesian coordinates

Greek Symbols

α	Angle of attack
δ_{ij}	Kronecker delta
Δ	Subgrid length scale
ϵ	Dissipation
κ	Kármán constant
μ	Viscosity
ν	Kinematic viscosity
ν_t	Turbulent Eddy viscosity
ψ	Gravitational potential
ρ	Density
τ_{ij}	Stress tensor

Subscripts

t	Turbulent

Superscripts

$\overline{x}$	Time mean
$'$	Turbulent fluctuation
$\tilde{x}$	Adjusted

List of Acronyms

ADES	Attached Detached Eddy Simulation
CFD	Computational Fluid Dynamics
CPU	Central Processing Unit
DES	Detached Eddy Simulation
DDES	Delayed Detached Eddy Simulation
DNS	Direct Numerical Simulation
FW	Front Wing
GIS	Grid Induced Separation
GTE	Grand Touring Endurance
IDDES	Improved Delayed Detached Eddy Simulation
LES	Large Eddy Simulation
LLM	Log Layer Mismatch
LMP	Le Mans Prototype
MSD	Modelled Stress Depletion
PANS	Partially Averaged Navier-Stokes
PIV	Particle Image Velocimetry
RANS	Reynolds-Averaged Navier-Stokes
RH	Ride Height
RPM	Rotations per Minute
RW	Rear Wing
SA	Spalart-Allmaras
SEM	Synthetic Eddy Method
SGS	Subgrid-Scale
SST	Shear Stress Transport
VLES	Very Large Eddy Simulation
WEC	World Endurance Championship
WMLES	Wall-Modelled Large Eddy Simulation
ZDES	Zonal Detached Eddy Simulation

List of Figures

List of Tables

1 Introduction

Competition and complexity are two words that perfectly describe the world of motorsport. They are tied together, since the desire to outperform can only be satisfied by improving the design, often leading to increasing complexity. In motorsport, maximum speed and thus optimization for drag reduction is often the first aspect that comes to mind. Downforce however, another aerodynamic consideration, might be even more important. This influences the handling capabilities of the car, therefore not increasing the maximum speed of the car directly but the maximum speed at which it can still take a corner or do other manoeuvres [20]. Balancing all of the aerodynamic forces around the car, as well as external forces that might work on it, needs to be done properly. This means that a proper estimation of the aerodynamic forces is vitally important. This estimation can then be used to adjust the design, increase the performance and ensure victories for the cars that are being developed. The victories with the LMP1 in the 24 Hours of Le Mans from 2015 to 2017 show the abilities of the Porsche Motorsport Aerodynamics department to do so. Motorsport is always evolving though and potential improvements are still invited.

There are multiple ways to determine the aerodynamic forces around race cars. Wind tunnel testing and track testing are two of them. These allow pressures and velocities to be measured, from which the forces and their origins can be determined. These methods are costly however, both regarding time and resources. Additionally, sometimes a maximum number of testing hours is set by regulations in the motorsport world. An alternative or a supplement to these methods is the usage of computer simulations. Computational Fluid Dynamics or CFD provides information about the entire flow field instead of just at the measurement points and is becoming increasingly important. The most important question that remains in CFD is how well the simulations represent the actual physical circumstances.

Figure 1.1: Porsche 911 RSR 2019

Over time, many different CFD methods have been formulated, developed and tested. Two criteria to differentiate between these methods include the accuracy of the simulation and the costs involved. These costs are primarily related to the computation time and the memory required to run the simulation. The accuracy refers to how well the simulation is able to predict the actual behaviour. Direct Numerical Simulation (DNS) solves the Navier-Stokes equations governing all continuum flows directly. This ensures a high accuracy but is computationally very expensive. Modelling instead of resolving the flow structures that are low in energy results in Large Eddy Simulation (LES). This method is less time and memory consuming as is does not resolve all the turbulent scales, but also less accurate. Modelling even more of the flow and averaging over the time results in the Reynolds-Averaged Navier-Stokes (RANS) equations. This is an attractive method in industry due to the relatively low costs involved, but it does give less insight into the flow. The main topic of this paper is a hybrid CFD method, Detached Eddy Simulation, combining the RANS method with the LES method. The aim is to obtain more insight and accuracy than RANS while staying economically more attractive to use in industry than LES.

Detached Eddy Simulation or DES thus attempts to combine the advantages of RANS and LES to get an accurate prediction without using too many computational resources. The method simulates the attached boundary layer with RANS. This saves costs related to both the mesh and the time step compared to using LES. LES would need a very fine mesh and time step to resolve that region. When the flow is separated however, RANS is unable to do accurate predictions and the LES method outperforms it easily. The DES method therefore switches to LES in these regions. RANS is currently the standard method used at Porsche motorsport due to the limited costs involved and the short simulation time. DES could be used to increase the accuracy of the predictions especially regarding unsteady flow phenomena with a smaller cost and time penalty than LES.

The main purpose of this thesis is therefore to explore how Detached Eddy Simulation can be applied in the motorsport industry in order to increase the accuracy of the CFD predictions in an efficient way. This includes finding the optimal combination of simulation settings for the types of geometry and conditions considered. Results obtained are compared to wind tunnel data and the standard RANS methods used, to assess the value of the method. Additionally, the method is prepared such that it can actually be put to use by the team at Porsche. This along with a motivation of the recommended settings allows for the practical usage of the method.

Multiple smaller objectives have been formulated for the thesis, which can also be observed in the structure of this report. Outlining the theoretical background as a preparation for the thesis is the first objective. This has partially been done in the accompanying literature study and is extended for the thesis itself. The background of the DES method and the challenges that are still tied to the method are the first part of this theoretical overview. The most important settings that can and might be varied for the DES method are also explored. This is related to the requirements and constraints set by the CFD software that is used, STAR-CCM+ v11.02. The main purpose here is to direct the investigation to within the realistically achievable boundaries. These boundaries are further defined by the application domain, external aerodynamics in motorsport. With all of these topics, the first objective is satisfied and the foundation for the investigation into the DES method is present.

The investigation into the application of the DES method can be divided into two parts, a phase where limited span airfoil models are simulated and a phase where car cases are simulated. The full car simulations are closely related to the final objective, but they are computationally expensive. This is why only a wing section is considered to do the preliminary investigations into the method. The aim of this part of the investigation is to gain practical insight into the influence of the simulation settings. A baseline is formulated on which a number of parameter changes are tested. The simulation results based on these changes can give insight in the properties of the DES method and how these properties can be optimized. The final purpose of this part of the investigation is to formulate a combination of settings advised for the use of the wing model, along with an assessment of the performance compared to RANS and experimental results.

The settings found for the airfoil models can then be used to define a baseline for the full car model simulation. With the knowledge of the airfoil model study the car case set-up can be specified with more practical knowledge making the investigation more efficient. One aim of this final part of the thesis is to define the settings best suited for these simulations. More importantly, the aim is to assess where the DES method with these settings outperforms the standard RANS method used and where improvements are still needed. This ensures it can be used as a simulation tool, but also that a starting point for further explorations is clearly defined.

Overall, the report should provide insight into how the DES method is best applied in industry and which

settings are recommended for this application domain. Additionally, the extensive research done into the variation of the results with certain settings can also aid in defining settings for other industries. Similarly to the way the airfoil results are used to set a baseline for the full car, the recommended settings here can also be used as a baseline for other applications. This makes the research done not only valuable to the Porsche team where it will be applied, but also to others looking to apply this method in industry.

This report is divided into three parts adhering to the three main objectives discussed previously: the theoretical background, the airfoil study and the full car study. Part I starts with Chapter 2 discussing the Detached Eddy Simulation method in general. A more thorough introduction into turbulence and CFD methods is given to put the DES method into context. Also, the initial formulation of the DES method is explained along with a number of variants derived from it. Finally, an overview of the challenges that are still being faced and addressed in literature is given. Chapter 3 then discusses the practical usage of DES as a simulation method. This includes the different parameters that influence the results, like the mesh size and the time step, as well as the implementation of DES into STAR-CCM+. Part I then ends with Chapter 4, where the motorsport context is set. This includes some background information about the different cases chosen for the full car, as well as the motivation for them. Before that however, it discusses the two airfoil models that will be used in the airfoil study and why these have been chosen. The first is the IDF rear wing, and the second the NACA 0012 airfoil. For the latter some experimental data is also given which is used in Part II to assess the performance of DES.

Part II then focusses on the study of the airfoil models. the two models used for this are a high downforce rear wing for a car referred to as the IDF rear wing and a NACA 0012 profile. The baseline set-up for both airfoil models is first documented in Chapter 5. The results obtained with this baseline are presented in Chapter 6, which defines the starting point for the airfoil studies. From here, several parameters are varied to assess their influence. These results and comparisons are presented in Chapter 7. This shows the sensitivity of the method to settings and leads to a combination of recommended settings. Also, some initial conclusions about the capabilities of the method are given. The recommended settings to do rear wing or other airfoil simulations are then given in Chapter 8. In this chapter, a reflection on the processes and results in the airfoil study is also included. This concludes the airfoil study and concludes Part II of this report.

Part III finally focusses on full car simulations using the DES method. The findings from the airfoil studies are used to define a baseline set-up for the full car simulations. This baseline set-up, defined for the GTE car of 2019 developed by Porsche, is documented and motivated in Chapter 9. The results of this baseline are presented in Chapter 10. In the same chapter, a number of alterations to this set-up are tested and compared. The comparisons done are based on RANS results obtained through the standard CFD process in the department, as well as experimental force data from the wind tunnel. The results of the second car studied are given in Chapter 11. This second car is the LMP1 car developed by Porsche for 2015, and two different variants of this car are analysed. More insight into the performance of the method is given here, making use of both force and PIV data from the wind tunnel. Combining the results obtained for the GTE19 and the LMP1 car results in some conclusions drawn with respect to accuracy and costs. This gives a proposed set-up for the car cases which is discussed in Chapter 12. This concludes the full car simulations and Part III of this thesis.

The overall conclusions and recommendations based on this thesis are then included in Chapters 13 and 14. These could serve as a starting point to develop the work further and improve the ratio between the accuracy and the resources needed for the DES method. The three appendices, Appendix A, B and C, provide additional information about the CFD cases. The first gives some insights into the meshes and settings used, while the second focussed on force data resulting from the simulations. The third provides an overview of the settings used in STAR-CCM+ v11.02.

I

Theoretical Background

In Part I of this report, the theoretical background for the application of the Detached Eddy Simulation method in the motorsport industry is given. The theoretical background serves as the baseline from which the investigation into the applicability of DES is started. This first part of the report is divided into three chapters. This ensures that the context of the method, using the method and the application domain all get their deserved overview.

Chapter 2: "Characteristics of the Detached Eddy Simulation Method" contains the theoretical background needed to understand the DES method and to be able to apply it properly. It starts by placing DES in the context of turbulent flows and other CFD simulation methods. Thereafter, it discusses the formulation of the Detached Eddy Simulation method along with a number of its different variants. Finally, the undesirable characteristics of the method are discussed. These are the known sources of error related to DES specifically. This discussion helps identifying them when the method is applied in Parts II and III.

Chapter "3: Detached Eddy Simulation as a Simulation Method" then discusses the practical considerations for using the DES method in general. It mentions some of the parameters that can be adjusted to influence the accuracy and costs of the method. Additionally, the capabilities of the software that is used throughout the thesis, STAR-CCM+ v11.02, are reviewed. This includes the various DES models available, as well as other models potentially involved when using the DES method.

Chapter 4: "The Application of Detached Eddy Simulation to Motorsport" gives an introduction into the application domain: motorsport aerodynamics. Before discussing the full cars that are simulated in Part III of this report, the two airfoil models for Part II are discussed. This includes a discussion of the experimental data of the NACA 0012 airfoil used for the airfoil study. The introduction of the car models gives some background information about their purpose and the configurations considered. This section also states the key parts of the car that will be analysed in order to assess the performance of the DES method.

For a more extensive theoretical background, the literature study accompanying this thesis can also be consulted. Here, more information about topics like DES variants or turbulence models can be found. The choice was made to stay within the constraints originating from STAR-CCM+ and the application domain in the theoretical background of Part I. The literature study also evaluates more results as documented in literature. This includes wing studies with the DES method and a number of automotive related simulations.

2

Characteristics of the Detached Eddy Simulation Method

This chapter puts the Detached Eddy Simulation (DES) method in context and explains a number of the characteristics of the method. The DES method aims to combine the properties of the Reynolds-Averaged Navier-Stokes (RANS) equations method and the Large Eddy Simulation (LES) method. Understanding the motivation behind the formulation of the DES method and understanding the formulation itself is vital for applying it, as its behaviour is not always intuitive. This chapter therefore aims to provide the background information needed concerning this CFD method in order to understand the results obtained in the application.

Before diving into the DES method, an introduction into turbulent flows is given in Section 2.1. The DES method in general is aimed at simulating turbulent flows, which means that understanding this type of flow is important for the understanding of the DES method. Other CFD methods commonly used to simulate turbulent flows are also discussed in this section. These other methods include Direct Numerical Simulation (DNS), Large Eddy Simulation (LES) and the Reynolds-Averaged Navier-Stokes (RANS) equations. Discussing these ensures that the DES method can be explained properly and can be compared to its competitors.

Section 2.2 then focusses on DES completely. The DES97 method, the very first formulation of DES, is discussed first to explain the basic concept. This is the simplest version linking RANS and LES through a single formulation. From here the various DES variants have been derived and some which are relevant for this thesis are discussed. DES variants that are not available in STAR-CCM+ are not discussed in this thesis.

Finally, Section 2.3 reflects the difficulties still present is the application of the DES method despite the many developments. These issues include Modelled Stress Depletion, the grey area problem and the Log-Layer Mismatch. All of these are issues inherently present in the DES method and can introduce sources of error. With these challenges, the final characteristics of Detached Eddy Simulations are covered and the application of the method can be discussed in Chapter 3.

2.1. Simulating Turbulent Flows

In this section, the purpose of the DES method is discussed. This starts off with a general introduction into turbulence in Section 2.1.1. Afterwards, three of the Computational Fluid Dynamics methods often used to simulate turbulent flows are discussed in this section. These are respectively Direct Numerical Simulation (DNS), Large Eddy Simulation (LES) and the Reynolds-Averaged Navier-Stokes (RANS) method. Finally, Section 2.1.5 is devoted to giving a concise overview of some other CFD methods which can be used. These methods aim to increase the accuracy compared to RANS and decrease the costs compared to DNS/LES. These methods have a similar aim to DES, but try to achieve it in different ways.

2.1.1. Introduction to Turbulent Flows

Automotive flows, as many other industrial flows, are often turbulent. Detached Eddy Simulation aims to model these flows and capture the unsteady behaviour related to it. Turbulent flow in general can be described with the aid of the continuity equation [31],

$$\frac{\delta \rho}{\delta t} + \nabla \cdot (\rho u) = 0, \tag{2.1}$$

and the Navier-Stokes equations in all three directions [31],

$$\rho \frac{Du_j}{Dt} = \mu \frac{\delta^2 u_j}{\delta x_i \delta x_j} - \frac{\delta p}{\delta x_j} - \rho \frac{\delta \Psi}{\delta x_j}. \tag{2.2}$$

A solution to these equations has not been found, but by formulating boundary and initial conditions they can be computed numerically. This is discussed in Subsection 2.1.2.

Turbulent, wall-bounded flows contain many irregularities in the velocity field and these can have a big impact on the large scale flow behaviour. Turbulence is often associated with complex behaviour and unsteady flow structures of various length and time scales. These different flow structures are also referred to as turbulent eddies and they are continuously changing in both space and time. Large eddies present in the flow decay into smaller eddies, which in turn decay into even smaller eddies until the smallest turbulent length scale, the Kolmogorov length scale, is reached. The process of large, high energy scales breaking down in small, low energy scales is called the turbulent energy cascade. The smallest length scale towards which the energy cascade extends is governed by the Reynolds number. Flows with a higher Reynolds number have a smaller Kolmogorov length scale and therefore a larger range of length scales to resolve in order to predict turbulence [32].

In automotive aerodynamics, the flow is always wall bounded. This means that the influence of the wall has to be modelled as well, which complicates the simulation. At the wall, the velocity of the flow is zero and in a relatively short distance the flow speed increases until it approaches the free stream velocity. The part of the flow close to the wall where this velocity increase takes place is called the boundary layer. This boundary layer can be divided into multiple layers, where different phenomena are governing the flow behaviour. Close to the wall is the inner layer where viscous shear dominates. This inner layer starts with the viscous sublayer at the wall, with negligible Reynolds stresses and viscous forces dominating this laminar flow layer. The next part of the inner layer is the buffer layer, where the transition to the turbulence dominated layers takes place. The second part of the boundary layer, the outer layer, is dominated by turbulent shear and the pressure outside the boundary layer [48]. Between this inner and outer layer is the overlap layer, also called the log layer. Here, the variables can be approximated as logarithmic functions making the flow properties of the inner and the outer layer line up. Like the outer layer, the log layer is very dependent on the pressure gradient of the flow outside the boundary layer [48]. Modelling the boundary layer accurately is key for prediction of separation and other turbulent phenomena. The complexity of this layer however, makes modelling or resolving it accurately a challenge. The influence of this challenge on the formulation and accuracy of the Detached Eddy Simulation method is discussed in Section 2.3.

The final aspect of turbulence that is important to understand is transition, which is how a laminar flow becomes turbulent. Laminar flow has less unsteady structures and is characterised by smooth patterns. It can have some instabilities however, and transition takes place when these instabilities grown and cause the flow to become turbulent. Laminar flow on a flat plate compared to turbulent has a thinner boundary layer, a less steep velocity gradient in the lower part of the boundary layer, a lower wall shear stress and less mixing within the boundary layer. One method to visualize transition is therefore to look at the wall shear stress. Other methods include the visualization of the unsteady eddies which are present in turbulent flow and not in laminar flow. Laminar flow, like turbulent flow, can also separate and due to the lack of mixing is even more sensitive to it. This separation, on an airfoil, can results in a full loss of lift or in a turbulent reattachment of the flow.

2.1.2. Direct Numerical Simulation (DNS)

Direct Numerical Simulation aims to resolve all of the turbulent scales present in the flow by directly solving the Navier-Stokes equations. This includes the smallest time and length scales, thus up to the Kolmogorov length scale. To be able to resolve this length scale with its characteristic time scale, the grid and the time step used need to be very fine [32]. The time and memory required to be able to do the simulation is very high because of this. The costs related to DNS increase with increasing Reynolds number, as an increasing Reynolds number decreases the length of the Kolmogorov scales and therefore demands a finer grid. DNS has been shown to scale as $O(Re_l^3)$, where Re_l is the Reynolds number based on the integral scale l [33]. In industry, for example automotive, Reynolds numbers go towards 10^5 to 10^7, which means that it is too expensive to use DNS to simulate these turbulent flows [18].

2.1.3. Large Eddy Simulation (LES)

As discussed, turbulent flow consists of flow structures with various length and time scales. The very small structures usually have little energy and are relatively similar for different flows. This means that instead of resolving them, they can also be modelled. Large Eddy Simulation uses this concept to greatly reduce the computational costs compared to DNS and still give accurate flow predictions. The time step and grid size can be increased compared to DNS as they are now governed by the size and speed of the smallest eddies that need to be resolved and not by the smallest eddies present in the flow [32].

A filter is used, often related to the mesh size, to get rid of the small eddies in the flow and the large structures are then resolved. In explicit LES, which is used in the DES formulation, the influence of the small eddies is modelled using a Subgrid-Scale (SGS) model. This SGS model is an additional forcing term in the governing equations which represents all of the interactions between the resolved and the unresolved scales. The type of SGS model influences costs and accuracy, as does the length scale of the smallest length scale that is still fully resolved. Implicit LES on the other hand, chooses a numerical method such that the error of the numerical method cancels the error of not resolving the smallest eddies [33].

Near the wall, the small eddies still have a lot of influence on the general flow behaviour, meaning that the grid needs to be very fine in order to resolve the turbulent behaviour sufficiently. The grid there needs to be refined almost up to the Kolmogorov length scale making the method very computationally expensive for wall bounded flows. Modelling high Reynolds number turbulent flow was in 1997 (and still is today) too expensive to simulate with LES for commercial purposes [41][40]. This is one of the reasons that the DES method was formulated and is still used, as it allows for a coarser mesh at the wall and therefore a reduction in costs.

2.1.4. Reynolds-Averaged Navier-Stokes (RANS)

A method that is often used in industry due to the limited costs is based on the Reynolds-Averaged Navier-Stokes equations or RANS equations. As the name implies, the method uses a Reynolds decomposition splitting the flow variables in a mean part and a fluctuating part around that mean. The mean, or averaged, part of the solution is solved, while the influence of the fluctuating part is only modelled. This greatly reduces costs compared to LES but also decreases the accuracy of the predictions. Averaging the Navier-Stokes equations results in

$$\frac{\delta \overline{u_i}}{\delta t} + \frac{\delta}{\delta x_j}(\overline{u_i}\,\overline{u_j}) = -\frac{1}{\rho} + \frac{\delta \overline{p}}{\delta x_i} + \nu \frac{\delta^2 \overline{u_i}}{\delta x_j \delta x_j} - \frac{\delta}{\delta x_j}(\overline{u_i' u_j'}), \tag{2.3}$$

where $\overline{u_i' u_j'}$ is the Reynolds stress tensor [1]. This Reynolds stress tensor can be expressed as

$$\tau_{ij} = \overline{u_i' u_j'} = \frac{2}{3}\kappa \delta_{ij} - \nu_t \left(\frac{\delta \overline{u_i}}{\delta x_j} + \frac{\delta \overline{u_j}}{\delta x_i} \right), \tag{2.4}$$

with the eddy viscosity ν_t as an unknown [1]. This quantity needs to be modelled, which is done using a turbulence model. There are various turbulence models that can be used to model this eddy viscosity, some of which are discussed in Subsection 3.1.1 as they are also used for DES. The turbulence model used influences both the costs and the accuracy of the RANS method. Different RANS models suit different flow types making the selection of an appropriate model important.

2.1.5. Other CFD Methods

Detached Eddy Simulation is not the only CFD method that aims to get close to the accuracy of LES at a cost similar to RANS. One variation of RANS that aims for this is the Unsteady RANS (URANS) method. An unsteady term is added to the RANS equations, allowing the method to simulate some of the flow fluctuations. This means that flows with large scale unsteady motions can be approximated better. The costs involved however, are higher than RANS as multiple time steps need to be computed. The accuracy however, is lower than LES as still not all unsteady motions are computed [52].

Scale Adaptive Simulation (SAS) is similar to an Unsteady RANS method but portrays behaviour like a hybrid RANS-LES method. In stable flow regions the method behaves like a RANS method. In unstable flow regimes, like separated flow, the break-up of turbulent structures is allowed and part of the turbulent spectrum is resolved using the von Kármán length scale. This is the Scale Resolving Simulation (SRS) mode [28]. The method and motivation behind the method is quite similar to the DES method, but for DES the method goes from RANS to LES instead of from RANS to SRS.

There are also other hybrid CFD methods based on a transition from RANS to LES in the flow domain. The main difference between the methods is the way the transition between RANS and LES is done, and whether the RANS and LES are used simultaneously in some locations or not. The differentiation of DES with respect to these methods is that the transition between RANS and LES is dependent on the local grid size and the distance to the wall. Also, there are regions with pure LES, regions with pure RANS and there is a transition region in between. More about hybrid RANS-LES methods can be found in the literature study accompanying this thesis.

2.2. Definition of the DES Method

The Detached Eddy Simulation (DES) method was first formulated in 1997, after the authors of [41] concluded that LES for a long time would be too expensive to use in industry. The DES method was designed especially for massively separating flows, where pure RANS is not able to model the unsteady flow phenomena well enough to capture the mean flow behaviour. This section starts by discussing the formulation of the original DES method, DES97, in Section 2.2.1. The rest of this section is dedicated to three other DES variants. These variants are Delayed Detached Eddy Simulation (DDES), Improved Delayed Detached Eddy Simulation (IDDES) and Zonal Detached Eddy Simulation (ZDES). More DES variants have been formulated and a few others have also been tested, but these will not be discussed as they are less relevant in the context of the thesis. Well-known DES variants that are not discussed include Attached and Detached Eddy Simulation (ADES), Dynamic Detached Eddy Simulation and Shear-Layer-Adapted Subgrid Length Scale DDES.

2.2.1. The Original Formulation: DES97

DES97 is used to refer to the original formulation of the Detached Eddy Simulation method presented in 1997 [41]. The main purpose of the DES method is to use LES when the grid refinement is sufficient, and RANS where it is too expensive to refine the grid for LES. In practice, this means that the RANS method is used in the attached boundary layers where it is very expensive to use LES, and LES in the separated flow regions where RANS is not able to capture the influence of the unsteady flow behaviour. This results in a reduction in computational costs compared to LES [41].

The DES97 model was originally formulated for the Spalart-Allmaras turbulence model only, although the method was later extended to apply to more RANS models. In this initial formulation, the Spalart-Allmaras model is used both as a RANS model and as a Subgrid-Scale model in LES mode without many alterations. The Spalart-Allmaras model scales the eddy viscosity (ν_t) as

$$\nu_t \propto S d^2, \tag{2.5}$$

where d is the wall distance and S is the local deformation rate [9]. This wall distance plays a role in the destruction term of the Spalart-Allmaras model. In the Smagorsinky model, often used as a Subgrid-Scale model in LES, the eddy viscosity scales as

$$\nu \propto S\Delta^2, \tag{2.6}$$

where Δ is the characteristic length scale [41]. This characteristic length scale governs the length scale of the smallest eddies which are resolved by the LES method. All of the smaller eddies are modelled by the SGS model. Replacing the wall distance (d) in the Spalart-Allmaras model by Δ therefore results in the Spalart-Allmaras model acting as an SGS model. In this formulation, the wall distance d in the Spalart-Allmaras model can be replaced by

$$\tilde{d} = min(d, C_{DES}\Delta), \tag{2.7}$$

resulting in a model that switches between a RANS model and an SGS model [41]. Close to the wall, the wall distance is small and RANS mode is activated. Further away from the wall however, if the grid is sufficiently refined, the LES mode takes over since the characteristic length scale is smaller than the wall distance. The characteristic length scale is governed by the local grid spacing, defined as

$$\Delta = max(\Delta_1, \Delta_2, \Delta_3). \tag{2.8}$$

This ensures that the model only switches to LES mode if the grid can resolve sufficient eddy scales. The parameter C_{DES} is a constant which has been calibrated to 0.65 for the Spalart-Allmaras model based on the turbulent energy cascade in [37]. It is discussed in more detail in Section 3.1.

The principle of using a characteristic length scale to switch between RANS and LES has been used in other RANS models as well, for example in the $k-\omega$ SST model in [44]. The formulation is adjusted slightly,

but the principles remain the same. For the $k-\omega$ SST-DES97 model, the dissipation term is adjusted to contain the adjusted length scale. In this case also, the parameter C_{DES} is adjusted and is even a function of whether the model is in $k-\epsilon$ or $k-\omega$ mode. More about the exact formulation can be found in [44]. Other RANS models need similar alterations, but the definition of the DES length scale always remains dependent on the dominant length scale in the RANS model, a calibrated value for C_{DES} and the local grid spacing. Turbulence models in a DES context are discussed in more depth in Section 3.1.1.

2.2.2. Delayed Detached Eddy Simulation (DDES)

The principle of the DES97 method as discussed in Section 2.2.1 is simple but effective. There is however, one issue with the method. The formulation sometimes results into a transition from RANS to LES while not enough turbulent scales can be resolved to represent the flow yet. The DES method was designed to compute the attached boundary layers with RANS, but when using a (too) fine grid this transition can already take place within the attached boundary layer. The modelled stresses are reduced, while the resolved stresses are not fully present as not enough scales can be resolved on the local grid. This results in Modelled Stress Depletion (MSD) and possibly Grid Induced Separation (GIS). These two phenomena introduce errors in the results and are more extensively discussed in Section 2.3. One solution is to delay the transition from RANS to LES to outside attached boundary layer. Adjusting the grid spacing can help to prevent this, but this is not always desirable and puts even more strain on the grid design. The Delayed Detached Eddy Simulation was proposed in 2004 to delay this transition without adjusting the grid for the $k-\omega$ SST turbulence model in [29]. The solution proposed is to use blending functions to ensure that the boundary layer is shielded from the LES mode, regardless of the local grid spacing.

This initial formulation of the DDES method was only defined for a single RANS model, the $k-\omega$ SST model. It uses the blending functions of that model designed to switch between the $k-\epsilon$ and $k-\omega$ mode to keep the full boundary layer in RANS mode. A general formulation of the DDES method, applicable to multiple turbulence models, is presented in 2006 in [42]. The general formulation is described in this section, for the $k-\omega$ SST-DDES specific one [29] should be consulted. In the Delayed Detached Eddy Simulation method, the definition of the DES length scale is adjusted to

$$\tilde{d} = d - f_d \max(0, d - C_{DES}\Delta), \tag{2.9}$$

for the DDES formulation. Note that the only actual change compared to Equation 2.7 is the inclusion of the blending function f_d. This blending function f_d is given by

$$f_d = 1 - \tanh\left([C_{dt} r_d]^3\right) \qquad \text{and} \qquad r_d = \frac{\nu_t + \nu}{\sqrt{U_{i,j}U_{i,j}}\kappa^2 d^2}, \tag{2.10}$$

dependent on the wall distance d, the velocity gradients $U_{i,j}$, the molecular viscosity ν and the kinematic eddy viscosity ν_t. A second model constant is introduced, C_{dt}, which has a value of 8 for the Spalart-Allmaras model. The blending function ensures that r_d is 1 in the inner part of the boundary layer making f_d zero resulting in pure RANS. Towards the edge of the boundary layer, r_d falls to 0 giving $f_d = 1$ and recovering the DES97 solution. The method still chooses between LES and RANS based on the wall distance and the mesh size outside the boundary layer.

2.2.3. Improved Delayed Detached Eddy Simulation (IDDES)

The Improved Delayed Detached Eddy Simulation (IDDES) extends the capabilities of the DDES method discussed previously. It consists of two branches, where the first one is the DDES method and the other one the Wall-Modelled Large Eddy Simulation (WMLES) method. WMLES generally models the inner part of the boundary layer and does an LES in the remainder of the flow domain. This means that part of the boundary layer is resolved with LES. The method is difficult to use for complex geometries but is very suitable to combine with the DDES method [30]. In practice, the IDDES method is in DDES mode when there is no turbulent content or when the grid resolution does not support resolving the dominant eddies in the outer boundary layer. In these cases, the IDDES method simplifies to the DDES method presented earlier. If there is turbulent content and the grid is fine enough, the WMLES branch is active [38]. Including the WMLES possibility results in an additional blending function to switch between RANS and LES mode, defined as

$$f_b = \min\left(2e^{-9\alpha^2}, 1\right) \qquad \text{and} \qquad \alpha = 0.25 - \frac{d}{h_{max}}. \tag{2.11}$$

The blending function satisfies $f_B = 1$ for $0 < d < 0.5h_{max}$ resulting in a RANS region close to the wall, and $f_B = 0$ for $0.5h_{max} < d < h_{max}$ resulting in LES further out. Besides this blending function, an elevating function f_e is also used in the WMLES definition of the IDDES length scale. This elevating function prevents the reduction of modelled Reynolds stresses around the transition to LES. This prevents the log-layer mismatch (LLM) as discussed in Section 2.3 [38]. The overall formulation for the WMLES length scale is now

$$l_{WMLES} = f_B(1 + f_e)l_{RANS} + (1 - f_B)l_{LES}, \tag{2.12}$$

where for the Spalart-Allmaras model $l_{RANS} = d$ and $l_{LES} = C_{DES}\Delta$. The DDES formulation is almost the same as the original formulation, only the molecular viscosity ν is not used, resulting in

$$f_{dt} = 1 - \tanh\left([C_{dt}r_d t]^3\right) \qquad \text{and} \qquad r_d = \frac{\nu_t}{\sqrt{U_{i,j}U_{i,j}}\kappa^2 d^2}. \tag{2.13}$$

Combining the DDES branch and the WMLES branch in a single formulation results in the following formulation for the IDDES length scale

$$\tilde{l} = \tilde{f_d}(1 + f_e)l_{RANS} + (1 - \tilde{f_d}t)l_{LES} \qquad \text{and} \qquad \tilde{f_d} = \max\left\{(1 - f_{dt}), f_B\right\}. \tag{2.14}$$

The strength of the IDDES method is that if the grid allows it and there is a need to resolve part of the boundary layer it is able to, but that for insufficient grid refinement the safer DDES method is recovered. It performs well in both modes according to [38]. If the WMLES mode is preferable, the costs are increased further due to the grid resolution needed in the outer part of the boundary layer. Various applications however, do show favourable results [16][23].

2.2.4. Zonal Detached Eddy Simulation (DDES)

The desire to have more control over the switch between RANS and LES lead to the development of Zonal Detached Eddy Simulation. The user has to define RANS and LES zones, where grid refinement can be applied only to the LES regions and does not affect the other areas. The specified RANS areas are save from MSD addressed in Section 2.3, thus omitting the need for DDES if the zones are specified properly [10]. As is discussed in [11], the main disadvantage often associated with this method is the need to know the separation point beforehand in order to specify the zones appropriately. A new mode can be added to ZDES however, where the location of the separation is not known and a more DDES like behaviour is observed. The definition of the boundaries in ZDES is the main difficulty and this is the reason that it is not used for this thesis.

2.3. Challenges in the Application of DES

Three major issues that arise during the application of the DES method are Modelled Stress Depletion, the grey area problem and the Log-Layer Mismatch. This section concisely discusses these sources of error and explains how they may be mitigated or recognised.

2.3.1. Modelled Stress Depletion

As discussed in Section 2.2.2, it can happen that the grid spacing is fine enough to do an LES computation according to the DES length scale, but not fine enough to fully resolve the needed velocity fluctuations. This causes Modelled Stress Depletion (MSD). The turbulent eddy viscosity is reduced, as are the modelled Reynolds stresses. These modelled Reynolds stresses however, have not yet been replaced by the resolved ones from the LES computation causing the error. MSD can in turn lead to a specific type of separation, called Grid Induced Separation (GIS) [47]. The DDES method was developed in order to prevent this effect, delaying the transition from RANS to LES to outside the boundary layer to ensure that the stresses can be resolved sufficiently. Still however, the phenomena can occur in the DDES and the IDDES formulation as well. Especially when the grid is refined too much in the streamwise direction, the blending function can break down and cause an early switch from RANS to LES. This is mainly a problem for automatically generated grids used in industry. Parameters in the blending function can be recalibrated and adjusted to prevent the break-down of these blending functions, as proposed in [2].

2.3.2. The Grey Area Problem

The grey area problem refers to the region where the model switches from RANS to LES, as the switch between the two methods is not instant. Here, RANS and LES are both partially used, which might also introduce a

source of error. An abrupt switch means that there is a smaller domain where a mixture of RANS and LES is used. Calibration of this region is difficult, meaning it is more desirable to decrease its extend [40]. Depending on the values used in the blending functions, DDES and IDDES can have a more abrupt change from RANS to LES than DES97. Still however, it remains a source of error and especially when blending functions are tweaked for MSD mitigation, the grey area problem should also be taken into consideration [2]. Changing the model coefficients might ensure more shielding of the boundary layer but might at the same make this switch between RANS and LES too gradual.

2.3.3. Log-Layer Mismatch

The Log-Layer Mismatch occurs when the log layers of the RANS and the LES domains do not line up. The inner log layer comes from the RANS computation and the outer log layer comes from the LES computation. There are still debates as to for which variants for DES this effect is most important, but that it introduces a source of error is clear. This mismatch reportedly causes an underprediction in the skin friction coefficient of about 15% [17]. Generally speaking, various methods from blending to scaling to forcing have been employed to try to get rid of this mismatch. The mismatch itself and thereby the appropriate solution is highly dependent on the numerical scheme used, as well as the turbulence model and the DES variant. There is not a single solution that works best, and most of the approaches are not robust and based on picking the right settings for the case considered [21].

3

Detached Eddy Simulation as a Simulation Method

With the overview of the main characteristics of the Detached Eddy Simulation method in mind, the focus can now shift to using the method in simulations. There are various options that need to be taken into consideration for the DES method. A number of parameters that influence the performance of the method are discussed in Section 3.1. This section begins by discussing the underlying turbulence models which are commonly used in the DES formulation. After this, also other settings like the time step, the mesh refinement and model coefficients are discussed. The second part of this chapter, Section 3.2, focusses on the software that will be used for this thesis, STAR-CCM+ of Siemens. The limitations and options posed for the DES method related to the software are given, along with some other models that are being used together with the DES method. The version of STAR-CCM+ that is being used is STAR-CCM+ v11.02. The reason for that is that the current processes are run in that version which makes it the best comparison and the easiest implementation for the team at Porsche.

3.1. Parameters of Influence

The behaviour of Computational Fluid Dynamics simulations generally depends on many parameters. The discretization in space and time is important, as is the model used and the way that model is calibrated. These factors related to DES specifically are discussed in this section. The influence of changing a certain parameter is not always well defined and not always intuitive for this particular CFD method. This is why many of these factors will come back and are explored with simulations in Part II and Part III of this report. This section starts by discussing a number of different turbulence models. It then continuous with a settings related to time and to mesh design. Finally, some of the model coefficients present in the DES models are discussed. Together these settings influence the way the DES method behaves, changing the accuracy and costs of the simulation.

3.1.1. Turbulence Models

In this section, a number of different turbulence models are discussed. These turbulence models can be used as underlying turbulence models for the DES method or aid in the understanding of other turbulence models. The models discussed are respectively the Spalart-Allmaras model, the $k-\omega$ model, the $k-\epsilon$ model and variations of the latter. In the DES method, these turbulence models act as a RANS model in the attached boundary layers and as a Subgrid-Scale model in the unsteady wake.

The Spalart-Allmaras model was formulated in 1992 [9] by Spalart and Allmaras, who are also two of the founders of the DES method. The DES method was initially formulated only for this turbulence model. In the Spalart-Allmaras model, one transport equation is used to model the eddy viscosity. The equation for the variable $\tilde{\nu}$, closely related to this eddy viscosity, contains a production term, a diffusion term, a destruction term and a trip term. The full formulation of the model can be found in [9]. The DES method is realised by replacing the wall distance, the dominant length scale, in the destruction term by the DES length scale. The model as a RANS model behaves well in steep pressure gradients. On the other hand, it is neither good at predicting transition nor at predicting the decay of homogeneous isotropic turbulence. Also, it was developed

for aerospace purposes and not for general industrial applications.

The $k-\omega$ model is a two equations model, which uses two transport equations for computing turbulence properties. It uses one equation for the turbulent kinetic energy and one equation for the specific dissipation rate ω.The $k-\omega$ shows good agreement for attached boundary layers and has been adapted to also perform well for free shear and separated flow. It is however, sensitive to the free stream value of the specific dissipation rate [27].

The $k-\epsilon$ model is another two equation model similar to the $k-\omega$ model. Instead of the specific dissipation rate however, an equation for the turbulence dissipation rate ϵ is included. More about the formulations of these two-equation models can be found in [49]. The $k-\epsilon$ model does not have the same sensitivity as the $k-\omega$ model to the free stream value of the specific dissipation rate. It odes perform less well in terms of separation prediction. Because of the complementary advantages, combining the two has led to the formulation of the $k-\omega$ Shear Stress Transport (SST) model in 1994 [26].

The $k-\omega$ SST model, like the Spalart-Allmaras model, is often used in combination with DES. It uses the $k-\omega$ model in the inner region of the boundary layer and the $k-\epsilon$ elsewhere reducing the sensitivity to the free stream value of the specific dissipation rate. The two methods are blended using a blending function. Another blending function is used to take into consideration the transport of turbulent shear stress for adverse pressure gradients, hence the name of the method. The two blending functions used are F_1 and F_2, both designed to approach 1 inside the boundary layer and 0 away from the surface. In the DDES formulation of the $k-\omega$ SST model these blending functions are used instead of the ones described before in Section 2.2.2. These blending functions in the $k-\omega$ SST-DDES are still used to delay the transition from RANS to LES to outside the boundary layer. This is the way the DDES method was initially formulated before it was generalized for other turbulence models, as described in [29].

There are several other variations of the $k-\epsilon$ model, some of which reportedly have also been used in the DES formulation. The Realizable $k-\epsilon$ model is one of these, which improves the prediction of flow separation ensuring the realizability constraints are satisfied and by making one of the model constants a function of the eddy viscosity [36]. This model is often used for RANS in industrial applications and also the model used at Porsche Motorsport. Especially in Part III of this report, this is the method that DES is compared to in terms of accuracy and costs.

The $V2-f$ model is another variation of the $k-\epsilon$ model that has also been used in a DES context, featuring three transport equations and an elliptic relaxation equation. The third transport equation transports the energy of the fluctuations normal to the streamlines ($\overline{v^2}$). It was formulated in 1995 by Durbin to predict separating flows and does not need additional wall damping [13].

The Elliptic Blending Model is based on the same principles as the $V2-f$ model. It was derived from the Elliptic Relaxation Model from Durbin [12], but features only a single elliptic equation instead of six. It uses this elliptic equation to accurately blend the redistribution term throughout the boundary layer. The method promises to model the influence of the wall well without the need for additional wall damping models. The full formulation of this model can be found in [24]. A DES variant using this turbulence model is available in STAR-CCM+.

Generally speaking, no consensus has been reached regarding what the best turbulence model is underlying the DES method. So far, limited influence of the turbulence model on the accuracy has been reported in literature [38] [44]. On the other hand, the onset of separation is prediction still by the RANS model intuitively indicating that the ability of the RANS method to predict this will have an influence. This matter will be investigated further in Chapter 7.

3.1.2. Time Step and Time Simulated

Time is another important factor in DES, impacting both the accuracy and the costs of the method. The time step must be small enough to resolve the relevant small time scales, but a very small time step greatly increases the overall computation time. There are a number of tools to estimate the appropriate time step. For vehicle simulations, the recommendation from STAR-CCM+ is to use around 100 time steps for a particle to travel the length of the vehicle [5]. This results in the following estimate for the time step needed:

$$\Delta t_{vehicle} = \frac{Vehicle\ Length}{100 \cdot U_{inf}}. \tag{3.1}$$

The Strouhal number can also be used to estimate the appropriate time step to capture the time scales of the turbulent motions. The Strouhal number in nature is often around 0.2, for example for vortex shedding behind cylinders [48]. Relating the Strouhal number to the shedding frequency can be done as

$$St = \frac{fL}{u}, \tag{3.2}$$

where from the frequency or period of the pressure signal can be computed. For this, a number of time steps needs to be chosen to represent one period, for example 20-100 time steps. The manual of STAR-CCM+ also discusses this method for defining the time step [5]. The time step can then de written as

$$\Delta t_{Str} = \frac{1}{N_T} \frac{L}{u \cdot St} \tag{3.3}$$

with N_T being the number of time steps desirable per time period.

These two methods based on the turbulent time scale however, are not the only criteria. The Courant number is another method to determine a time step. The Courant number can be derived from the CFL condition. For an explicit numerical scheme, this condition must be satisfied for the scheme to be stable. Although an implicit scheme and thus an inherently stable scheme will be used for these simulations, it is still a good indication for the time step. The Courant number, computed as

$$C = u \frac{\Delta t}{\Delta x} \leq C_{max}, \tag{3.4}$$

must be below 1 (C_{max}) to satisfy the CFL condition for explicit schemes [7]. This is also advised to apply for implicit schemes, although in the industry often higher values of the Courant number are deemed acceptable to reduce the turnaround time. The Courant criteria posed on the time step can be written as

$$\Delta t_{Cou} = \frac{C \Delta x}{u}. \tag{3.5}$$

The Δx is based on the finest or critical part of the grid. Ideally, the time step should be based on a Courant number that is below 1. Satisfying all of these conditions for the time step would lead to

$$\Delta t = min(\Delta t_{vehicle}, \Delta t_{Str}, \Delta t_{Cou}), \tag{3.6}$$

with often the Courant based time step being the leading one. This however, might lead to a very costly simulation. This is why not always all of the time criteria are satisfied. In practice, the estimate for $\Delta t_{vehicle}$ is used for the vehicle simulations greatly reducing the costs.

In terms of inner iterations, STAR-CCM+ indicates that 8 should be sufficient to converge a time step but that fewer (between 5 and 3) can be used to speed up the simulation. The number of inner iterations needed and the time step are linked, where a smaller time step with fewer inner iterations if preferred over a larger time step with more inner iterations [5].

Finally also, the physical time to compute and the time to average over need to be determined. For averaging, a number of time periods can be chosen after the periodic flow field has been reached. Determining the time needed to achieve this can for example be done by evaluating the pressure signal in the wake of the airfoil or car. When this pressure signal has reached a periodic state, the averaging can start. Shortening the time this takes can be done by initialising with a converged, steady RANS simulation [5]. Alternatively, for LES 2-5 flow-throughs are recommended before averaging and 5 for the averaging by STAR-CCM+, where one flow-through is the time it takes a particle to travel the field. A final consideration to reduce the simulation time is the initialization with a steady RANS simulation. This can reduce the physical time needed to get a stable solution and hence the number of steps required.

3.1.3. Mesh Refinement

The mesh plays a major role in the performance of the DES method, since it governs the locations of the RANS and the LES regions. Besides this, in the LES regions the mesh influences the smallest eddies that can be resolved, and therefore how much of the solution is modelled and how much is resolved. As discussed in Section 2.3.1, improper mesh design can lead to Modelled Stress Depletion (MSD) and even Grid Induced Separation (GIS). Additionally, in regions where the choice between RANS and LES is ambiguous due to the grid design, the grey area problem as described in Section 2.3.2 can occur.

The Delayed Detached Eddy Simulation formulation already reduces the influence of the mesh design, as the boundary layer is shielded better and MSD is prevented. Still however, the dependence of the LES regions on the local grid refinement are an inherent part of the method. More dependent on the local refinement is

the IDDES method, as it can move into WMLES mode depending on the local grid. This motivates a thorough exploration of the influence of the mesh design for the current applications which will be done in Parts II and III. STAR-CCM+ provides guidelines for designing the mesh adequately which are used to design some of those meshes. These guidelines use the converged results of a steady state RANS simulation to asses the quality of the mesh. The length ratio for the mesh is defined as

$$LR = \frac{l_{turb}}{2 \cdot V^{1/3}}, \tag{3.7}$$

where V is the local cell volume. The turbulent length scale, for a steady RANS simulation with the $k-\omega$ SST turbulence model, can be computed with

$$l_{turb} = 0.09^{-1} \frac{\sqrt{k}}{\omega}, \tag{3.8}$$

using the turbulent kinetic energy (k) and the specific dissipation rate (ω). In the critical areas, the length ratio should be larger than 1 [5].

3.1.4. Model Coefficients

There are several model constants in the formulation of the DES method, partially stemming from the various turbulence models used and partially from the DES formulation itself. A few reportedly can be varied in order to improve the behaviour of the simulations.

The first model coefficient that comes to mind regarding the DES method is C_{DES}. In the DES97 formulation it was the only DES specific model coefficient. The influence of this coefficient is reportedly not very high, as various values have been used to produce good results [43]. The value has been calibrated for different turbulence models separately, where the SST model has two C_{DES} values depending on whether the $k-\omega$ or the $k-\epsilon$ branch is active [5][29].

A coefficient that has been reported to highly influence the results when adapted is C_{dt}, which is present in one of the blending functions (see Equation 2.13). This coefficient influences how much of the boundary layer is shielded from the LES mode and has a different value dependent on the turbulence model. Changing this value therefore changes the resulting division between RANS and LES domains. In order to overcome the Modelled Stress Depletion discussed in Section 2.3.1, the value can be increased delaying the transition to LES further thus shielding the boundary layer more. Recalibration is discussed in [2] and [4]. One of the issues with adjusting this model coefficient is that it could increase the grey area problem discussed in Section 2.3.2.

3.2. DES in STAR-CCM+ v11.02

A number of different DES models are implemented in STAR-CCM+. The software has three different turbulence models underlying the DES method, the Spalart-Allmaras (SA) model, the $k-\omega$ SST model and the Elliptic Blending $k-\epsilon$ model. Within the SA and the SST model, the user can choose to use either the DDES or the IDDES variant. For the Elliptic blending model, only the standard DES method is available. In this section, all three implementations are discussed to gain some insight into their respective options and the differences between the STAR-CCM+ implementation and the literature formulation. Afterwards, some other, general options related to the DES method in STAR-CCM+ are discussed.

3.2.1. Spalart-Allmaras (I)DDES

The Spalart-Allmaras model is the by STAR-CCM+ recommended DES modelling option [5]. The method contains both the DDES and the IDDES formulation of the DES method. Other options include a low-Reynolds number correction, the choice between first and second order convection and the option to apply a curvature correction. Implemented is also a relation to correct values of u^* for coarse meshes, different from the original formulation of the SA model. Additionally, there is the option to use the Synthetic Eddy Method to generate inflow and initial conditions with turbulent content. This method is discussed in Section 3.2.6.

The DDES formulation agrees with the one presented in [47], where the value $C_{dt} = 8$ in the blending function f_d can not be adjusted by the user. Some sources in literature recommend to adjust this value to enhance the performance of the blending function and shield the boundary layer better, for example [2]. The IDDES formulation of the Spalart-Allmaras DES method is as presented in [38]. In this case, it is possible to adjust the C_{dt} value in the blending function.

3.2.2. $k-\omega$ Shear Stress Transport (I)DDES

Another option used in literature which is available in STAR-CCM+ is to use the $k-\omega$ SST turbulence model from Menter [29][3][23]. Again, the two DES variants available are the DDES and the IDDES formulation. Other options here include the choice between first and second order convection, the option to do a curvature correction, a realizability option, a compressibility option and a low Reynolds number damping modification. Additionally, the $\gamma-Re_\theta$ (or Gamma Reynolds Theta) transition model, discussed in Section 3.2.4, can be used alongside the $k-\omega$ SST-(I)DDES model.

Similar to the SA-(I)DDES, the constant in the blending function f_d can only be adjusted for the IDDES formulation. Note that for this model the DDES formulation follows [29] and does not contain the blending function f_d. Instead, the blending function for the transition between RANS and LES is based on the blending function switching between the $k-\omega$ and the $k-\epsilon$ model inherently part of the SST-RANS model. This blending function still causes a delay in the transition, ensuring it takes place outside the boundary layer. The IDDES variant does comply fully to [38], making use of the blending function f_d instead of the one inherently part of the SST-RANS formulation [5]. Again, the constant C_{dt} could be adjusted for the IDDES formulation. The default value here is 20, which is different from the SA-(I)DDES formulation.

3.2.3. $k-\epsilon$ Elliptic Blending DES

According to STAR-CCM+, the Elliptic Blending turbulence model allows for a better description of near-wall flow behaviour [5]. The Elliptic Blending DES method is relatively new in the version of STAR-CCM+ used (v11.02), making the information available about the exact implementation limited. In the user guide of a later version of the method, it is stated that the Elliptic Blending turbulence model is implemented into the DDES variant [39]. In the version used for simulations however, nothing is stated about the DES variant used. This might mean that the DES97 model is implemented, or that the DDES variant is already implemented as is done in later versions. The IDDES version is for sure not available. This means that when using the Elliptic Blending DES method, WMLES can not be entered. The Elliptic Blending turbulence model features its own blending functions governing the redistribution terms, as explained concisely in Section 3.1.1.

3.2.4. $\gamma-Re_\theta$ Transition Model

Turbulence models themselves can not always predict transition accurately, hence the potential need for a transition model. In STAR-CCM+, the $\gamma-Re_\theta$ (or Gamma Reynolds Theta) transition model is available for the $k-\omega$ SST-(I)DDES method. This model is formulated specifically for unstructured CFD codes and needs as an input the free stream edge of the boundary layer. The user specifies the edge of the boundary layer through a field function and the needed variables can be transported from there into the boundary layer by the code. Additional transport equations are solved increasing the computational costs per time step. Also, the number of iterations needed to converge is often increased and some additional noise is added to the solution [5].

Besides the $\gamma-Re_\theta$ transition model, there is also the Turbulence Suppression Model available for all RANS methods. The Turbulence Suppression Model sets the Reynolds stresses, the turbulent viscosity and the production terms in the turbulence transport equations locally to zero and uses laminar flow methods there. It does so in a specified region, meaning that the location of the transition point should be known beforehand. This method has therefore not been further explored as it is unavailable for DES and needs the transition location [5].

3.2.5. Hybrid Spatial Discretization

Because of the hybrid nature of the DES method itself, it is only natural that the solver also uses a hybrid method. For steady-state RANS computations, the second-order upwind scheme is most suitable, while for the unsteady LES methods a central differencing scheme is preferred. As DES uses both RANS and LES within the flow domain, it is desirable to be able to switch between the two. This is why a hybrid second-order upwind/central scheme becomes available for DES in the Segregated Flow model. Like DES itself, it uses a blending function that decides which branch is active locally. This blending function, σ can be calibrated by the user such that the LES domains and the central differencing domains coincide (blending function is 0), as well as the second-order upwind domains with RANS domains (blending function is 1)[5]. This is done by adjusting C_{desT}. The hybrid discretization scheme is available with bounded differencing or without. With bounded differences, the scheme is defined as follows

$$(\dot{m}\phi)_f = \dot{m}\left(\sigma\phi_{sou} + (1-\sigma)\phi_{bcd}\right) \tag{3.9}$$

where the blending is given by the function σ dependent on C_{desT}. Furthermore, the mass flow is given by $\dot{m}$ at face f. The discretization schemes are given by ϕ, where ϕ_{sou} is the second-order upwind scheme and ϕ_{bcd} the bounded-central differencing scheme.

3.2.6. Synthetic Eddy Method

The Synthetic Eddy Method (SEM) is a method implemented in STAR-CCM+ to generate inflow turbulence. For LES, it is important that the turbulence level of the inflow conditions is representative in order to resolve the eddies and the SEM is an effective way of doing so [32]. Furthermore, IDDES chooses between the DDES and the WMLES branch partially based on the turbulent content present locally. This turbulent content can develop in the flow, but can also be generated at the inflow to ensure WMLES wherever the grid allows it [38].

The inflow turbulence can be set specifying an intensity and viscosity ratio, by running a precursor simulation or by recycling turbulence from within the simulation domain [33]. Another method is to generate synthetic turbulence, which is the idea behind the SEM. It superpositions eddies produced at the inlet plane by a shape function. Different parts of the inlet plane can get differently defined eddies, which also influences the costs of the method [19]. The synthetically generated eddies are convected downstream and develop the proper correlations of real turbulence in the simulation domain, meaning sufficient space must be present before the geometry. In STAR-CCM+ it can be specified using an intensity and a length scale, or using Reynolds stresses and a length scale [5]. These can come from another simulation or from approximations based on the wall distance and wind tunnels data.

An additional feature that is available in this function is the mass flow scaling, which ensures a constant mass flow at the inlet. The fluctuations at the inflow plane are then scaled to prevent issues with the solver [5].

4

The Application of Detached Eddy Simulation to Motorsport

This chapter is dives into the application domain the Detached Eddy Simulation method is applied to in this thesis. The main purpose of the thesis is to optimize and evaluate the performance of DES for car geometries, hence the various car cases discussed. To ease the exploration of the DES method however, the method is first applied to smaller, less complicated geometries. This chapter gives insight into the different geometries used and why they were chosen as base for this thesis. First, the two airfoil models used for the airfoil model study in Part II are discussed in Section 4.1. These models serve as a test case to try different settings. The two airfoil models are the IDF rear wing and the NACA 0012. For the NACA 0012 airfoil, some experimental data is also discussed that can be used to assess the performance of DES. Finally in Section 4.2, the full car is discussed. The Porsche 911 RSR or GTE19 car is introduced as well as the LMP1 car of 2015, the 919 Hybrid. Additionally, some of the automotive terminology used is introduced as well as the key areas of the car that are assessed in Part III. This concludes the overview of the application domain.

4.1. Simulating Airfoil Geometries

The airfoil geometries discussed in this section are used for the airfoil model study in Part II. By studying the behaviour of the method on a smaller model first, more tests can be done and more settings can be explored than when starting with the full car immediately. The choice to simulate an airfoil comes from the fact that it is easy to isolate in the geometry and that it is also a typical aerodynamic shape to simulate. The two different airfoil geometries that will be simulated, the IDF rear wing and the NACA 0012, are now discussed consecutively.

4.1.1. The IDF Rear Wing

The IDF rear wing is a high downforce wing designed by Porsche. A wing like this is often simulated as part of the full car, but separate studies also take place. This means that a slice of the wing profile is simulated separately to evaluate and improve the performance of the wing without the need to run the full car. This makes simulating the IDF rear wing not only a good test case to prepare for the full car simulations. The set-up can also be used for future rear wing Detached Eddy Simulations by the team. The IDF rear wing features a quite thick, cambered main component and a flap. It is designed to generate high downforce at low angles of attack. Even though this is a good test case in terms of usability for the team, no experimental data is available making it hard to draw definite conclusions regarding the performance of the DES method.

4.1.2. The NACA 0012

The main purpose of simulating the NACA 0012 is therefore to be able to compare the CFD results to experimental data. The NACA 0012 is less representative for motorsport but serves as a good reference due to the available data. It is not a simple airfoil to simulate due to the sudden stall behaviour, but with the ability of the DES method to model separation well it seems like a suitable challenge. Together with the IDF rear wing, both representation and comparison possibilities are therefore covered by the airfoil study.

Experimental data has been retrieved from literature for the NACA 0012 airfoil in order to assess the accuracy of the various simulations using DES. Different Reynolds numbers are shows in order to allow for an assessment of the influence of the Reynolds number as well. The relevant Reynolds numbers for the application under consideration, rear wings for motorsport vehicles, are in the order of $10^5 - 10^6$. This section presents some data for the separation behaviour of the NACA 0012, along with some background information about the experiments it stems for. Since the IDF rear wing is usually assessed at a Reynolds number around 0.8 million, this is one of the Reynolds numbers for which data is presented. The other Reynolds number chosen for the assessment of the performance of the DES method on the NACA 0012 is 0.5 million.

The first source used to learn more about experimental data of the NACA 0012 is [15] and discusses several experiments with the NACA 0012 at low Reynolds number. The report explains the difficult stall behaviour that the airfoil exhibits which is very dependent on the Reynolds number. This challenging separation behaviour is one of the reasons to choose this model, as the DES method promises to predict separation behaviour well. The NACA 0012 airfoil is therefore an interesting test case. The surface of the NACA 0012 profile can be described as

$$\pm\, y/c = 0.6\left[0.29690\sqrt{x/c} - 0.126(x/c) - 0.35160(x/c)^2 + 0.28430(x/c)^3 - 0.10150(x/c)^4\right] \text{[15]}. \tag{4.1}$$

As this source only presents data for Reynolds number that are slightly larger than the envisioned Reynolds numbers, other sources are used for the actual experimental data.

One of these sources is Sheldahl and Klimas [35], which contains data for various symmetric airfoil profiles at various Reynolds numbers. The Reynolds numbers for which the data is collected are 0.36 million, 0.5 million, 0.7 million and 1.76 million. The experiments for the lowest three Reynolds numbers are done with the same airfoil. This airfoil has a chord of 0.1524 m. The highest Reynolds number experiment is done with an airfoil with a chord of 0.381 m, this makes it easier to attain the higher Reynolds number. The results obtained for the various Reynolds numbers are visualised in Figures 4.1a and 4.1b.

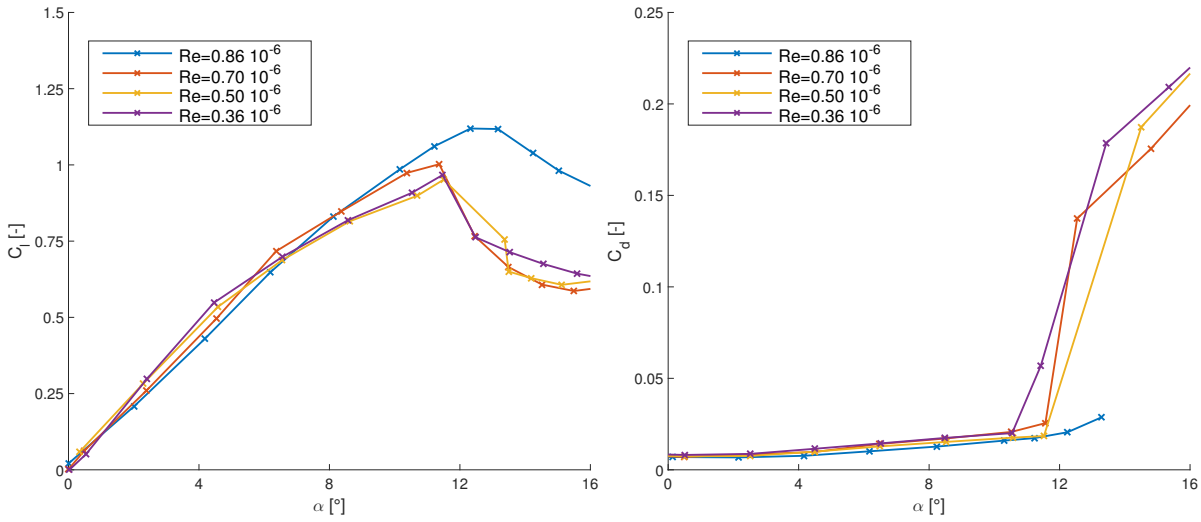

(a) C_l-α graph.

(b) C_d-α graph.

Figure 4.1: Experimental data from Sheldahl and Klimas [35].

The second source used for experimental data is Critzos et al. [6]. The motivation for using two different data sets is the reported spread in force coefficients between different experiments [46]. The full range of angles has been tested, but case only the domain of interest is presented. The lift and drag coefficients are respectively given in Figures 4.2a and 4.2b. Again, the Reynolds number of 0.5 Million is present along with the results for a higher Reynolds number. The figures show that separation occurs at a higher angle of attack and lift coefficient for the higher Reynolds number flow, in agreement with the other experimental data and theory.

Comparing the two sets of data shows that the separation point is not exactly the same, but it is clear that the flow should stay attached until around 11°, and be fully separated around 14°. The aim will be to capture this separation trend with Detached Eddy Simulation. The focus is to capture the results at Re =500,000, for

which both papers have data sets. Due to the spread between these two sets, the aim is to capture the correct trend and not the exact point of separation. This is done in the parameter studies presented in Chapter 7, where both the IDF rear wing and the NACA 0012 are discussed.

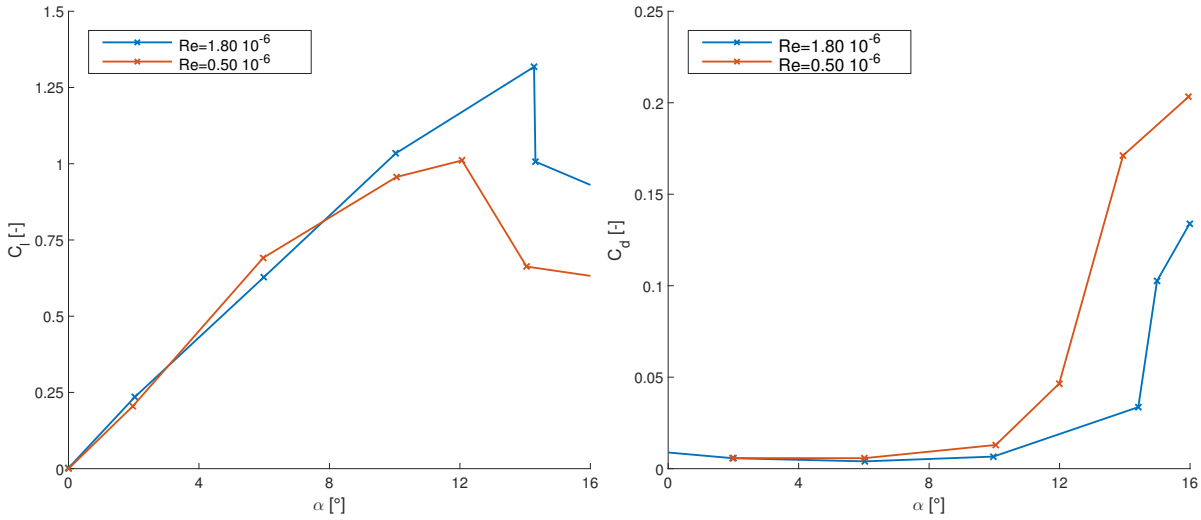

(a) C_l-α graph. (b) C_d-α graph.

Figure 4.2: Experimental Data from Critzos et al. [6].

The third and final set of data is from de Paula et al. [8]. It is data at a lower Reynolds number, around 290,000, but with some insights into the laminar separation bubble that occurs on the airfoil. The lift coefficient is as shown in Figure 4.3. This Reynolds number is lower than the one simulated during this thesis, but the paper contains some insights into the laminar separation bubble formed on the NACA 0012 airfoil as well. This can aid in Section 7.4 to assess the validity of the results obtained for the lowest Reynolds number simulated. Note that this is still higher than the Reynolds number in this paper. The experimental results show the increase in gradient of the lift curve at the lower angles of attack. This is related to the laminar separation bubbles on the airfoil and the aim is to capture this trend. This paper also shows the full chord separation of the NACA 0012 airfoil through experimental flow visualization. The laminar separation bubble and the leading edge separation at higher angles of attack are the aims to predict with the DES method.

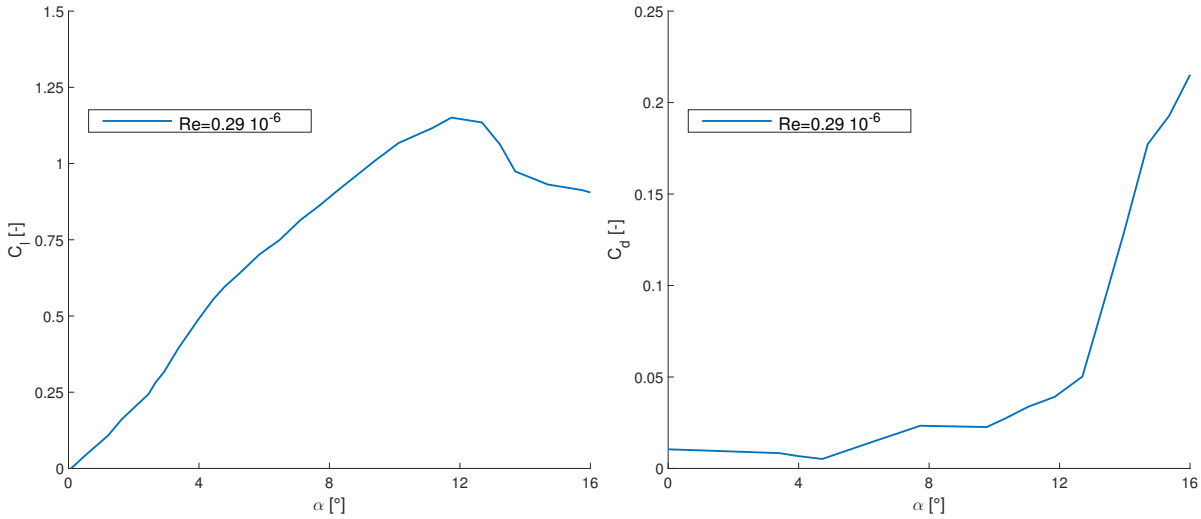

(a) C_l-α graph. (b) C_d-α graph.

Figure 4.3: Experimental Data from de Paula et al. [8].

4.2. Simulating Full Car Geometries

For the full car simulations, a number of different car configurations are chosen. This section describes the differences between the geometries used and their value. Also, a bit of background about the cars themselves is provided. The GTE19 car and the LMP1 car are discussed consecutively. In the final part of this section, the focus areas are highlighted for aerodynamic design in motorsport. This justifies why certain areas of the car are refined and discussed while others are hardly touched upon. First however, some automotive terms are explained as well as the wind tunnel configuration used for the simulations.

4.2.1. Automotive Terminology

A number of different configurations are simulated in Part III of this report. For both cars, at least one straight line and one cornering case is used. A straight line case simulates the car driving in a straight line at a constant velocity. The air is coming straight from the front and the wheels are also straight and spinning at a speed conform the radius and the air speed. The left and the right wheel are rotating at the same velocity. For the straight line case, only half of the car needs to be simulated as the car is symmetric. This reduces the computational costs compared to the cornering case.

In the straight line case, a front and rear ride height are always specified. These indicate the clearance between the car and the floor at the front and rear respectively. With a lower front ride height, the front wing is more loaded due to the ground effect creating additional suction. Combining the low front ride height with a high rear ride height results in the car being pitched downwards more making the front more loaded and the rear of the car less loaded. This means that the front downforce is increased and the rear downforce is reduced. This changes the balance of the car. The balance is the contribution of the front downforce to the total downforce. A higher balance therefore means more front loading and a lower balance more rear loading. This balance is important for handling capabilities since the downforce governs how hard the wheels are pressed into the track [20]. For the cornering case, more parameters are specified. Front and rear ride height are still important, but so are the yaw angle, the roll angle and the steer angle. The yaw angle defines the angle at which the air moves with respect to the car. The roll angle is related to the height of the car at the left and at the right wheels. The steer angle finally is the angle of the wheels with respect to the rest of the car. When going around the corner, the wheels are often not aligned with the rest of the car body. Different corners can be simulated using by adjusting these parameter.

Since the aim is to match the values from the wind tunnel, the wind tunnel domain is partially included in the CFD simulations. This means that the car is standing on a moving belt. This belt moves at the same speed of the air and extends further out than the car in all directions. This mimics the car moving with respect to the road. This moving belt can also rotate realizing the yaw needed for the cornering case. In this case, the air is still coming front the front but the car and the belt are at an angle with respect to the flow. Since the car is lifted, the wheels can be positioned at an angle with respect to the belt as well to include the sidewards sliding of the car in corners.

4.2.2. The GTE19 Car

The GTE19 car, or Grand Touring Endurance car of 2019, as designed by Porsche is called the 911 RSR. It was released in July 2019 and had its first race in September 2019. Its predecessor won in the 2018/2019 season of the FIA World Endurance Championship (WEC) both the GTE manufacturers and the GTE drivers title. The new GTE19 car is expected to defend these titles in the 2019/2020 season. This model will compete for three years in these endurance races. Due to the newness and sensitivity of the design, a number of figures have been altered to hide design features or absolute values throughout the report.

One late stage design configuration is for the simulations and the analysis. This configuration is a very recent and therefore representative case, with some wind tunnel data available for comparison. A straight line case at a single ride height and a cornering case with one specific ride height, yaw, steer and roll are considered. The ride height is chosen such that the car is reasonably flat. Due to the reduced costs involved, most of the simulations on the GTE19 car are done on the straight line case. For the cornering case, a low speed corner was chosen. The reason for this is that the high speed corner is closer to the straight line case since the corner has a larger radius. To see the difference between the straight line and the cornering case better, the case furthest away from the straight line case is used. For the cornering case the full car is simulated doubling the resources needed.

4.2.3. The LMP1 Car

The LMP1 car, or Le Mans Prototype car, of Porsche is called the 919 Hybrid. This car also took part in the FIA World Endurance Championship, where Porsche competed from 2014 to 2017. Porsche won both the manufacturers and drivers championships from 2015 to 2017 and then stopped competing.

Two configurations from the 2015 design process are discussed in the report. The first configuration is referred to as the S09 and is chosen to compare the DES results with PIV data discussed also in [14]. For this case, both straight line and cornering cases are simulated. The second configuration, the S15, was tested at two different ride heights and is compared with global force data. In the second ride height, the nose is closer to the ground and the rear of the car is further up. For the S15, only straight line simulations are done to limit the costs involved. This car is more complex than the GTE19 and is simulated at a higher speed. It is chosen to broaden the research and to show that the settings chosen for the GTE19 can be transferred to another car.

4.2.4. Analysis of the Car Results

Full car CFD simulations generate a lot of data and information about the car. In order to allow for an in-depth view of the results, a number of focus points are defined. The overall forces are compared with different CFD simulations as well as with wind tunnel data. Besides this however, the focus of the aerodynamic comparison will lie mainly on the front wing, the rear wing and the floor of the car.

The wings play a big role in the generation of downforce on race cars. The balance between front and rear downforce is very dependent on the performance of the two wings, and in turn influences the performance of the car. Too little downforce at the front compared to the rear creates understeer meaning that the car is not able to go around the corner. Too much downforce created at the front compared to the rear is also not desirable however, as it creates oversteer resulting in the front wheels taking the corner sharper than the back wheels. Both phenomena reduce the speed at which the car can take a corner and need to be avoided [54]. The rear wing can be positioned at different angles of attack and adjusts this balance. Similarly, the ride height can be adjusted to influence the performance of the front wing and the floor. These parts use the ground effect to improve their performance, hence the impact of the ride height. The flow over the bottom side of the front wing accelerates which creates suction underneath the wing hence increasing downforce. Also, the wake from the front wing has influences the downforce generation of the remainder of the floor due to total pressure losses.

The floor also makes use of the ground effect to produce downforce. The velocity underneath the floor is high and the pressure is low resulting in downforce. The diffuser can enhance this performance of the floor. The underbody surface is swept upwards increasing the effective cross section of air under the vehicle. This helps the air the decelerate and expand towards the ambient flow conditions behind the car. Due to the elliptic nature of low speed aerodynamics however, the air is accelerated in front of the diffuser and keeps this high speed at the start of the diffuser. From there, the deceleration begins. Often, there are side plates present encompassing the diffuser and ensuring the air expands as desired. The diffuser is influenced highly by both the front and the rear wing, as well as on the ride height of the car [54]. Vortices can be enclosed between the side plates which create up-wash over the diffuser. This makes it easier to keep the flow attached to the diffuser. If the diffuser stalls, these vortices can also assure the reattachment of the flow in the diffuser [20].

II

Airfoil Model Study

In Part II of this report, an overview of the analysis of two different airfoil models is given. The first airfoil is a high downforce rear wing model of limited span, also referred to as the IDF rear wing. The second airfoil is the NACA 0012, a wing profile often simulated to test methods. Both airfoil models are used to study the behaviour of the Detached Eddy Simulation method in STAR-CCM+ at lower costs than the full car model. This gives some first insights in the abilities of DES and the influence of certain options. These insights can be used to more efficiently do the full car simulations and analysis in Part III.

Chapter 5: "Baseline Settings Airfoil Models" gives an overview of the baseline from which the airfoil models are analysed. The most important physics models are discussed, as well as the settings within these physics models. Besides this, also some of the boundary conditions and the time step are discussed. The design of the mesh is discussed for the two models separately, with an explanation of the differences between their baselines. These baselines are used to evaluate the influence of adjusting certain parameters in Chapter 7.

Chapter 6: "Baseline Results Airfoil Tests" then discusses the results for the baseline discussed in Chapter 5. Analysing these results already gives a number of conclusions about the DES method and serves as a starting point for the parameter studies in Chapter 7. This chapter includes results for both the IDF rear wing and the NACA 0012 airfoil model.

Chapter 7: "Airfoil Parameter Variations" then dives into the application of the DES method to both the IDF rear wing and the NACA 0012 airfoil. It explains which settings are changed and what the influence of these changes is. Examples of settings to adjust include the DES variant, the underlying turbulence model, the time step and the mesh refinement. This should give some first conclusions to use for the set-up of the full car simulations.

Chapter 8: "Recommendations for Simulating Airfoil Models" finally gives an overview of the proposed settings for the simulation of this and other rear wings. The conclusions presented here follow from Chapter 7 and include not only the settings, but also the motivations behind them. These settings can directly be used for rear wing analysis in the team at Porsche and will also serve as the baseline for the analysis performed in Part III. This chapter also reflects on the results obtained and the validity of the methods used.

5

Baseline Settings Airfoil Models

An IDF rear wing airfoil and a NACA 0012 airfoil are used to do preliminary investigations regarding the performance of the DES method. Based on initial experience and guidelines found in literature, a baseline is formulated from which the tests are started. These settings are partially set in the simulation file that is used, and partially specified through a Java macro that is being used to run the simulations. A number of these baseline settings are the same for the IDF rear wing and the NACA 0012. These are discussed in Section 5.1. Afterwards, some specific settings for the IDF rear wing, focussing especially on its initial mesh design, are discussed in Section 5.2. The same is then done for the NACA 0012 airfoil in Section 5.3. After this, the desired output used for the analysis is presented in Section 5.4. This ensures the appropriate information can be extracted from the simulations to judge the performance of the method under different circumstances.

5.1. General Airfoil Settings

An extensive list of settings is available in STAR-CCM+. Often, default parameters and models are chosen based on other models. This section provides an overview of the chosen models and other settings chosen as a baseline. First, the models used are discussed in Section 5.1.1. After this, the settings within these models are discussed. Here, only key settings and any alterations from the default STAR-CCM+ settings are addressed.

5.1.1. Physics Model Selection

The “Physics Models" are chosen in STAR-CCM+ to set-up the simulation. These contain the different models needed to use Detached Eddy Simulation, like Implicit Unsteady flow, and other models to improve the results, like Cell Quality Remediation. Not all models model the physics itself, but they all below to this category in STAR-CCM+ and are needed to support the models that acutally do model the physics. DES is an inherently three-dimensional, unsteady method which governs a number of the models which need to be chosen. The DES method needs the following models [5]:

- Three Dimensional
- Implicit Unsteady
- Segregated Flow
- Turbulent

Additionally, the following general models are chosen for the baseline:

- Gas
- Constant Density
- Cell Quality Remediation
- Gradients

A few notes about the choice for the different models here. Starting with the latter, Cell Quality Remediation helps to get solutions on cells with a poor quality. This model is therefore valuable when automatic mesh generation is used. The model works only around cells with bad quality and might increase computational costs if mesh changes occur during the simulation [5]. Since the airfoil models do not have mesh changes during the simulation this increase in costs is less important than the increase in robustness of the solution.

The Constant Density model simply assumes that the density does not vary through the continuum. This is a valid assumption for subsonic flows at Mach numbers below 0.3, which is a criterion these simulations satisfy. It is one of the options when the “Gas" model is selected, among Real Gas and Ideal Gas. It assumes an ideal gas with density as a constant. Finally, the Gradients model is the only Gradient Metrics model available with the settings needed for DES. Regarding the DES formulation specifically, the following settings were chosen as a baseline:

- Detached Eddy Simulation
- Spalart-Allmaras Detached Eddy
- Exact Wall Distance
- All y+ Wall Treatment

These are the baseline settings recommended by STAR-CCM+. The Spalart-Allmaras turbulence model is the model for which the DES method was originally formulated. In terms of the wall distance, the Exact Wall Distance or the PDE Wall Distance are available, where the first is recommended due to its more accurate behaviour. The PDE Wall Distance reportedly is faster however. The All y+ Wall Treatment method is the most general wall treatment model, recommended to use whenever available [5]. For the SA-DES method the Low y+ Wall Treatment model is also available, but this should only be used if $y+ < 1$ everywhere which is not ensured on the full car nor on all of the airfoil simulations.

5.1.2. Model Settings

The settings chosen within these models are discussed in this section. First of all for the Spalart-Allmaras Detached Eddy model, the curvature correction is turned off, the convection is 2nd-order, the Low Re Correction is turned on and the IDDES formulation is used. This IDDES formulation allows for the adjustment of a number of IDDES coefficients, which for now are left at their default values. The value $C_{dt} = 8$ will however, can be increased as suggested in literature to prevent grid induced separation [2].

As is recommended for DES, the Hybrid-BCD or Bounded Central Differencing scheme is used for the convection term in the Segregated Flow model. This is the automatic and recommended setting by STAR-CCM+. This blends between Second Order Upwind and the Bounded Central Differencing scheme depending on whether a RANS or an LES domain is encountered. A blending factor can be adjusted here as well, adjusting where the transition between the models takes place. This is left to the default of C_{desT}=0.15 as STAR-CCM+ recommends to leave it unchanged. This factor corresponds to the theory as discussed in Section 3.2.5.

Air is chosen as an ideal gas to represent the continuum. The density is set to 1.18415 kg/m^3 and the dynamic viscosity is set to $1.85508 \cdot 10^{-5}$ Pa s. These are chosen to match the full car simulations. The purpose of the airfoil simulations at Porsche normally is to design the rear wing separately at a lower cost, but then it is desirable to simulate it at the same conditions as the full car. In terms of the reference values for the physics settings, the Minimum Allowable Wall Distance is set to $1.0 \cdot 10^{-6}$ m ensuring that no numerical errors occur in bad cells. The Maximum Number of Eddies is set to 1000 and tied to the Synthetic Eddy Method. When this number is set too low, the initial turbulence can be destroyed as not all eddies are formed. Forming too many eddies however, can increase computational resources needed. Until the Synthetic Eddy Method is used to specify initial turbulence this settings should not influence the solution. Lastly, the reference pressure to which all other pressures are set, is set to 101325 Pa.

5.1.3. Boundary and Initial Conditions

For the continuum, the initial conditions feature a 0 Pa pressure difference with the reference value, no Synthetic Turbulence and a turbulence specification based on the turbulent viscosity Ratio and turbulence intensity. The turbulent viscosity ratio has a constant value of 10 and the turbulent intensity has a value of 1%. The turbulence settings are chosen based on the settings that will be used for the full car. Additionally, an initial velocity is set equal to the free stream velocity. In the baseline simulations, this initial velocity is always at a zero angle of attack even if the angle is increased. At the boundaries, the same initial conditions are present.

For the airfoil, a no-slip, smooth wall is used. The outlet is a pressure outlet at 0 Pa pressure difference with the reference value. Additionally, the Backflow Specification is Boundary-Normal. Components would be another option more suitable in case very large angles of attack are simulated. Since the angles simulated are based on finding separation and not on simulating fully separated flow, they will stay low and Boundary-Normal can be used. The inlet is a Velocity Inlet. As a default, the Synthetic Turbulence Specification is turned off, as is the Mass Flow Scaling option linked to it. The velocity is specified with X and Z components, based

on the free stream velocity and the angle of attack. The two sides have symmetry conditions posed on them, meaning that the gradients are set to 0 at the boundaries.

For the IDF Rear Wing Airfoil, the same flow domain and boundary conditions are used as for the NACA 0012 wing. The boundary conditions for the flap are the same as the boundary conditions for the main wing. Note that for both the IDF Rear Wing and the NACA 0012 Airfoil, a positive angle of attack is defined as the air coming in from above. This is illustrated in Figure 5.1.

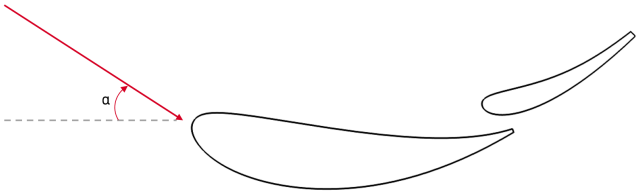

Figure 5.1: Definition of the Angle of Attack with respect to the Airfoil.

5.1.4. Solving and Stopping Criteria

All of the Under-Relaxation factors and other expert properties are kept at their defaults. The time step is set to 0.001 or 10^{-3} s with a first order Temporal Discretization. The time step is based on one of the three criteria for the time step, Equation 3.3. The Strouhal number is 0.2 and the velocity of 50 m/s. As a length scale, the chord of the airfoil is taken. Using around 25 steps per time period of 0.025 s this results in the given time step. Note that using the thickness of the airfoil might be a better indicator for the period. This would result in a smaller period and only about 3 steps per time period. This already indicates the possible need to decrease the time step to about 10^{-4} s, something that is evaluated in Chapter 7. This Strouhal number is an assumption based on vortices coming off a cylinder [48]. More about the time step can be found in Section 3.1.2. Note that the other two criteria for the time step are not satisfied. The first criterion in Equation 3.1 is defined specifically for vehicle simulations and does not apply here. The Courant criterion in this case would result in a time step of $O(10^{-5})$ due to the very fine mesh. The fact that the Courant number is around 1 is further discussed in Section 7.3.

The default number of inner iterations is 3 per time step. This is the recommended minimum from STAR-CCM+ [5]. The total physical simulation time is set to 1.05 s, where the final 0.05 s are used for averaging. This corresponds to 2 periods to average over and is reviewed after the initial results. This comes down to a maximum of 3150 iterations per simulation. Since all of these settings are aimed at simulating at the minimum costs possible, they are evaluated in Chapter 7 to see how they affect the accuracy.

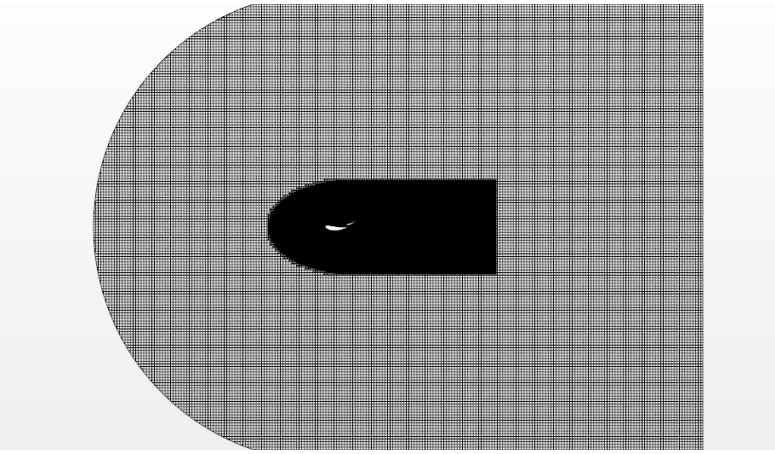

Figure 5.2: IDF Rear Wing Mesh Full Domain.

5.2. IDF Rear Wing Specific Settings

The velocity at which all of the IDF simulations have been executed is 50 m/s. The reference area is 0.00492 m^2. This value is based on a span of 0.02 m and a chord of about 0.246 m, which means that a slice of about

8% of the chord of the airfoil is simulated. The Reynolds number considered is 0.785 million.

The mesh is as depicted in Figures 5.2 to 5.4. The base of the mesh features hexahedral, isotropic volume cells with an edge length of 0.2 m. A number of refinement areas are defined. The coarsest refinement region, shown in Figure 5.2, has an anisotropic refinement in X and Z to an edge length of 0.005 m. Similarly, the refinement region shown in Figure 5.4 has an anisotropic refinement in X and Z to 0.001 m. This figure also shows the wake refinement around the airfoil. This refinement goes up to 0.3125 mm in X and in Z.

Figure 5.4 shows the prism layers of the mesh, which are present up to 0.0012 m from the surface. The first cell at the surface has a thickness of $5.0 \cdot 10^{-6}$ m and the stretch ratio is 1.2765. The prism layers are isotropic in the non wall normal directions only. The edge length in Y is therefore refined up to the 0.3125 mm in the prism layers. Since the Growth Rate of the Wake Refinement is set to Slow, the Y direction also already features refinement outside the prism layers. This is illustrated in Figure 5.6a.

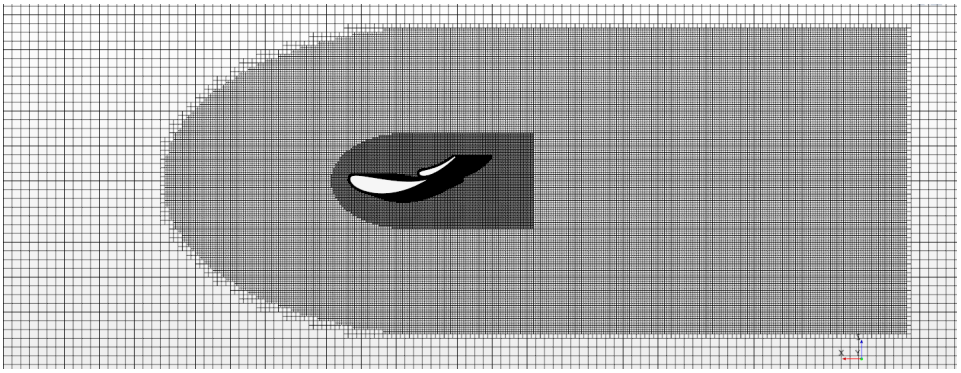

Figure 5.3: IDF Rear Wing Mesh Zoomed in.

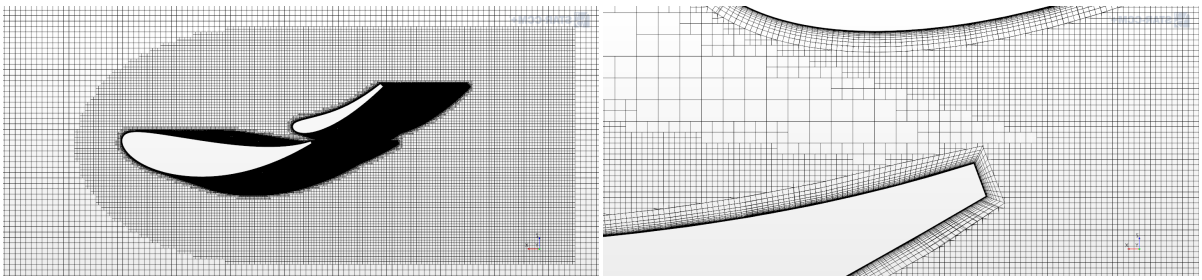

Figure 5.4: IDF Rear Wing Mesh Close-Up.

5.3. NACA 0012 Airfoil Specific Settings

The NACA 0012 is run at two different velocities, namely the 50 m/s which is the standard for the IDF rear wing and 37.7 m/s. The reason for choosing two different velocities is to be able to compare the results to experimental data at two different Reynolds numbers, 0.8 and 0.5 Million respectively. The reference area for the NACA 0012 is 0.005 m^2. The span is the same as the IDF rear wing, 0.02 m and the chord is 0.25 m. Again, the span is approximately 8% of the chord. The mesh around the NACA 0012 airfoil is as depicted in Figure 5.5.

The base of the mesh again features hexahedral, isotropic volume cells with an edge length of 0.2 m. The two refinement areas are similar to the ones described for the IDF Rear Wing, although this time isotropic refinement was chosen. The coarsest refinement region has an isotropic refinement 0.005 m and the refinement region shown in Figure 5.4 has an isotropic refinement of 0.001 m. Also the wake refinement is isotropic, up to the same value of 0.3125 mm as in the IDF rear wing. Additionally, a slightly coarser wake refinement is added around the normal wake refinement to transition from the coarse to the fine mesh slower. This has an isotropic value of 0.625 mm.

The prism layer has exactly the same features as the IDF Rear Wing, with a total thickness 0.0012 m, a stretch ratio of 1.2765 and a thickness of the near wall prism layer of $5.0 \cdot 10^{-6}$ m. Because this mesh features isotropic refinement regions, the main difference between the meshes can be seen in Figure 5.6b, where the mesh in spanwise direction is shown. Figure 5.6a shows very stretched cells with high aspect ratios for the IDF

rear wing, while the NACA mesh has isotropic cells up to the prism layers shown in Figure 5.6b. Theoretically, the NACA 0012 mesh should be more suitable in this case, since the longest edge length influences the smallest eddies that can be resolved by LES. This would make an isotropic mesh more attractive. It is discussed in more detail in Section 7.2.

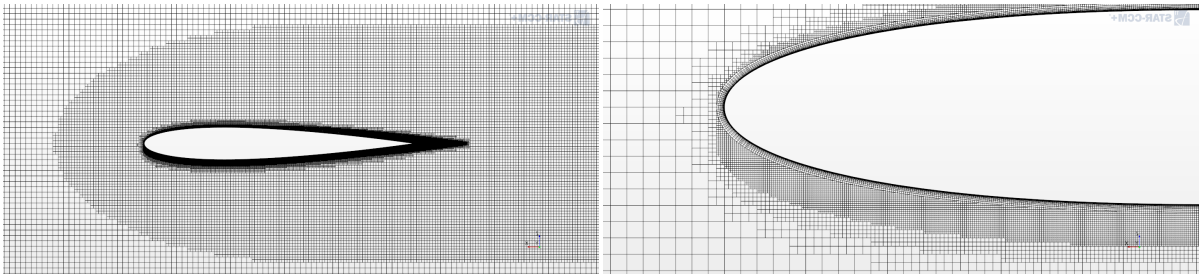

Figure 5.5: NACA 0012 Airfoil Mesh Close-Up.

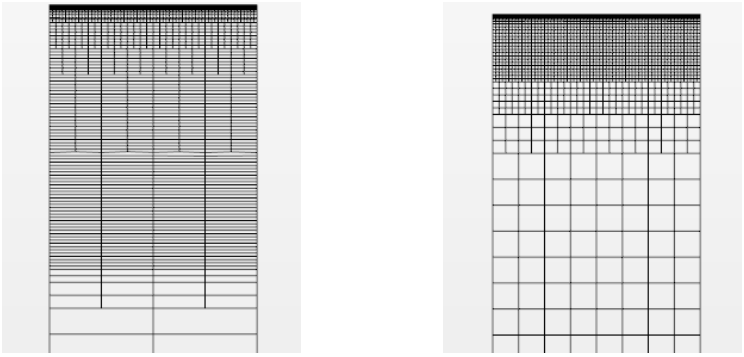

(a) IDF Rear Wing. (b) NACA 0012 Airfoil.

Figure 5.6: Spanwise Refinement Airfoil Meshes.

5.4. Post Processing Information

A number of different outputs are generated during and after each simulation. This section gives an overview of which outputs are generated and why they are used. The simulation has two types of output, the first are images and the second are CSV files. As described in Section 5.1.4, a period of 0.05 s is used to average results over. This is to ensure that at least two time periods are captured. This setting is chosen to minimize simulation costs but might not be long enough to capture the results well and is therefore reviewed in Section 7.3. During this period, for some variables multiple images of the flow field are exported which can be put together into a movie to visualize the unsteady flow phenomena. Examples for variables visualized this way are the Total Pressure Coefficient and the Turbulent Viscosity. Besides this, a number of images are created based on the results averaged over this time period to create mean values. Examples here are the Courant Number and again the Total Pressure Coefficient. Finally with respect to pictures of the flow field, some instantaneous fields are only outputted for the final time step. Examples here are y+ values at the surface or the vorticity.

All of the aforementioned examples are based on field functions automatically generated by STAR-CCM+ based on the chosen models. There is also an option to include user defined functions and create flow field images from those. Different blending functions, as well as the Length Ratio, all of which are discussed in Chapter 3, could also be included in the post processing this way. For the hybrid blending function, not only flow field images are exported. XY-plots with the value of the hybrid function over the wall distance in the boundary layer of the airfoil are also created. This makes it easier to identify the RANS and the LES domains in the boundary layer. Other than that, the forces in C_X and C_Z are outputted for every iteration. These are also included in a CSV file which can be used to compute the lift and drag coefficients. Finally, also the pressure coefficient distribution over airfoil (and flap) is outputted both as a plot and as a CSV file to ease comparison. Together, all of these forms of post processing data aid in the analysis of the results.

6

Baseline Results Airfoil Tests

This chapter uses the settings presented in Chapter 5 to analyse simulation results of the IDF rear wing and the NACA 0012 airfoil. For the IDF rear wing, no experimental data is available and the baseline results serve as a starting point from which various settings are tested. The influence of changes can be assessed, but the absolute values obtained can not be evaluated in terms of accuracy. The NACA 0012 airfoil fulfils this purpose, as the results obtained can be compared with the experimental data in Sheldahl and Klimas [35] and Critzos et al. [6]. First the IDF rear wing is discussed in Section 6.1. Even though this chapter serves as a discussion of the baseline settings, RANS results are also presented to put the results into perspective. Section 6.2 then does a similar analysis on the NACA 0012 airfoil, where besides the RANS results also experimental data is used for the comparison. Conclusions obtained from these simulations are the input for the parameter variation in Chapter 7, where the purpose is to improve the results and acquire the knowledge needed to set up the full car simulations.

6.1. IDF Rear Wing Results

The results for the IDF rear wing contain the angles from 0° to 12° with 2° intervals. The wing is designed to produce a reasonably high downforce already at the operationally low angles of attack. Due to confidentiality, the generated lift coefficients are hidden but for the purpose of comparison the axis for the IDF rear wing are kept equal throughout this chapter. Since no experimental data is available for the wing on its own, the exact separation value is not known. This issue is addressed in Chapter 4 and is the primary reason that a second airfoil, the NACA 0012, is part of this airfoil study.

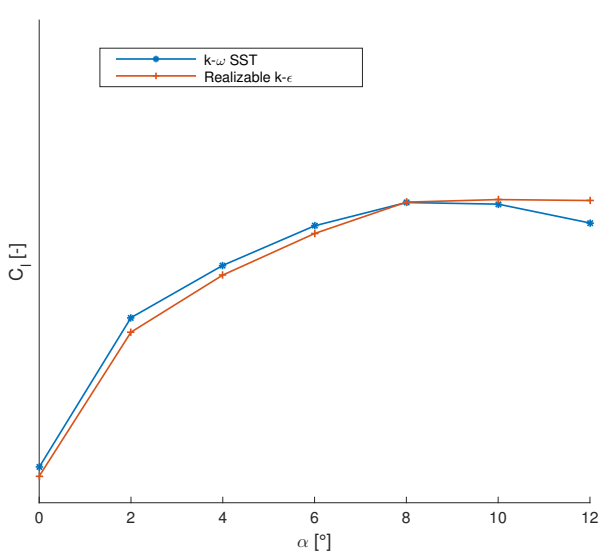

Figure 6.1: IDF Rear Wing C_l-α Polar Realizable $k-\epsilon$ RANS Model.

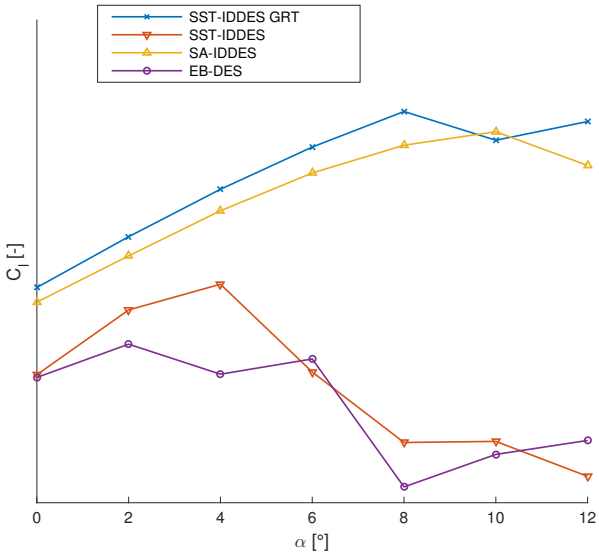

Figure 6.2: IDF Rear Wing C_l-α Polar for Multiple IDDES Simulations.

Figure 6.1 shows a lift curve obtained with the CFD model that is usually used by the Porsche Motorsport team for their full car simulations, the Realizable $k-\epsilon$ RANS model. These results are obtained for the baseline mesh used for DES as well and the lift curve is shown up to 12°. No full separation is visible for the Realizable $k-\epsilon$ RANS model, although the lift curve does flatten out. The $k-\omega$ SST-RANS model shows a gradually decreasing lift curve. The first purpose of the simulations on this airfoil is to assess the differences between these results and the results obtained with DES.

Results obtained with the DES method are shown in Figure 6.2. Note that beside the SA-IDDES model defined as the baseline, the other options from STAR-CCM+ v11.02 are also presented. This allows for a comparison between the different turbulence models and a quick evaluation of the validity of the initial choice. Two of the simulations show a graph quite similar to the RANS results in Figure 6.1. As the scale is the same in the two graphs, the DES method does seem to predict a higher lift coefficient. The other two simulations show a much more separated flow already at lower angles of attack. Since little documentation is available about the EB-DDES method and the initial results seem furthest off it is not extensively discussed here. Also the other lift curves on their own do not show too much about validity of the results, especially since the actual flow behaviour is not known. Because of this, the results are assessed in a bit more detail before the parameter variations are performed.

The IDDES method is characterised by its blending functions. Although the model coefficients are different between the SA-IDDES and the $k-\omega$ SST-IDDES, they can be compared quite easily. Figure 6.3 shows such a comparison, where the instantaneous blending functions at 4° are compared. The blending functions are quite constant over time, with fluctuations mainly present in the regions between the red and the blue regions. Note that blue in this case indicates the region where LES is used allowed and red where RANS should be used. This comparison shows that the SA-IDDES has a much smaller RANS region than the $k-\omega$ SST-IDDES simulations and therefore does an LES up to much closer to the wall. Important to note here is the fact that sometimes there is an LES area close to the wall, while there is a RANS area further out. This indicates a break-down of the blending functions and is undesirable behaviour which might be mitigated by redesigning the mesh. The Elliptic Blending model is not included in this comparison since not enough information about the implementation into STAR-CCM+ is available to compute the RANS and LES regions.

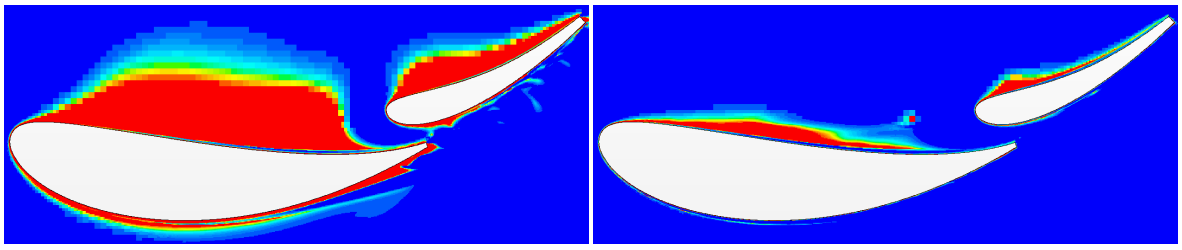

(a) $k-\omega$ SST-IDDES. (b) SA-IDDES.

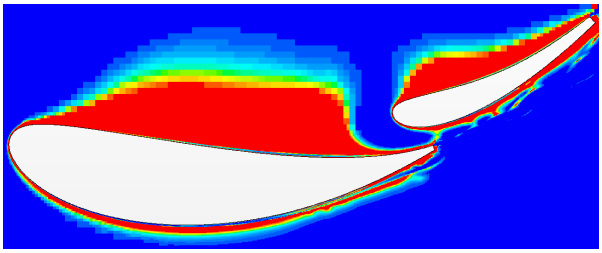

(c) $k-\omega$ SST-IDDES including $\gamma - Re_\theta$ Transition Model.

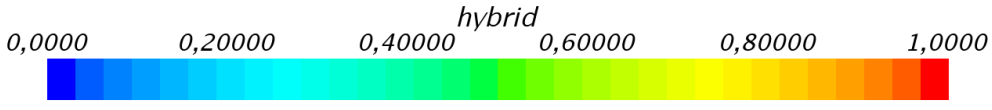

Figure 6.3: $\tilde{f}_d$ Comparison Baseline at 4°.

Interesting to compare is also the pressure distribution over the airfoil, which is done for the SA-IDDES model, the $k-\omega$ SST-IDDES model and the $k-\omega$ SST-IDDES model with the transition model. Figure 6.4 shows these distributions at the final time step and for a plane in the middle of the simulation domain. The $k-\omega$ SST-

IDDES without transition model has a much lower pressure peak on the main wing and a separation near the trailing edge. This explains the lower lift coefficient visible in the lift curve. The other two models have more similar profiles. The instantaneous pressure distribution of an unsteady method is plotted causing some of the unsteadiness of the wake to be visible near the trailing edge of the main plane. The transition model has a major impact on the results, although the origin of this impact can not be identified here. This is something to investigate further in Chapter 7.

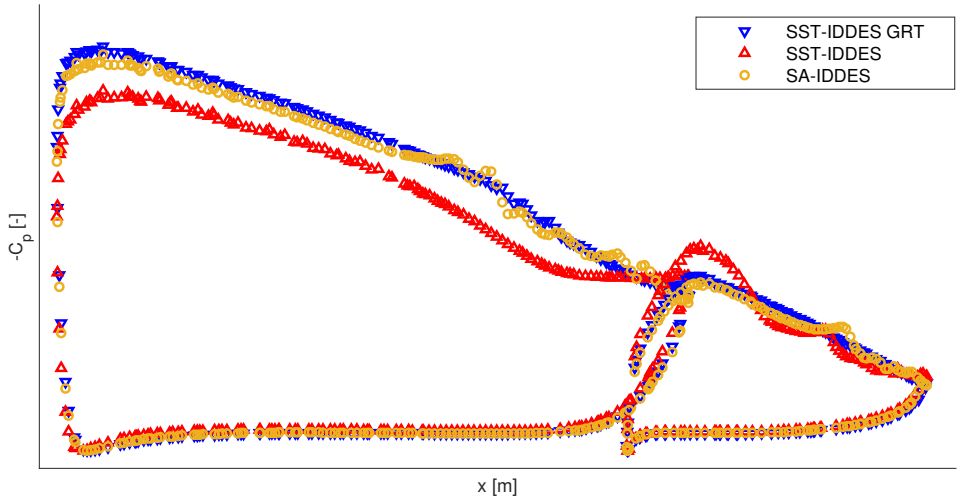

Figure 6.4: IDF Rear Wing Pressure Distribution at α=4°.

6.2. NACA 0012 Airfoil Results

For the NACA 0012 airfoil, the results for the lift and the drag coefficients averaged over the final 0.05 s at Re=0.8 million are shown in Figures 6.5a and 6.5b. The baseline is simulated at an angle of attack from -4° until 16° with 2° intervals. The Reynolds number for these results is a similar to what is used for the IDF rear wing. The lift curve shows that the gradient of the lift coefficient does flatten slightly at the high angles of attack, but rapid stall is expected at a lower angle of attack and lower lift coefficient already. This phenomena is discussed in Section 4.1.2. The $k-\omega$ SST-IDDES simulation without transition model does show a separated flow at 14°, but due to the unsteadiness of the solution the lift coefficient increases again at 16°.

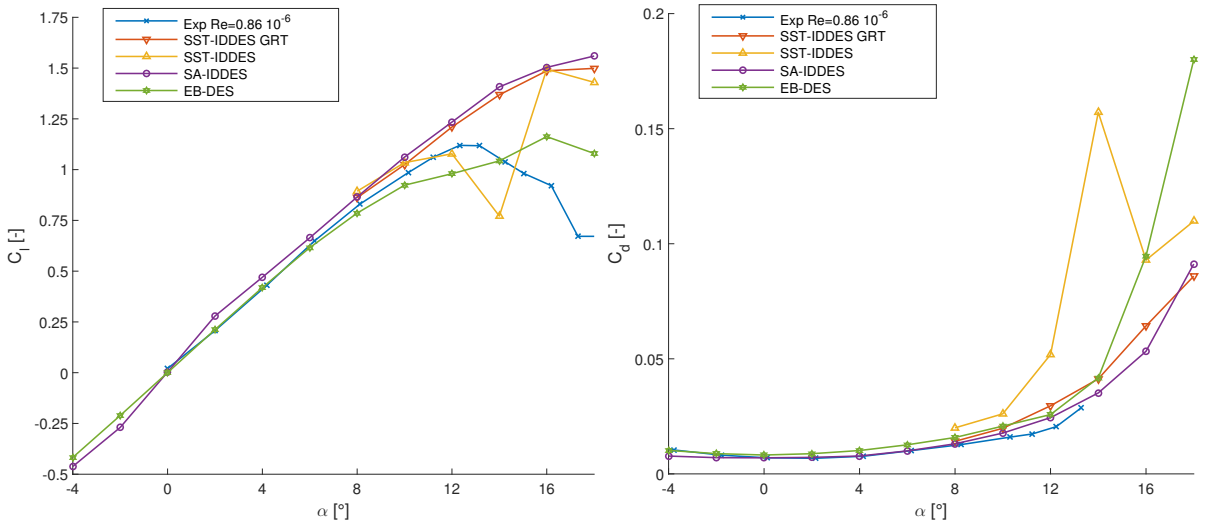

(a) C_l-α. (b) C_d-α.

Figure 6.5: NACA 0012 Airfoil Baseline polars Re=0.8·10^6, experimental data from Sheldahl et al. [35].

An explanation for this is the convergence behaviour for the baseline set-up. The development of the forces over time for the $k-\omega$ SST-IDDES model is shown in Figure 6.6. It shows that the solution is not converged to a stable value yet at the end of the simulation time. This means that the averaging period of 0.05 s is not enough to give accurate results and explains the odd lift curve in Figure 6.5a. Oscillations are expected since it is an unsteady solution and not a convergence to a steady value, but these oscillations are expected around a more stable value. Improving this is one of the aims of Chapter 7. Possibilities here are improving the mesh, the time simulated and the temporal discretization.

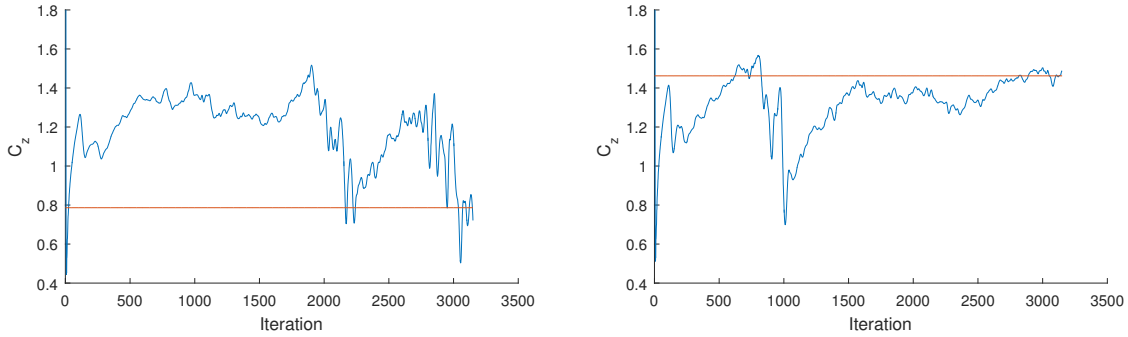

(a) α=14°. (b) α=16°.

Figure 6.6: NACA 0012 Airfoil Stability $k-\omega$ SST-IDDES Re=0.8E6.

Figures 6.7a and 6.7b then show the lower Reynolds number for which experimental data has been gathered. The different models are closer together and all keep a high lift coefficient also at the highest angles of attack. The SA-IDDES model and the $k-\omega$ SST-IDDES model with transition model do show a flattening lift curve now at 16°. Still the maximum lift coefficient attained is higher than in the experimental data, it is attained at a higher angle of attack and the lift curve does not drop as sudden. The $k-\omega$ SST-IDDES without the transition model no longer separates and reaches the highest lift coefficient of all. This is contrary to general trends related to the Reynolds number.

The oscillations in the forces on the airfoil are also observed for the low speed simulation. This indicates that changes in general are needed to obtain a more stable solution for the airfoil. An increased stability is believed to improve the results and get a better prediction. The baseline results are quite far away from the experimental data, motivating the different comparisons done in Chapter 7 in order to obtain better predictions for both airfoil models using Detached Eddy Simulation.

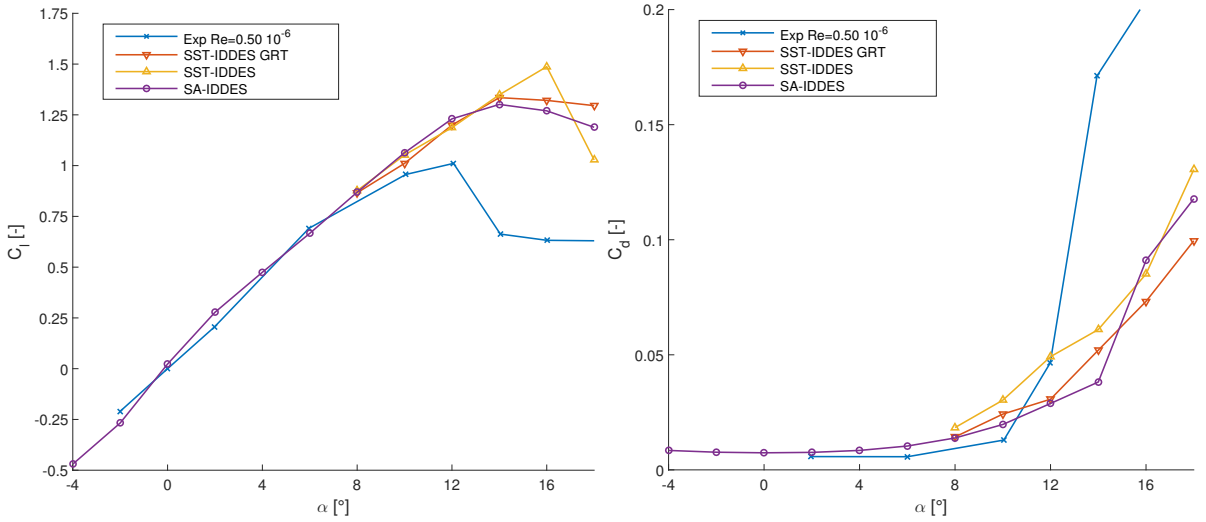

(a) C_l-α. (b) C_d-α.

Figure 6.7: NACA 0012 Airfoil Baseline polars Re=0.5·10^6, experimental data from Critzos et al. [6].

7

Airfoil Parameter Variations

For this chapter, a number of parameters are varied and the influence of these variations is summarized. This is done for both the NACA 0012 airfoil and for the IDF rear wing. Again, the NACA 0012 airfoil is tested since experimental data is available and the IDF rear wing since it is a more realistic application in motorsport. The first factor that is investigated is the mesh design. This section is especially important due to the different sensitivities of (ID)DES to the local mesh. Section 7.1 is devoted to this and discusses both airfoil profiles. A parameter called the length ratio is used to redesign the mesh in order to improve the accuracy of the results, although it increases the computational costs as well. The influence of using a span of only 8% of the chord is assessed in Section 7.2. The limited span helps to keep the computational costs down, but since DES is a 3D method and also computed 3D flow structures. The main question is therefore whether this airfoil slice is wide enough for these structures to develop. The comparisons here are only done for the NACA 0012 wing. Section 7.3 then takes the conclusions regarding the mesh and investigates the influence of the time step and the number of inner iterations. The link between the mesh and the time step is also discussed here. In the final part of the chapter, an effort is made to improve the simulation of the NACA 0012 in particular. This is done through a number of adjustments, most importantly by initializing with RANS and adjusting the prism layer settings. The results for this new set-up are promising and show major improvements over the results in the rest of the chapter. This concludes the variations and gives the final information needed to formulate the default settings for the airfoil presented in Chapter 8.

7.1. Grid Design

Grid design is known to have a major influence on CFD simulations and on DES in particular. This section therefore evaluates a number of meshes and compares them to capture this influence. Before this however, one particular way to design the mesh for a DES is described in Section 7.1.1. It discusses the length ratio and the mesh that emerges if the mesh is designed based on this. Section 7.1.2 then compares the mesh generated with this length ratio to the base mesh discussed in Chapter 5. This is done for both the NACA 0012 airfoil and the IDF rear wing.

7.1.1. Generation of Length Ratio Based Grid

One way to design the mesh is to compute a length ratio based on the local grid size and the turbulent length scale. This turbulent length scale can be estimated from a steady $k-\omega$ SST-RANS simulation. The mesh should then be designed such that all domains of interest have a length ratio above one. For the NACA 0012 and the IDF rear wing, the length ratios achieved with the baseline mesh and with the redesigned mesh for a single angle are shown in Figures 7.1 and 7.2 respectively.

The adjustments to the NACA 0012 mesh to satisfy the length ratio result in almost twice as many cells as the baseline mesh used in Chapter 5. This baseline has about 3.7 million cells and the new mesh 7.3 million. This illustrates the contribution of the necessary refinement of the DES method to the increase in computational costs. The baseline mesh however, is too coarse and does need the refinement of the redesigned mesh. The new mesh has a number of wake refinements extending into the wake and in front of the airfoil. It has the same minimum cell size of 0.3125 mm around the airfoil itself, but this region has been extended. More refinement regions have been added to cover both the wake and the initial acceleration of the flow over the

leading edge. The air further away from the airfoil still does not satisfy the length ratio. Because of the costs involved in refining the full flow domain however, the mesh is left relatively coarse.

For the rear wing, the redesigned mesh a higher length ratio in the overall domain as the mesh is no longer anisotropic. In an LES, the largest edge length defines the smallest scales that can be resolved. By making the mesh refinement isotropic with a length equal to the smallest edge length, smaller scales can be resolved. The redesigned mesh should therefore be more suitable to do a proper DES and give better results than reported in Chapter 5. The number of cells for the new IDF rear wing mesh is similar to the new NACA 0012 mesh.

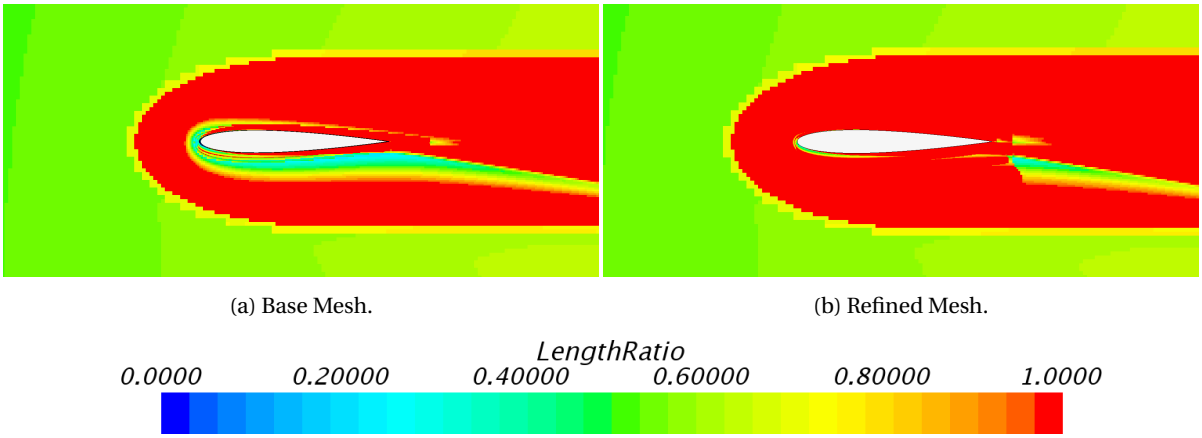

(a) Base Mesh. (b) Refined Mesh.

Figure 7.1: NACA 0012 Mesh Length Ratio at 10°.

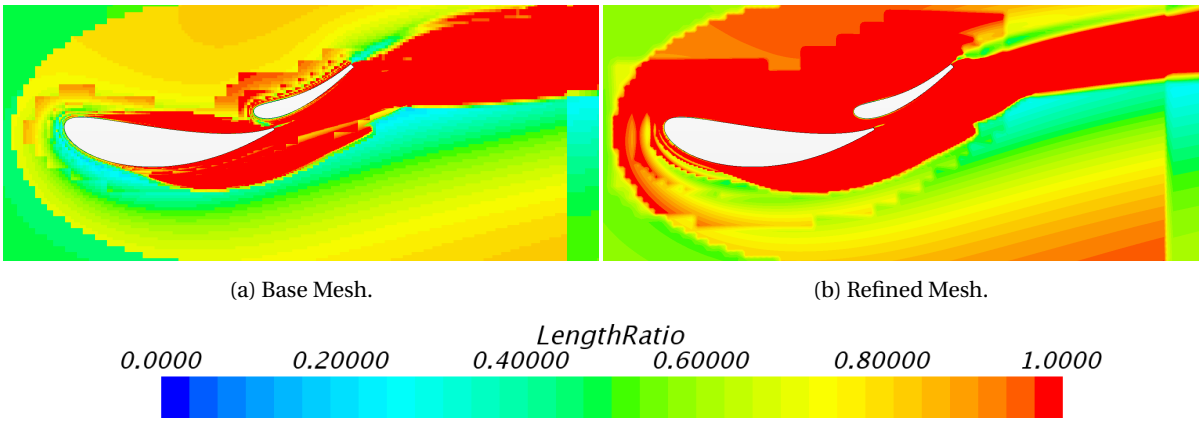

(a) Base Mesh. (b) Refined Mesh.

Figure 7.2: IDF Rear Wing Mesh Length Ratio at 10°.

7.1.2. Grid Influence on the Airfoil Models

Results for the baseline mesh and the redesigned mesh for the NACA 0012 airfoil are compared in Figures 7.3 and 7.4. Unfortunately, the results on the finer mesh are not much closer to the experimental data than the results on the coarser mesh. The Spalart-Allmaras model now keeps a positive lift slope instead of flattening at the higher lift coefficients. The results for the $k-\omega$ SST-IDDES model do seem more smooth and realistic, with a lift curve that already starts to decline gradually at a lower angle of attack. None of the results show the trend from the experimental data however, indicating that something else than the mesh refinement still needs improvement. From these results, the $k-\omega$ SST-IDDES method seems to be the best one to pursue further.

For the IDF rear wing, the lift and drag curves are shown in Figures 7.5 and 7.6. The Elliptic Blending result is still quite far away from the other results and is not considered in the remainder of this chapter. Results for this model tested on the full car are presented in Section 10.5. The influence on the SA-IDDES results is very small and the results for the $k-\omega$ SST-IDDES model with the transition model turned on are even further away from the experimental results than before. The $k-\omega$ SST-IDDES result however, has become

far closer to the other models and the RANS results. For both the NACA 0012 airfoil and the IDF rear wing, the change in mesh has the biggest impact on this turbulence model. The lift curve seems more stable and flattens out at the higher lift coefficients. This is closer to the RANS results in case of the IDF rear wing and to the experimental data in case of the NACA 0012. Even though the results are not entirely the same yet, the grid design does seem to have a big impact on the results. Based on these results, the $k-\omega$ SST-IDDES method is used for the next parameter variations.

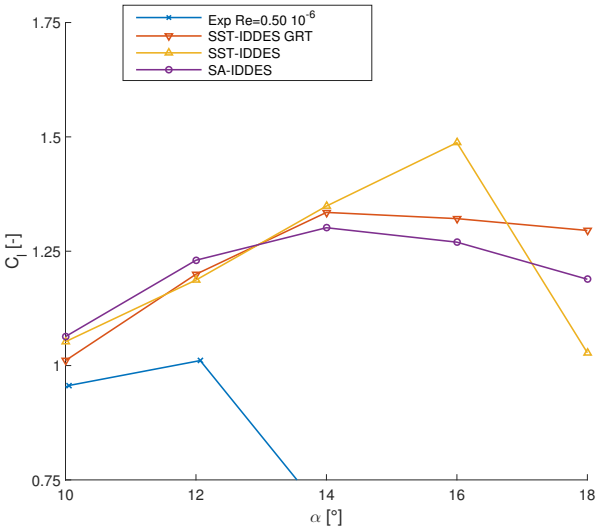

Figure 7.3: NACA 0012 coarse mesh Re=0.5E6 C_l-α polar.

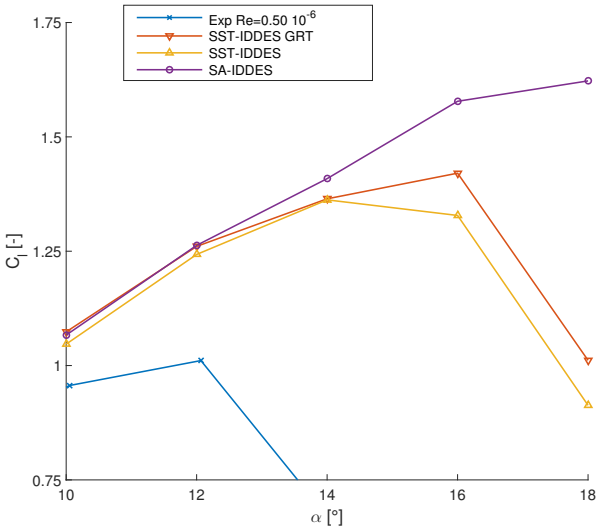

Figure 7.4: NACA 0012 LR mesh Re=0.5E6 C_l-α polar.

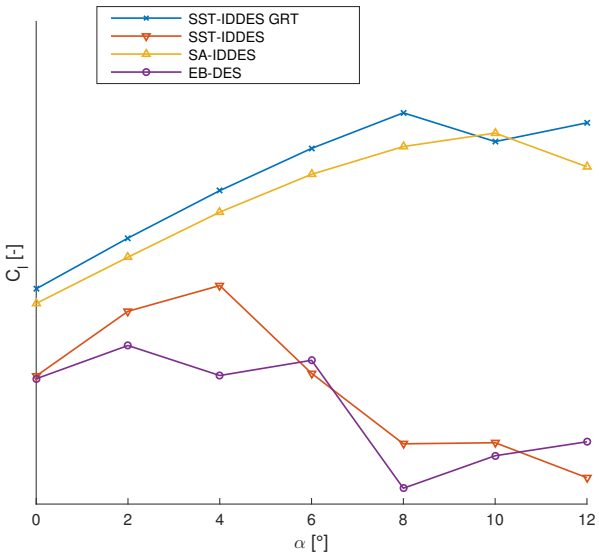

Figure 7.5: IDF Rear Wing coarse mesh Re=0.8E6 C_l-α polar.

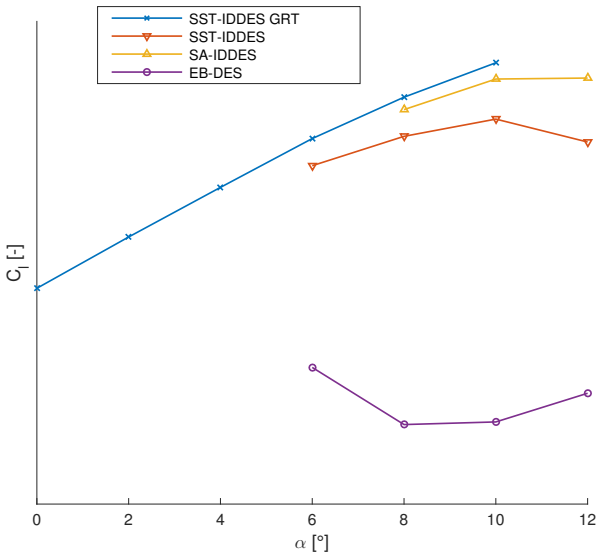

Figure 7.6: IDF Rear Wing LR mesh Re=0.8E6 C_l-α polar.

The development of the forces on the airfoil over time is still quite unstable. The lift and drag curves seem more smooth, but the oscillations in the solution are still not around a reasonably stable value. This therefore has not been solved by adjusting the mesh and needs additional changes to the baseline settings.

The blending function for the $k-\omega$ SST-IDDES model on the new mesh is shown in Figure 7.7. Compared to the blending functions on the old mesh shown in Figure 6.3a, less of the flow around the airfoil is modelled. Especially on the pressure side of the airfoil LES is allowed closer to the wall due to the added refinement there. This should allow the method to capture the unsteady flow phenomena better and therefore predict separation behaviour better. The difference in the blending functions for the SA-IDDES model is smaller, possibly because the RANS regions are already smaller on the coarser mesh.

Overall, the NACA 0012 results still do not agree with the experimental data. For the IDF rear wing the RANS data is for now used as a reference which also shows different behaviour. This indicates the need to adapt more than just the mesh in order to improve the results. This motivates the next topics to explore: the influence of the span and the influence of the time step, time scheme and simulated time. The $k-\omega$ SST-IDDES model seems most promising on the fine mesh and is therefore used in the majority of the remaining simulations.

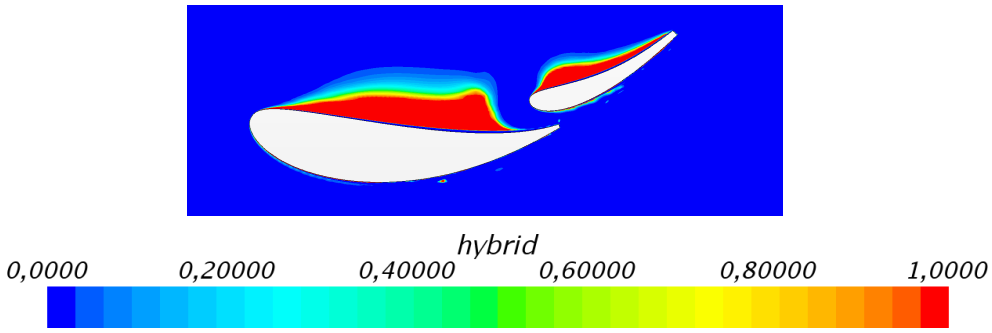

Figure 7.7: $\tilde{f}_d$ $k-\omega$ SST-IDDES New Mesh Baseline at 6°.

A closer look at the $k-\omega$ SST-IDDES results on the NACA 0012 airfoil with and without transition model can explain some of the differences. The simulation with the transition model transitions somewhere quite close to the leading edge and still has quite a full profile. The simulation without the transition model has a laminar separation bubble transitioning the flow from laminar to turbulent. Neither of the results are in agreement to the experimental data, since the lift coefficient should be much lower at this angle and Reynolds number combination. Since without transition model transition is also predicted, the choice is made to leave the transition model off for now and to let the DES do the transition prediction.

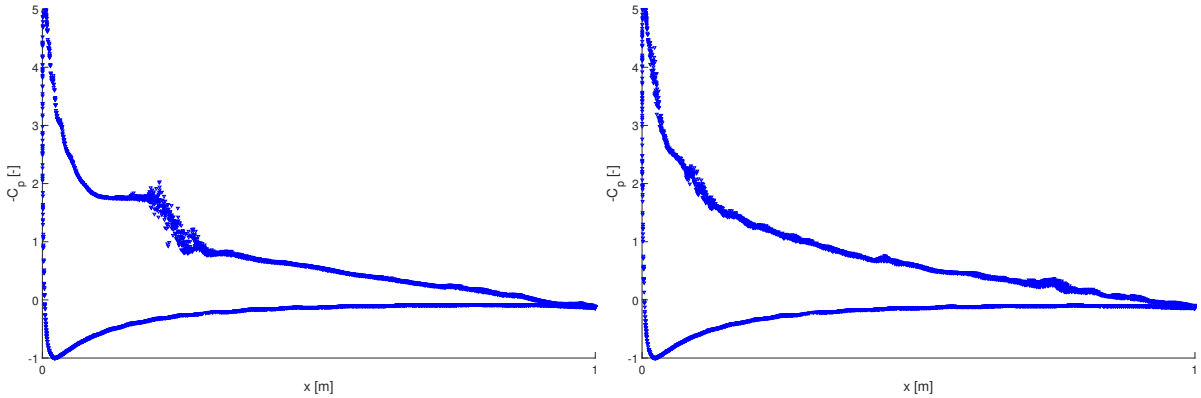

(a) No Transition Model.

(b) With Transition Model.

Figure 7.8: NACA 0012 Pressure Distribution $k-\omega$ SST-IDDES at α =10°.

7.2. Span Influence

Less relevant for the full car settings but very relevant for the simulation of airfoil models is the influence of the span. The span is limited as much as possible to save the computational costs. When RANS simulations on a rear wing are done, about 8% of the chord is simulated as a default. Since DES is a more three-dimensional method than RANS, the choice was made to look at varying the span and its impact on the flow behaviour. This could be an explanation for not capturing the flow phenomena well with DES, since it is not able to form all of the structures that make up these phenomena. Both symmetry boundary conditions and periodic boundary conditions have been imposed to investigate their effect. This investigation has been performed on the NACA 0012 airfoil only since the simulation time is quite high. First, an even coarser mesh than the baseline mesh was used to keep the computation time low. The coarser mesh of the NACA 0012 airfoil is still

an isotropic mesh, as shown in Figure 5.6b, but misses the final layer of refinement making the minimum edge length outside the prism layers 0.625 mm instead of 0.3125 mm. The results of this analysis are discussed in Section 7.2.1. Because of the sensitivities of the DES method to the grid as discussed in Section 7.1, the investigation was thereafter repeated on a finer grid. This is discussed in Section 7.2.2. The differences between these two sections once again illustrate the importance of grid design for the DES method.

7.2.1. Span Influence Coarse Grid

The span is studied with two different meshes, the first of which is reasonably coarse and different from the baseline mesh. The mesh has a minimum cell size of 0.625 mm, which is one step coarser than the baseline. Based on the results in Section 7.1, the $k-\omega$ SST-IDDES model is chosen. It shows more signs of separation and the aim of this study is to try and get it more stable. Since DES should be able to capture transition on its own, something that is discussed for the full car in Section 10.3, the choice was made to keep the transition model turned off.

The spans simulated are 8%, 16%, 30% and 100%. For all of these spans, both the symmetric and the periodic boundary conditions are tested. The original set-up has symmetric boundary conditions and a span of 8%. If the sides are far enough from each other, periodic boundary conditions should be more suitable. This is because the condition that the gradients need to be zero at the symmetry plane is not imposed. Too close together would have the two interfaces directly influencing each other resulting again in non physical conditions imposed.

An averaged value of lift coefficient for the different set-ups is shown in Figure 7.9. The results indicate that the span has a big influence on the results. The tests were done at the challenging angle of 14°, since this is where separation should take place for the NACA 0012. The results indicate that some of the simulations result in separation, while others stay attached.

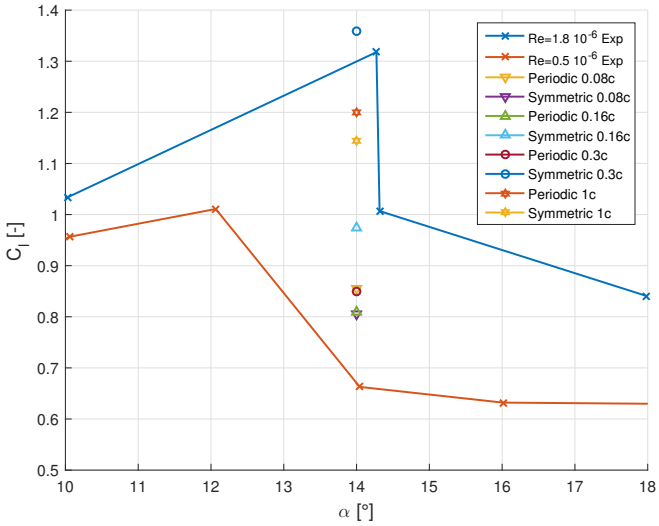

Figure 7.9: NACA 0012 Lift Coefficients at Re=0.5·10^6.

For all of the separated flows, the values of the lift and drag coefficients fluctuate over time, only the symmetric 30% chord span has quite a steady lift coefficient. The results presented in Figure 7.9 are averaged over the final 0.05 s but still show a wide spread because of this. It is difficult to draw any conclusions based on these lift coefficients, both regarding the span and the boundary conditions. To evaluate the influence of the boundary conditions, the vorticity magnitude in the wake is compared in Figures 7.10a and 7.10b.

Figure 7.10 illustrates that the symmetric boundary condition results in a larger wake close to the boundaries than in the middle, while for the periodic boundary conditions this phenomena is not present. This is the case for both the 100% and 30% spans. For the smaller spans this is not observed, possibly because the boundaries are too close together. For higher span simulations, the periodic boundary conditions therefore seems to give more physical results. For lower spans however, the opposite is true. An important note here is the fact that the symmetric boundary condition is also imposed on the car simulations of the straight line cases. The findings here could imply that at the symmetry condition non physical phenomena can also occur for the car simulations. This is a factor that needs to be evaluated in Chapters 10 and 11.

An important conclusion from the grid study performed in Section 7.1 is that although the influence of the span is large, there are still other factors preventing a good prediction. One of these factors could be the mesh, which is why the length ratio based mesh discussed in Section 7.1.1 is used for a second analysis of the influence of the span.

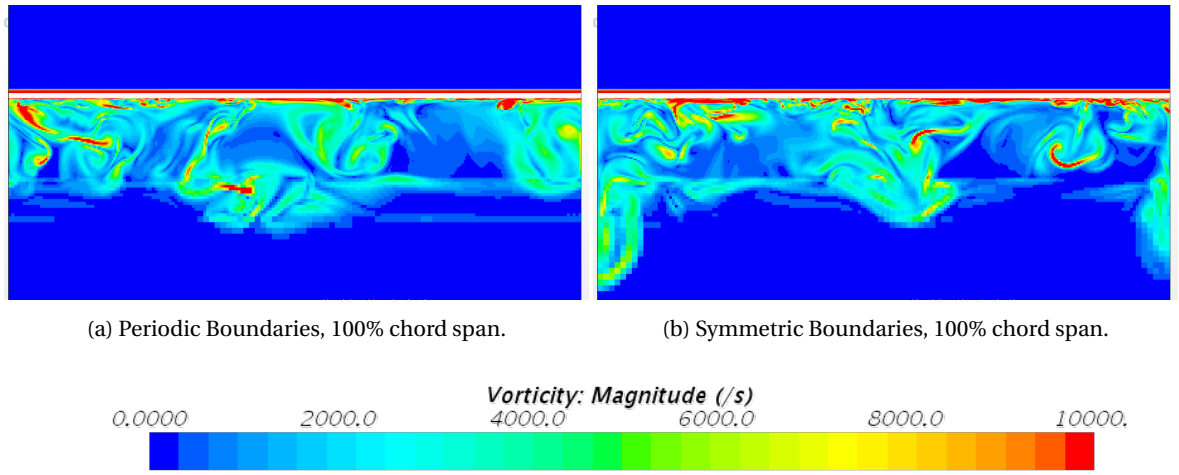

(a) Periodic Boundaries, 100% chord span.

(b) Symmetric Boundaries, 100% chord span.

Figure 7.10: Instantaneous Vorticity Magnitude at 14° and Re=0.5E6.
Spanwise View near the Trailing Edge of the NACA 0012 on Coarse Mesh.

7.2.2. Span Study Influence Fine Mesh

The mesh used here is as discussed in Section 7.1.1, which means that the smallest cells have an edge length that is halve the edge length used in the previous section. In the simulations performed on this coarser mesh, big differences between the different spans were observed. On the fine mesh however, the differences are smaller as is shown in Figures 7.11 and 7.12. The two spans compared here are the standard of about 8% and the larger span of 50% chord. Symmetry conditions are used for the spanwise boundaries in both cases.

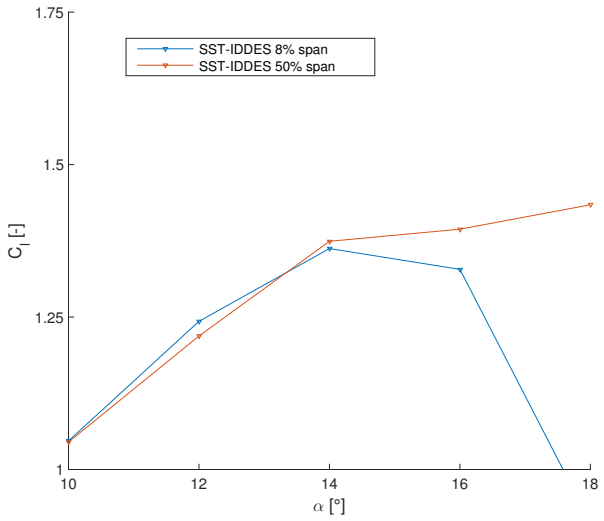

Figure 7.11: NACA 0012 Re=0.5E6 C_l-α polar.

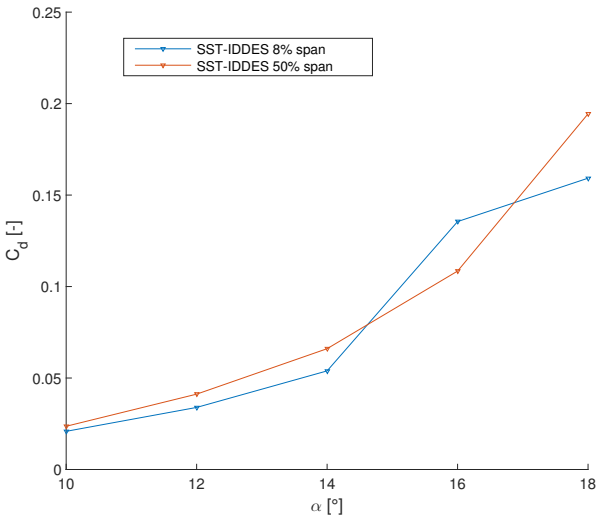

Figure 7.12: NACA 0012 Re=0.5E6 C_d-α polar.

At $\alpha = 14°$, there is hardly any difference at all between the two spans, which is the angle computed for the coarse mesh. The biggest difference is present at $\alpha = 18°$, which is highly influenced by the averaging period due to the instabilities in the forces. The high span wing is averaged over approximately the highest value the forces around the airfoil attain, while the average of the low span wing represents the actual average better. For both the small span and the large span simulation, the forces on the airfoil still vary over time. This lack of stabilization might indicate either that the total time should be compared or that the separation can not be captured fully for some other reason. One reason for this could be the Courant Number that is too large.

This is shown in Figure 7.13. Ideally, the Courant Number should be around 1 in the critical areas, indicating that the time step is currently far too large with local maxima up to 400. This is evaluated and improved upon in Section 7.3.

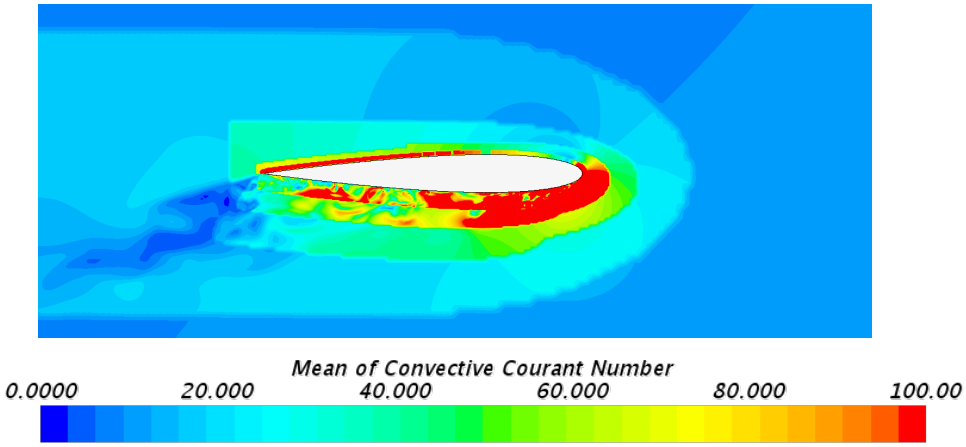

Figure 7.13: NACA 0012 Courant Number fine span study at 14° and Re=0.5E6.

Figure 7.14 shows the 3D flow field around the high span airfoil at 10° and at 18°. These show that at 10°, the dominant 3D structures are much smaller than the span. Compared to the often used 8% span wing, the 3D structures are quite large however. This would indicate that although the lift and drag coefficients are very similar, the higher span can capture these structures very well, but the smaller span can also capture them to some extend. For the 18° flow, the structures present are much larger than the low span wing could capture. The impact of the symmetric boundary condition seems a lot smaller here, implying that on a finer mesh the error made in the assumption in smaller. Unfortunately however, the symmetry plane in the car is quite coarse which might still results in a visible influence of the symmetry condition.

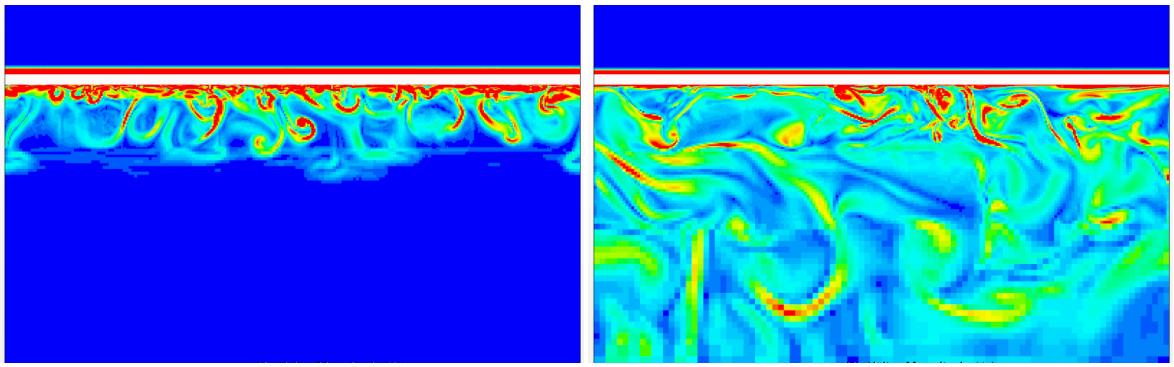

(a) α = 10°, Span = 50% chord.

(b) α = 18°, Span = 50% chord.

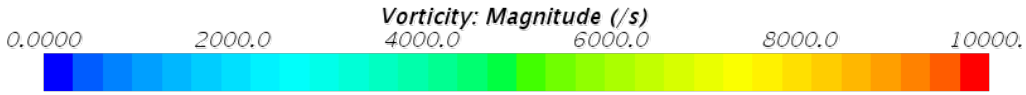

Figure 7.14: Instantaneous Vorticity Magnitude at Re=0.5E6.
Spanwise View near the Trailing Edge of the NACA 0012 on Fine Mesh.

One explanation for the difference between the coarse and fine mesh at 14° is the spanwise refinement. According to [25], the spanwise refinement is more important than the spanwise extend for flows before separation. On the fine mesh, the flow does not separate meaning the span influence is limited. After separation however, the span does have an influence on the results according to [25]. This would be in agreement with the results presented and the size of the vortical structures observed for the large span at α = 12°.

The separation behaviour from the experimental data is not observed however, implying that there are other settings which should still be adapted to allow the DES method to capture the flow properly. These

settings will therefore be assessed in the next sections. Because of the simulation time involved in the higher span and the limited influence on the lift and drag polars, the choice was made to continue with the refined low span mesh.

7.3. Time Discretization and Solver Settings

This section evaluates settings related to time discretization and solver settings like physical time and averaging. The influence of the size of the time step and the number of inner iterations is evaluated for the length ratio based mesh discussed in Section 7.1.1. Again, the $k-\omega$ SST-IDDES method is used. The discussion is based on both the NACA 0012 airfoil and the IDF rear wing. First, variations that stay close to the baseline are discussed. This includes varying the number of inner iterations and the size of the time step. After exploring these small variations for both the NACA 0012 and the IDF rear wing, the entire set-up is adjusted to test the solver settings.

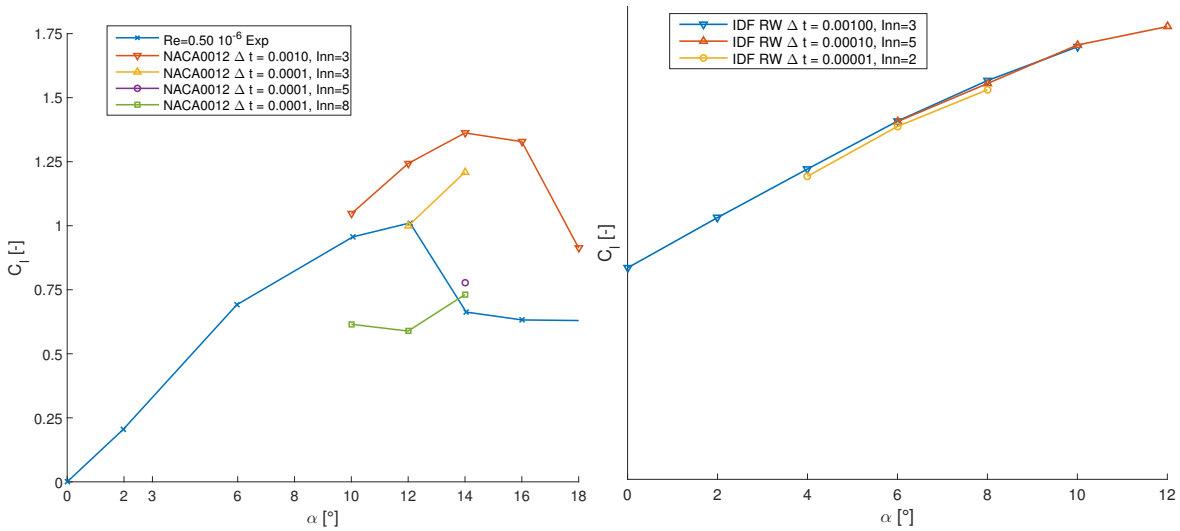

(a) NACA 0012 $C_l - \alpha$.

(b) IDF Rear Wing $C_l - \alpha$.

Figure 7.15: Time Step and Inner Iterations Influence on Lift Polar

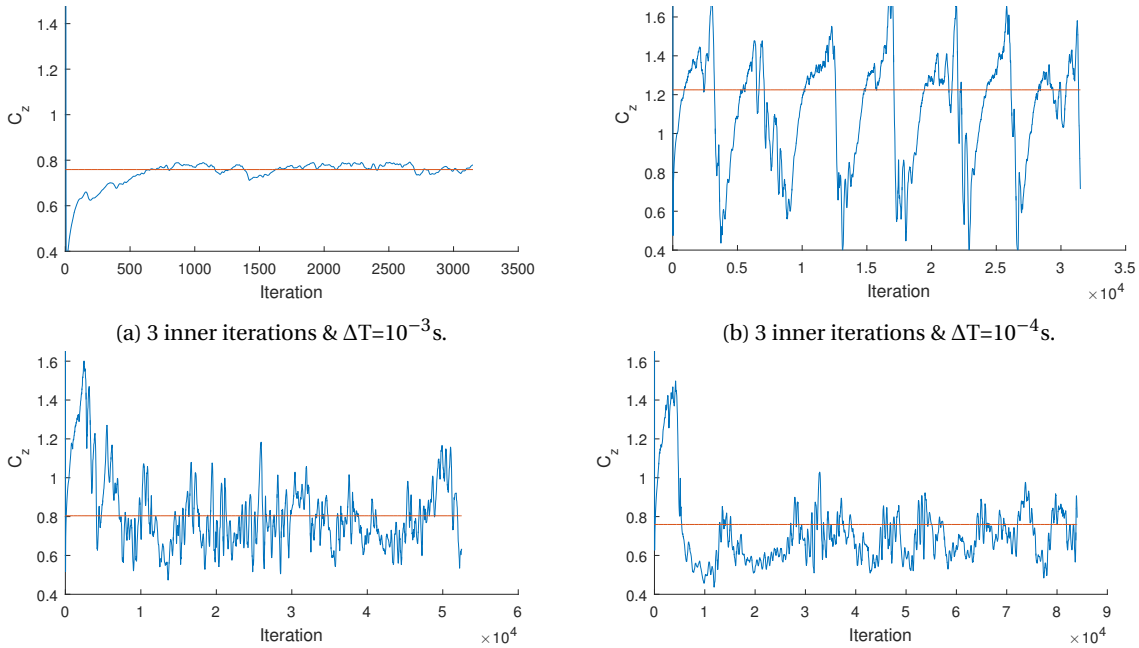

(a) 3 inner iterations & $\Delta T=10^{-3}$s.

(b) 3 inner iterations & $\Delta T=10^{-4}$s.

(c) 5 inner iterations & $\Delta T=10^{-4}$s.

(d) 8 inner iterations & $\Delta T=10^{-4}$s.

Figure 7.16: NACA lift convergence at 14°.

The results for the variations to the baseline are shown in Figure 7.15. This immediately shows the ambiguity related to varying the time. For the NACA 0012 airfoil, the number of inner iterations is varied at a time step that is 10 times smaller than the baseline. The resulting lift coefficients are shown in Figure 7.15a together with some experimental data points. The results are not satisfying and although they indicate that the time step and the number of inner iterations is important, they do not lead to a clear conclusion as to which setting is most appropriate. Generally speaking, the highest number of inner iterations should lead to the best results. Since these results still not match the experimental data, additional steps might be needed to further improve the simulation, after which the number of inner iterations can be evaluated again.

The differences in convergence of the simulations is shown in Figures 7.16a to 7.16d. These indicate the instabilities in the force on the airfoil, which increase for the smaller time step rather than decreases. The angle of attack in these figures is 14°, which is where separation should have taken place already. One reason for the increase in the instabilities in the forces is that the largest time step still predicts an attached flow making the flow more stable. This means that for the smaller time steps some oscillations in the lift and drag data are expected. The size of the oscillations in Figure 7.16d seems most reasonable, but the irregularities indicate that the solution might need longer to stabilize. Possible explanations are issues with the mesh or a too short simulation time. Note also that these simulations are started immediately as a DES and only use a first order temporal discretization. The latter two factors are explored towards the end of this section.

To further explore the topic, a number of simulations on the IDF rear wing are also analysed. Again, the baseline has 3 inner iterations and a time step of 0.001 s (or 10^{-3} s). This baseline is compared with two more simulations. The first has 5 inner iterations and a time step of 10^{-4} s. The second has 2 inner iterations and a time step of 10^{-5} s. The resulting lift polars are shown in Figure 7.15b. This figure indicates a very limited influence of the time step on the results, which is quite different from the results obtained for the NACA 0012 airfoil. The similarities are also very visible in the total pressure coefficients shown in Figure 7.17. The structures in the wake are quite different, with especially Figure 7.17c showing smaller flow structures. The mean values however, are far less different. The baseline has a slightly larger wake but overall the wake seems quite similar. This explains the agreement in terms of the average lift coefficient.

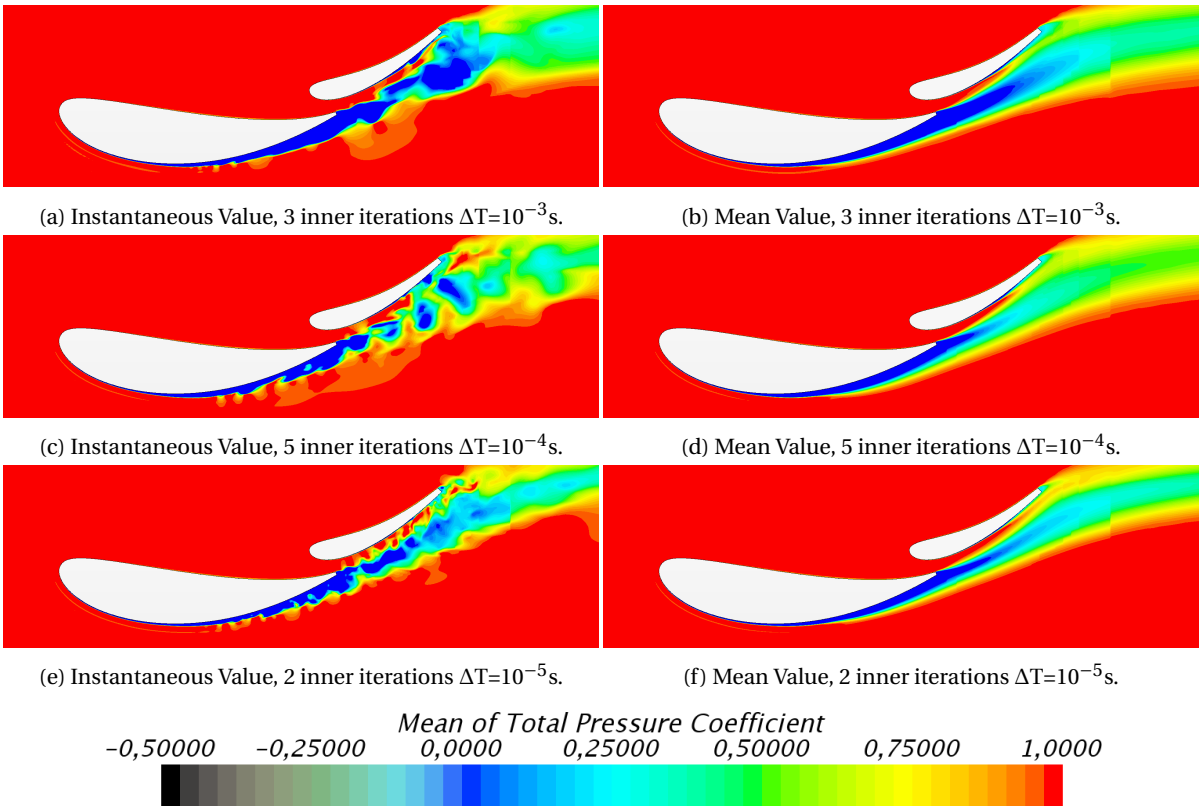

(a) Instantaneous Value, 3 inner iterations $\Delta T=10^{-3}$s.

(b) Mean Value, 3 inner iterations $\Delta T=10^{-3}$s.

(c) Instantaneous Value, 5 inner iterations $\Delta T=10^{-4}$s.

(d) Mean Value, 5 inner iterations $\Delta T=10^{-4}$s.

(e) Instantaneous Value, 2 inner iterations $\Delta T=10^{-5}$s.

(f) Mean Value, 2 inner iterations $\Delta T=10^{-5}$s.

Figure 7.17: IDF Rear Wing Total Pressure Coefficient.

An important remark for Figures 7.18a to 7.18c shown here is the physical time computed. For Figure 7.18a, this is 1.05 s. Due to the high number of iterations needed and the increase in stability observed for preliminary tests, this was reduced to 0.55 s and 0.35 s for Figures 7.18b and 7.18c respectively. Still however, steady values are obtained for the averaging period. The balance between increasing the physical time needed and decreasing the time step still needs to be found, but the results do indicate that there is the potential to reach a stable system. Note that these results are very different from the results obtained for the NACA 0012 airfoil. The tests done on the two airfoil models are different, but this does not explain why the behaviour is this different. It could partially be due to the difference in geometry and therefore stall behaviour. The results on the IDF rear wing could be reasonable, as the airfoil is designed to generate high lift (or downforce actually when installed on the car) and to not stall easily. The NACA 0012 however, does not portray the desired behaviour and needs further investigation.

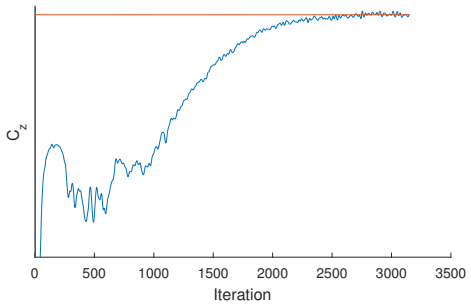

(a) 3 inner iterations for $\Delta T=10^{-3}$ s.

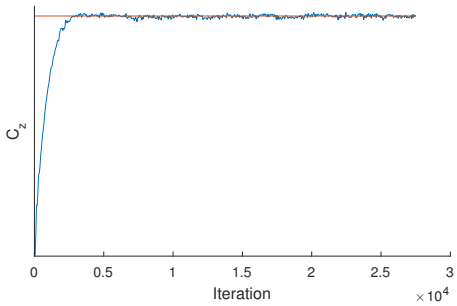

(b) 5 inner iterations for $\Delta T=10^{-4}$ s.

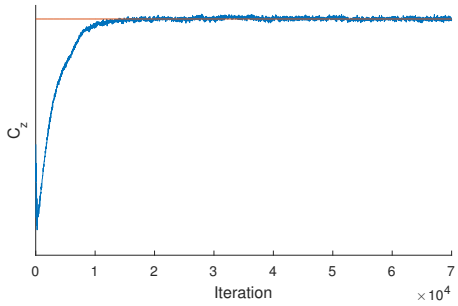

(c) 2 inner iterations for $\Delta T=10^{-5}$ s.

Figure 7.18: IDF Rear Wing lift convergence at 8.

7.4. Improving the NACA 0012 Results

A number of changes are made to the simulation set-up to obtain a better representation for the NACA 0012 airfoil. A wall y+ of 0.5 maximum is ensured, as well as a stretch factor of 1.15 through the prism layer refinement. The suction side of the airfoil still has an isotropic wake refinement up to 0.3125 mm, which is also present in the full boundary layer. Additionally, the orientation of the airfoil and the inflow is changed to ensure a perpendicular outflow boundary condition.

In order to improve the stability and the convergence of the simulations further, the solution can be initialized with RANS. In this case, using the steady $k-\omega$ SST-RANS model. This ensures that the DES starts from a reasonable flow field and enables it to more quickly go to the correct solution. Apart from this, the second order accurate temporal scheme is tested. This can be done either by switching immediately after the RANS simulation, or by first doing a number of 1st order steps and then switching to second order. To limit the number of time steps used, 500 RANS steps are used followed by 1500 $k-\omega$ SST-IDDES steps. Additionally, half the time step is used to reduce the Courant number. This results in a time step of $5 \cdot 10^{-4}$ s. This Courant number is still rather high as is shown in Figure 7.19, but is reduced to less than one third. This is also partially due to the adjustments to the mesh and the lower velocity used as motivated in the next paragraph. The set-up is only tested on the NACA 0012 airfoil since it increases the computational power required and this airfoil seems furthest away from its expected results.

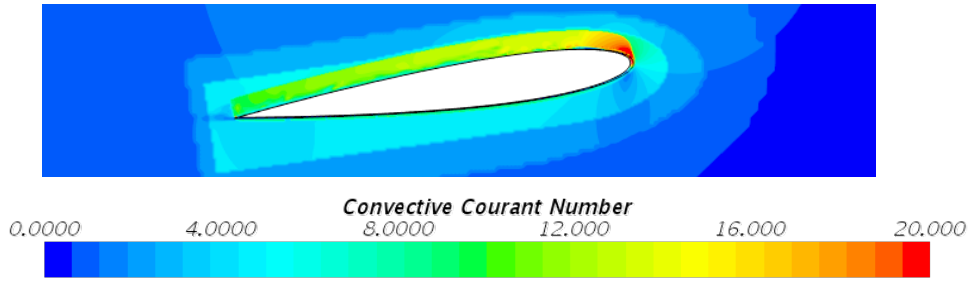

Figure 7.19: NACA 0012 Courant Number time study at 8° and Re=0.44E6.

The results for an angle of attack of 8° are discussed first, after which the lift curve is presented. The Reynolds number in this case is 440,000. The choice to lower the Reynolds number a bit further is motivated by the aim to investigate more than the separation behaviour. For Re < 500,000, a laminar separation bubble over the suction side is observed moving towards the leading edge for increasing angle in [50]. This bubble is also discussed in other papers like [34] and for lower Reynolds numbers [22]. From an experimental point of view, [8] shows the bubble for a lower Reynolds number of 290,000. The lift and drag curves for these results are given in Figure 4.3. The aim is to see if this behaviour can be captured and then to see if this leads to a proper separation prediction at higher Reynolds numbers.

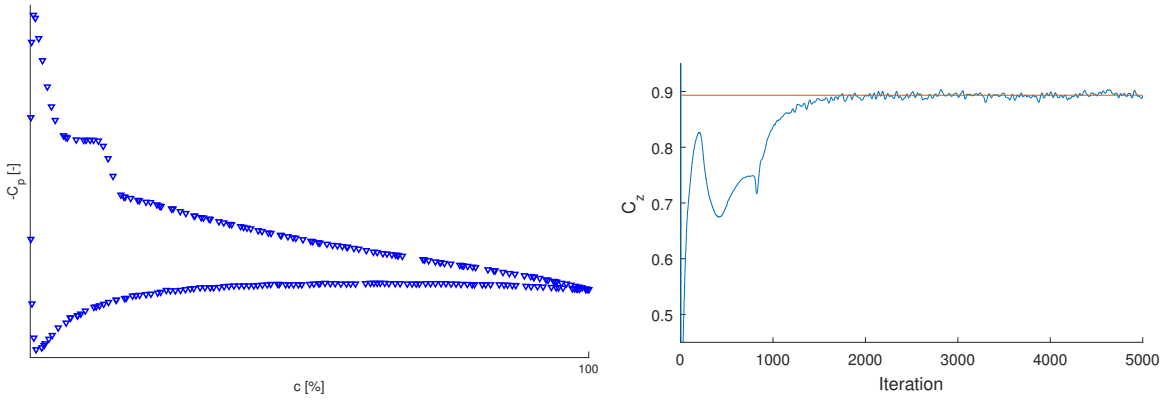

(a) Pressure Distribution at α=8°.

(b) Lift convergence at α=8°.

Figure 7.20: NACA 0012 revised set-up force insights.

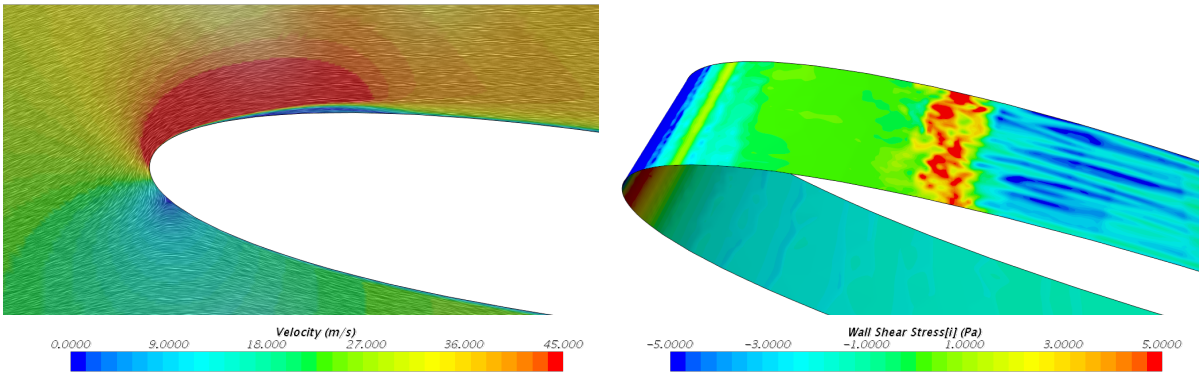

(a) Instantaneous Velocity Vector.

(b) Instantaneous Streamwise Wall Shear Stress.

Figure 7.21: Visualization of Laminar Separation Bubble NACA 0012 at α=8°

The mean of the pressure distribution is shown in Figure 7.20a. Here, the laminar separation bubble is clearly visible starting at about 7% of the chord. This bubble is also visible in a visualization of the velocity vectors and

the streamwise wall shear stress, in Figures 7.21a and 7.21b respectively. Figure 7.21a shows the recirculation and bubble shape over the airfoil, while Figure 7.21b shows the backflow through its locally negative wall shear stress. Capturing this bubble is seen as an indication that the settings have improved compared to the earlier simulations. This is further supported by the convergence of the lift coefficient in Figure 7.20b. The initial results with this new set-up are promising. The method is more costly than the base set-up, but far better results are obtained with it.

The next step is to simulate the full lift and drag polar to further analyse the performance of the current set-up. First of all, the ability of the DES method to capture the separation point can then be reassessed. Secondly, the laminar separation bubble should be further aft for the lower angles of attack. The lift polar with the new set-up is shown in Figure 7.23a. This immediately shows that the new set-up does not come closer to the experimental data in terms of the separation point. Before separation however, the revised results match the experimental data very well. The increase in lift coefficient due to the laminar separation bubble between 4° and 8° is captured well. Even the trailing edge separation at the pressure side that is discussed in de Paula et al. [8] is captured.

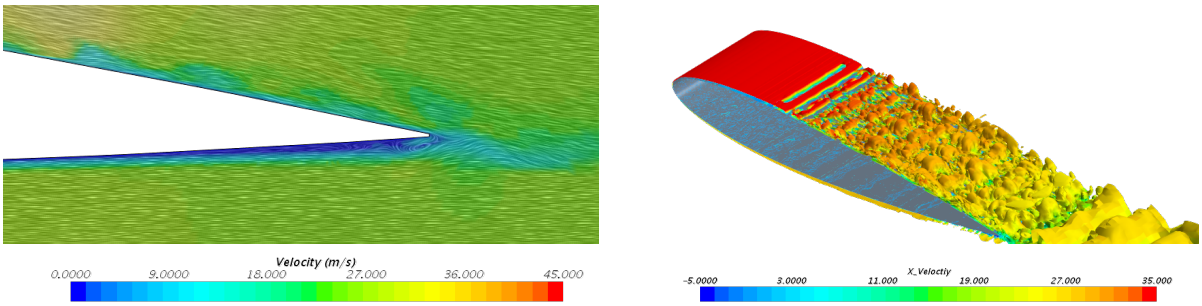

(a) Instantaneous Velocity Vector Trailing Edge.

(b) Vorticity based on λ_2 Criterion.

Figure 7.22: Visualization of Flow around the NACA 0012 at α=4°

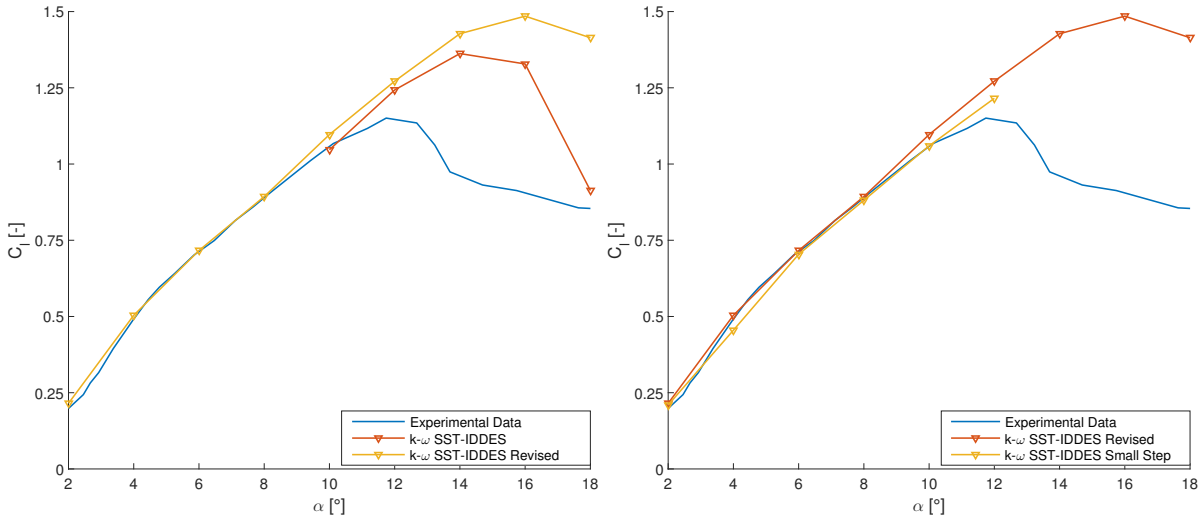

(a) NACA 0012 $C_l - \alpha$ revised set-up, experimental data from de Paula et al. [8].

(b) NACA 0012 $C_l - \alpha$ revised set-up and small time step, experimental data from de Paula et al. [8].

The next step is to fully satisfy both conditions for the time step on this mesh. For the time step based on the Strouhal number, this implies taking the airfoil thickness as length scale. For the time step based on the Courant number, this implies taking 1 as the Courant number. This gives:

$$\Delta t_{Str} = \frac{1}{N_T}\frac{L}{u\,St} \approx 2\cdot 10^{-4} s. \qquad \Delta t_{Cou} = \frac{C\Delta x}{u} \approx 1.2\cdot 10^{-5} s. \tag{7.1}$$

$$\Delta t = min\,(\Delta t_{Str}, \Delta t_{Cou}) = 1.2\cdot 10^{-5} s, \tag{7.2}$$

Note that the revised set-up shown in Figure 7.23a satisfies the condition derived from the Strouhal number, with $\Delta t = 10^{-4}$, but does not satisfy the criteria for the Courant number fully. The final adjustment made to the set-up is therefore to simulate with this small time step. The set-up entails first 500 time steps at a large time step and then 750 at the smaller time step. Per time step, also 6 inner iterations are used. This results in the lift curve of Figure 7.23b. The simulation results still are unable to capture the full chord flow separation at 12°, even though an appropriate time step is now chosen. A possible reason for this is that more time steps of the smallest time step are needed. There is the possibility that the smaller time step does ensure a separation earlier than the larger time step but this has not been tested. The main conclusion however, is that although the DES method applied in this manner is able to capture the unsteady flow phenomena at the lower angles of attack quite well, the full chord flow separation is not captured at the correct angle of attack currently. Note that at higher angles of attack, this full separation can be observed.

The final part of this section shifts the aim from being representable as a test case at Porsche motorsport to matching the experimental data from de Paula et al. [8]. For this, a range of angles from 6° to 16° is run at Re=290,000 with a turbulence intensity of 0.5%. Other than that, the simulation set-up at the start of this section is used. This means a second order discretization, 3 inner iterations, and a time step of initially 0.0005 s and then 0.0001 s. This reduces the costs involved compared to the previous simulations as the desired outcome was also not obtained with the higher costs. Also, RANS is used as an initialization for the first angle and an interpolated solution from the previous angle for the remainder of the lift curve. To reduce the Reynolds number, the chord of the airfoil is reduced which results in a high wall y+ value. This is monitored to ensure it stays below 1. The results of this simulation are shown in Figure 7.24a. The results show that although the separation is still at too high an angle, it is at a lower angle than for the higher Reynolds number. This is in agreement with the Reynolds number dependency of this airfoil. At 16°, the method does predict a separation at the leading edge but the lift generated is still too high. The laminar leading edge separation is thus not captured by the DES method with the current set-up.

Overall, this final section shows that the DES method is able to capture part of the unsteady flow behaviour around the NACA 0012 airfoil but not everything. The laminar leading edge separation is not captured, but the laminar separation bubbles and the turbulent trailing edge separation is.

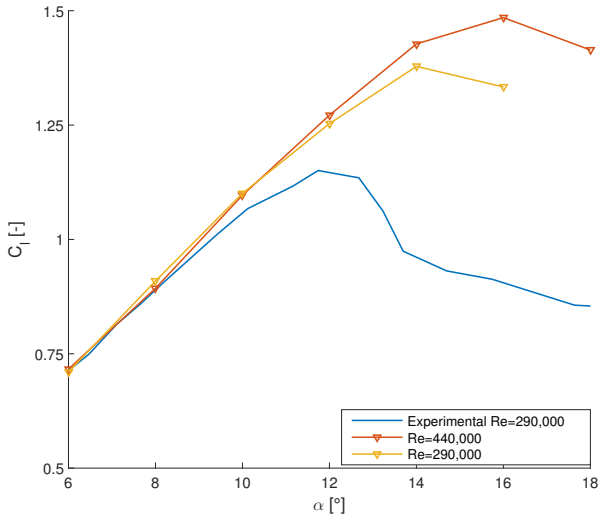

(a) $C_l - \alpha$, experimental data from de Paula et al. [8].

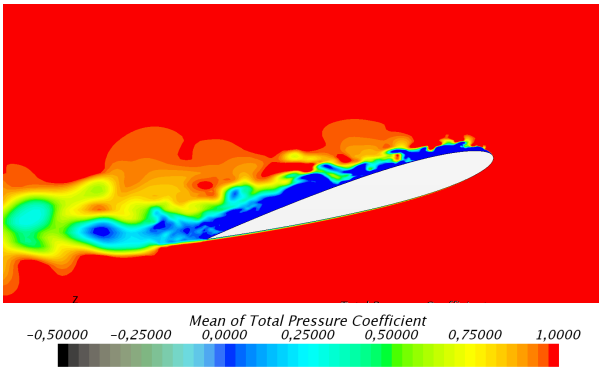

(b) Total pressure at α=16°.

Figure 7.24: NACA 0012 with revised set-up at Re=290,000.

8

Recommendations for Simulating Airfoil Models

This chapter translates the different variations tried on the airfoil into a set of recommended settings for airfoil simulations in general. This is done first and foremost with the IDF rear wing model in mind, as that is a representative case for Porsche Motorsport. For additional explanations regarding the background of these choices, Chapter 7 should be consulted. The recommended settings are followed by a number of monitoring methods for the simulation. This can help to adjust the settings better to the case under consideration. Finally, a valuable reflection on the approach and the results obtained in the airfoil model study is given in Section 8.3.

8.1. Recommended Settings Airfoil Model

This section discusses a number of recommendations for the settings in airfoil simulations using Detached Eddy Simulation. The recommended default settings should be regarded as a starting point and not a given set-up, since the method does not function perfectly yet. Mesh design is the first and foremost consideration. The number of prism layers and the smallest cell size can make the difference between capturing the laminar separation bubble or not. They therefore influence the results greatly but at the same time also influence the number of cells. Plotting the blending functions and the length ratio based on a $k-\omega$ SST-RANS simulation should give insight into the appropriateness of the mesh. Additionally, the stretch factor of 1.15 or 1.25 from literature can be kept in mind, as well as a suitable maximum y+ value, for example below 1.

The $k-\omega$ SST-IDDES method without the transition model seems the preferred method to use. The transition model changes the results slightly, but it neither seems to improve the wall shear stress patterns nor does it give the expected transition. Due to this and the costs associated with the transition model, the recommendation is to not use it. The $k-\omega$ SST-IDDES method without the transition model already predicts some form of transition on its own. This should be understood better before a separate transition model is added. Transition is further discussed in Section 10.3, where the full car is considered. The $k-\omega$ SST-IDDES method was on the fine mesh best at prediction at least a separation, even though it was for the NACA 0012 airfoil at a too high angle.

The span study did not render a conclusion concerning the impact of the span on the results. One explanation for this could be the fact that flow that is not separated is not influenced as much by the span as flow that is separated. This is in agreement with the statement from [25], where also the fact that the spanwise refinement is more important than the spanwise extend for non separated flows. This explains the big impact of the spanwise extension on the coarse mesh and the limited impact on the coarse mesh. The application, a separated flow or a non separated flow, therefore governs this parameter. The spanwise refinement is always important. A more important conclusion that can be drawn from the span study in the context of this thesis is the impact the symmetry condition can have, and that the impact should be assessed for the car simulations.

About the solver and stopping set-up some more concrete recommendations can be made. The averaging time can be determined with the use of pressure probes, a number of periods should be captured to be able to do a proper averaging. The overall simulation time depends on the number of time steps needed, the number of inner iterations and the mesh. In the end, the best results, keeping in mind the simulation costs,

were obtained by a RANS initialization and a second order accuracy for the time discretization. The results in Section 7.4 are obtained with a time step of 0.0005 s and 3 inner iterations. The results at the end of the section show that increasing the number of inner iterations as well as decreasing the time step to the time step criterion does not give a satisfactory improvement compared to the increase in costs.

Generally speaking, the cause for the lack of correlation regarding the separation point is still unknown. One option could be that combining several of the variations, for example a larger span and a smaller time step, are needed to get the desired results.

8.2. Recommended Checks and Monitors

Especially since the settings discussed do not always lead to the expected results, a number of checks are recommended to assess the results. These help in the identification of sources of error and therefore help to estimate the appropriateness of the settings chosen. First and foremost, like for many other CFD simulations, the residuals should be checked. In STAR-CCM+ the residuals are normalized based on the first iterations, which means that by switching the model the residuals can go above 1 without diverging. Still, they should initially decrease over time and drop enough within a single time step. To improve upon this, the time step or the number of inner iterations can be adjusted.

To look at the convergence of the method, the force coefficients over time can also be reviewed. Lift and drag or C_z and C_x can be plotted over time and often a convergence to a value is visible. Due to the unsteady nature of the method, unsteadiness will still be visible but the values should not still be rising or falling. This can also help in identifying the cause for differences between simulation results and irregular lift curves. Similarly, a number of pressure monitors can be included in the unsteady wake to capture this. These can also help to determine an averaging time and the time needed before averaging is begun.

Other checks include the length ratio, the blending functions, the wall y+ and the Courant number. These can indicate how appropriate the mesh and the time step are. In critical areas, a fine mesh with a length ratio above 1 is desired such that the blending functions display LES mode. The fine mesh needed to satisfy the length ratio results in a high value for the Courant number as well. This can be reduced by reducing the time step but that greatly increases simulation time. A balance between the mesh size and the time step therefore needs to be found.

8.3. Reflection on the Airfoil Model Study

Because the airfoil model study did not entirely result in the desired results, a short reflection on the methods used is in place. Looking back, starting the other way around might have been a better approach: satisfying all conditions fully in an overly expensive fashion and then varying parameters making the method cheaper without decreasing the accuracy too much. This would have given a better reference to work from with a known maximum capability of the DES method in mind.

Another point of reflection is related to the choice in airfoil models. The IDF rear wing results seem satisfactory, but a conclusion from them can not be drawn due to the lack of experimental data. The NACA 0012 airfoil with its sudden laminar separation might not have been the best airfoil to correlate with experimental data. It is nice to see that the laminar separation bubble travelling over the airfoil between 2° and 8° is captured well, but the aim to capture the separation point was not achieved. An easier airfoil with a turbulent trailing edge separation might have been a better starting point to explore the method.

The purpose of the airfoil model study, to prepare for the full car simulations, was achieved however. A number of valuable points like the importance of mesh design, the impact of the symmetry condition and the choice in turbulence model are derived from this study. Also, the fact that the method is able to capture transition through a laminar separation bubble is an interesting result that can be further assessed on the full. The conclusions regarding the time step however, are not transferred to the full car as the airfoil study was finalised during the full car simulations and carrying this over was not an option any more. Also, although adjust the time step and the simulation set-up, for example RANS initiation and second order accuracy, did have a positive impact on the results, satisfying the Courant criterion did not solve all of the issues. Costs involved are therefore too high to do this on the full car.

III

Full Car Simulations

In Part III of this report, the application of Detached Eddy Simulation to complex, full car geometries is discussed. The conclusions from Part II are used to formulate a baseline for the full car model to work from. A number of variations to this baseline are tested in order to improve the performance of the method. The full car analysis is based on two different cars, the very recent GTE19 car and the LMP1 car from 2015. Simulating two very different cars ensures a broader overview of the capabilities of the process can be given. Also, it ensures that the first generalization step towards using it for the design of various vehicles is already completed.

Chapter 9: "Baseline Settings GTE19 Car" starts by explaining the baseline of the full GTE19 car along with all of its settings. The choices made for all settings are justified, including models used, boundary conditions and solver settings. Apart from the settings, the mesh design for the full car is presented. The design method used is emphasized here, based again on the length ratio and the blending functions from DES. Even though the chapter concerns the GTE19 specifically, this set-up and methodology can be regarded the starting point for the full car simulations in general.

Chapter 10: "Results GTE19 Car" then assesses the results obtained for the baseline car and set-up. Some adjustments are tested regarding both the mesh and settings to improve the performance compared to the baseline described in Chapter 9. The results are compared to other CFD simulation results and wind tunnel data. The wind tunnel data here includes global force data and some pressure tap data. Besides an assessment of the accuracy, the computation times are also documented and compared. Results here are used for a new formulation of the baseline settings for future simulations.

Chapter 11: "Settings and Results LMP1 Car" takes these newly formulated baseline settings and tests them on the second car geometry: the LMP1 car. The complexity of this car is higher, as is the simulated free stream velocity and thereby the Reynolds number it is simulated at. Again, other CFD results are used to compare the results as well as wind tunnel data. Wind tunnel data here includes PIV data between the car floor and the ground, as well as global force data. This chapter illustrates the difficulties related to translating the set-up to a different car and concludes the preparation for the set-up specifications.

Chapter 12: "Recommendations for Simulating Full Cars" contains the proposed settings for full car simulations in general, as well as the motivation behind these choices. The set-up is based on the results obtained by both the GTE19 and the LMP1 2015 car. Some remarks regarding the set-up and the performance of the method with this set-up are also included. This concludes the investigation into the ability of Detached Eddy Simulation to perform well in full car simulations.

9

Baseline Settings GTE19 Car

This chapter discusses the baseline set-up for the DES simulations on the GTE19 car. This baseline configuration is based on the recommendations made by STAR-CCM+ as well as the findings during the airfoil model study. Some restrictions in terms of computational time, memory and costs can influence these settings however. First, the general settings for the simulation are discussed in Section 9.1. These include the settings for the physics models, the solver itself, the boundary conditions and the stopping criteria. The mesh used and how it is designed is discussed in Section 9.2. This mesh is designed with a RANS mesh as a starting point. Even though this chapter discusses the set-up for the GTE19 car, the settings discussed here are, unless stated otherwise, also used for the LMP1 car. The results obtained for the baseline along with the adjustments based on them are then discussed in Chapter 10. A number of results from the simulations discussed in Chapter 10 are already mentioned in this chapter however, in order to verify some of the choices for the settings.

9.1. General Car Model Settings

For the full car, most of the settings are derived from the recommended settings found in the airfoil study. A concise overview is therefore provided in this section, but for more information about the settings Chapter 5, 8 and Appendix C can be consulted. The settings discussed here include the settings for the physics models, the settings within these physics models, the boundary and initial conditions, the solver settings and the stopping criteria. Note that any settings not mentioned are left to the STAR-CCM+ defaults. Together with the mesh discussion in Section 9.2, this gives the baseline set-up. The geometry of the car discussed is shown in Figure 9.1. Note that the car simulated also contains the wheels, the suspension and the radiators, this is only the surface design. The three boxes from left to right indicate the front wing, the car floor and the rear wing. These areas are discussed in more detail in Section 9.2.

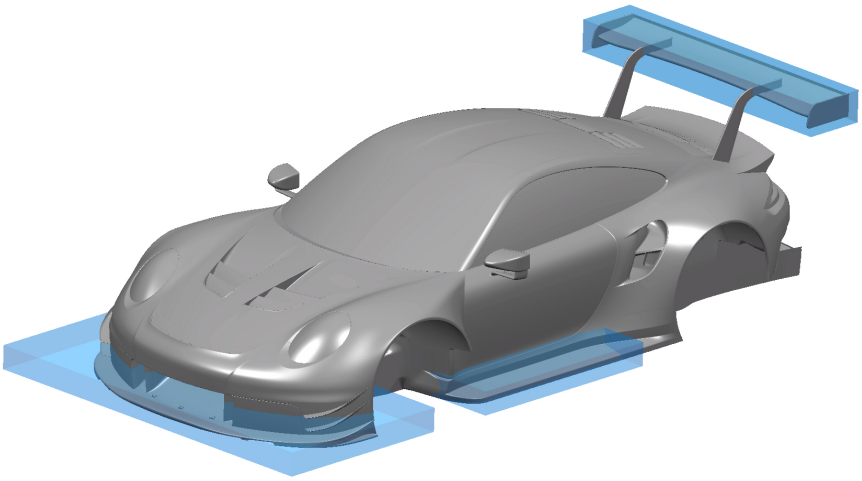

Figure 9.1: GTE19 Straight Line, Boxes from Left to Right show Front Wing, Forward Floor and Rear Wing.

9.1.1. Car Simulation Cases

Two cases have been chosen to study this car model. The first is a straight line case, which means that because of symmetry only half the car needs to be simulated. This symmetry condition is one of the factors evaluated in the airfoil model study and its validity for the full car case is assessed in Chapter 10. The car is reasonably flat in this case, which means that the lowest point at the front of the car has about the same ground clearance as the lowest point at the back of the car. The velocity at which the car is simulated is 27.5 m/s, which corresponds to around 100 km/h. This is lower than the top speed of this car in a straight line, which is about three times as high. The reason that this speed is simulated is because it corresponds to the situations where the car needs high downforce, like braking and accelerating. Downforce is less critical at top speed in a straight line and therefore these cases are less interesting to simulate and analyse.

The second case is a car in cornering. Due to the lack of symmetry, the full car now needs to be simulated which doubles the required resources. In this case, the average height of both the front and the rear of the car is increased, as happens in reality in a low speed corner. This reduces the ground effect and therefore makes the front wing and the floor less efficient. The car however, now also has a yaw, roll and steer angle. The yaw angle changes the angle of the incoming floor with respect to the car and the steer angle changes the angle of the wheels with respect to the car. The roll angle causes one side (left or right) of the car to be closer to the ground than the other. The average ride height can be found in the symmetry plane of the car, with one side moving up and the other moving down from there. This overall results in an asymmetric flow over the car quite different from the straight line case. The velocity is again 27.5 m/s.

9.1.2. Physics Model Selection

As discussed in Section 5.1.1, the “Physics Models" are chosen in STAR-CCM+ to set-up the simulation. The models chosen for the baseline car are almost the same as for the airfoil model study in Chapter 5, the only difference is that the $k-\omega$ SST-IDDES method is used as the baseline. This goes against the recommendations from STAR-CCM+ but it shows better results on the finer meshes of the airfoil models, as discussed in Section 8.3. This gives the following physics models as a baseline:

- Three Dimensional
- Implicit Unsteady
- Segregated Flow
- Turbulent
- Gas
- Constant Density
- Cell Quality Remediation
- Gradients
- Detached Eddy Simulation
- SST (Menter) K-Omega Detached Eddy
- Exact Wall Distance
- All y+ Wall Treatment

9.1.3. Model Settings

Due to the change from the SA-IDDES to the $k-\omega$ SST-IDDES method, the model constant C_{dt} in the IDDES model is changed. For $k-\omega$ SST-IDDES, C_{dt} is 20 by default instead of 8. Additionally, the curvature correction option is on by default (instead of off), the Low Re Damping Modification is turned off and the convection is still second order. For completeness, the other settings of interest are:

- Air as the Gas continuum
- Air density is 1.18415 kg/m^3
- Air dynamic viscosity is $1.85508 \cdot 10^{-5}$ Pa-s
- Hybrid-BCD scheme for convection
- Blending factor Hybrid-BCD scheme (C_{desT}) of 0.15
- The Minimum Allowable Wall Distance is 10^{-6} m
- The Maximum Number of Eddies is 1000
- The reference pressure is 101325 Pa

- The under relaxation factor of the turbulent viscosity solver is 0.7
- The AMG Linear Solver group size is 4
- The turbulence intensity is 1% for both inflow and initial turbulence
- The turbulent viscosity ratio (μ_t/μ) is 10 for both inflow and initial turbulence

9.1.4. Boundary and Initial Conditions

As said before, for the straight line case only half of the car is simulated and the symmetry condition is imposed in the middle of the car and the wind tunnel domain. For the cornering case this boundary condition is not present as the full car is simulated. The domain in the case of a full car simulation is shown in Figure 9.2. In both cases a velocity magnitude and direction is imposed on the inlet of the wind tunnel and a pressure outlet is used on the other side. The floor is the most complex part of the wind tunnel, which has a moving belt like in the wind tunnel. Similarly, the wheels have rotating boundary conditions at a set rpm. For all of the other wind tunnel parts a free slip wall is imposed. Figure 9.2 shows that the car is quite close to the inlet of the wind tunnel domain, but that there are multiple car lengths of domain behind the car to facilitate the capturing of the car wake.

As stated in the model settings, turbulence is used in the baseline settings. This turbulence is needed by the LES part of the solution to create the fluctuations. This turbulence is specified as both an initial condition and an inflow condition, as is advised for LES simulations. The turbulence is based on an intensity and a viscosity ratio. The baseline settings used are an intensity of 1% and a viscosity ratio (μ_t/μ) of 10. The aim is to compare the CFD results to wind tunnel data. The flow in the wind tunnel has a some turbulence in the inflow. The exact turbulence from the wind tunnel is not known, but it is low according to [45] motivating the choice for the low inflow turbulence for the CFD simulations. The values 1% and 10 are currently used as the standard practice by the team based and are in agreement with the advice from STAR-CCM+ for simulating turbulent flows.

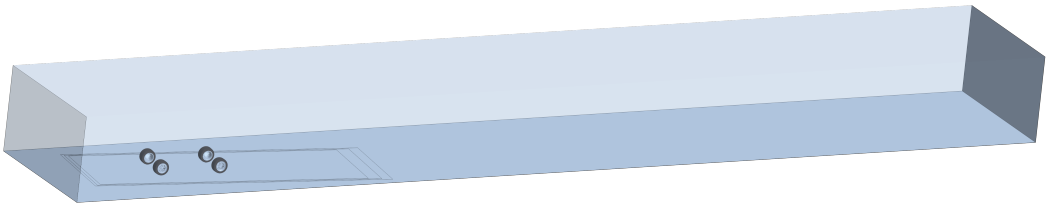

Figure 9.2: Wind Tunnel Lay-out in CFD, Cornering case.

9.1.5. Solving and Stopping Criteria

The simulations are started as a steady RANS simulation, using the $k-\omega$ SST model. This is run for 1000 steps before changing to the $k-\omega$ SST-IDDES model. For 1200 time steps, the IDDES model is run with a first order accurate scheme for the convection. The last 800 time steps are run with a second order accurate scheme. During the IDDES part of the simulation, 3 inner iterations are used resulting in an overall total of 7000 iterations. The 3 inner iterations is the minimum amount advised by STAR-CCM+ [5]. Since the airfoil results concerning the impact of the number of iterations are inconclusive, this minimum is kept to keep the costs low.

Section 3.1.2 discusses a number of ways to estimate the time step. One method, based on the advise from STAR-CCM+ for vehicle simulations Based on Equation 3.1, a car that is approximately 4.6 m long and drives at a speed of 27.5 m/s should be simulated with a time step of 0.0017 s. The time step chosen is slightly below that at 0.001 s. The Courant number for the redesigned DES mesh is shown in Figure 9.3 and serves as an evaluation of the appropriateness of this value. The design of this mesh is explained in Section 9.2.2. The Courant number here is based on the baseline fine mesh discussed in Section 9.2.2 and corresponds to the results discussed in Section 10.1. The Courant Number indicates that in the highly refined areas a smaller time step could be desirable. These areas include the front wind and the rear wing primarily. The Courant number is over 25 there reaching up to 50 which is too large. Note that as an implicit unsteady method is used, a Courant number under 1 is desirable but not required.

Due to the costs related to decreasing the time step and thereby the Courant number, the vehicle based time step estimation is used as a base. This is one of the recommendations of STAR-CCM+ and gives the time step of 0.001 s, even though this gives a locally too high Courant number. A disadvantage of this choice could

be that the time step is too small to capture the structures that could otherwise be captured by the fineness of the mesh. This would reduce the efficiency of the mesh refinement. This choice is not in agreement with the results obtained in the airfoil model study, as discussed in the reflection in Section 8.3.

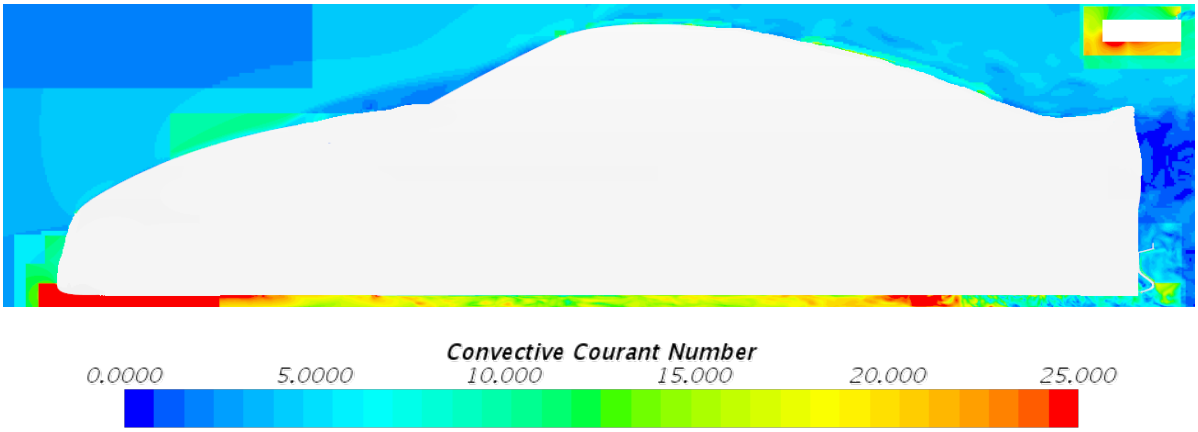

Figure 9.3: GTE19 Straight Line Courant Number on DES Mesh, Side View.

9.2. Car Model Mesh

Compared to the mesh used for the RANS simulations, the mesh is locally refined much further for the DES simulations. This is done based on the recommendations of STAR-CCM+ in combination with knowledge about the expected flow behaviour. This expected flow behaviour primarily differentiates between regions where unsteady small structures are important and attached flow regions without too much impact from these small scales. The recommendations of STAR-CCM+ are again linked to the length ratio discussed in Section 7.1. This section discusses the changes made to the RANS mesh to create the baseline DES mesh and the resulting length ratio in the mesh. The different regions discussed correspond to the highlighted regions in Figure 9.1 and are the rear wing, the front wing and the underbody or floor of the car. First however, the mesh used for the RANS simulations and the DES simulations on the RANS is discussed.

9.2.1. RANS Mesh

In general, isotropic hexahedral cells are used for the mesh around the car. The base cell size is 64 mm and the mesh is locally refined by a factor of 2 every step for certain domains. The RANS mesh makes use of refinement boxes, where regionally a specific mesh size is imposed. The minimum cell size used in the RANS mesh is 2 mm (or 3.125% of the base size). The vicinity of the car as well as the first part of the wake has a mesh refinement up to 8 mm. The far wake is refined to 16 mm. Areas refined to 4 mm include the front wing, the rear wing, the mirrors, the rear part of the diffuser and the wheels. Part of the wheel wakes and the air between the underbody and the floor are refined up to 2 mm. This refinement however, is partially anisotropic in order to save cells. This anisotropic mesh is only present for the RANS simulations and for the DES simulations on the RANS mesh run for comparison to the fine mesh. Under the floor of the car, this results in an edge length of 4 or 8 mm in streamwise direction and 2 mm in the other directions. All of these refinements are defined with the aid of refinement boxes. Additionally, curvatures are also refined automatically by STAR-CCM+ up to 2 mm or 4 mm. The RANS mesh and its length ratios are visually compared to the DES mesh in Section 9.2.3. The total number of cells is approximately 85 million. This mesh is the first mesh given in Table A.1 in Appendix A, where an overview of all full car meshes is kept.

9.2.2. DES Mesh

To transform the RANS mesh into a mesh suitable for DES, a number of regions are refined further. These include the rear wing, front wing and underbody. These regions are all discussed separately in this section. In order to capture the influence of the mesh on the results for DES simulations in general, DES simulations are also done on the original RANS mesh.

One of the regions that is refined for the DES mesh is the rear wing. The length ratio shows that further refinement is needed, although a refinement box up to 4 mm is already present. A new box is defined closely around the rear wing, where the mesh is refined up to 2 mm. In order to save some cells, the original refine-

ment box present for the RANS simulation is reduced in size, since the length ratio illustrates that part of the air captured by the box does not need the refinement up to 4 mm and can stay at 8 mm. The same is applied to the end plates of the rear wing, where a reasonably tight 2 mm box is added.

Underneath the front wing, a 1 mm box is added to capture the flow that goes underneath the car. This region has quite some influence on the front downforce and therefore needs to be captured well. Around this 1 mm box, also a 2 mm box is added that refines the domain around the 1 mm box. This includes the air in front of the front wing and over the top side of the front wing. The front part of the underbody is already refined up to 2 mm for the RANS mesh, which is sufficient to satisfy the length ratio for DES too. The mid part has 2 refinement boxes which refine up to 2 mm in two directions, but need additional refinement in streamwise direction to generate the isotropic mesh desired by the LES domain. For the rear part of the underbody that is above the refinement of the wind tunnel floor, a finer cell size of 2 mm is specified only at the boundary of the part, which makes the mesh locally around the boundary finer. Besides this, a box is added just behind the leading edge of the floor plate with a 1 mm cell size to capture the vortices generated there.

For the moment, the refinement around the wheels is kept the same as the RANS mesh. The reason for this is that the discussion of the results will be focussed on the wings and the floor, the downforce creating parts of the car. Also, for the front wing, the rear wing and the floor the number of prism layers is increased from the 7 or 8 present in RANS to 12. With the near wall cell size this gives a stretch ratio of 1.25 as discussed in [43]. Ideally, they could be increased to 16 layers at a later stage in order to get a stretch ratio of 1.15 which is closer to what has been used in literature lately [4][51]. The other car parts have fewer prism layers. The total number of cells with the 12 prism layers is approximately 182 million. With 16 prism layers, this even increases to 191 million. The $y+$ value of the near wall cell is below 5 in the critical areas. A concise description of this particular mesh and the simulations run with it is given in Table A.1 in Appendix A. This is the Baseline DES mesh.

9.2.3. Mesh Comparison

In this section, the RANS and the DES meshes are compared based on the mesh sizes, the length ratio and a DES blending function. The comparison is mainly done for the straight line case. The differences with the cornering case are discussed at the end of this section. The overall mesh used for RANS is shown in Figure 9.4. Because the resolution of the picture does not show the difference between a 1 mm, 2 mm and 4 mm (an)isotropic mesh, this view is almost the same for the DES mesh and the RANS mesh. Visible are the refinements around both the wings and the floor, which are already present in the RANS mesh.

Figure 9.4: GTE19 Straight Line RANS Mesh, Side View.

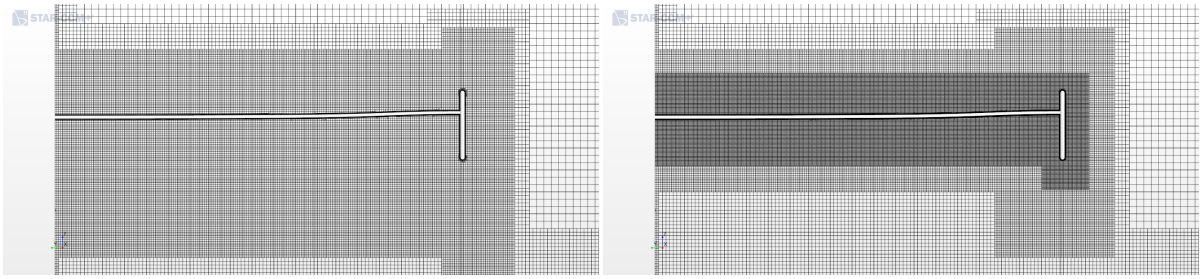

(a) RANS Mesh. (b) DES Mesh.

Figure 9.5: GTE19 Straight Line, Front View Rear Wing.

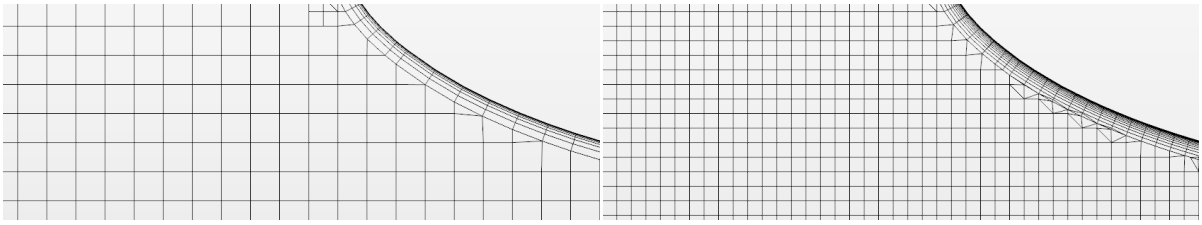

(a) RANS Mesh. (b) DES Mesh.

Figure 9.6: GTE19 Straight Line, Side View Rear Wing Leading Edge.

Figures 9.5 and 9.6 show the differences between the RANS and the DES mesh focussing on the rear wing. The increased number of prism layers is visible, as well as the additional refinement box of 2 mm around the airfoil. The changes in box size around the rear wing and its endplates are also visible. Note also the steps from the finest box to the coarser ones. Part of this is done automatically by STAR-CCM+ to ensure a smooth transition to and from the refinement regions. It is a setting that can be influenced by the user however. In this case, a gradual change was chosen to prevent sudden changes in mesh refinement. The location of the rear wing with respect to the car is shown in Figure 9.1.

The length ratio, as discussed is Section 3.1.3 and Section 7.1, for both the RANS and DES mesh is shown in Figure 9.7. Figures 9.7a and 9.7b show the air between the bottom side of the front wing and the wind tunnel ground, with the air flowing from left to right. This section of the car corresponds to the most left box in Figure 9.1. Figure 9.7a in particular shows the need for refinement between the front wing and the floor. Due to the very low length ratio here, the choice for a 1 mm mesh was made. The increase from about 85 million to 182 mesh elements is for almost 70% caused by this refinement and by the increase in the number of prism layers in the same area. Adding the refinement to 2 mm and the increase in prism layers between the floor of the car and the ground accounts to more than 90% of this increase.

The final 10% of the increase in mesh elements is due to the rear wing. Figures 9.7c and 9.7d show a front view of this rear wing, similar to Figure 9.5 but now extending on both sides of the symmetry plane. The length ratio around the rear wing on the DES mesh is still not fully satisfied everywhere. The criterion is satisfied better however, and the part that does not satisfy the criterion fully is reasonably close to the desired values. This means that the refinement around the rear wing stays at 2 mm and is not decreased further to 1 mm. This choice is evaluated in Section 10.3. There are other regions around the car that do not fully satisfy the length ratio criteria, but these are expected to have a limited influence on the results in the regions of interest. An example of this is the topside of the front of the car.

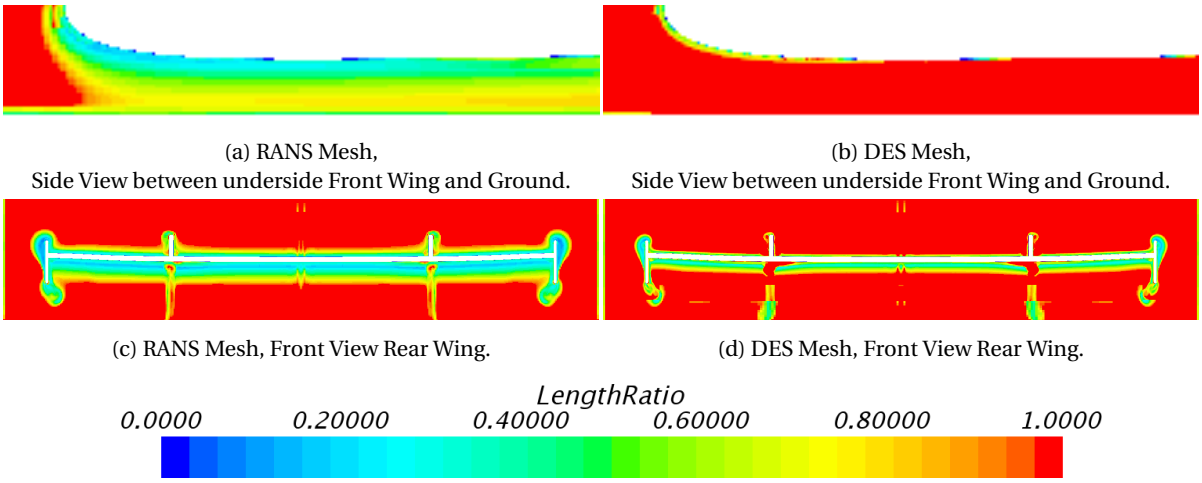

(a) RANS Mesh,
Side View between underside Front Wing and Ground.

(b) DES Mesh,
Side View between underside Front Wing and Ground.

(c) RANS Mesh, Front View Rear Wing.

(d) DES Mesh, Front View Rear Wing.

Figure 9.7: GTE19 Straight Line Length Ratio Comparison RANS and DES Mesh.

While the length ratio indicates whether the mesh is refined enough to support a DES, the blending functions indicate where RANS and where LES can be used by the DES method. Since the $k-\omega$ SST-IDDES method is used, the blending function $\tilde{f}_d$ can be visualised in Figure 9.8. This blending function is programmed into STAR-CCM+ based on the equations used according to the user manual [5]. It is not a direct output from the code and therefore an approximation, but the equations also agree with the equations documented in literature [38]. The blending functions shown are also discussed in Section 2.2.3.

These blending functions show that for the RANS mesh, the mesh is not fine enough between the wind tunnel floor and the car floor to support an LES computation in the middle. Figure 9.8a again shows the region between the front wing and the ground, with the air still going from left to right. Figure 9.8b then shows the same flow further downstream, between the floor of the car and the wind tunnel ground. This corresponds to the middle box in Figure 9.1. The red illustrates that the blending functions shield the wall from LES and prefer a RANS solution. Since the floor is a critical area, LES is desirable which motivates the refinement increase used for the DES mesh. The result of this refinement is shown in Figures 9.8c and 9.8d, which seems more desirable. Still underneath the front wing mostly RANS is used. Chapter 10 tries to improve upon this with more prism layers and different inflow conditions. The blending between RANS and LES around the rear wing shown in Figures 9.8e and 9.8f is improved by the refinement and looks satisfactory.

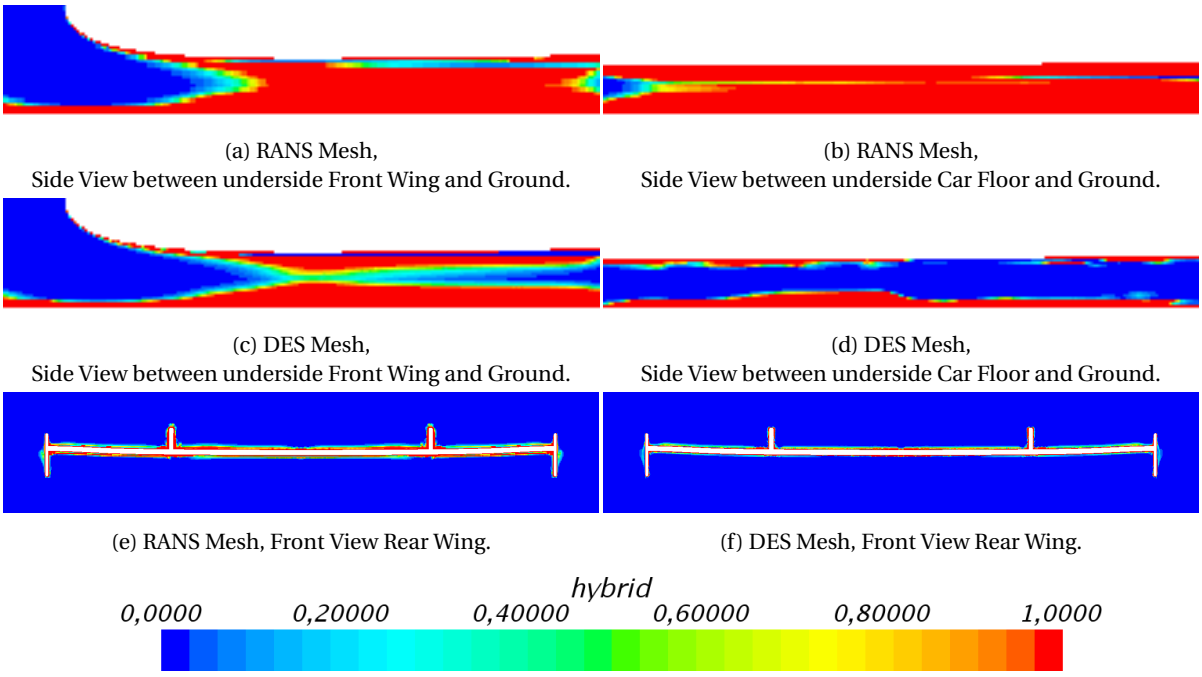

(a) RANS Mesh, Side View between underside Front Wing and Ground.

(b) RANS Mesh, Side View between underside Car Floor and Ground.

(c) DES Mesh, Side View between underside Front Wing and Ground.

(d) DES Mesh, Side View between underside Car Floor and Ground.

(e) RANS Mesh, Front View Rear Wing.

(f) DES Mesh, Front View Rear Wing.

Figure 9.8: GTE19 Straight Line $\tilde{f}_d$ Comparison RANS and DES Mesh using $k-\omega$ SST-IDDES.

For the cornering case, exactly the same refinement boxes are used and mirrored in the symmetry plane of the car. The refinement boxes are defined with respect to the yaw axis of the car, which means that if the car is positioned at a yaw angle with respect to incoming flow so are the refinement boxes. The roll angle is ignored by the boxes, but since it is a small angle the boxes are still able to capture the geometry. This means that some of the extreme parts of the car, like the endplates of the rear wing, might be close to the edge of the refinement box. On the other hand, the refinement regions that stretch to the ground are still stretching to the ground which might change if the boxes would be rotated with the roll angle. The mesh is assessed before the simulation is run to ensure that all parts in need of refinement are encompassed by the refinement boxes. Results for the blending functions and length ratios are similar to the straight line case and are therefore not shown here.

10

Results GTE19 Car

This chapter discusses the various simulation results obtained for the GTE19 car. First, the results for the straight line case on the original RANS mesh and the baseline DES mesh are presented. This is done in Section 10.1 and gives a first estimate of the capabilities of DES. The influence of initial and inflow turbulence on this straight line case is then discussed in Section 10.2. Section 10.3 discusses the transition phenomena present in the runs discussed thus far and how these can be used to redesign the mesh and improve the simulation. The influence of using the Synthetic Eddy Method for inflow turbulence is then discussed in Section 10.4. Similarly, the influence of changing the DES model to the $k-\epsilon$ Elliptic Blending DES method is given in Section 10.5. The cornering case is then discussed in Section 10.6. For the DES mesh, some adjustments based on the straight line results are already implemented. An overview of these alterations is also given at the start of the section. A comparison with experimental data for both the straight line and the cornering case is then given in Section 10.7. This should indicate which areas of the car are well represented by the DES simulation and where improvements are still needed. For the straight line case, a second ride height is also compared to the experimental data. The purpose of this is to do a first comparison regarding the differences predicted instead of the absolute value. Finally, an overview of the simulation times and CPU hours for the different simulations is given in Section 10.8. This illustrates the increase in costs associated with this method and should, along with Section 10.7, serve as an indicator for the potential of the DES method for this type of simulation. All of the conclusions drawn in this chapter serve as input for Chapter 11 where the more complex LMP1 car is simulated.

10.1. Straight Line Baseline Results

This section discusses the results for the initial baseline DES simulations. To show the need for the refinement boxes added, the DES method is used on both the designed DES mesh and the original RANS mesh. The DES mesh is designed with the aid of the Length Ratio as described in Section 9.2. The mesh used here is the baseline DES mesh as given in Table A.1 in Appendix A. The results are compared to each other and to the results obtained with the Realizable $k-\epsilon$ RANS method. This is the method usually used by the team and therefore serves as a way to measure improvements in the process. The results for the other simulations are all given as a difference in percentage compared to the Realizable $k-\epsilon$ RANS results. This allows for a clear comparison between the normal process and the DES method and removes the need to show absolute values. The percentages for the initial straight line simulations are given in Table 10.1. For more elaborate data, Appendix B can be consulted. The contributions of the wings and floor to the change in front and rear downforce are split there. An important note about these numbers is the fact that for the RANS simulation, the results are averaged over the final 1000 iterations. The DES simulations however, are averaged over the final 400 time steps to get these values. Before generating the percentages, the forces are all non-dimensionalized to become force coefficients. This is needed for the comparison with wind tunnel data in Section 10.7.

Table 10.1 shows the differences between the various simulation results. When comparing the different simulations, the $k-\omega$ SST-RANS model predicts less downforce and also less drag compared to the Realizable $k-\epsilon$ RANS model. The main reason for the difference in rear downforce can be ascribed to the rear wing. In the Realizable $k-\epsilon$ simulation, the flow over the rear wing stays attached and the rear wing generates a lot of downforce. In the $k-\omega$ SST-RANS run however, the rear wing is fully separated. This is also visualized

in Figure 10.1. Additionally, the Realizable $k-\epsilon$ model predicts a lower pressure under the front floor, thus further increasing the downforce generated by this model. This indicates that already within RANS, the model choice can make quite a difference and that the wing plays an important role in this difference. The main purpose of this report however, is not to compare the two RANS runs but to compare the DES results to the RANS results.

Simulation	C_z	C_x	$C_{z,front}$	$C_{z,rear}$	Bal
Realizable $k-\epsilon$ RANS	-	-	-	-	-
$k-\omega$ SST RANS	-16.1%	-6.38%	-9.3%	-20.8%	7.98%
$k-\omega$ SST-IDDES on RANS mesh	10.3%	9.74%	6.42%	12.9%	-3.48%
$k-\omega$ SST-IDDES on DES mesh	7.46%	12.0%	-0.11%	12.7%	-7.05%

Table 10.1: GTE19 Straight Line Forces of Baseline CFD Simulations

First, the Detached Eddy Simulation on the coarse RANS mesh is assessed in more detail. As is shown in Figure 10.1c, a large wake is present on the rear wing. This along with the lower downforce produced by it leads to the conclusion that the flow over the rear wing separates for the DES simulation on the RANS mesh, similar to the $k-\omega$ SST-RANS simulation as shown in Figure 10.1b. The wing in this simulations only separates around the structural elements holing it up, which means that the loss in downforce is a lot smaller than for the $k-\omega$ SST-RANS run. Note that the decrease in downforce production only refers to the downforce produced by the rear wing, not the rear downforce in total. As shown in Table B.1, the rear floor generates a higher downforce in the coarse DES simulation. This increased downforce fully compensates for the loss in downforce from the rear wing. The difference with the Realizable $k-\epsilon$ RANS simulation can be seen in Figure 10.1a.

Unlike the $k-\omega$ SST-RANS simulation, the coarse DES produces more drag than the Realizable $k-\epsilon$ RANS simulation. The contributions to this are not further assessed, but the validity is discussed in the comparison with experimental data.

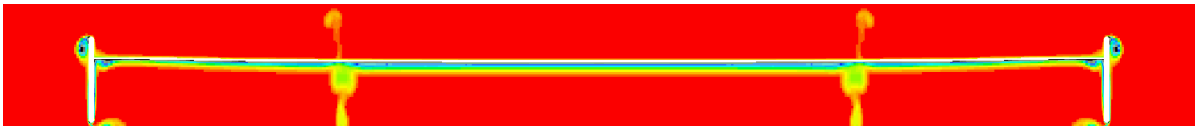

(a) Realizable $k-\epsilon$ RANS.

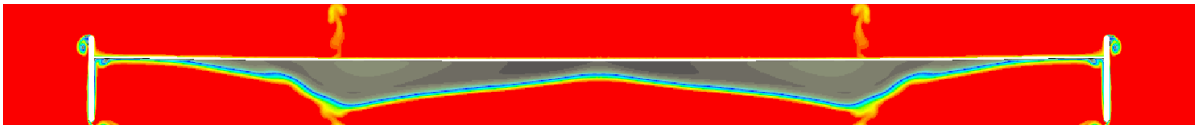

(b) $k-\omega$ SST-RANS.

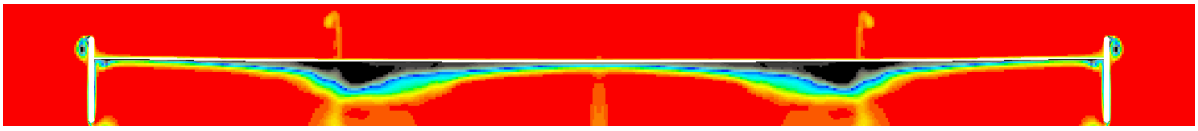

(c) $k-\omega$ SST-IDDES on RANS mesh.

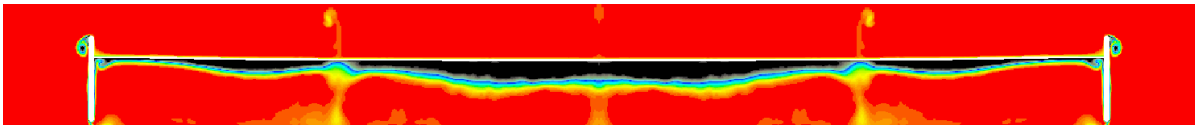

(d) $k-\omega$ SST-IDDES on Baseline DES mesh.

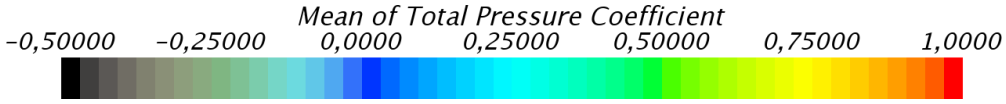

Figure 10.1: GTE19 Straight Line Total Pressure Coefficient, Front View Rear Wing.

The overall rear downforce generated by the coarse DES compared to the Realizable $k-\epsilon$ RANS is higher, contrary to what is expected based on the rear wing only. The loss in downforce from the rear wing is compensated by the downforce generated by the rear floor. This compensation is possible because in the coarse DES a lower pressure underneath the car and therefore higher downforce is predicted. Because of the size of the floor surface, the effect of this lower pressure on the overall downforce is large. Table 10.1 shows that this gives a higher downforce in the DES results even though some downforce is lost on the rear wing. The exact cause for this lower pressure underneath the floor is unknown and this is one of the areas that will be evaluated further in subsequent comparisons. Since the rear floor is slanted upwards, this lower pressure at the rear floor also increases the drag at the rear of the car, explaining around 40% of the difference in drag between the two simulations. This lower pressure also results in a lower pressure behind the car further increasing the drag resulting in a total contribution of over 80% of the difference.

The results on the baseline DES mesh give a downforce that is slightly closer to the Realizable $k-\epsilon$ RANS results, but the drag is even further off. To keep track of the different meshes, Table A.1 can be consulted. The separation over the rear wing is now spread over a larger part of the rear wing span but is less severe. This is visualised in Figure 10.1. Compensation by the rear floor is still present however, since the rear floor again has a lower pressure and a higher downforce as compared to the other DES. This again causes the overall rear downforce of the DES simulation to be higher than the downforce in the reference RANS simulation. The difference in drag again partially stems from the rear of the car, although the front wing now also plays a role.

The front downforce of the fine DES simulation is very close to the Realizable $k-\epsilon$ RANS simulation. The behaviour of the flow however, is quite different as can be seen in Figure 10.2. Towards the trailing edge of the front wing a separation and recovery takes place, increasing the suction on the front wing. The total downforce of the front of the car stays similar however, since the front floor behind the wing creates less downforce in the DES simulation and the front topside of the car a bit more. The front wing in particular is further discussed in Sections 10.2 and 10.3.

The differences between the base RANS and the DES results are quite large. The rear wing, rear floor and front wing being the main contributors to this difference. To improve the results, especially concerning the separating rear wing, turbulence and transition are more closely assessed in Sections 10.2 and 10.3.

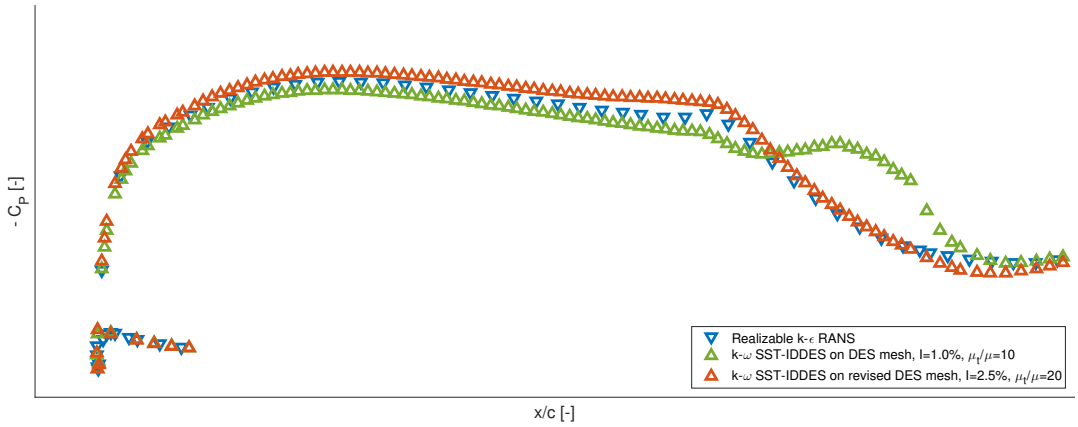

Figure 10.2: GTE19 Straight Line Pressure Distribution, Front Wing at Y=0.5 m (from Symmetry Plane).

One thing that can also be noted about the comparison in Figure 10.1 regards the symmetry plane. The rear wing as a whole is shown since the post processing step mirrors the side of the car that is simulated. In reality however, as discussed before, only half of the car is simulated and the symmetry condition is imposed on the mid-plane. As discussed in Section 7.2, this is not entirely correct and can give some wrong flow phenomena. The symmetry condition states that all of the gradients must be zero at the boundary, while in reality this is not true. Especially for an inherently three-dimensional model like DES, this condition can cause errors. This is probably what can be seen in the middle of the rear wing, since geometry-wise no reason for the loss in total pressure is present. In this case, the impact of the symmetry condition seems small as the pressure loss is limited, but ideally a full car would also be run in the straight line case or the results around the symmetry plane should be closely monitored.

10.2. Influence of Inflow and Initial Turbulent Content

In the baseline case, the turbulence intensity and the turbulent viscosity ratio are set to 1% and 10 respectively. This section evaluates the influence of adjusting these numbers in order to increase the turbulence level. For the first case, the turbulent viscosity ratio is left at 10 and the turbulence intensity is increased to 2.5%. For the second, the turbulence intensity is kept at 2.5% and the turbulent viscosity ratio is increased to 20. The initial values used correspond to the minimally advised values in the STAR-CCM+ user guide. Increasing the turbulence intensity should increase the turbulent kinetic energy at the inlet. The viscosity ratio is an indication for how turbulent the flow is, with a more turbulent flow at a higher viscosity ratio. In general, increasing these number should result in more turbulence in the flow and in the case of IDDES enable LES regions closer to the walls.

In both cases the baseline DES is used but with one additional change. The number of prism layers is increased from 12 to 16, as is also proposed in Section 9.2.2. The mesh used here is the Revised DES mesh as given in Table A.1 in Appendix A. This step is aimed at capturing the flow over both wings better. The airfoil study shows that the number of prism layers influences amongst others if and how well transition is captured. This means that not all changes in the results are due to the difference in turbulence settings, some may be due to the number of prism layers. Again, the values are compared to the original RANS value and the baseline DES value on the fine mesh. This is shown in Table 10.2. Again, the contributions to the differences on the front wing, rear wing and floor are given separately in Appendix B.

Simulation	C_z	C_x	$C_{z,front}$	$C_{z,rear}$	Bal
Realizable $k-\epsilon$ **RANS**	-	-	-	-	-
$k-\omega$ **SST-IDDES**, I=1.0% (μ_t/μ)=10, 12 prism	7.46%	12.0%	-0.11%	12.7%	-7.05%
$k-\omega$ **SST-IDDES**, I=2.5% (μ_t/μ)=10, 16 prism	10.7%	12.8%	7.97%	12.6%	-2.49%
$k-\omega$ **SST-IDDES**, I=2.5% (μ_t/μ)=20, 16 prism	10.4%	12.3%	6.65%	13.0%	-3.41%

Table 10.2: GTE19 Straight Line Forces when varying Turbulent Content

The difference between the two runs at 2.5% turbulence intensity is only to a limited extend visible both in terms of drag and downforce. The pressure distribution over the rear wing changes a bit, but no major differences are observed. The difference between these two results and the baseline DES run is larger, especially in terms of downforce distribution. The runs with the increased turbulence result in more downforce production at the front of the car. A closer look at the results reveals that one of the reasons for the difference in the front downforce is the front wing. This pressure distribution is more similar to the one captured by the Realizable $k-\epsilon$ RANS model, as shown in Figure 10.2. The pressure peak is higher however, resulting in a higher downforce production by the DES on the revised mesh. This flow underneath the front wing is discussed in more detail in Section 10.3. Note that additionally, the loss in downforce over the front floor is smaller further contributing to the increase in front downforce. Since the difference between the 2 runs at a higher turbulence intensity is very small, this effect could very well stem from the increase in the number of prism layers instead of from the inflow turbulence.

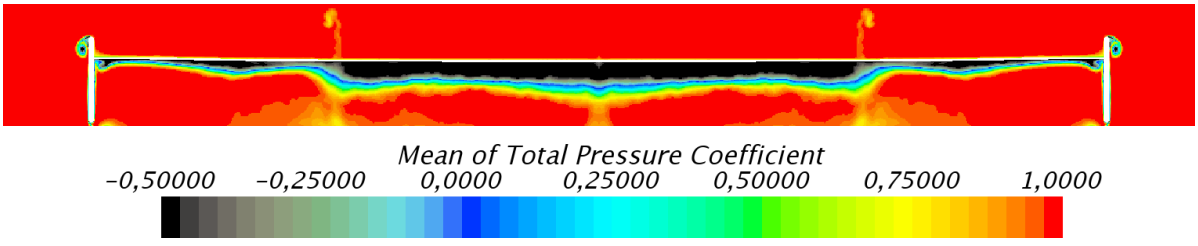

Figure 10.3: GTE19 Straight Line Total Pressure Coefficient, Front View Rear Wing.
SST-IDDES on Revised DES Mesh with Increased Turbulence.

The rear wing still separates as is shown in Figure 10.3, and even does so over a large span. Almost the full span between the two structures holding the wing up is now separated. The influence of the turbulence and the number of prism layers here thus decreases the downforce created by the rear wing a bit. On the other

hand, the downforce generated by the rear floor increases a bit compared to the base DES run. This keeps the rear downforce relatively similar between the three runs. The behaviour of the rear wing, although it should be verified with the wind tunnel experiments, still does not seem to be captured well by the DES method.

The main difference caused by the changes to the turbulence and the number of prism layers is the pressure distribution over the front wing. Sections 10.3 and 10.7 provide more information about these results. Based on the results in this section however, the choice was made to increase the number of prism layers for the DES mesh cornering case discussed in Section 10.6. This mesh with 16 prism layers is also referred to as the Revised DES mesh (see Table A.1).

10.3. Transition Phenomena

As has been stressed throughout the first part of this chapter, the front and rear wing influence the total downforce greatly. Transition plays an important role there, and in this section that phenomena is investigated further. The front wing pressure distribution seems to display some sort of transition. This phenomena is analysed and compared between different simulations in the first part of this section. In the second part, transition over the rear wing is also simulated in an effort to prevent separation. Capturing transition over the rear wing can be achieved by refining the mesh around the rear wing further, up to 1 mm, as has been done around the front wing. The transition on the front wing is revisited in the final part of this section. A close-up of the boundary layer is reviewed in order to understand the phenomena captured by the DES method better. To put the method in context, the boundary layer is compared to results obtained with a $k-\omega$ SST-URANS simulation with a transition model. The transition model is the $\gamma - Re_\theta$ model discussed in Section 3.2.4. The ability of the DES method to capture complex phenomena like laminar separation bubbles and at least through there transition was already discussed for the NACA 0012 airfoil in Section 7.4.

10.3.1. Front Wing Transition

For the front wing, comparisons are done using various models. Like the comparisons so far, various DES simulations are compared to the Realizable $k-\epsilon$ RANS results. The Realizable $k-\epsilon$ RANS model is not able to capture transition fully however. In order to compare the transition point to RANS results, a $k-\omega$ SST-URANS simulation with a transition model is used. This transition model is the $\gamma - Re_\theta$ model discussed in Section 3.2.4. This can give some more insight into the transition patterns observed for the DES simulations. The URANS simulations presented are based on another version of the same car. Small changes to the geometry are therefore present, but the bottom side of the front wing is very similar. Most of the floor behind the front floor has also stayed the same. The results obtained with URANS are given in Figure 10.6. Note that the left figure uses the Realizable $k-\epsilon$ turbulence model for the URANS simulation on this front wing and the right figure uses the $k-\omega$ SST model along with the $\gamma - Re_\theta$ transition model.

Figures 10.4 and 10.5 show results for the Realizable $k-\epsilon$ RANS simulation and three DES simulations. An instantaneous plot of the wall shear stress on part of the bottom side of the front wing is shown. One indicator for transition could be a laminar separation bubble as discussed for the airfoil in Chapter 7, or visible unsteady turbulent structures in the instantaneous wall shear stress. Comparing first the two runs on the RANS mesh, one RANS and one DES simulation, indicates that none of these phenomena are clearly visible through the wall shear stress. Lower wall stress is attained close to the symmetry plane but turbulent structures can not be observed. Note that Figure 10.4b displays an instantaneous flow field but that no unsteady, turbulent structures seem present. The Realizable $k-\epsilon$ RANS solution therefore looks quite similar to the $k-\omega$ SST-IDDES solution on the RANS mesh. The wall shear stress over the full front wing is just slightly lower for the $k-\omega$ SST-IDDES run, resulting in a slightly higher downforce.

On the baseline DES mesh, which has a cell size of 1 mm underneath the front wing and 12 prism layers, turbulent structures can be observed in Figure 10.5a. These are also visible in the simulation on the revised DES mesh with increased turbulence in Figure 10.5b. Both indicate a small separation region transitioning the flow from laminar to turbulent. This separation region is indicated by the very low wall shear stress, implying separated flow or recirculating flow. There is however, a clear difference in the location where this very low wall shear stress occurs. This location is moved more towards the leading edge (upwards in the figure) for the revised mesh with higher turbulence. Downstream of the potential transition, both simulations show unsteady flow structures in this instantaneous wall shear stress plot.

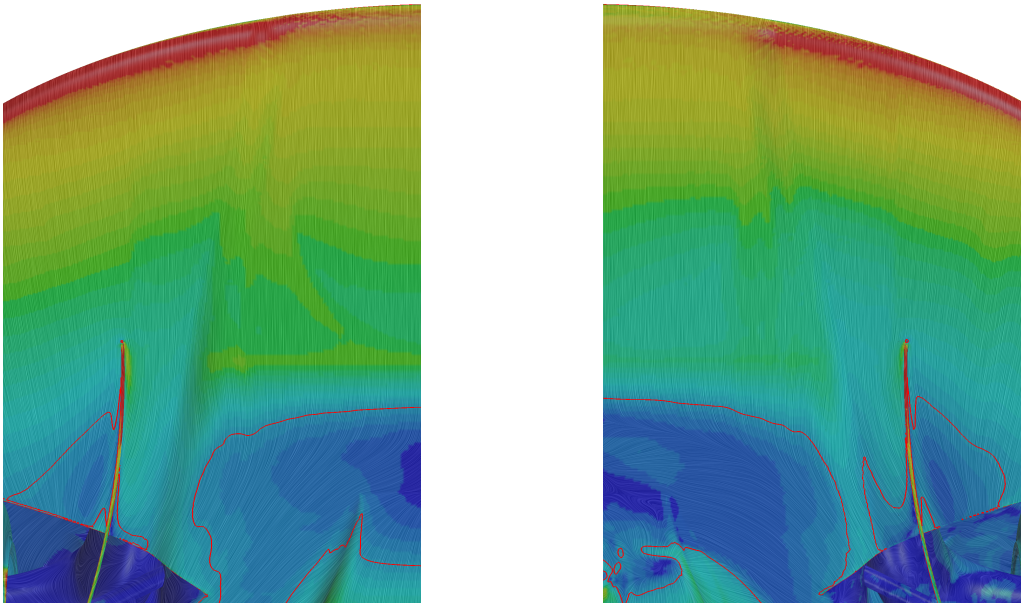

(a) Realizable $k-\epsilon$ RANS.

(b) $k-\omega$ SST-IDDES on RANS mesh.

Figure 10.4: GTE19 Straight Line Wall Shear Stress, Bottom View Front Wing (Suction Side).

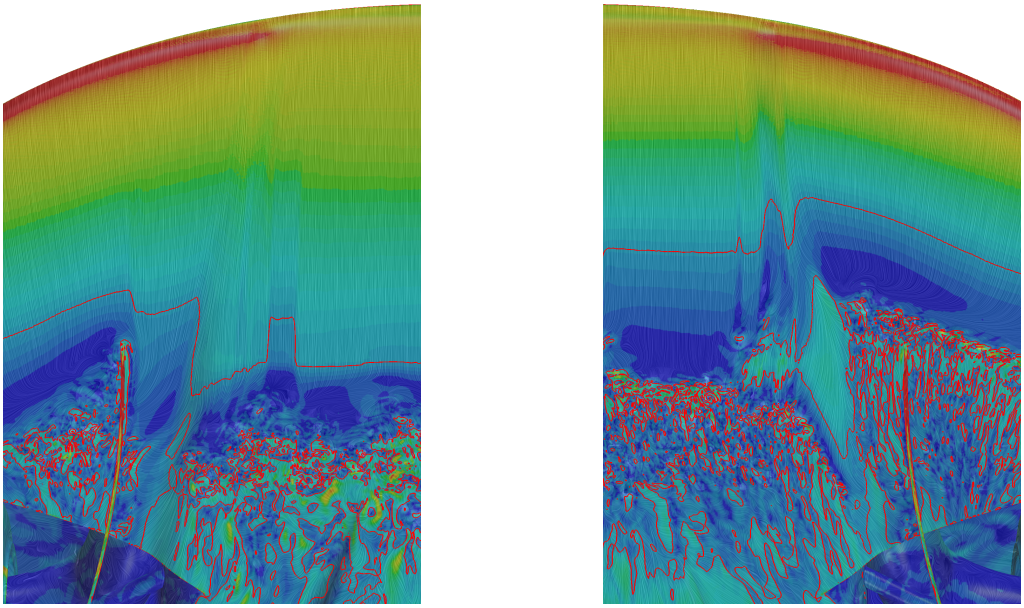

(a) $k-\omega$ SST-IDDES on Baseline DES Mesh. Low Turbulence.

(b) $k-\omega$ SST-IDDES on Revised DES Mesh. High Turbulence.

Figure 10.5: GTE19 Straight Line Wall Shear Stress, Bottom View Front Wing (Suction Side).

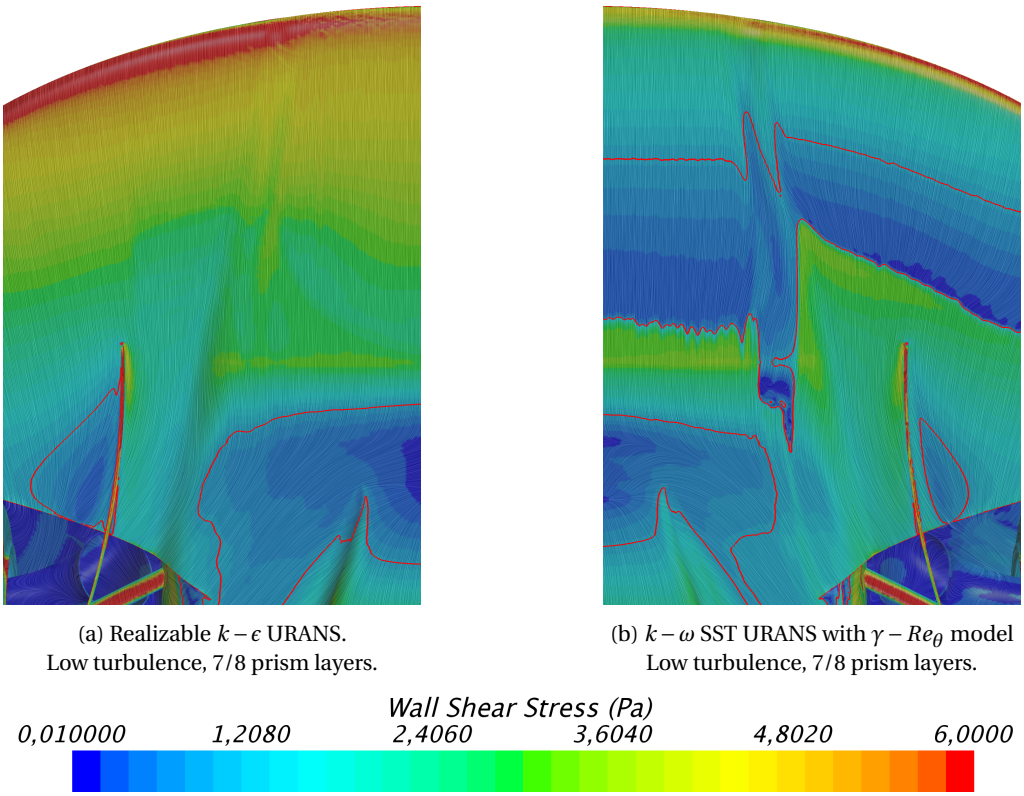

(a) Realizable $k-\epsilon$ URANS.
Low turbulence, 7/8 prism layers.

(b) $k-\omega$ SST URANS with $\gamma - Re_\theta$ model
Low turbulence, 7/8 prism layers.

Figure 10.6: GTE19 Straight Line Wall Shear Stress, Bottom View Front Wing (Suction Side).

The URANS simulation with the transition model turned off, Figure 10.6a, has a similar pattern to Figures 10.4a and 10.4b. The URANS simulation with the $\gamma - Re_\theta$ turbulence model turned on is shown in Figure 10.6b. The sudden increase in wall shear stress is an indicator of transition, since turbulent flow has a different velocity gradient in the boundary layer than laminar flow. Contrary to the DES simulations, the wall shear stress does not show a locally separated flow nor does it show unsteady flow structures. The location of this transition is most similar to the high turbulence results on the revised mesh. It is even further towards to the leading edge though. The turbulent structures after transition however, are not as well represented in the URANS runs. URANS should be able to capture some unsteady flow phenomena but models and does not resolve the unsteady turbulent structures. Another post-processing method would be needed to extract the information about the unsteady turbulent structures from the URANS simulation. Resolving these structures directly instead of computing their effect is one of the strengths of the DES method and could be a reason to accept the increased costs.

The transition model in the URANS model also increases the costs noticeably. Based on estimates from the airfoil model study, this is an increase around 40%. Reportedly for the full car, the time increase for the full car could be even higher than this 40% but since no URANS simulations have been performed for the thesis, they were done by other members of the team, this can not be confirmed. This increase in simulation time is still lower than the increase for the DES simulations due to the mesh requirements. It does however, puts the time increase for the DES method in perspective since the DES does capture more details in the flow and in the transition. More about the time involved in DES simulations is discussed in Section 10.8. A closer look into the boundary layer of the flow over the front wing is discussed in Section 10.3.3. This should confirm the expectation from the wall shear stress analysis that transition is captured. Although transition phenomena in various CFD simulations are discussed in general, the part used to visualize the transition is still the front wing. Before this however, the transition on a second wing is discussed: the rear wing.

10.3.2. Rear Wing Transition

Because of the major impact of the mesh on the transition on the front wing, the choice was made to also trigger the transition on the rear wing. Triggering this transition is done by refining from 2 mm to 1 mm around the rear wing, making the mesh resolution similar to the front wing. The results show that this mesh

change indeed has a big influence on the results on the rear wing. To compensate (partially) the increase in cell count needed for this, the mesh around the rear diffuser is coarsened back to the RANS mesh. This can also influence the results, especially regarding the rear floor. The mesh used here is the Revised DES RW mesh as given in Table A.1 in Appendix A.

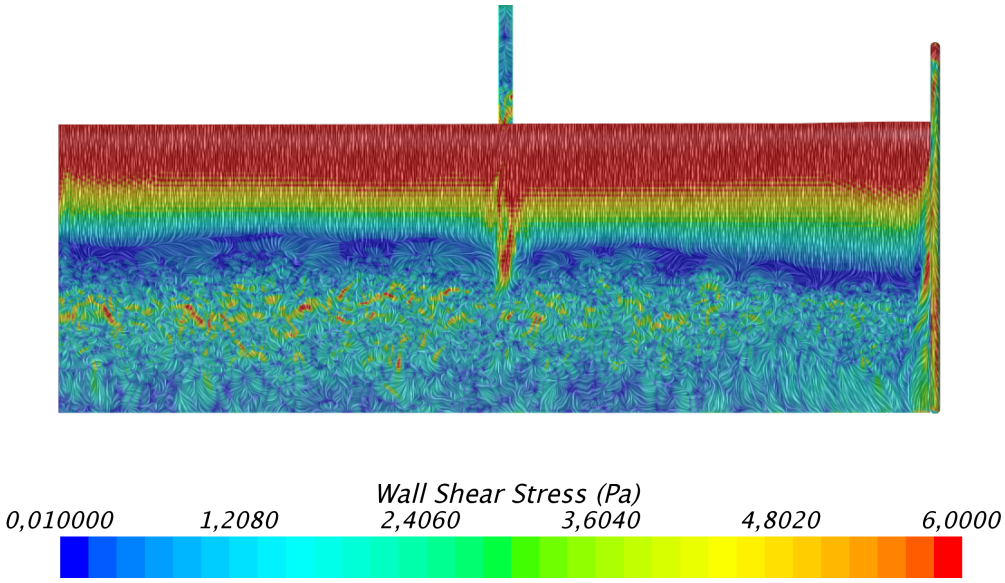

Figure 10.7: GTE19 Straight Line Wall Shear Stress, Rear Wing Bottom View (Suction Side)
1 mm Rear Wing Box with 16 Prism Layers.

The simulation results show the transition present over the underside of the rear wing, illustrated in Figure 10.7. The leading edge of the rear wing is at the top of the figure and the air is flowing from top to bottom. The bottom side of the rear wing is shown, which corresponds to the suction side. The wing shows a very low wall shear stress around midway, with unsteady flow structures afterwards. This could again be the transition from laminar to turbulent flow. This turbulent flow results in an attached flow over the full span of the rear wing and therefore in more downforce generated by the rear wing. Only a local separation is present in the transition region. The total pressure coefficient around the attached rear wing is shown in Figure 10.8. The performance of the rear wing is now fairly similar to the Realizable $k-\epsilon$ RANS simulation, creating only slightly less downforce than in the Realizable $k-\epsilon$ model.

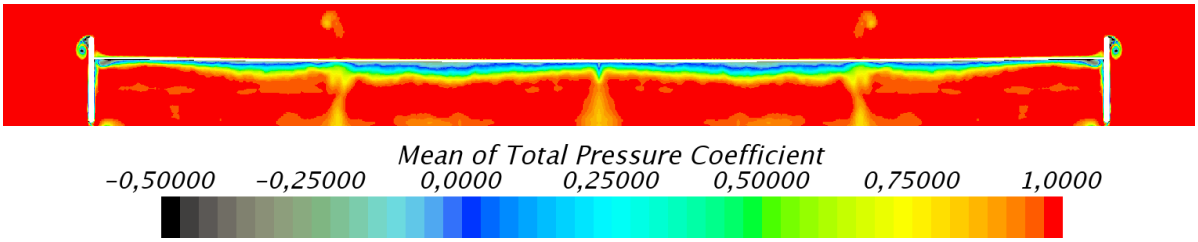

Figure 10.8: GTE19 Straight Line Total Pressure Coefficient, Front View Rear Wing.
$k-\omega$ SST-IDDES on Revised DES Mesh with Refined Rear Wing.

The comparison of the overall forces for this simulation are shown in Table 10.3. The DES simulation with and without the rear wing refinement with 16 prism layers and high turbulence are compared. The downforce at the rear is still very similar. This is because of the increase in downforce on the rear wing and a decrease on the rear floor.

The mesh with the refined rear wing also has a coarsened rear floor to compensate the number of cells. This means that the decrease in downforce production on the rear floor could also be due to this coarsening of the mesh. On the other hand, it could also be because the wake from the car is changed now that the rear

wing stays attached. The wake is pulled up by the rear wing which could also change the pressure distribution underneath the floor. Since the front wing stays similar and the front floor also produces less downforce, the front and overall downforce are reduced for the refined rear wing run. Overall, the refinement around the rear wing makes the results closer to the Realizable $k-\epsilon$ RANS simulation. This is a good first indicator since the RANS method used has been optimized by the team over time in order to do a good global flow prediction. Still, the results of the $k-\epsilon$ RANS do deviate from the wind tunnel experiments motivating a comparison to wind tunnel data directly as well. This is done in Section 10.7.

Simulation	C_z	C_x	$C_{z,front}$	$C_{z,rear}$	Bal
Realizable $k-\epsilon$ **RANS**	-	-	-	-	-
$k-\omega$ **SST-IDDES**, I=2.5% (μ_t/μ)=20	10.4%	12.3%	6.65%	13.0%	-3.41%
$k-\omega$ **SST-IDDES**, RW refined	5.59%	12.3%	-1.95%	10.9%	-7.15%

Table 10.3: GTE19 Straight Line Forces with and without Rear Wing Refinement

10.3.3. Identification of Transition Phenomena

This section is devoted to the transition found on the front wing. From the wall shear stress and the pressure distribution it is clear that some sort of transition from laminar to turbulent flow takes place. The exact nature of the transition however, needs a closer look. A number of flow features are therefore presented and discussed to get a better feel of the behaviour captured by the method leading to the transition.

Before discussing the transition captured by the DES method, the $k-\omega$ SST-URANS with the transition model shown in Figure 10.6b is discussed again. In this case, the boundary layer does not show too many instabilities before the transition takes place. What is very clear however, is the difference between the velocity gradients near the wall in the laminar and turbulent domain. This is shown in Figure 10.9. There is quite a quick transition between the two, but without realizing a laminar separation bubble.

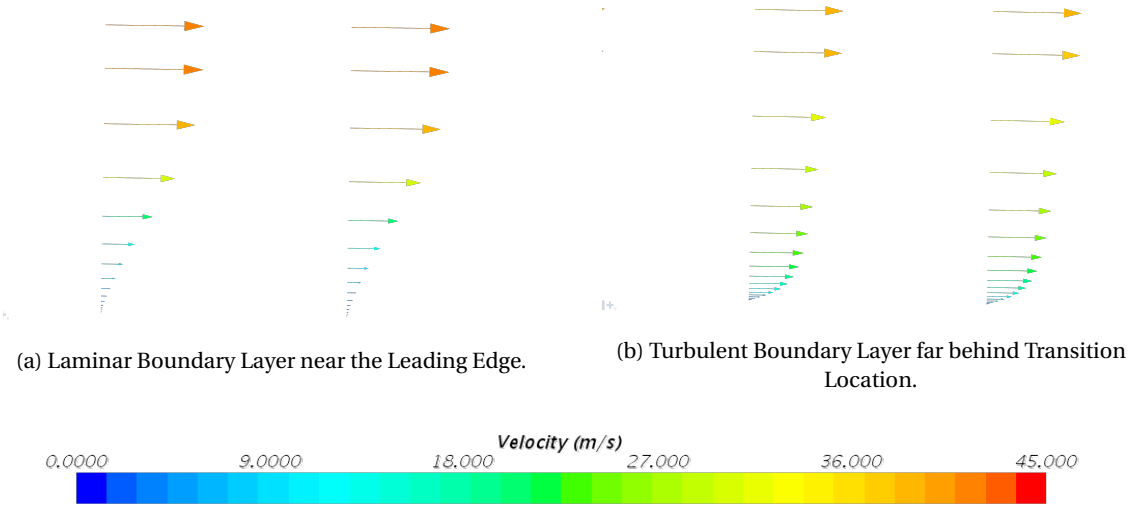

(a) Laminar Boundary Layer near the Leading Edge.

(b) Turbulent Boundary Layer far behind Transition Location.

Figure 10.9: Velocity Gradient Comparison in the Boundary Layer of a $k-\omega$ SST-URANS Simulation.

The DES results have a less clear change in this respect, as the instantaneous turbulent part of the boundary layer is dominated by unsteady vortices changing the direction of the velocity vectors locally. One thing that can be visualized nicely in the DES is the reverse flow region that emerges in the transition region. This is shown in Figure 10.10. This reverse flow is not present in the transition of the URANS with the transition model.

The exact nature of the transition remains unidentified. The flow and geometries are quite complex in this region. The bottom side of the front wing is neither flat in streamwise nor in spanwise direction causing cross flow and spanwise variations in the flow. Also, the DES method might not capture all of the details, since part of the boundary layer could still be modelled with RANS instead of partially resolved with LES.

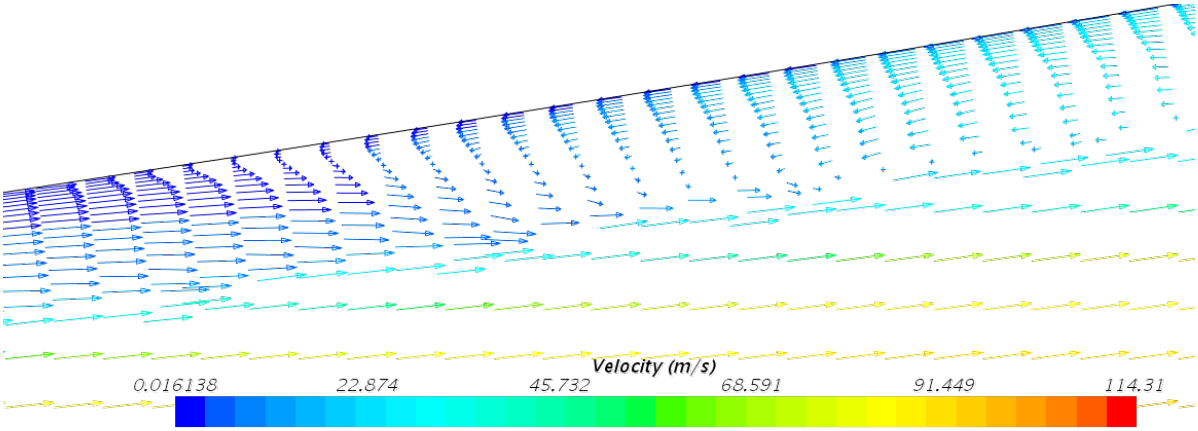

Figure 10.10: Reverse Flow in $k-\omega$ SST-IDDES Simulation on Fine Mesh.

In [53], a different DES variant called adaptive DES is used to capture different types of transition. This model switches between DDES and wall-resolved LES instead of between DDES and wall-modelled LES as IDDES does. It is stated that if the RANS region stays below $y^+ = 5$, the model performs the same as wall-resolved LES. This would make the model better at capturing transition than other models as is DES motivated in the paper.

The DES method used for the GTE19 car considered switches between DDES and wall-modelled LES. With the fine grid used around the front wing, wall-modelled LES is probably active resulting in quite a thin RANS region. This RANS region however, is still much thicker than the $y^+ = 5$ from the paper, it is in the range of $y^+ \sim 10^1 - 10^2$. This means that most of the outer part of the boundary layer is resolved instead of modelled, but that the inner part is modelled. This is in agreement with the definition of WMLES as given in [21].

The same author argues that WMLES is not able to predict transition properly, since turbulent flow is assumed by the wall models already in the laminar boundary layer. This however, applies to a type of WMLES that uses wall-stress models in the unresolved part. In the case of IDDES, RANS is used instead of these wall-stress models which assume turbulent flow and therefore predict the laminar boundary layer wrongly. An under resolved LES without wall-stress models, is capable of prediction the transition point but is not capable of predicting the turbulent skin friction well [21]. Hybrid (WM)LES-RANS methods are not discussed in this context in [21]. The main question that arises therefore is whether the RANS model that models the skin friction in both the laminar and the turbulent boundary layer is able to handle the transition. The current results and the airfoil study seem to suggest so, but more detailed data about the exact transition location is needed to draw a solid conclusion about the ability of IDDES to properly predict the location of transition.

10.4. Influence of the Synthetic Eddy Method

To evaluate the effect of inflow turbulence better, the Synthetic Eddy Method is used at the inlet boundary. During the steady part of the simulation the 2.5% turbulence intensity and the viscosity ratio of 20 are kept. With the start of the DES simulation however, the inflow boundary is adjusted to generate the synthetic turbulent eddies. The turbulence intensity of 2.5% is kept and a turbulent length scale of 0.004 m is used. This turbulent length scale is estimated based on the aforementioned turbulence settings, the flow properties and the relation for the turbulent length scale for the $k-\omega$ SST method shown in Equation 3.8. The results for this simulation are given in Table 10.4.

Simulation	C_z	C_x	$C_{z,front}$	$C_{z,rear}$	Bal
Realizable $k-\epsilon$ **RANS**	-	-	-	-	-
$k-\omega$ **SST-IDDES**, RW refined	5.59%	12.3%	-1.95%	10.9%	-7.15%
$k-\omega$ **SST-IDDES**, SEM	8.95%	12.8%	2.40%	13.5%	-6.02%

Table 10.4: GTE19 Straight Line Forces with and without Synthetic Eddy Method

The results obtained by the Synthetic Eddy Method are further away from the Realizable $k-\epsilon$ RANS simulation in terms of forces, but closer in terms of balance. The main cause for this is an increase in downforce

for both the front and the rear floor. Both the front and the rear wing still exhibit the transition behaviour but do generate a bit less downforce. On the front wing, a clearer reattachment area after the separation is present and the separation is more regular. This is shown in Figure 10.11a. For comparison, Figure 10.5b is repeated here to illustrate the results for the DES simulation with high turbulence on the revised mesh. Both simulations also have the exact same mesh including the refined rear wing. This is referred to as the Revised DES RW mesh in Table A.1 in Appendix A.

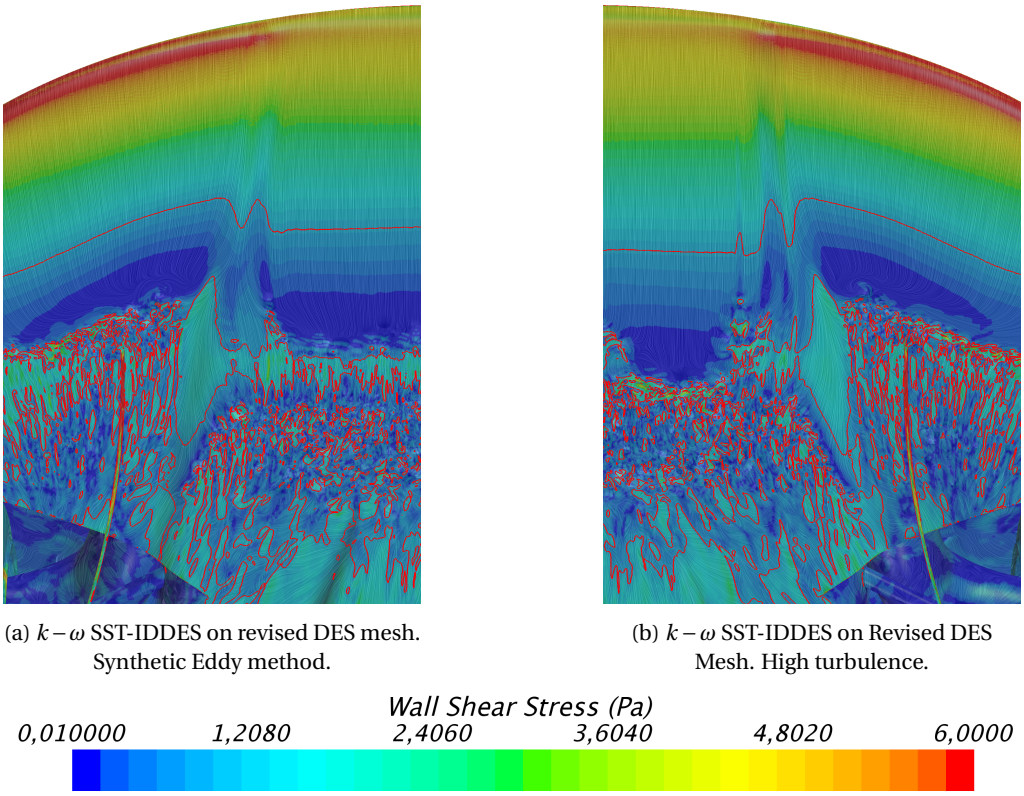

(a) $k-\omega$ SST-IDDES on revised DES mesh. Synthetic Eddy method.

(b) $k-\omega$ SST-IDDES on Revised DES Mesh. High turbulence.

Figure 10.11: GTE19 Straight Line Wall Shear Stress, Bottom View Front Wing (Suction Side).

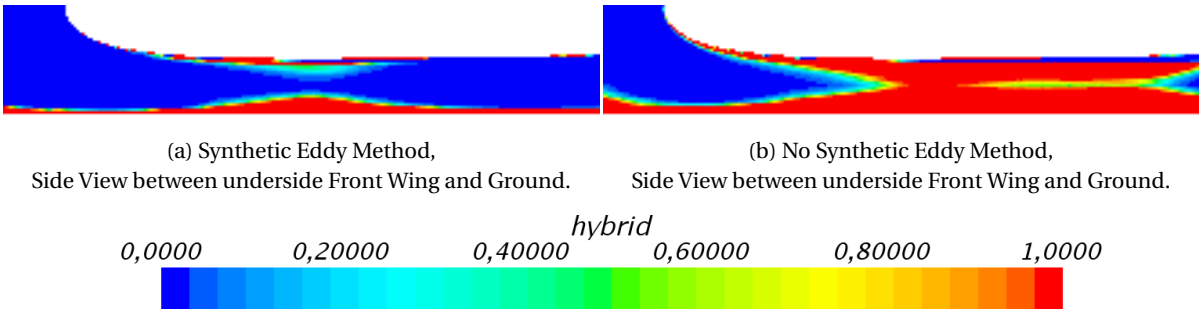

(a) Synthetic Eddy Method, Side View between underside Front Wing and Ground.

(b) No Synthetic Eddy Method, Side View between underside Front Wing and Ground.

Figure 10.12: GTE19 Straight Line $\tilde{f}_d$ Influence SEM on Revised DES Mesh using $k-\omega$ SST-IDDES.

A possible origin for the difference in downforce could be the value of the blending functions underneath the front wing. The hybrid blending function $\tilde{f}$ is computed to see where the boundaries are shielded ensuring RANS and where LES is possible. This difference is shown in Figure 10.12. The part of the car that Figure 10.12 shows correspond to the left box in Figure 9.1, where the car as a whole is shown. A larger part of the air underneath the front wing and the floor is computed with LES instead of RANS. The only difference between the two runs is the Synthetic Eddy Method at the inlet, but this has quite a big impact on the blending functions. The explanation that the Synthetic Eddy Method allows for more LES can be found in the definition

of the IDDES method. If turbulence is present in the flow, the simulation tends to go into WMLES mode. LES is then performed even close to the walls inside the boundary layer. Without turbulence, DDES mode is chosen and more of the boundary layer is shielded by RANS. Even though for the base simulation turbulent content is present, the generation of synthetic turbulence enhances this effect and enables LES closer to the walls.

10.5. Turbulence Model Comparison

For all of the simulations on the GTE19 car so far, the same DES method was used: the $k-\omega$ SST-IDDES method. STAR-CCM+ however, also has some other models that can be used. One of these uses the $k-\epsilon$ Elliptic Blending (EB) DDES method. Even though the results in Part II with this method are not as good as expected, the capabilities of this turbulence model in RANS are worth trying in a DES as well. The turbulence model in RANS does not use additional wall damping models but directly models the influence of the wall through blending variables throughout the boundary layer. The $k-\epsilon$ EB-DDES is only tested on the straight line case due to the costs involved with the cornering case. The mesh used here is the Revised DES RW mesh from Table A.1 in Appendix A. It has 16 prism layers on critical parts and a 1 mm refinement box around both the front and the rear wing is used. Additionally, the high turbulence settings with a turbulence intensity of 2.5% and a turbulent viscosity ratio of 20 is used.

Simulation	C_z	C_x	$C_{z,front}$	$C_{z,rear}$	Bal
Realizable $k-\epsilon$ **RANS**	-	-	-	-	-
$k-\omega$ **SST-IDDES**, RW refined	5.59%	12.3%	-1.95%	10.9%	-7.15%
$k-\epsilon$ **EB-DDES**, RW refined	1.83%	10.3%	-0.58%	3.51%	-2.38%

Table 10.5: GTE19 Straight Line Forces with different Turbulence Models

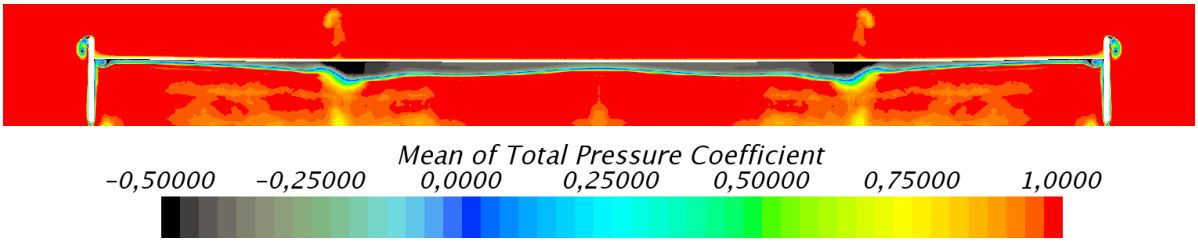

Figure 10.13: GTE19 Straight Line Total Pressure Coefficient, Front View Rear Wing.
$k-\epsilon$ Elliptic Blending-DDES on Revised DES Mesh with Refined Rear Wing.

Table 10.5 shows the results obtained with this method compared to the $k-\omega$ SST-IDDES run with exactly the same settings. The results obtained with the $k-\epsilon$ EB-DDES simulation are closer to the Realizable $k-\epsilon$ RANS results than the $k-\omega$ SST-IDDES, especially when comparing the overall downforce. Closer evaluation however, shows that there are quite a number of differences between the RANS run and this $k-\epsilon$ EB-DDES run. The rear wing for example, again separates even though the 1 mm refinement box is present. This is shown in Figure 10.13. This reduces the downforce generated by the rear wing. The $k-\omega$ SST-IDDES predicts transition on the rear wing allowing the flow to stay attached, but this phenomena is not captured to the same extend by the $k-\epsilon$ EB-DDES method.

The transition on the front wing, extensively discussed in Section 10.3, is also different for the $k-\epsilon$ EB-DDES method. Some sort of transition seems to be present very close to the leading edge as shown in Figure 10.14, but this is much earlier than predicted with the other simulations. Also, the unsteady flow features can not be identified even though it is still the instantaneous wall shear stress is plotted. These differences result in a much lower downforce generated by the front wing compared to the other fine DES simulations. The $k-\epsilon$ EB-DDES simulation does the a higher downforce over the rear floor, like the other DES simulations. This balances the reduced downforce from the rear floor and the front floor giving results that are closer to the Realizable $k-\epsilon$ RANS results.

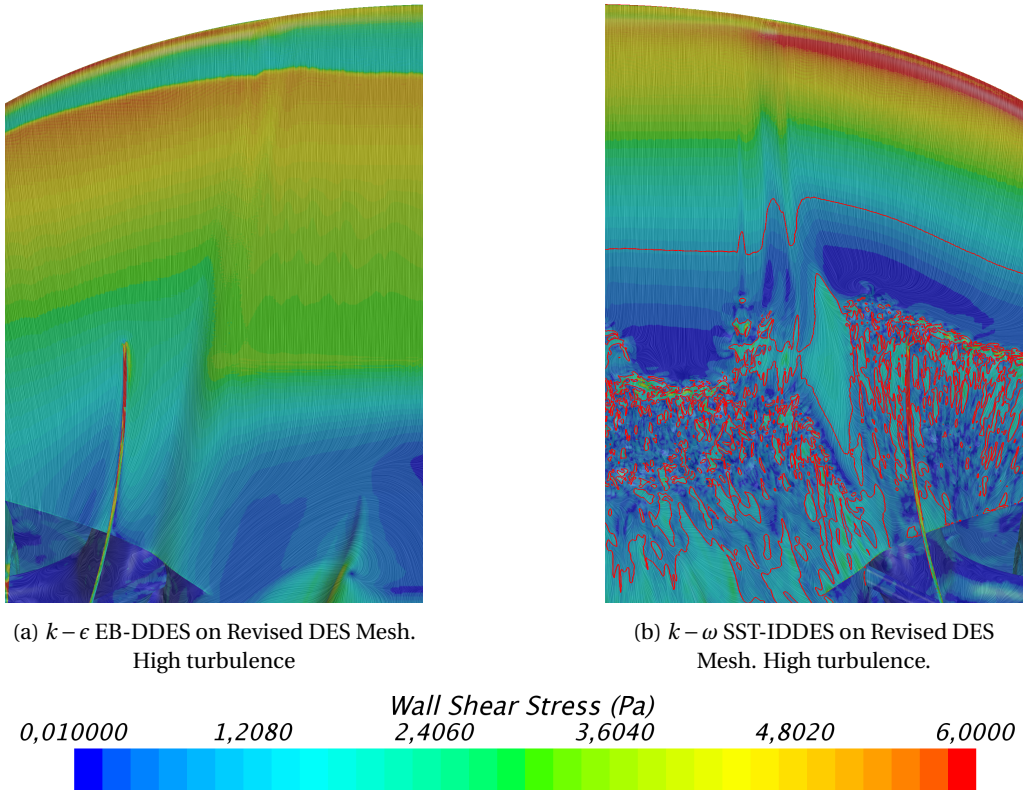

(a) $k-\epsilon$ EB-DDES on Revised DES Mesh. High turbulence

(b) $k-\omega$ SST-IDDES on Revised DES Mesh. High turbulence.

Figure 10.14: GTE19 Straight Line Wall Shear Stress, Bottom View Front Wing (Suction Side).

10.6. Cornering Baseline Results

Since the cornering simulations were done after the straight line simulations, the 16 prism layers and rear wing refinement are used for the fine DES mesh from the start. This gives a cell count around 495 million cells but ensures that few of these simulations are needed to assess the results. More information about this mesh is given in Table A.1 in Appendix A. Using only one fine DES mesh allows for a quick assessment of the method to handle the asymmetric flow, without the need to recalibrate the set-up. Note that the cell count is more than double the cell count of the straight line simulations. This is because the space between the car and the ground, the most refined part of the simulation, is larger on average thus increasing the cell count further. The turbulence intensity and the turbulent viscosity ratio are kept to the baseline values of 1% and 10 respectively. This corresponds to the values used in the Realizable $k-\epsilon$ RANS simulation. Similar to Section 10.1, the downforce and drag values are the primary means of comparison.

Simulation	C_z	C_x	$C_{z,front}$	$C_{z,rear}$	Bal
Realizable $k-\epsilon$ RANS	-	-	-	-	-
$k-\omega$ SST-IDDES on RANS mesh	8.47%	8.12%	9.67%	7.67%	1.11%
$k-\omega$ SST-IDDES on DES mesh	12.4%	12.7%	11.6%	12.8%	-0.65%

Table 10.6: GTE19 Cornering Forces of Baseline CFD Simulations

There are a number of differences between the straight line and cornering case. These are visible in the flow over the body, but also in the total forces. In general, the cornering case produces slightly less downforce both at the front and the rear axle. The general trends however, agree quite well. This is related to the sensitivity of the car. A good design often has a similar performance over a range of yaw angles to ensure easy handling for the driver. In this case however, the differences between the cornering and straight line case on their own are not important. The main purpose of this section is to see how the DES method performs in cornering, since the geometry encountered by the flow seems quite different because of the yaw and roll angle. Table 10.6 shows the differences between the Realizable $k-\epsilon$ RANS run, the DES run on the RANS mesh and the

DES run on the fine mesh. As for the straight line case, Table B.1 contains more data about the distribution of the downforce differences over the wings and the floor.

When comparing the overall forces and the balance within the CFD results, the DES on the RANS mesh is closer to the Realizable $k-\epsilon$ RANS results than the DES on the fine mesh. The rear wing of the Realizable $k-\epsilon$ RANS simulation is fully attached and generates more downforce than both of the DES simulations. Part of this difference in downforce is explained by the higher pressure peak predicted by the RANS simulation, as can be seen in Figure 10.15. The transition in the pressure distribution is again only predicted by the DES simulation on the fine mesh. The rest of the pressure distribution shown in Figure 10.15 seems fairly similar to the coarse DES results in particular. For a large portion of the span, it is also quite similar to the Realizable $k-\epsilon$ RANS results, with a slightly lower peak as the only difference. For a small part of the span however, the distribution is quite different. This spanwise difference in the flow around the rear wing is shown in Figure 10.16. Around one of the rear wing structures the wing separates in the DES simulations, while it does not for the Realizable $k-\epsilon$ simulation. This is predicted by both DES simulations, but more prominently in the DES simulation on the fine mesh. The transition bubble that is present in Figure 10.15 seems to burst and cause the flow separation locally. This also contributes to the lower downforce from the rear wing predicted by the DES simulations.

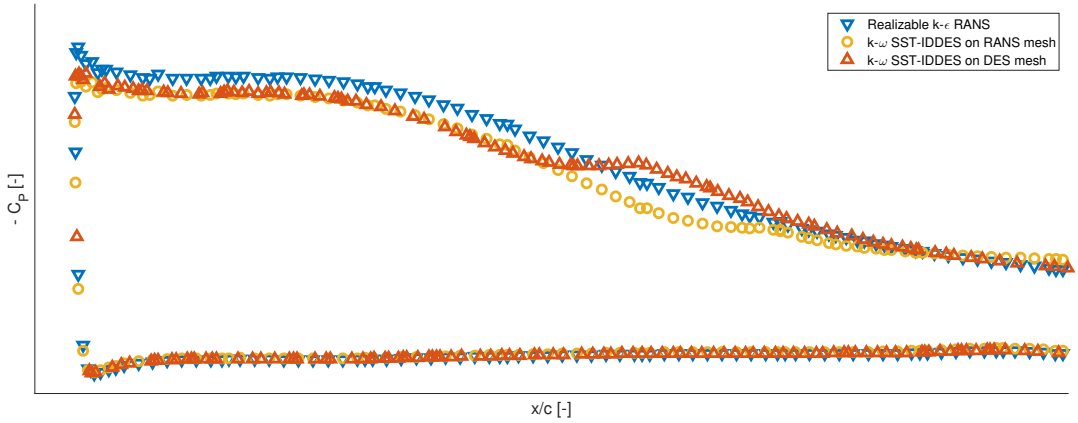

Figure 10.15: GTE19 Cornering Pressure Distribution Rear Wing at Y=0.5 m (from Symmetry Plane).

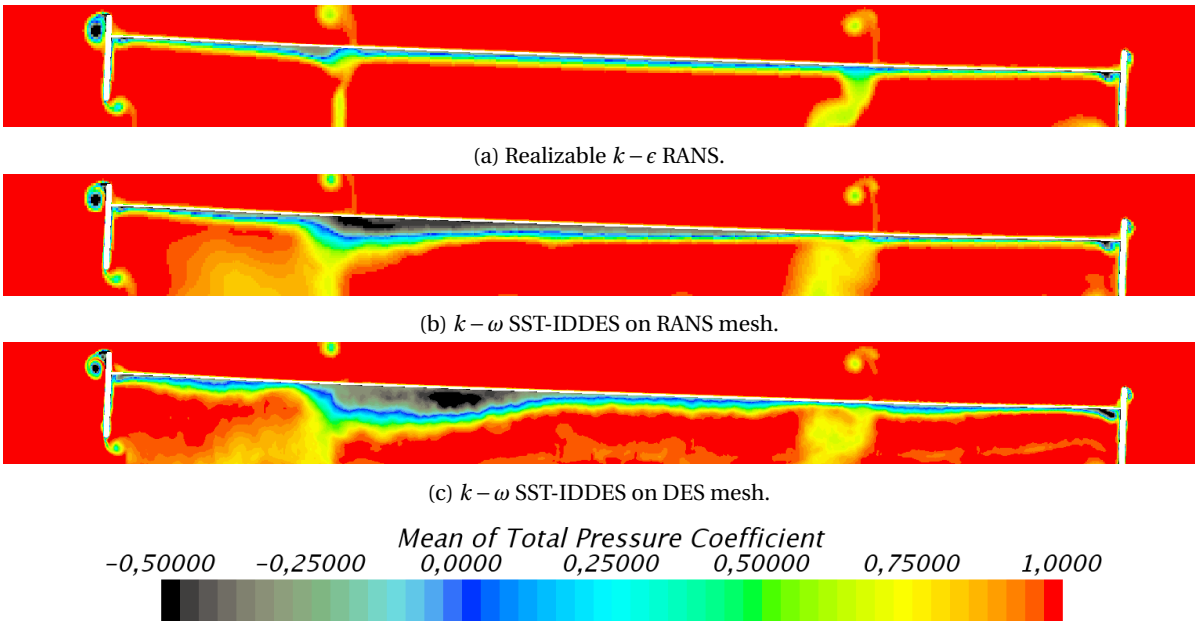

(a) Realizable $k-\epsilon$ RANS.

(b) $k-\omega$ SST-IDDES on RANS mesh.

(c) $k-\omega$ SST-IDDES on DES mesh.

Figure 10.16: GTE19 Cornering Total Pressure Coefficient, Rear Wing Front View.

The lower downforce from the rear wing however, implies the opposite of the difference in rear downforce shown in Table 10.6. The difference in the rear downforce is again caused by the rear floor, which has an overall lower static pressure and therefore a higher downforce. This is to a lesser extend also true for the front floor. Most of the additional downforce on the front axle is however, generated by the front wing. The DES on the fine mesh again captures a transition there, as is shown in Figure 10.17. The transition pattern is asymmetric now, as the flow comes from the top right corner. The Realizable $k-\epsilon$ RANS simulation and the DES on the RANS mesh give a very similar pressure distribution over the front wing. Due to the turbulence captured by the DES on the fine mesh however, the fine DES simulation does give different results. The transition is visible in the pressure distributions as well, and the overall pressure is lower increasing the downforce. This causes most of the increase in the front downforce from the RANS to the DES simulation.

Overall, the same trends and differences are seen for the cornering case as for the straight line case, including the increase in drag and downforce as well as the transition on the wings. One difference is the lack of symmetry condition in the cornering case, removing the total pressure loss beneath the middle of the rear wing in Figure 10.16 compared to Figure 10.1.

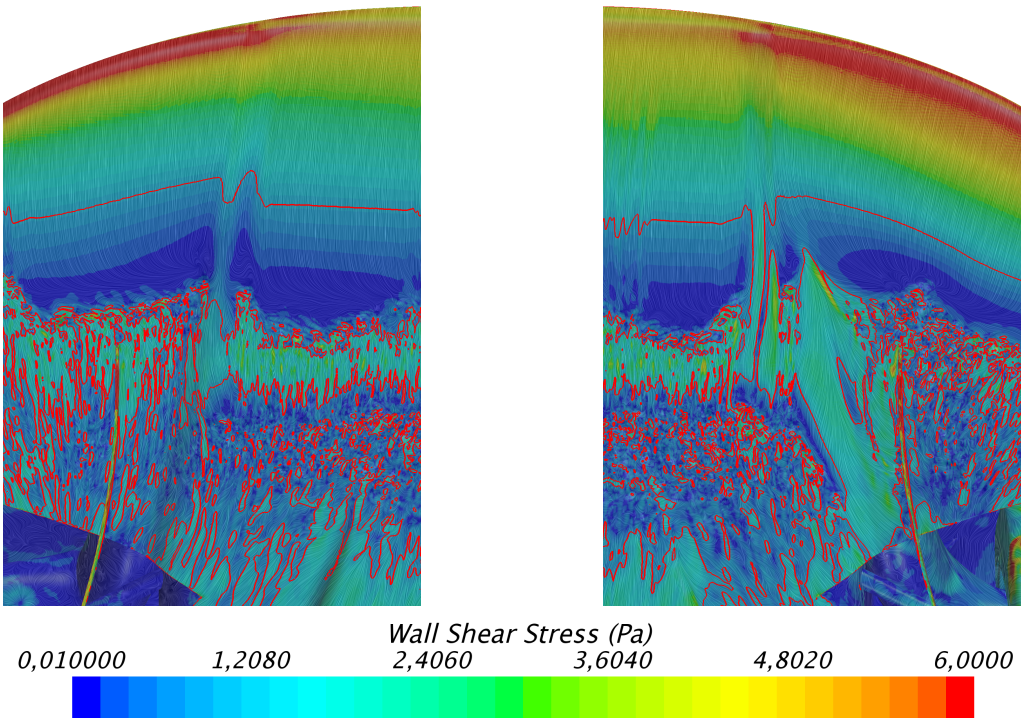

Figure 10.17: GTE19 Cornering Wall Shear Stress, Bottom View Front Wing (Suction Side).

10.7. Correlation with Experimental Data

Wind tunnel data can now be used to dive deeper into the results obtained so far. This section should give insight into where the DES method outperforms the Realizable $k-\epsilon$ RANS method when trying to predict the wind tunnel values. A number of different sets of data are available. This data is obtained either in the 60% scale wind tunnel or the full scale wind tunnel. The full scale wind tunnel is run at almost twice the speed as the CFD simulations, 50 m/s, which makes it twice the Reynolds number. The 60% scale also runs at this speed, but because of the reduction in geometry size the Reynolds number should match the one in the CFD simulations. Still, in both wind tunnels and in the CFD simulations the Reynolds number is $O(10^6)$ limiting the influence of the difference. An additional advantage of the scale model is that the deflections of the parts under the aerodynamic forces are small. This means that the car in the wind tunnel stays very similar to the geometry used for the CFD simulations. For the 60% scale wind tunnel, a correction is needed due to the angle of the rear wing as explained in Section 10.7.1.

Only total forces are available for this tunnel. In the full scale wind tunnel, data is also obtained through

pressure taps. First, the comparison with experimental data for the straight line case is discussed in Sections 10.7.1 to 10.7.3. This covers the force results of the 60% scale wind tunnel, the force results of the full scale wind tunnel and the pressure data from the full scale wind tunnel. More concise is the discussion of the cornering case in Section 10.7.4. Both comparisons give an insight into the correlation of the DES method with wind tunnel data.

10.7.1. Straight Line Correlation 60% Wind Tunnel

For the 60% scale wind tunnel, the data needs to be corrected for the comparison. The corrected data is the data shown in Table 10.7. This correction is needed because of a small difference between the geometry used for the simulations and the geometry tested in the wind tunnel: a 2° difference in the angle of attack of the rear wing. The data is corrected using a different configuration of the same car, where multiple rear wing angles were tested. The influence of the difference in rear wing angle on the front and rear downforce as well as the drag is computed. This influence is used to correct the wind tunnel results. Since the rear wing angle is increased by 2° with respect to the wind tunnel test, the balance is reduced. This is because the rear downforce increases while the front downforce decreases slightly. The correction results in a reduction in front downforce of about 3% and an increase in rear downforce of about 7%. This means that the balance decreases by about 6 %. This 6% on the balance therefore changes the assessment of what is the best CFD prediction, making the argument less strong. The correction does make the difference between this set of wind tunnel data and the set discussed in Section 10.7.2 smaller in terms of balance.

The resulting comparison between the different CFD simulations and the 60% scale wind tunnel data is given in Table 10.7. Note that this time the percentage difference with respect to the wind tunnel data is shown instead of the difference with the Realizable $k-\epsilon$ RANS results.

Simulation	C_z	C_x	$C_{z,front}$	$C_{z,rear}$	Bal
Wind Tunnel Results	-	-	-	-	-
Realizable $k-\epsilon$ RANS	8.94%	-16.2%	17.9%	3.50%	8.23%
$k-\omega$ **SST-IDDES on RANS mesh**	20.1%	-8.03%	25.5%	16.9%	4.47%
$k-\omega$ **SST-IDDES on Baseline DES Mesh**	17.1%	-6.16%	17.8%	16.7%	0.60%
$k-\omega$ **SST-IDDES**, I=2.5% (μ_t/μ)=20	20.3%	-5.86%	25.7%	17.0%	4.54%
$k-\omega$ **SST-IDDES**, RW refined	15.0%	-5.91%	15.6%	14.7%	0.50%
$k-\omega$ **SST-IDDES**, SEM	18.7%	-5.48%	20.7%	17.5%	1.72%
$k-\epsilon$ **EB-DDES**, RW refined	10.9%	-7.54%	17.2%	7.14%	5.66%

Table 10.7: GTE19 Straight Line Forces Comparison with Corrected 60% Scale Wind Tunnel Data.

The balance of the car is predicted best by the $k-\omega$ SST-IDDES simulation with the refined rear wing. Note that balance is one of the most important considerations for the handling of the car. The reason for this prediction is that the front downforce is overpredicted to about the same extend as the rear downforce. Note that this is also the simulation that shows the closes front downforce in general. The rear downforce of the Realizable $k-\epsilon$ simulation and the $k-\epsilon$ EB-DDES simulation is better, but this increases the balance too much. The balance of the car is generally higher than in the wind tunnel for most of the $k-\omega$ SST-IDDES simulations. This indicates that they predict a higher portion of the downforce to stem from the front of the car. The high downforce generated by the front floor might play a role in this.

The simulation that is closest to the wind tunnel data in terms of drag is the $k-\omega$ SST-IDDES simulation with SEM and refined rear wing. It underpredicts the drag still with more than 5% according to the wind tunnel results. This is much close than the drag prediction of the Realizable $k-\epsilon$ RANS simulation however, where an underprediction of more than 16% is found. This shows that although DES consistently overpredicts the downforce generated by the car more than the Realizable $k-\epsilon$ RANS simulation, the drag prediction is better. Note that the $k-\omega$ SST-IDDES simulation with the refined rear wing is quite close to this value as well with an underprediction of 6%, further indicating that this might be the best settings for the simulation.

The source of the over prediction of downforce by the front and rear floor is unknown. Still, the flow phenomena governing the trends seem to be captured best by the $k-\omega$ SST-IDDES simulation with the refined rear wing. This expectation is investigated further with the aid of the full scale wind tunnel data. An interesting observation is that the Realizable $k-\epsilon$ RANS simulation is furthest away in terms of balance from the wind tunnel data. It is quite close for the rear downforce but has a higher front downforce worsening the balance.

10.7.2. Straight Line Correlation Full Scale Wind Tunnel

This section uses a second set of wind tunnel data, from another wind tunnel, to do a second assessment concerning the accuracy of the CFD simulations. Interestingly, there are quite some differences visible between the two sets of data. The drag in the full scale wind tunnel is lower than the drag in the 60% scale wind tunnel. The same is true for the balance, the front and the rear downforce. This illustrates that although the wind tunnel data serves as a reference to compare the different CFD results, there also is an error present here. Still, the trends are the same and by comparing both sets of data a better supported conclusion can be drawn.

Table 10.8 shows the differences between the full scale wind tunnel data and the different CFD simulations. Due to the differences between the sets of data, the $k-\omega$ SST-IDDES simulation with the refined rear wing now has the closest balance. This supports the conclusion that refining the mesh around both wings improves the performance of the method.

Generally speaking, the drag data of the DES simulations are closer to the wind tunnel data than in the 60% scale wind tunnel. The DES run closest in terms of drag is the $k-\epsilon$ EB-DDES run, but the balance of this simulation is further off this time. Since the $k-\epsilon$ EB-DDES simulation generates less downforce in general, the overall downforce is also closer to the wind tunnel data than any of the other DES simulations. Still, the $k-\omega$ SST-IDDES with the 16 prism layers and refined rear wing has the overall best performance. The drag prediction of this simulation is in between the two wind tunnel predictions, which seems promising. The Realizable $k-\epsilon$ RANS results in too low a drag and a much too high balance still. The overprediction of both the front and rear downforce of the DES simulations is very visible, but other than that the predictions are quite good.

Simulation	C_z	C_x	$C_{z,front}$	$C_{z,rear}$	Bal
Wind Tunnel Results	-	-	-	-	-
Realizable $k-\epsilon$ RANS	12.3%	-9.50%	21.3%	6.82%	7.97%
$k-\omega$ SST-IDDES on RANS mesh	23.8%	-0.71%	29.1%	20.6%	4.22%
$k-\omega$ SST-IDDES on DES mesh	20.7%	-1.31%	21.1%	20.4%	0.36%
$k-\omega$ SST-IDDES, I=2.5% (μ_t/μ)=20	24.0%	1.64%	29.3%	20.7%	4.28%
$k-\omega$ SST-IDDES, RW refined	18.6%	1.59%	18.9%	18.4%	0.26%
$k-\omega$ SST-IDDES, SEM	22.4%	2.05%	24.2%	21.3%	1.48%
$k-\epsilon$ EB-DDES, RW refined	14.4%	-0.18%	20.1%	10.6%	5.40%

Table 10.8: GTE19 Straight Line Forces Comparison with Full Scale Wind Tunnel Data.

10.7.3. Straight Line Correlation Pressure Tabs

Pressure taps which are positioned on the front wing during wind tunnel testing can provide some additional insight into the behaviour of the flow. Pressure distributions based on CFD results as well as some points from the wind tunnel are plotted in Figures 10.18a and 10.18b. A number of points from the pressure data are shown alongside the CFD results from the baseline RANS run and the $k-\omega$ SST-IDDES run with the Synthetic Eddy Method as inflow condition. To generate these results, the pressure from the pressure taps, which is the difference between the ambient pressure and the static pressure, was normalized with the wind tunnel speed and the air density in the wind tunnel. The results indicate that the general trend on the front wing is captured by both CFD methods, but that neither one gets the exact same results. The DES method over predicts the low pressure more than the Realizable $k-\epsilon$ RANS, but does capture the higher pressure near the trailing edge in Figure 10.18a better.

A number of things are important to keep in mind for these results. The first is that there is a small difference between the locations of the measurements and the plane of the CFD data. This is because using CFD data exactly at the symmetry plane is undesirable and because the pressure taps are not situated in a straight line. Secondly, the pressure data provided here does not correspond to the same wind tunnel run as the overall force data. The pressure taps were not connected during the wind tunnel run from which the force data was retrieved. The pressure data is valid as the front wing is the same, but an overall lower downforce generation on the front axle was reported for this wind tunnel run. This could be an explanation why the trends do seem to fit while the pressure is everywhere higher. Finally, the CFD values are the instantaneous values at the final time step, while the wind tunnel data are averaged values. All in all, the pressure comparison shows that not only the force values but also the pressure distributions are captured reasonably well. No pressure

tap data is available for the rear floor which means that it is hard to explain the origin of the overall higher downforce produced by the floor. The topic will be revisited in Chapter 11, which at least illustrates whether it is typical for the GTE19 car only or for all of the DES simulations.

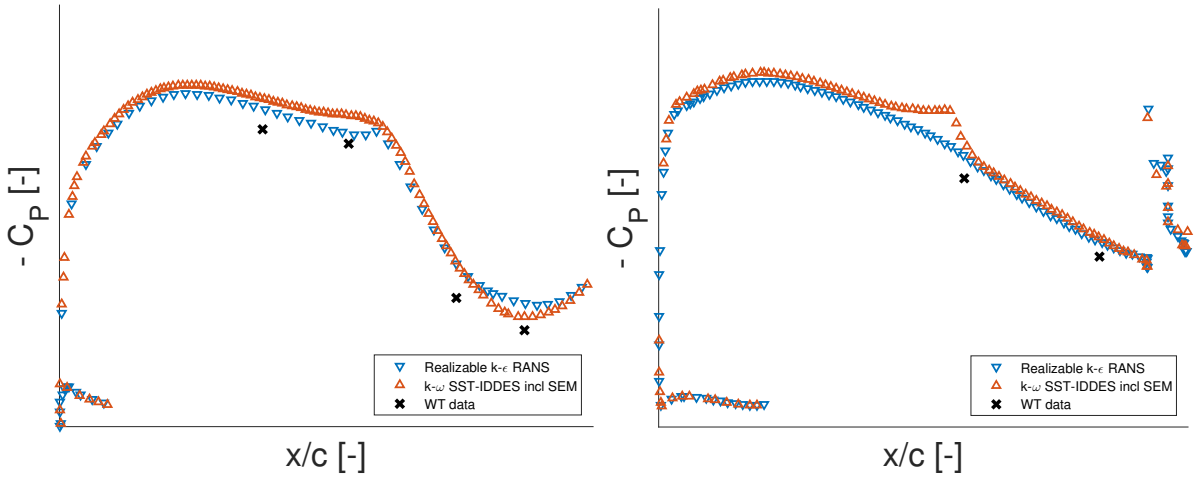

(a) Front Wing between Y=0 and Y=0.05 m (from Symmetry Plane).

(b) Front Wing between Y=0.45 and Y=0.55 m (from Symmetry Plane).

Figure 10.18: GTE19 Straight Line Pressure Distribution and Taps, CFD and Wind Tunnel Data.

10.7.4. Cornering Correlation

The differences with the wind tunnel data for the cornering case are given in Tables 10.9 and 10.10. The DES on the fine mesh is again the best model in terms of drag prediction. It is more difficult however, to assess the best performing model in terms of balance. In the 60% scale tests, the DES on the fine mesh outperforms the RANS simulation in this regard, but in the full scale wind tunnel this is the other way around. The Realizable $k-\epsilon$ RANS result is almost spot on. Still, in terms of absolute downforce the DES method overpredicts both the front and the rear massively like in the straight line case. Interesting to notice is also again the difference between the two wind tunnel predictions. In terms of drag for example, one of the wind tunnels predicts a larger value than the DES results and the other a smaller value. Because of this, absolute values in both wind tunnels and CFD simulations are often less important than the "deltas" due to geometry changes. This concept of comparison deltas instead of absolute values is assessed with the LMP1 S15 car, by simulating two different ride heights. The difference between the results is then more important than the separate absolute numbers themselves.

Simulation	C_z	C_x	$C_{z,front}$	$C_{z,rear}$	Bal
Wind Tunnel Results	-	-	-	-	-
Realizable $k-\epsilon$ RANS	8.25%	-12.8%	13.2%	5.2%	4.65%
$k-\omega$ SST-IDDES on RANS mesh	17.4%	-5.71%	24.2%	13.3%	5.82%
$k-\omega$ SST-IDDES on DES mesh	21.6%	-1.75%	26.4%	18.7%	3.97%

Table 10.9: GTE19 Cornering Forces Comparison with Corrected 60% Scale Wind Tunnel Data.

Simulation	C_z	C_x	$C_{z,front}$	$C_{z,rear}$	Bal
Wind Tunnel Results	-	-	-	-	-
Realizable $k-\epsilon$ RANS	15.9%	-9.38%	15.9%	15.9%	-0.05%
$k-\omega$ SST-IDDES on RANS mesh	25.7%	-2.02%	27.1%	24.8%	1.06%
$k-\omega$ SST-IDDES on DES mesh	30.2%	2.09%	29.4%	30.8%	-0.70%

Table 10.10: GTE19 Cornering Forces Comparison with Full Scale Wind Tunnel Data.

10.8. Simulation Time Evaluation GTE19

The CPU hours for all the different straight line simulations are summarised in Table 10.11. Similarly, the cornering CPU hours and times are shown in Table 10.12. The increase in simulation time compared to the RANS simulations can be split into two parts. The number of cells has increased massively, but also the methodology has been changed. The tables show that on the RANS mesh, the DES methodology has a simulation time similar to the RANS and URANS times. With the current set-up, a similar number of steps is needed for the DES method compared to the RANS and URANS methods. This would indicate that the number of cells is leading at the moment and can therefore directly be used to estimate changes in simulation costs. The reason why the generation of the straight line 192 million cell mesh took longer than the trends would indicate is unknown and could be related to the cluster running the simulations on.

Related to the DES method is the usage of the Synthetic Eddy Method, which could lead to a better representation of the inflow turbulence. This method seems to only increase the simulation time with a few percent. Another conclusion that can be drawn is the fact that the Elliptic Blending variation of the DES method is more computationally expensive than the $k-\omega$ SST-IDDES variant. This is in agreement with the RANS formulation of this turbulence model, as illustrated in Table 11.7 in Chapter 11. Note however, that in the LMP1 comparison the Elliptic Blending RANS simulation is done on a finer mesh than the Realizable $k-\epsilon$ RANS simulation.

Simulation Set-Up	**Cells** *Millions*	**Pre Step** *CPU-Hour*	**Solve** *CPU-Hour*	**Solve n=1080** *Hour*
Realizable $k-\epsilon$ RANS	85	~8	-	~2.5
$k-\omega$ SST URANS	85	~8	-	~2.5
$k-\omega$ SST-IDDES RANS Mesh	85	7.8	2573	2.4
$k-\omega$ SST-IDDES Baseline Mesh	182	9.2	5768	5.3
$k-\omega$ SST-IDDES Revised Mesh	192	11.6	6356	5.9
$k-\omega$ SST-IDDES Revised Mesh RW 1 mm	215	10.1	7176	6.6
$k-\omega$ SST-IDDES Revised Mesh RW 1 mm SEM	215	10.1	7371	6.8
$k-\epsilon$ EB-DDES Revised Mesh RW 1 mm	215	10.1	8063	7.5

Table 10.11: GTE19 Straight Line CPU Hours and Simulation Time.

The simulation times for the cornering cases show a similar relation between the number of cells and the time it takes to solve. The main difference between the straight line and the cornering case is the fact that only half of the car is simulated with a symmetry boundary condition for the straight line case, and the full car is simulated for the cornering case. This approximately doubles the number of cells needed. Since the number of cells is doubled, the computation time would double approximately too. In order to prevent this, the cornering case is run on double the number of cores. The CPU hours and simulation times for the various cornering cases are shown in Table 10.12. Note that the time to perform the pre step does increase for a similar number of cells in the mesh, probably due to the larger surface mesh and prism layer extrusion in the full car mesh.

Simulation Set-Up	**Cells** *Millions*	**Pre Step** *CPU-Hour*	**Solve** *CPU-Hour*	**Solve n=2160** *Hour*
Realizable $k-\epsilon$ RANS	178	~15	-	~4
$k-\omega$ SST URANS	178	~15	-	~4
$k-\omega$ SST-IDDES on RANS mesh	178	15.0	8610	4.0
$k-\omega$ SST-IDDES on fine DES mesh	495	22.7	15532	7.2

Table 10.12: GTE19 Cornering CPU Hours and Simulation Time.

11

Settings and Results LMP1 Car

This chapter discusses the baseline set-up and the simulation results for the LMP1 2015 car. The results for two different configurations are discussed, the LMP1 S09 and the LMP1 S15. The set-up for this car is based on the baseline set-up og the GTE19 combined with the findings from Chapter 10, which means that only deviations from that baseline are concisely discussed. These adjustments are given in Section 11.1. Most important in the set-up however, is the design of the mesh. Mesh design for the LMP1 car is therefore discussed separately in Section 11.1.2. The set-up is discussed for the LMP1 S09 car in particular.

The rest of the chapter is devoted to discussing the results obtained with DES for the LMP1 car. First, the LMP1 S09 car in straight line is discussed in Section 11.2. The cornering case for this configuration is then discussed in Section 11.3. Both sections first compare the DES results to various RANS results in terms of overall forces and balance. The main purpose of these simulations however, is to assess how well vortices and their decay are captured by the DES method. This is done using PIV data for two planes underneath the car, the first at X=1.4 m and the second at X=1.915 m as seen from the front of the car. The PIV data is available for both the straight line and the cornering case (on one side of the car). Section 11.4 then discusses the LMP1 S15, where a comparison between different CFD simulations and wind tunnel data is included. For this configuration two different straight line cases are simulated. This allows for a comparison of the absolute forces on the car as well as the force changed due to the change in ride height. Finally, some conclusions based on the accuracy and the simulation time about the performance of the DES method are drawn in Section 11.5. This concludes the analysis of the performance of DES for the LMP1 car.

11.1. Adjustments to Simulation Settings

The simulations for the LMP1 car are all based on the knowledge acquired from the GTE19 car. Most of the set-up is kept the same, but some of the features and differences are highlighted in this section. This is done first for the simulation settings in Section 11.1.1. After this, the design of the mesh for the LMP1 car is discussed in Section 11.1.2. This mesh has been designed partially based on the GTE19 results, but still keeps in mind the length ratio recommendations from STAR-CCM+.

11.1.1. General Settings

Most of the simulation settings are kept the same as for the baseline GTE19 car. The main difference is the speed for which the simulations are performed, this is increased to 55 m/s which is double the speed of the GTE19 car. This speed is chosen since corresponds to the speed used for the collection of the PIV data discussed in Section 11.2.2. One of the most important settings in this context is the DES method used, and this has not been changed. The DES model is again the $k-\omega$ SST-IDDES model. The $k-\epsilon$ Elliptic Blending DDES model was also tested on the GTE19 car but the $k-\omega$ SST-IDDES performed better both in the airfoil model study and the GTE19 car. The turbulence settings in the flow are kept the same as the baseline GTE19 car. This means that a turbulence intensity of 1% and a turbulent viscosity ratio of 10 are used as initial and inflow conditions without the Synthetic Eddy Method.

The time step is kept at 0.001 s. Since the speed is higher, the validity of the time step should be re-evaluated. Equation 3.1 from the STAR-CCM+ user guide for vehicle simulations results in a time step which is around 0.0009 s, indicating that the time step should be reduced only slightly compared to the GTE19 car.

Because of the small difference, the time step is kept at 0.001 s even though it is slightly too large. The Courant number around the car is shown in Figure 11.1. The Courant number does again indicate that the time step should be smaller, but cost restrictions keep it large. Peaks in the Courant number in this case go up to 100. Note that this choice is again not in line with the reflection in Chapter 8, but that the results of the GTE19 car do not give a need to change this.

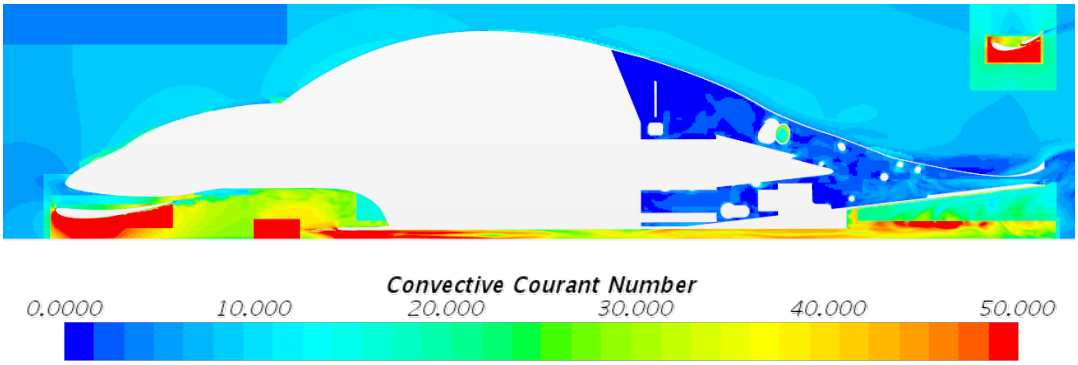

Figure 11.1: LMP1 S09 Straight Line Courant Number on DES Mesh, Side View.

11.1.2. Mesh Design

The geometry of the LMP1 car is quite different from the geometry of the GTE19 car. Many of the conclusions drawn from the GTE19 car can still be implemented into the LMP1 mesh however. Like in the revised GTE19 mesh, the number of prism layers has been set to 16 on the focus parts. These again include the entire floor of the car and both the front and rear wing. The RANS mesh has a refinement up to 4 mm around the front wing and up to 2 mm underneath the floor. In the DES mesh, a 1 mm refinement box is added around the front wing to capture the transition there. Also, a 1 mm box is added around the footplate to capture the vortices formed there. Much of the remainder of the flow underneath the front of the car is refined up to 2 mm. For the rear wing, a 1 mm refinement box is also added to capture the flow behaviour on the suction side of both the rear wing and the flap. Figures 11.2a to 11.3b illustrate some of the differences between the RANS and the DES mesh for the LMP1 car. The number of cells for the RANS mesh is about 85 million. The RANS mesh with 16 prism layers, as used for the Elliptic Blending $V2-f$ RANS simulation, has 106 million cells. The DES mesh has 203 million cells. These meshes as well as any adaptation to these meshes are shown in Table A.2 in Appendix A.

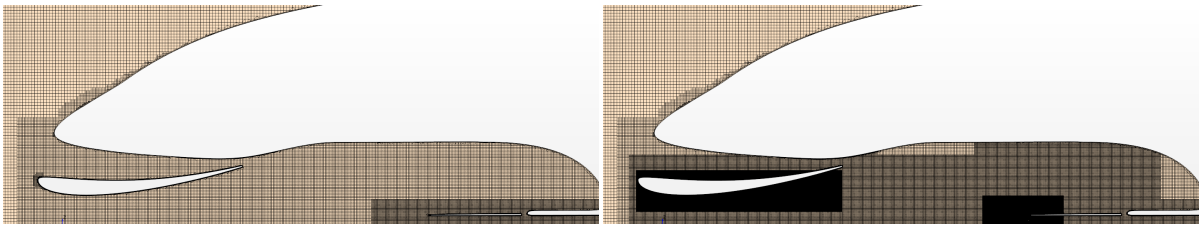

(a) RANS Mesh. (b) DES Mesh.

Figure 11.2: LMP1 S09 Straight Line, Side View Front Wing.

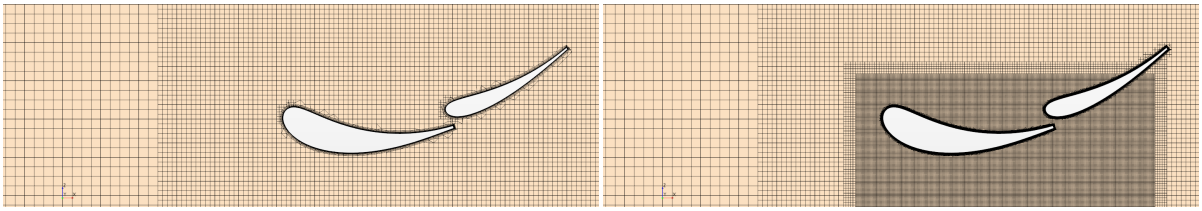

(a) RANS Mesh. (b) DES Mesh.

Figure 11.3: LMP1 S09 Straight Line, Side View Rear Wing.

The length ratio on both the RANS mesh and the DES mesh is shown in Figure 11.4. The length ratio indicates the need for refinement in the RANS mesh and the resulting improvement on the DES mesh. Ideally, the refinement region around the footplate should extend further in streamwise direction. The region where the vortices should be formed is refined sufficiently however, which should be enough to capture them. There are still a number of other areas around the car where the length ratio is not satisfied. These however, are believed to have less critical flow criteria and are left coarser in order to save mesh and time. This is similar to the approach used for the GTE19 car.

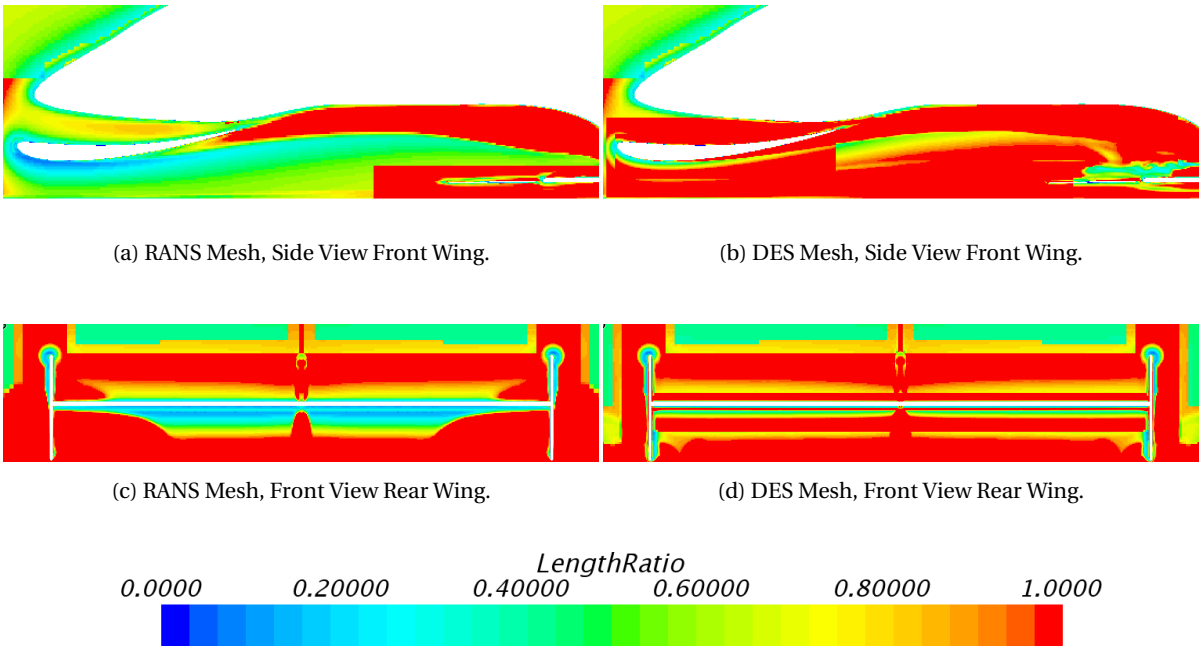

(a) RANS Mesh, Side View Front Wing.

(b) DES Mesh, Side View Front Wing.

(c) RANS Mesh, Front View Rear Wing.

(d) DES Mesh, Front View Rear Wing.

Figure 11.4: LMP1 S09 Straight Line Length Ratio Comparison RANS and DES Mesh.

11.2. Straight Line Results LMP1 S09

The first configuration of the LMP1 car is the S09 of the 2015 car. The second configuration is also of the 2015 car but at a later stage, referred to as the S15. For the S09, a comparison between CFD and PIV data is done underneath the floor of the car. This is a continuation of the comparison documented in [14]. The comparison is done on two planes, the plane X=1.4 m and the plane X=1.915 m as seen from the front of the car. The location and strength of the different vortices formed underneath the car floor are compared within different CFD simulations and with PIV data from the wind tunnel. Before this however, first the different RANS and DES methods are compared in terms of overall forces and forces on car parts to get a first feel for the differences between the methods on this car.

11.2.1. Straight Line CFD Comparison

Wind tunnel data of the overall forces is not available for this configuration. The different methods can however, be compared to each other and the origins for some of their differences can be identified. The deviations of the CFD results are again given with respect to the Realizable $k-\epsilon$ RANS, as shown in Table 11.1. More information about the downforce differences on the wings and floor separately is given in Table B.2 of Appendix B. Note that in this case the Elliptic Blending model is used as a RANS turbulence model, not in its DES formulation. Generally speaking, the differences between the results for the methods are smaller than for the GTE19 car. This section assesses the front and rear wings to see their contribution to these differences. Additionally, the forces on the floor are compared to see if a similar increase in predicted downforce as for the GTE19 is present. This topic is also discussed using the PIV data in Section 11.2.2.

In this case, four different DES simulations are run. Two of the DES simulations are run on the RANS mesh, of which one has 16 prism layers instead of 7/8. The two other DES simulations are run on the fine DES mesh. The first fine DES mesh has a refined rear wing and a small refinement region where the PIV vortices are formed. The second fine DES mesh has no refinement around the rear wing but a large refined region

underneath the floor of the car. This region covers both the formation of the vortices visualized with PIV and the decay of the vortices. This should allow the DES method to capture the vortices better and thereby correlate better to the PIV results. Both of these fine DES meshes do have the fine rear wing region. An overview of these meshes and their characteristics is given in Table A.2 in Appendix A.

Simulation	C_z	C_x	$C_{z,front}$	$C_{z,rear}$	Bal
Realizable $k-\epsilon$ **RANS**	-	-	-	-	-
Elliptic Blending $k-\epsilon$ **RANS**	-3.71%	0.64%	-4.73%	-2.90%	-1.06%
$k-\omega$ **SST RANS**	-10.7%	-1.71%	-9.68%	-11.5%	1.11%
$k-\omega$ **SST-IDDES** RANS mesh	-5.75%	8.27%	-9.56%	-2.72%	-4.05%
$k-\omega$ **SST-IDDES** DES mesh	-2.57%	5.72%	1.45%	-5.75%	4.12%
$k-\omega$ **SST-IDDES** RANS mesh 16 prism	-7.44%	7.27%	-12.6%	-3.37%	-5.54%
$k-\omega$ **SST-IDDES** DES mesh refined PIV region	-0.48%	7.37%	-0.26%	-0.66%	0.22%

Table 11.1: LMP1 S09 Straight Line Forces of CFD Simulations

Table 11.1 provides the opportunity to compare the difference in downforce. The highest front downforce is generated by the baseline DES mesh. This is the only simulation that gives a higher front downforce than the Realizable $k-\epsilon$ RANS simulations. The DES on the second fine mesh, with the refined PIV region, predicts a downforce very close to the base RANS results. The DES simulations on the coarse RANS mesh however, predict less front downforce. The difference in total pressure behind the front wing between the DES on the RANS mesh and the DES on the first fine DES mesh is shown in Figure 11.5. The RANS mesh generates a bigger wake behind the front wing decreasing the downforce produced both by the front wing and by the front floor. This can be seen in Table A.2.

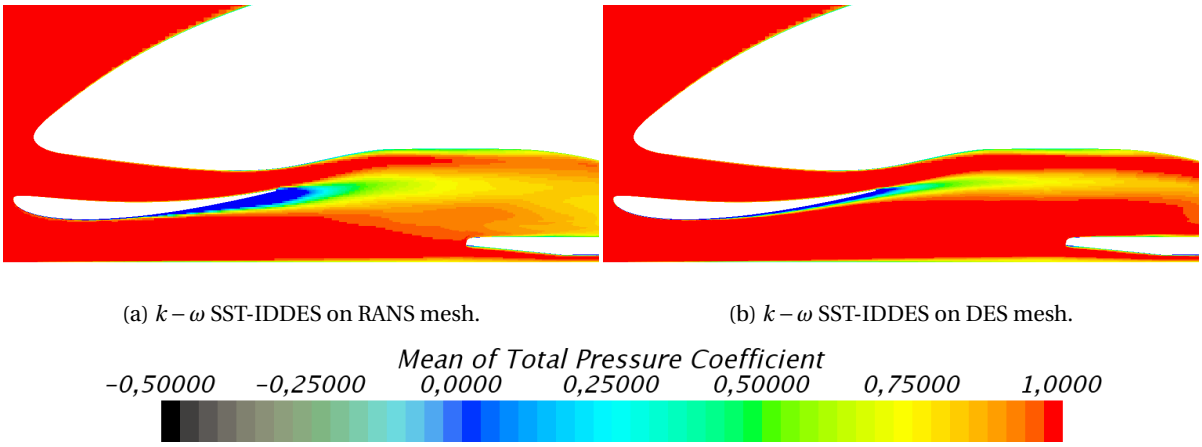

(a) $k-\omega$ SST-IDDES on RANS mesh.

(b) $k-\omega$ SST-IDDES on DES mesh.

Figure 11.5: LMP1 S09 Straight Line Total Pressure Coefficient, Side View Front Wing.

The differences in front downforce between the two fine DES simulations and the Realizable $k-\epsilon$ RANS simulation is quite small. To investigate the difference further, the pressure distribution over the front wing for these three simulations is shown in Figure 11.5a. It is clear that the DES on the second fine mesh has a slightly smaller pressure peak and thus a slightly lower downforce compared to the other DES simulation. The difference is very small however. The difference between both DES predictions and the RANS prediction is bigger. The DES simulations predict a bubble on the suction side of the front wing which results in a higher downforce, of about 4-5%. This increase in downforce from the front wing between the first fine DES and the RANS simulation is more than the 1.45% in Table 11.1. The difference is reduced by the lower downforce produced by the front floor in the DES simulation. The first DES simulation has a slightly bigger wake and a higher pressure over the front floor compensating part of the downforce created by the front wing. For the second fine DES, this effect is amplified resulting in an overall slightly lower front downforce.

The pressure distribution over the front wing of the two DES simulations on the RANS mesh are shown in Figure 11.6b. The RANS mesh with the increased number of prism layers shows a transition, but much

weaker and further towards the trailing edge than in the fine DES simulations. Apart from this, the influence of the number of prism layers seems quite limited on this coarse mesh. Both of them have a lower pressure peak than the results in Figure 11.6a, which explains the reduction in downforce compared tot the finer mesh and the Realizable $k-\epsilon$ RANS simulation. The coarse DES mesh is not able to capture the same flow over the rear wing as the other simulations.

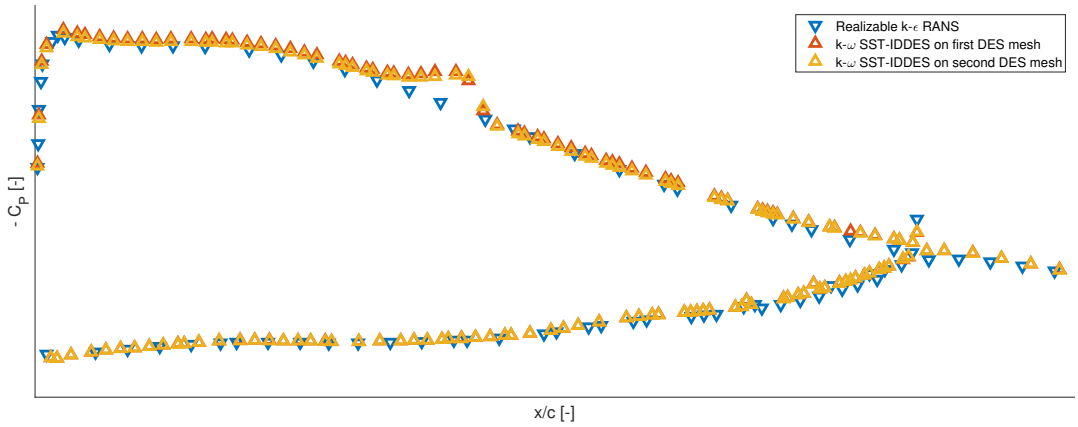

(a) Realizable $k-\epsilon$ RANS and $k-\omega$ SST-IDDES on DES Mesh.

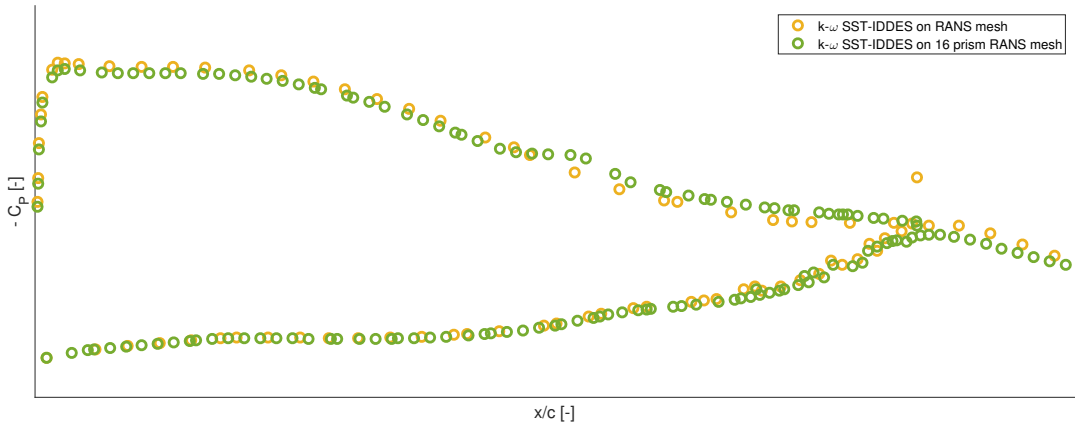

(b) $k-\omega$ SST-IDDES on RANS mesh with 7/8 and with 16 Prism Layers.

Figure 11.6: LMP1 S09 Straight Line Pressure Distribution, Front Wing at Y=1.0 m (from Symmetry Plane).

The transition on the suction side of the front wing visible in Figure 11.6a can also be visualized with the aid of the Λ_2 criterion. This is shown in Figure 11.7 for the simulation of the second fine DES mesh. The leading edge of the front wing is on the left side of the picture and the trailing edge on the right side, the air flows from left to right. The surface of the front wing is shown in grey. On the left side, the flow accelerating around the leading edge satisfies the Λ_2 criterion and is therefore displayed. Note however, the consistency in this region lacking the unsteady vortical shapes. These shapes are visible on the right side of the figure however, where the transition and the turbulent flow are visualized. The location of the transition shown here agrees with the location of the bubble in the pressure distribution and in the wall shear stress. More insights into the vortical structures around the transition point are shared about the GTE19 car in Section 10.3.3.

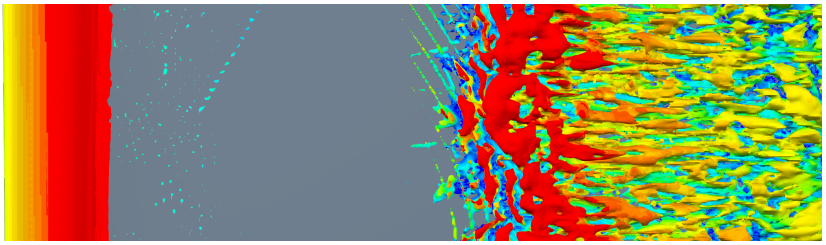

Figure 11.7: λ_2 Criterion Front Wing Bottom View Coloured by Velocity Magnitude, Leading Edge Left.

The pressure distribution over part of the rear wing is shown in Figure 11.8. The graph contains the results for the Realizable $k-\epsilon$ RANS simulation and the DES simulation on the first fine mesh. Note that the other three DES simulations, none of which have the 1 mm refinement box around the rear wing, give approximately the same pressure distribution. This can also be seen from the downforce differences in Table A.2. No transition is present there, no separation and the pressure peaks also are almost the same. These results would indicate that for all of these simulations, the RANS solution around the rear wing is computed. The difference in the rear downforce in Table 11.1 therefore stems from the rear floor. The pressure peak of the $k-\omega$ SST RANS simulation is slightly lower resulting in a slightly lower downforce generated, but the general behaviour of this rear wing is also the same.

The pressure distribution predicted by the DES on the first fine DES mesh is also shown in Figure 11.8, note that this is the only simulation of this configuration that has a refined rear wing up to 1 mm. The pressure distribution is very different from the simulations on the RANS mesh. The pressure peak on the main element is lower and separation takes place towards the trailing edge, both on the main element and on the flap behind it. This separation is present over the full span of the rear wing. All of this reduces the downforce on the rear wing and therefore the rear downforce of the DES simulation. This separation might be a case of Grid Induced Separation, a phenomena discussed in Section 2.3.1. In short, it means that the blending functions break down and allow LES to be used close to the wall while actually the grid is not fine enough to do this. The DES run on the RANS mesh with 16 prism layers serves as a test to see if an improvement compared to the DES run on the RANS mesh could be realised without creating this ambiguous grid refinement around the rear wing. Unfortunately with the 16 prism layers, less detail is be captured on the front wing and the same RANS solution around the rear wing was found. Further or anisotropic refinement could be tested but since the rear wing is not the priority for this car this has not been tested. No force data and no pressure taps are available to assess the results properly.

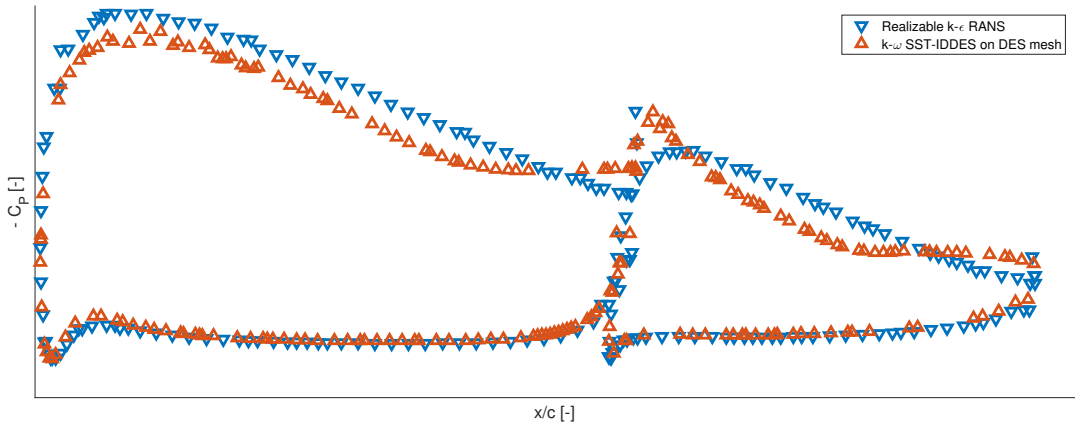

Figure 11.8: LMP1 S09 Straight Line Pressure Distribution, Rear Wing at Y=2.0 m (from Symmetry Plane).

The downforce generated by the floor of the car is the final topic to compare. All of the simulations generate less downforce on the rear floor than the Realizable $k-\epsilon$ RANS simulation. The DES simulations on the fine mesh are closer than the two DES simulations on the RANS mesh. The second DES simulation on the fine mesh, with the refinement box under a large section of the floor, is very close to it. For the front floor, the trends are the same. These results are quite different compared to the GTE19 results, where in general the DES simulations produced more downforce by the floor than the RANS simulations. The origin of the higher suction underneath the floor in the Realizable $k-\epsilon$ RANS results stems from the floor leading edge and extends downstream until past the rear wheels. The vortices generated near the leading edge of the front floor are stronger which could be an explanation. This is further compared in the next section.

11.2.2. Straight Line PIV Comparison

In this section, the various CFD simulations discussed in Section 11.2.1 are compared to PIV data from the full scale wind tunnel. The first plane to compare is at X=1.4 m from the front of the car, and the second plane is at X=1.915 m from the front of the car. To illustrate the spanwise extend of the PIV plane, the front wing is also shown in the figures. The left side of the images is approximately the symmetry plane of the car and the right side of the image corresponds almost at the side of the car. Note that the velocity scale in all

images is the same. Since the streamwise component is not captured by PIV, the velocities in the CFD pictures also contain only the other two components. A line integral convolution plot is made with the two velocity components to indicate the velocity streaks and the figures are coloured by the velocity magnitude of the two velocity components. To illustrate the location of the planes discussed, Figure 11.9 is included. The Courant number where the vortices are formed is around 100 and reduces towards 40 in the region where the data is presented.

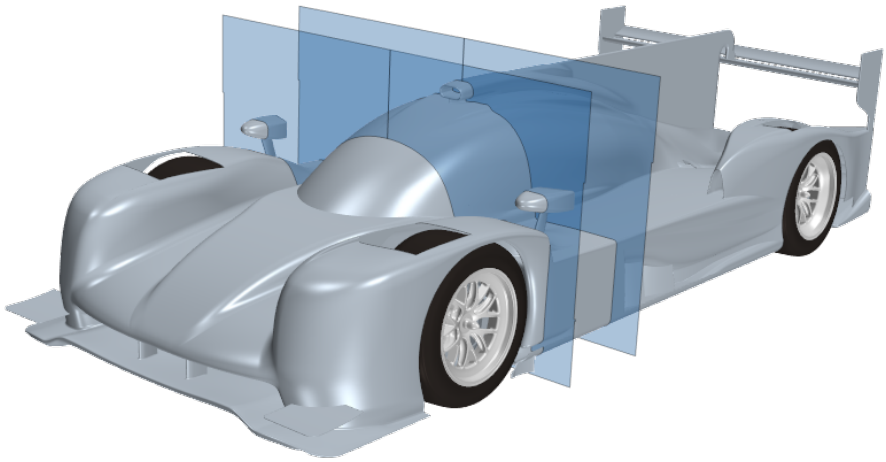

Figure 11.9: LMP1 S09 Straight Line Geometry with PIV Planes at X=1.4 m and X=1.915 m.

Figure 11.10 shows the different data sets at the plane X=1.4 m. This plane is quite close to where the vortices are formed. Three vortices are visible, which will be identified as vortices 1 to 3 from left to right. First the RANS results are compared to the PIV data and then the DES results. This gives some insight into the capabilities of the DES method compared to RANS.

The Realizable $k-\epsilon$ RANS results again serve as a baseline to work from. The strength of the vortices predicted by the simulation is higher, especially vortices 1 and 2. This is a general trend in all of the CFD results. Vortices 1 and 2 are located slightly to the left and upwards as well compared to the PIV data. The Elliptic Blending $k-\epsilon$ method and the $k-\omega$ SST method show similar results, although the spanwise location of vortex 2 seems better. Vortex 3 is flatter in all three RANS simulations with an overall higher speed. Also, it is located further from the ground. This comparison shows that the RANS simulations are able to capture the vortices to some extend, but not perfectly. The velocity magnitude is very similar between the different RANS simulations as well. As found in Section 11.2.1, the suction underneath the floor in the Realizable $k-\epsilon$ RANS results is higher than in the other RANS results. As in-plane velocity components do not explain the difference in downforce, this difference must be caused by a higher streamwise velocity not captured by the PIV planes.

The DES simulations show more similarities to the RANS simulations than to the wind tunnel data. Comparing first the DES on the RANS mesh to the PIV data shows that the three vortices are all moved upwards and to the left slightly. The DES on the first fine mesh, has vortex 2 and 3 moving upwards and to the right slightly. Also, vortex 3 is more round than the RANS and DES simulations on the RANS mesh resembling the PIV data more. The DES simulation on the RANS mesh with 16 prism layers is somewhere in between these two DES simulations. Vortex 1 and 3 are in the same location as for the DES on the RANS mesh, but vortex 2 is located in agreement with the PIV data. Still, the strength of all three DES simulations is higher than in the PIV data. This implies that the DES method is not able to fully capture the vortices.

The final DES simulation, shown in Figure 11.10h, has a fine 1 mm mesh throughout the entire area visualized by the PIV data. This DES is still not able to fully capture the vortices. The vortices are too strong but the locations are reasonably good. Vortex 2 and vortex 3 are slightly too high up, but vortex 1 and the spanwise location and 2 and 3 is match the wind tunnel data. The added refinement does not result in the expected improvement of the results, as the difference is strength is still large.

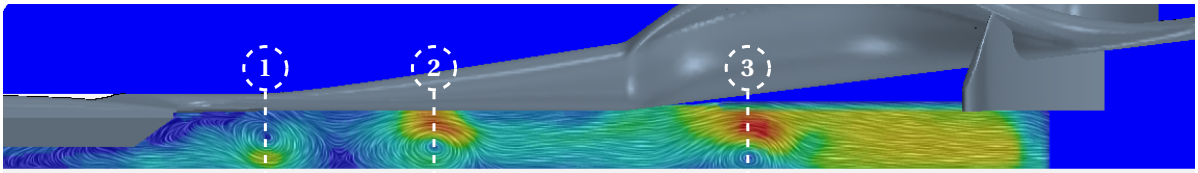

(a) PIV Data Full Scale Wind Tunnel.

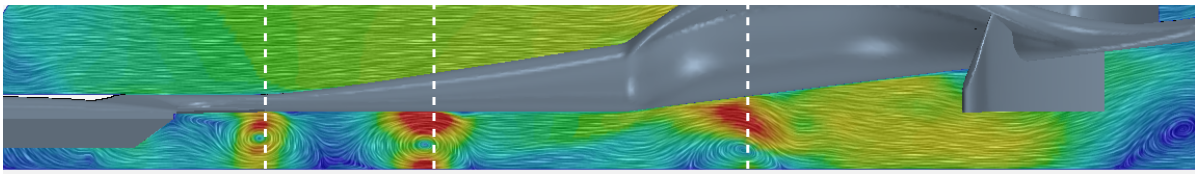

(b) Realizable k-ϵ RANS.

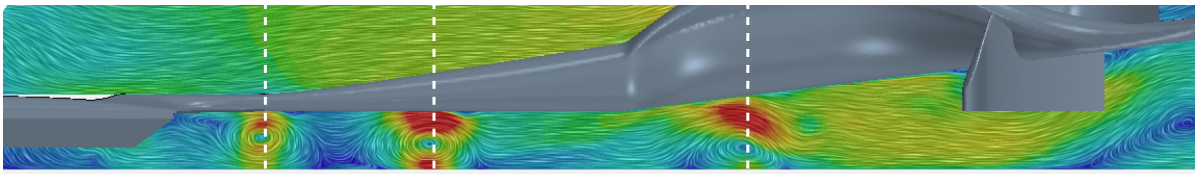

(c) k-ϵ Elliptic Blending RANS.

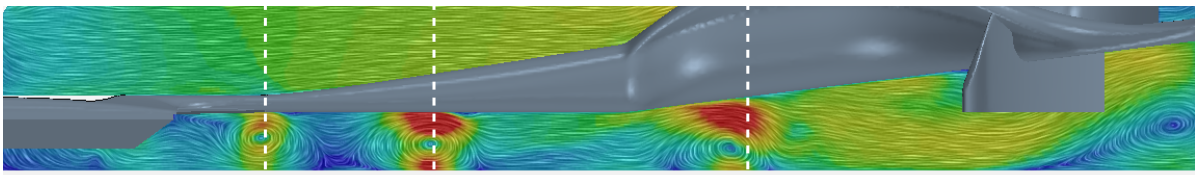

(d) $k-\omega$ SST RANS.

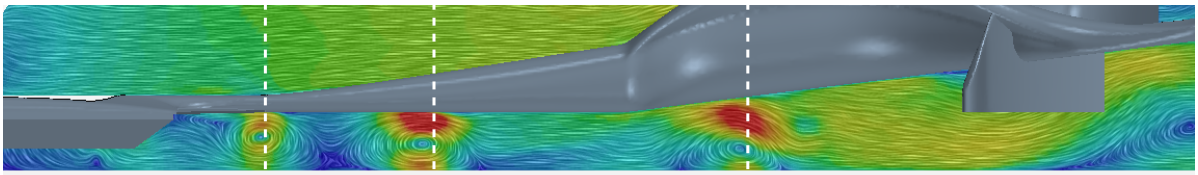

(e) $k-\omega$ SST-IDDES on RANS mesh.

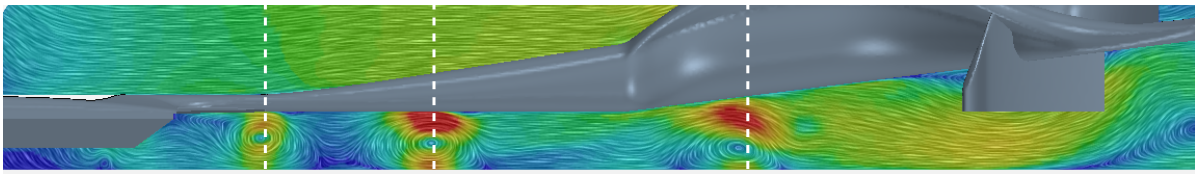

(f) $k-\omega$ SST-IDDES on RANS mesh 16 prism layers.

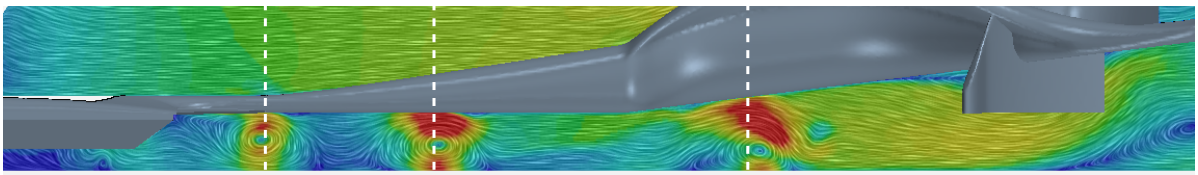

(g) $k-\omega$ SST-IDDES on DES mesh.

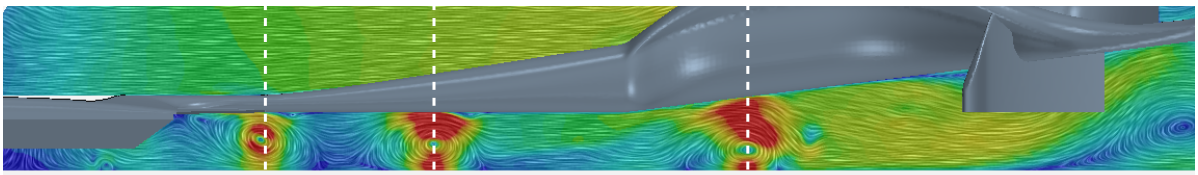

(h) $k-\omega$ SST-IDDES on DES mesh PIV region refined.

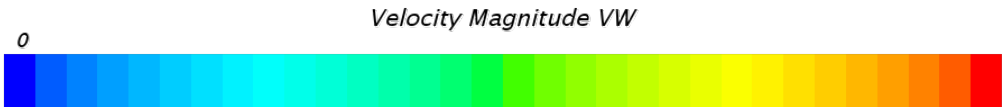

Figure 11.10: LMP1 S09 Straight Line PIV Comparison, Front View underneath Car Floor at X=1.4 m.

The differences between the CFD simulations are larger for the plane further downstream at X=1.915 m. Figure 11.11 shows how the vortices are all still far too strong compared to the PIV data, especially when using the DES methods. The PIV data shows a decay of the original vortices and an emergence of smaller, counter rotating vortices due to the original vortices. Because the original vortices in the plane X=1.4 m are too strong already in the CFD results, the vortices downstream and the counter rotating vortices generated by them are also too strong. Again, the RANS results are evaluated first, after which the various DES simulations are also assessed.

As said, the velocities predicted by the RANS simulations are higher than in the PIV data, especially for the $k-\omega$ SST model. All three simulations have the location of vortex 1 too much to the left. Also, the counter rotating vortex formed on the right of vortex one is too strong and too big. The vortices on the left of vortex 1 are captured better. The vortices are less round in the CFD data but this could be explained by the fact that the main vortex is moved to the left giving them less space in the CFD results. Vortex 2 is too high up in the RANS simulations and has a too strong counter rotating vortex on the right. In the $k-\omega$ SST RANS simulation the vortex is also moved too much to the left, but for the other two RANS simulations the spanwise position is quite good. Vortex 3 has almost disappeared in the PIV data but is very present in the RANS simulations even generating a counter rotating vortex in the top right corner. This indicates that the dissipation is too little to predict the decay of the vortices.

The DES simulations are even worse in this respect. The vortices have even higher velocities than the RANS simulations increasing the difference with the PIV results. In the DES simulations vortex 1 is shifted a bit to the left, which is similar to the RANS results. The shift to the left for the DES simulations is further than for the RANS simulations. This shift was not yet present in the X=1.4 m plane and therefore has to do with the way the vortex is transported with the flow. The smaller vortices to the left of vortex 1 are captured less well by the DES simulation than by the RANS simulations. Only one is formed with quite a different shape. Especially for the second fine DES, this vortex is also much too strong. The location of vortex 2 is also too far to the left for all DES results. Again, the DES with additional refinement in the DES region shows the biggest deviation. Vortex 2 is much stronger and is shifted quite far to the left. Vortex 3 is still very strong for all three DES runs, generating multiple vortices to the left and right of it. The position of this vortex is predicted less well than for the $k-\epsilon$ RANS runs and too much to the left.

The DES simulation that has the additional refinement underneath the car floor does not seem to capture the vortices better than the other CFD simulations. The increased strength of the vortices is even more present in these results, also making the counter rotating vortices stronger. The refinement therefore has the counter intuitive effect of worsening the results instead of improving them. This would imply that other settings should be adapted than the mesh refinement.

All in all, the Realizable $k-\epsilon$ RANS simulation outperforms the other methods, even the DES with a fine mesh in the region of interest. None of the methods satisfactorily predicts the plane X=1.915 m due to the strength of the vortices formed. Improvements to the set-up are needed to better predict the formation and cascade of vortices like this. Changing the turbulence settings for the inlet could lead to a more dissipative solution which might result in a closer correlation with the wind tunnel data. The results presented in [14] have been obtained with a much higher turbulent intensity and a higher viscosity ratio. These results are quite different and show the influence that settings like these might have. The current simulations however, should agree better with the wind tunnel specifications. More research into the proper turbulence settings might therefore lead to a better prediction of the vortices.

The influence of the mesh on the DES results is not straight forward. The refinement underneath the car floor seems to improve the first PIV plane but not the second. Also, the results of the DES on the RANS mesh are in general closer to the PIV data than the results of the DES on the RANS mesh with 16 prism layers. This would indicate that a refined boundary layer with a non refined area outside the boundary layer gives a worse approximation. An explanation here could be the found in the blending functions. The DES on the normal RANS mesh has LES further away from the boundary layer underneath the floor. The 16 prism layers cause the blending functions to break down and allow for LES close to the wall, while the mesh is actually not able to support this. This is mesh ambiguity should be avoided in the mesh design to have clear RANS and LES domains able to use the respective models.

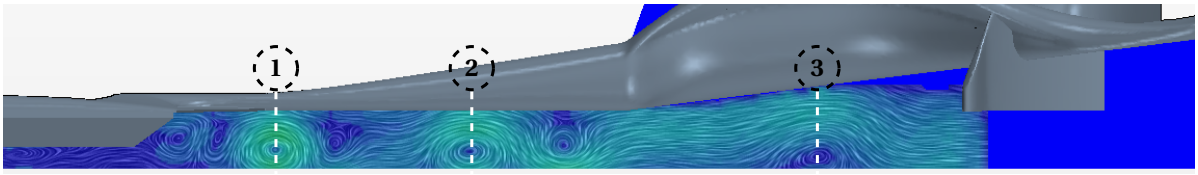

(a) PIV Data Full Scale Wind Tunnel.

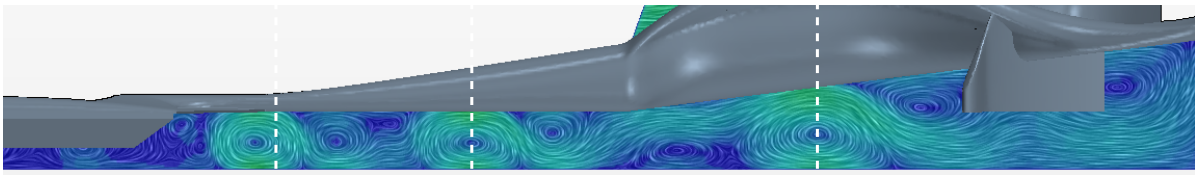

(b) Realizable k-ϵ RANS.

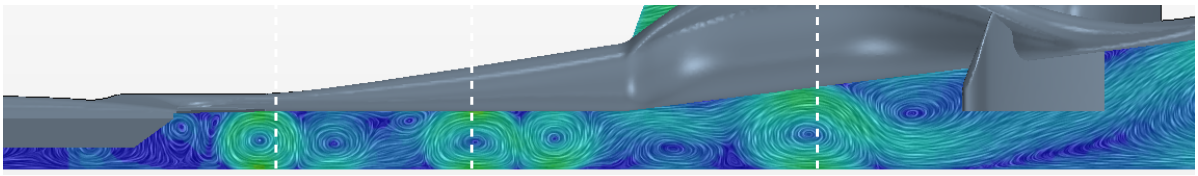

(c) k-ϵ Elliptic Blending RANS.

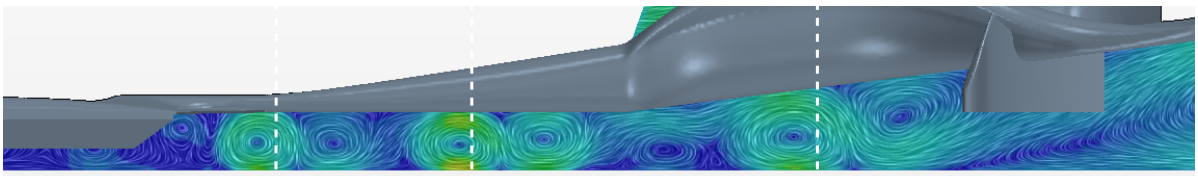

(d) $k-\omega$ SST RANS.

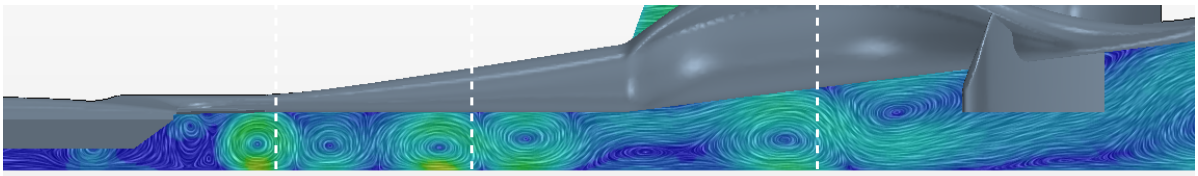

(e) $k-\omega$ SST-IDDES on RANS mesh.

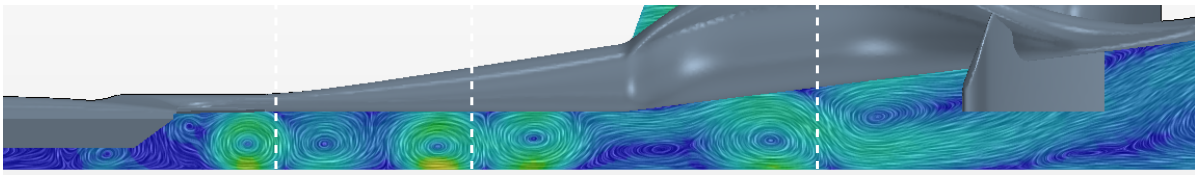

(f) $k-\omega$ SST-IDDES on RANS mesh 16 prism layers.

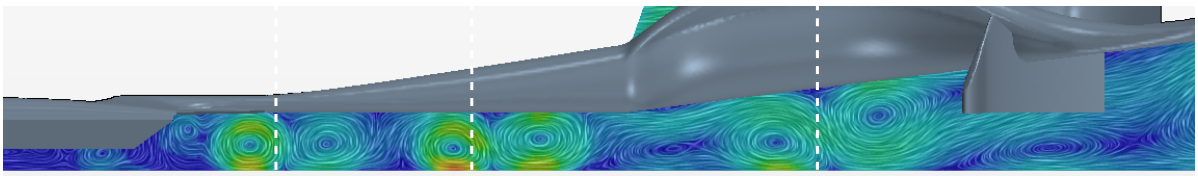

(g) $k-\omega$ SST-IDDES on DES mesh.

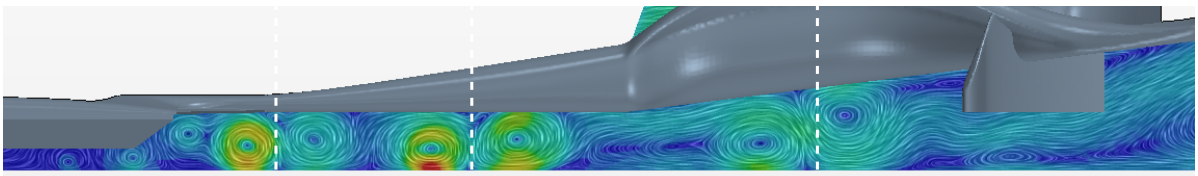

(h) $k-\omega$ SST-IDDES on DES mesh PIV region refined.

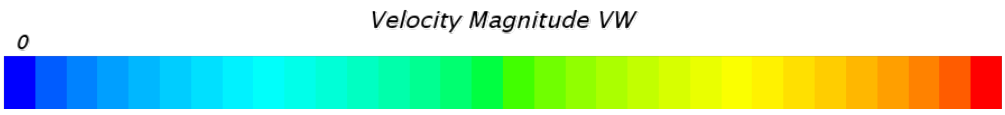

Figure 11.11: LMP1 S09 Straight Line PIV Comparison, Front View underneath Car Floor at X=1.915 m.

11.3. Cornering Results LMP1 S09

The LMP1 S09 geometry is also run as a cornering case. The cornering case has no steer and no roll this time. There is only a yaw angle which is set to 4°. These settings are chosen since they agree with the wind tunnel PIV data available. This PIV data is again obtained for the planes X=1.4 m and X=1.915 m. The planes are rotated with the car and are therefore also set at an angle of 4° with respect to the inflow velocity. This means that the velocity profile in the exact same geometry section is captured. Also, it means that part of the streamwise component of the velocity vector is now an in-plane velocity and captured by the PIV results. This is corrected in the CFD results. The PIV results are compared to different CFD simulations in Section 11.3.2. The overall force data for the different CFD runs is discussed first. This provides some insight into the overall difference between the runs and puts the PIV differences in a larger context. Note that the DES simulation on the DES mesh only features the refinement around the formation of the vortices. This is similar to the initial straight line DES mesh without the refinement under a large part of the floor. The mesh characteristics can again be found in Table A.2 of Appendix A.

11.3.1. Cornering CFD Comparison

The force and balance data for this case is given in Table 11.2. The DES simulations predict a much larger drag than the RANS simulations. Apart from the drag however, the difference between the DES on the fine mesh and the Realizable $k-\epsilon$ RANS results is very small, less than 1%. The additional drag predicted by the DES simulation is in line with earlier results and is expected to be in agreement with wind tunnel data. Unfortunately, like for the straight line case, force data from the wind tunnel are not available.

The DES simulation predicts a higher downforce generated by the front wing due to the transition creating additional suction. The front floor on the other hand has a slightly higher static pressure in the DES results which decreases the front downforce. These two effects cancel each other out resulting in the close agreement between RANS and DES. Something similar occurs for the rear wing and rear floor. The DES simulation loses downforce on the rear wing due to a separating trailing edge. At the same time, the rear floor has a lower static pressure compensating for the downforce loss at the rear wing. Regarding the DES on the coarse mesh, the rear wing again moves into RANS mode resulting in a pressure distribution very close to the Realizable $k-\epsilon$ RANS results. The rest of the prediction on the coarse mesh is further away from the RANS and DES results however, which is in agreement with the results for the straight line car. The splits in downforce on the wings and the floor is given in Table B.2 in Appendix B.

Simulation	C_z	C_x	$C_{z,front}$	$C_{z,rear}$	Bal
Realizable $k-\epsilon$ RANS	-	-	-	-	-
Elliptic Blending $k-\epsilon$ RANS	-6.63%	-0.54%	-5.65%	-7.40%	1.05%
$k-\omega$ **SST RANS**	-12.0%	-1.22%	-13.4%	-10.8%	-1.64%
$k-\omega$ **SST-IDDES** RANS mesh	-3.67%	8.13%	-12.0%	2.99%	-8.69%
$k-\omega$ **SST-IDDES** DES mesh	0.53%	6.78%	0.09%	0.88%	-0.44%

Table 11.2: LMP1 S09 Cornering Forces of CFD Simulations

11.3.2. Cornering PIV Comparison

The PIV results are again shown for the planes X=1.4 m and X=1.915 m in Figures 11.12 and 11.13 respectively. These planes are defined from the nose of the car and are rotated around the same yaw angle as the car. Part of the streamwise velocity is now included into the PIV and CFD data plotted, since part of the streamwise velocity component is parallel to the PIV planes. Similarly, part of the lateral velocity component is ignored since it is perpendicular to the PIV plane and therefore not captured by the measurements.

The comparison at X=1.4 m again shows an over prediction in-plane velocity of the CFD simulations. Two vortices can be identified in the PIV data, which from left to right will be referred to as vortex 1 and vortex 2. Vortex 1 seems very similar between the different CFD runs, located slightly too far to the left and with too much strength. The location of vortex 2 is captured better by the DES simulations than the RANS simulations. The RANS simulations position it too close to vortex 1. The DES on the RANS mesh here outperforms the DES on the fine mesh. The flow to the right of vortex 2 is captured best by the Realizable $k-\epsilon$ RANS simulation, since this is the only one that does not form additional vortices. Especially the $k-\omega$ RANS and the DES on the RANS mesh form quite a visible vortex that should not be there. Note that one of these vortices is present in the straight line case, but should decay before the plane X=1.4 m in cornering. This vortex can be seen in

Figure 11.10. The Realizable $k-\epsilon$ RANS simulation also forms this vortex in cornering but rightfully decays it in time.

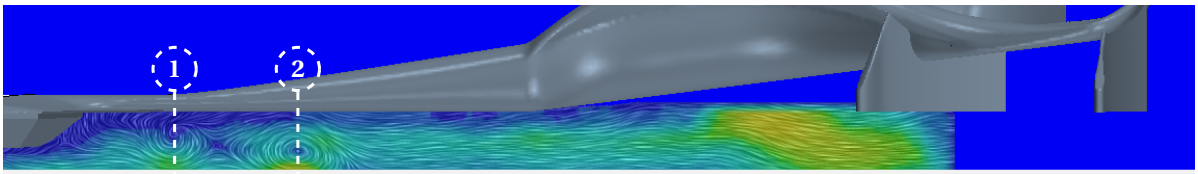

(a) PIV Data Full Scale Wind Tunnel.

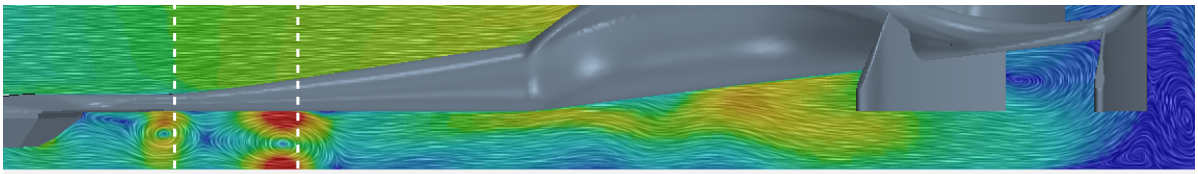

(b) Realizable k-ϵ RANS.

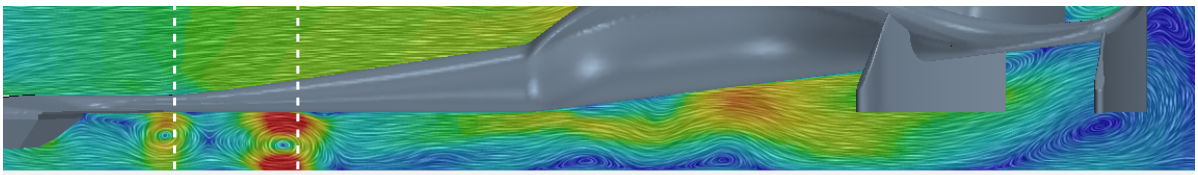

(c) k-ϵ Elliptic Blending RANS.

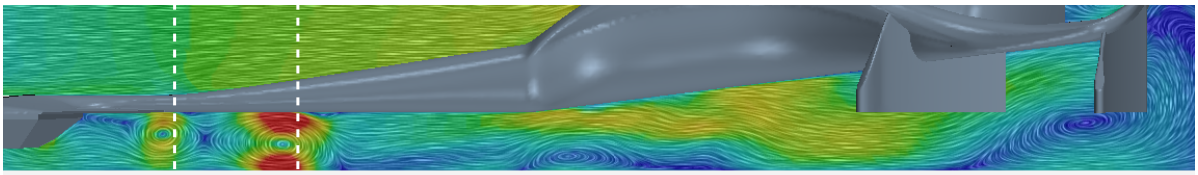

(d) $k-\omega$ SST RANS.

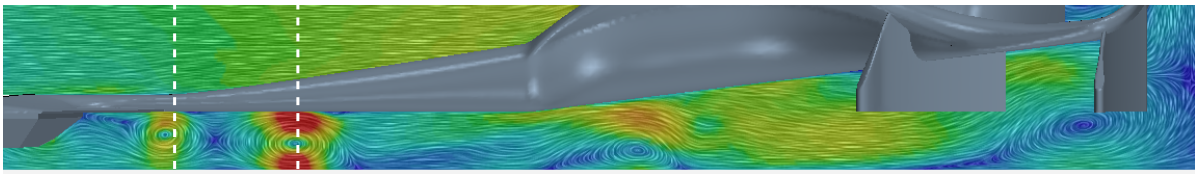

(e) $k-\omega$ SST-IDDES on RANS mesh.

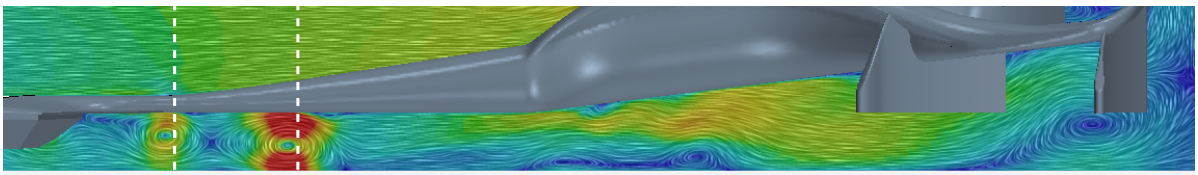

(f) $k-\omega$ SST-IDDES on DES mesh.

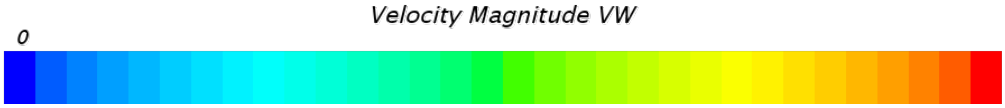

Figure 11.12: LMP1 S09 Cornering PIV Comparison, Front View underneath Car Floor at X=1.4 m.

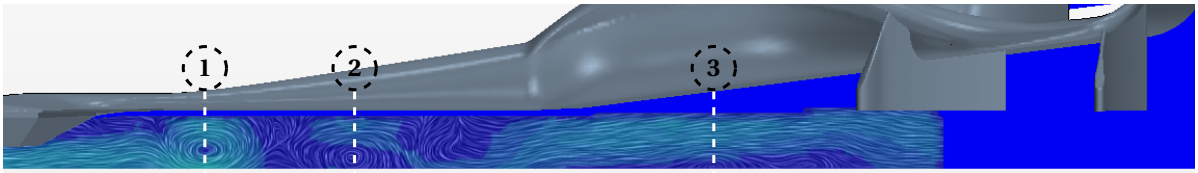

(a) PIV Data Full Scale Wind Tunnel.

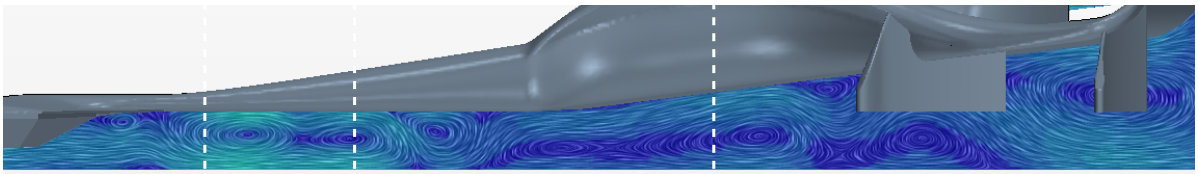

(b) Realizable k-ϵ RANS.

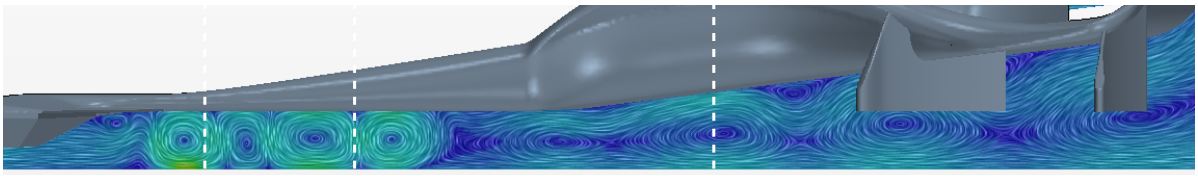

(c) $k-\epsilon$ Elliptic Blending RANS.

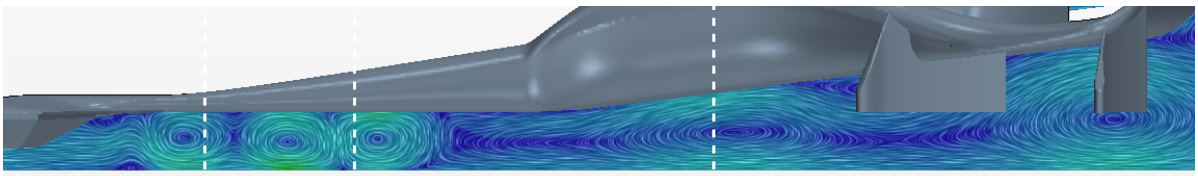

(d) $k-\omega$ SST RANS.

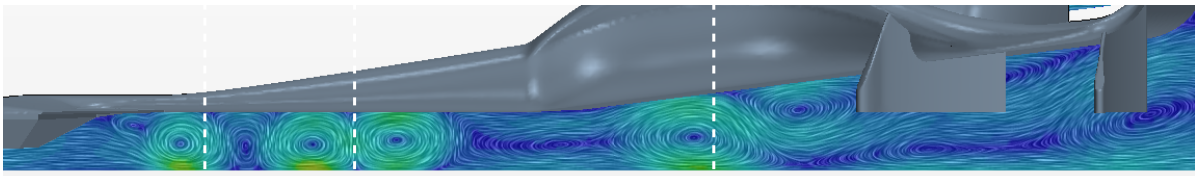

(e) $k-\omega$ SST-IDDES on RANS mesh.

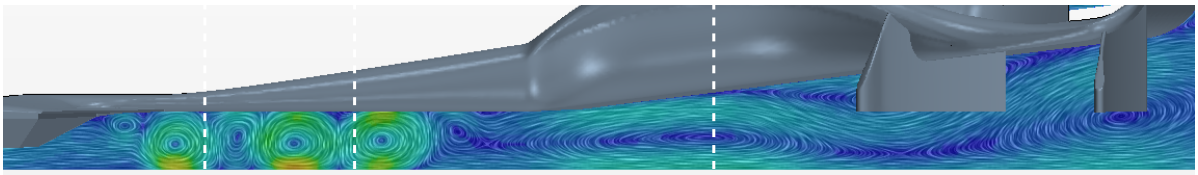

(f) $k-\omega$ SST-IDDES on DES mesh.

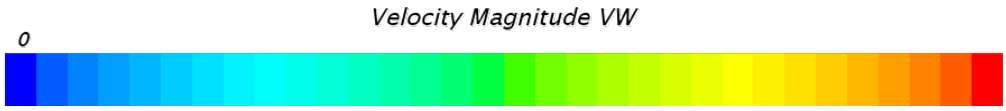

Figure 11.13: LMP1 S09 Cornering PIV Comparison, Front View underneath Car Floor at X=1.915 m.

Even though the cornering results seem a bit closer to the PIV data, the difference with respect to the vortex decay are already visible in this first plane. This problem in the vortex decay is even more visible in the plane X=1.915 m. The cornering CFD results agree less well with the PIV data than the straight line case. This again indicates that the transport of the vortices downstream is not captured well by any of the CFD methods. The in-plane velocities in general are much higher than in the PIV data, and far too many additional vortices are

formed. The Realizable $k-\epsilon$ RANS result is in closest agreement with the PIV data. The agreement is quite good in terms of the number of vortices present in the plane, but their shape and location is still far off. These results indicate that with the current settings, this flow is not captured well, neither by the RANS simulations nor by the DES simulations. Possible improvements could be inflow conditions and mesh refinement.

In general, the conclusion from the comparison between CFD results and PIV data is that none of the methods are able to predict the flow. The Realizable $k-\epsilon$ method outperforms the others for both planes and in both straight line and cornering. The prediction is still off however, indicating the need for improvements. Improving the mesh for the DES in the straight line case does not have the desired effect, meaning other factors should be considered. These could include the turbulent inflow, as the results presented in [14] are very different due to different inflow conditions, or the time step, as the Courant number is quite high for the fine mesh. A combination of changes might finally lead to the desired results.

11.4. Straight Line Results LMP1 S15

The second LMP1 car analysed is the S15. As explained before, the reason that two different cars are simulated is that while for the S09 car two sets of PIV data are available, no force measurements are available. By also simulating the LMP1 S15 car, the overall forces can be compared not only to other CFD simulations but also to a wind tunnel test. The S15 car is simulated for two different ride heights. The first ride height is reasonably flat and thus comparable to the ride height simulated for the GTE19 and the LMP1 S09. The second ride height is more pitched, with the nose down. This means that at the front the ride height is reduced and at the rear the ride height is increased, as is discussed in Section 4.2.1. These two different configurations are respectively referred to as RH 40 50 and RH 30 60. This section first discusses the comparison of the DES simulations with the Realizable $k-\epsilon$ RANS simulations. Afterwards, wind tunnel data is used to assess the accuracy of the DES predictions. This time also the deltas between the two different ride heights are compared. These are quite important to get right since the CFD simulations are often used to assess the influence of a change and not necessarily to find the absolute forces.

11.4.1. CFD Comparison

A quick comparison between the Realizable $k-\epsilon$ RANS results and the DES results is given in this section. The DES method is again used on both the RANS mesh and the DES mesh. The RANS mesh is without the 16 prism layers, meaning it has 7/8 prism layers on the focus parts. The DES mesh is without the 1 mm refinement box around the rear wing to prevent it from separating. The aim is to achieve the RANS solution around the rear wing but still get the desirable amount of detail over the front wing. The characteristics of the mesh used for this geometry can be found in Table A.3 in Appendix A. The results for this configuration and set-up are shown in Table 11.3 for RH 40 50 and in Table 11.4 for RH 30 60. More data is again provided in Table B.2 of Appendix B.

Simulation	C_z	C_x	$C_{z,front}$	$C_{z,rear}$	Bal
Realizable $k-\epsilon$ **RANS**	-	-	-	-	-
$k-\omega$ **SST-IDDES** RANS mesh	0.14%	9.12%	-7.63%	7.09%	-7.75%
$k-\omega$ **SST-IDDES** DES mesh	-1.22%	6.78%	-7.40%	4.31%	-6.25%

Table 11.3: LMP1 S15 Straight Line RH 40 50 Forces of CFD Simulations

Simulation	C_z	C_x	$C_{z,front}$	$C_{z,rear}$	Bal
Realizable $k-\epsilon$ **RANS**	-	-	-	-	-
$k-\omega$ **SST-IDDES** RANS mesh	-8.10%	7.74%	-20.7%	5.20%	-13.7%
$k-\omega$ **SST-IDDES** DES mesh	3.02%	8.58%	-2.87%	9.24%	-5.72%

Table 11.4: LMP1 S15 Straight Line RH 30 60 Forces of CFD Simulations

Regarding RH 40 50, the DES on the RANS mesh shows a separation near the trailing edge of the front wing. This is also shown in the pressure distribution over the front wing, visualized in Figure 11.14a. The DES on the RANS mesh predicts the lowest pressure peak contributing to the lower front downforce. A laminar

separation bubble is captured by the DES simulation on the fine mesh starting around 55% of the chord. This causes a turbulent reattachment of the flow and thereby a transition. The rest of the pressure distribution is fairly similar to the Realizable $k-\epsilon$ RANS simulation. The higher front downforce predicted by the Realizable $k-\epsilon$ RANS results is for a small part caused by the front wing but mostly by the lower pressure underneath the front floor.

The other ride height, with a 30 mm clearance at the front, has more complicated differences between the CFD simulations. The DES simulation on the RANS mesh predicts a wake coming off the front wing that starts much closer to the leading edge than in the other CFD results. It therefore has a bigger wake and a lower pressure peak causing the front downforce to be a lot lower than the Realizable $k-\epsilon$ RANS result. Figure 11.14b shows the pressure distribution around the front wing for the three different simulations. The transition on the fine DES run is again clearly visible. These results show that the deviations from the Realizable $k-\epsilon$ model are quite similar between the two ride heights for the DES simulation on the fine mesh. Both have a lower pressure peak resulting in a lower downforce, but only of a few %. For the DES simulation on the RANS mesh however, the results for the different ride heights are very different. It is not able to capture the flow underneath the front wing well and this effect is enhanced with the lower ride height. The reason for this is that the front wing is much closer to the ground enhancing the ground effect. This makes it more important and more difficult to capture the flow around the front wing.

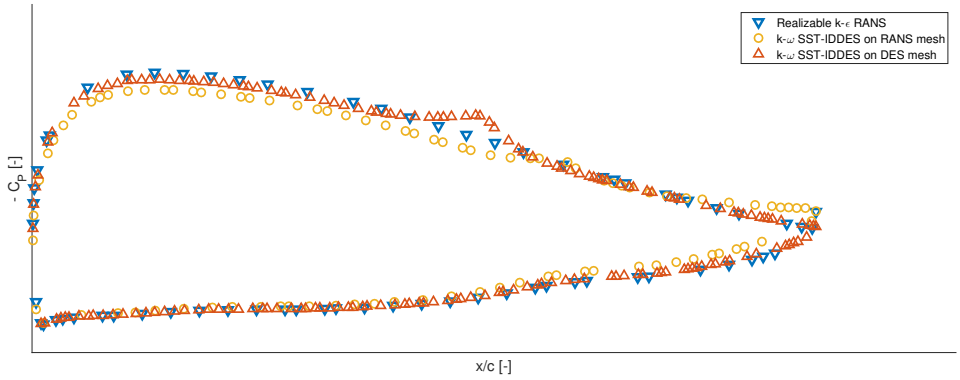

(a) RH 40 50.

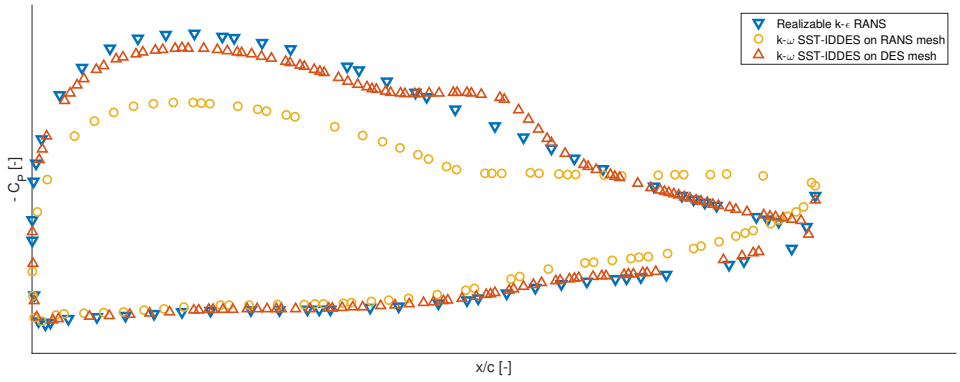

(b) RH 30 60.

Figure 11.14: LMP1 S15 Pressure Distribution, Front Wing at Y=1.0 m (from Symmetry Plane).

Regarding the rear wing, the choice to make mesh around relatively coarse there ensures that the two DES simulations have very similar results. The data points of the coarse DES simulation almost exactly coincide with those of the fine DES. The DES on the fine mesh now also does a RANS in the boundary layer of the rear wing. The Realizable $k-\epsilon$ RANS simulation also has a similar distribution. This is shown in Figure 11.15. The difference in rear downforce is therefore again caused by the rear floor generating more downforce in the DES runs. This is in agreement with the results obtained for the GTE19 car but not with the other LMP1 configuration.

For RH 30 60, the results on the rear wing are also very similar for all three simulations. The difference in

rear downforce in Table 11.4 stems from the rear floor, since the DES simulation has a lower pressure and thus more downforce. The influence of a higher ground clearance on the rear part of the car is therefore smaller than the difference in clearance on the floor. This is a logical finding, since the ground effect is very important for the front wing and less so for the rear wing.

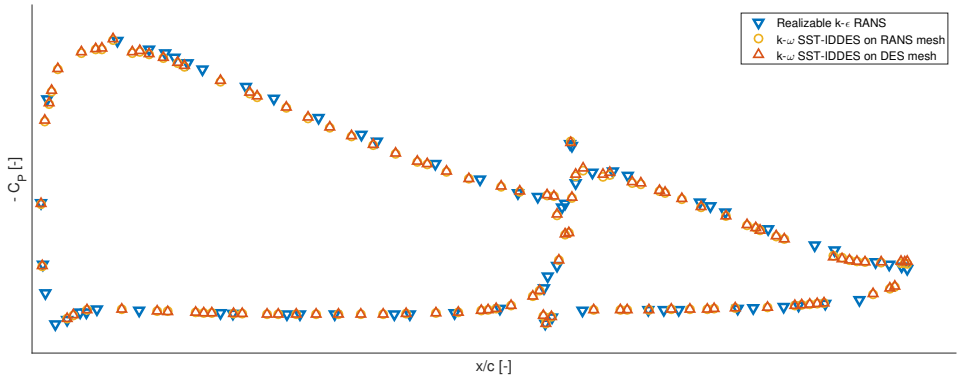

Figure 11.15: LMP1 S15 Pressure Distribution, Rear Wing at Y=4.0 m (from Symmetry Plane) RH 40 50.

11.4.2. Correlation Experimental Data

In order to assess the accuracy of the results discussed in the previous section, the CFD results are also compared to wind tunnel data. This is done based on the 60% scale model. This section first gives a short overview of the differences in the absolute values between the CFD simulations and the wind tunnel data. The main focus however, will be on the deltas towards the end of this section. The deltas are the differences in the forces due to a geometry or ride height change. In the design process, these values are often more important to get right than the absolute forces.

For the ride height 40 50 configuration, Table 11.5 contains the different results. The balance of the Realizable $k-\epsilon$ RANS simulation is better than both DES simulations, since both the front and the rear downforce are over predicted. In terms of drag and front downforce however, the DES simulations are much closer to the wind tunnel data. The DES on the RANS mesh has the best drag prediction and the DES on the DES mesh the best front downforce prediction. The comparison for the other ride height, 30 60, is shown in Table 11.5. The prediction of the front downforce of the DES on the RANS mesh is quite far off from the wind tunnel data. This is in agreement with the discussion in Section 11.4.1. Again, the DES on the DES mesh does reasonably well, although this time the baseline RANS model agrees slightly better in terms of the front downforce. Still, the DES prediction on the fine mesh is not far off except for the rear downforce.

Simulation	C_z	C_x	$C_{z,front}$	$C_{z,rear}$	Bal
Wind Tunnel Results RH 40 50	-	-	-	-	-
Realizable $k-\epsilon$ **RANS** RH 40 50	8.73%	-7.78%	6.72%	10.6%	-1.91%
$k-\omega$ **SST-IDDES** RANS mesh RH 40 50	8.88%	0.63%	-1.42%	18.4%	-9.52%
$k-\omega$ **SST-IDDES** DES mesh RH 40 50	7.40%	-1.53%	-1.18%	15.3%	-8.05%
Wind Tunnel Results RH 30 60	-	-	-	-	-
Realizable $k-\epsilon$ **RANS** RH 30 60	3.29%	-6.83%	-0.11%	7.10%	-3.37%
$k-\omega$ **SST-IDDES** RANS mesh RH 30 60	-5.08%	0.38%	-20.8%	12.7%	-16.6%
$k-\omega$ **SST-IDDES** DES mesh RH 30 60	6.41%	1.17%	-2.98%	17.0%	-8.89%

Table 11.5: LMP1 S15 Straight Line RH 30 60 Forces Comparison with 60% Scale Wind Tunnel Data.

The main purpose of this section however, is to compare the deltas. The delta is the difference in downforce or drag between two runs. Deltas are usually used to compare changes in the geometry. The purpose is for example to assess the impact of adding a different end plate to the rear wing. The absolute value is then less important than the difference it makes to the forces and balance. In this case, two different ride heights are compared instead of geometry changes. The deltas from the wind tunnel are subtracted from the deltas of the CFD data and the result is divided by the force in the 40 50 ride height case to find a percentage. Instead

of computing how well the DES method is able to predict the forces on the car, this measures how well it can compute the change in forces. In the design process, this can be even more important.

These deltas between the two different ride heights are given in Table 11.6. When looking at the deltas instead of the absolute values, the DES method seems like the best method to use. All of the deltas are within 3% of the wind tunnel deltas, which indicated the potential of the DES method in the design process. Note however, that the predictions of the Realizable $k-\epsilon$ method are also quite good, especially in terms of drag and balance. Both the Realizable $k-\epsilon$ RANS method and the DES method are therefore quite consistent in their errors.

Simulation	C_z	C_x	$C_{z,front}$	$C_{z,rear}$	Bal
Wind Tunnel Results	-	-	-	-	-
Realizable $k-\epsilon$ RANS	-5.13%	0.84%	-6.85%	-3.53%	-1.81%
$k-\omega$ **SST-IDDES** RANS mesh	-14.5%	-0.24%	-23.7%	-5.86%	-8.84%
$k-\omega$ **SST-IDDES** DES mesh	-0.38%	2.72%	-2.42%	1.50%	-1.77%

Table 11.6: LMP1 S15 Straight Line Change in Forces between RH 40 50 and RH 30 60, Comparison with 60% Scale Wind Tunnel Data.

The DES method predicts much better in terms of deltas than in terms of absolute values. An explanation for this is that the downforce on the rear floor is very consistently over predicted. An explanation has not been found yet and it would be preferable to find the origin of the difference. Still if geometry changes need to be assessed, a DES simulation could give a better prediction of the impact of the change than a Realizable $k-\epsilon$ RANS simulation. This however, needs to be verified by testing different add-ons on a certain geometry and verifying the deltas with wind tunnel data. This is a slightly different delta than the change in ride height.

11.5. Simulation Time Evaluation LMP1

The simulation times for the LMP1 car are summarized in Table 11.7. Since for the LMP1 S09 car the reference RANS simulations have been run as part of the thesis as well, more information about the difference between RANS and DES than for the GTE19 car is available. Unfortunately due to an issue during the simulation, the information for the DES on the RANS mesh is not available. The DES simulations on the LMP1 S15 are less computationally expensive since the mesh around the rear wing was kept coarser to prevent Grid Induced Separation. This reduces the mesh count and therefore the computational resources needed.

The computation times here are comparable to the times documented for the GTE19 car. The main conclusion is that if the DES method is used on the same mesh as for the RANS simulations, the method does not cost more time. Generally speaking however, at least double the number of cells is needed making the method twice as expensive.

Simulation Set-Up	**Cells** *Millions*	**Pre Step** *CPU-Hour*	**Solve** *CPU-Hour*	**Solve n=1080** *Hour*
S09 Realizable $k-\epsilon$ RANS	85	5.74	2047	1.9
S09 $k-\omega$ SST RANS	85	5.81	2347	2.2
S09 $k-\epsilon$ Elliptic Blending RANS	106	6.71	3586	3.3
S09 $k-\omega$ SST-IDDES on RANS mesh	85	5.77	-	-
S09 $k-\omega$ SST-IDDES on baseline DES mesh	203	9.18	6464	6.0
S09 $k-\omega$ SST-IDDES on RANS 16 prism	106	6.71	3522	3.3
S09 $k-\omega$ SST-IDDES on Revised DES mesh	216	9.9	7126	6.6
S15 40 50 Realizable $k-\epsilon$ RANS	85	~6	-	~2
S15 40 50 $k-\omega$ SST-IDDES on RANS 16 prism	107	7.21	3583	3.3
S15 40 50 $k-\omega$ SST-IDDES on DES mesh	171	9.0	5814	5.4
S15 30 60 Realizable $k-\epsilon$ RANS	85	~6	-	~2
S15 30 60 $k-\omega$ SST-IDDES on RANS 16 prism	107	6.8	3434	3.2
S15 30 60 $k-\omega$ SST-IDDES on DES mesh	171	9.0	5688	5.3

Table 11.7: LMP1 Straight Line CPU Hours and Simulation Time.

12

Recommendations for Simulating Full Cars

This chapter contains an overview of the recommended settings to perform full car simulations. These settings are based on the simulation results discussed in the previous chapters. A number of these settings are the same as the settings presented in Chapters 8 and 12. The aim of this chapter is to repeat the most important of these and to conclude some settings from the variations. For settings that are not mentioned in chapter, the baseline set-up from Chapter 12 are used. Note that some of the settings are mentioned nowhere, like most of the constants used in the $k-\omega$ SST-IDDES model. In this case, the recommended default settings from STAR-CCM+ v11.02 are used. An overview of many of the STAR-CCM+ v11.02 settings used is given in Appendix C. The influence of changing them has not been considered nor investigated. First, a general overview of the adjusted settings is given in Section 12.1. These settings are based on the straight line case, since that is the case used most throughout the thesis. The adjustments that need to be made for the straight line and cornering case respectively are then discussed in Sections 12.2 and 12.3. This chapter concludes the analysis of the full car simulations with the Detached Eddy Simulation method.

12.1. General Full Car Settings

The proposed settings can be divided into a number of categories. These include the model settings, the solver settings and the mesh settings. These three categories are discussed in this section to give a complete overview of the recommended settings for car simulations at Porsche Motorsport. Note that a more extensive overview of the basic settings used are discussed in Chapter 9. This section only gives an overview of the DES specific settings for Porsche Motorsport.

12.1.1. Full Car Model and Solver Settings

Based on the results from the wing study and the full car study, the $k-\omega$ SST-IDDES is chosen as the default model for the DES simulation. For the initialization with RANS, the $k-\omega$ SST model is used. Besides this, the turbulence intensity is set to 1% and the turbulent viscosity ratio to 10. The Synthetic Eddy Method can add value, it gives only a slight increase in computational costs and can help in the transition between RANS and LES. It amplifies the over prediction of downforce on the rear floor however, and is therefore not used as a default.

For the solver settings, the set-up chosen consists of an initialization with RANS of 1000 iterations. This results in a good estimate of the flow field as the initial condition for the LES computation. Thereafter, 2 seconds of physical time are simulated with a time step of 0.001 s. This time step for sure is suitable for the simulations at 27.5 m/s as is done for the GTE car. For higher speeds a slightly smaller time step might be worth investigating. Three inner iterations seem to be enough to drop the residuals within a time step. The 2 seconds are computed first with a first order scheme and then a second order scheme to ensure both stability and accuracy. The switch is after 1200 time steps. The final 400 time steps are used to average over. Note that 400 time steps corresponds to 1200 iterations due to the inner iterations.

12.1.2. Full Car Mesh Settings

The mesh, like any car mesh, is very dependent on the exact geometry. The purpose of this section is therefore to give some pointers for the design of a DES mesh from the design of a RANS mesh. The RANS mesh is

assumed as a starting point, such that a number of refinement boxes are already present. The RANS mesh assumed here would have a few prism layers on the full car and some additional in critical areas like the wings and the floor. Furthermore, a normal mesh size around the car of 8 mm would be present with refinement boxes of 2-4 mm around parts like the wheels, the floor and the wings.

Even though some refinement boxes are already present in this mesh, a number of additional ones are needed. Examples here are the front wing, the rear wing and the full floor. Plates, strakes and other aerodynamic add-ons can also benefit from more refinement. These have not been assessed in a lot of detail in this report. For the full car simulations discussed in Part III, refinement boxes of 1 or 2 mm are used along with 16 prism layers. This number of prism layers is based on a stretch ratio of 1.15 and is sufficient to capture transition as discussed in Chapter 10. The near wall cell is important here as well, and investigating a reduction might also be worthwhile. The current near wall cell used results in a y+ below 5, meaning that a reduction to below 1 could be interesting to investigate. To capture the transition however, also a local refinement of 1 mm is needed. This leads to the recommendation to refine areas where this needs to be captured up to that (or a lower) mesh size. Do note that the combination of the number of prism layers and a refinement greatly increases the cell count.

Important for the mesh is also to be aware of Grid Induced Separation, as discussed in Section 11.2.1. There might be a need to locally coarser or further refine the mesh depending on the allowed costs of the simulation. Coarsening the mesh would cause the simulation to go into RANS mode locally and prevent the phenomena. Transitional structures however, are then not captured any more. Refining further would theoretically ensure that the mesh can support an LES solution and also prevent the separation. This has not been tested however as it would exceed the reasonable costs for simulations. A cell count of about 310 and 630 million would be required for respectively the straight line and cornering cases.

12.2. Case Specific Settings: Straight Line

All of the principles discussed before are valid for both the straight line and the cornering case. One thing however, is important to be aware of for the straight line case specifically: the symmetry condition. As discussed in Sections 7.2, 10.1 and 10.6, the symmetry condition can impose a non-physical condition on the flow. In the airfoil model study, this is visualized through an increased vorticity further away from the wall close to the boundary, and in the car simulations as a total pressure loss. Ideally therefore the full car would also be run in the case of a straight line simulation, but cost considerations lead to keeping the symmetry condition. Monitoring of the impact however is advised, evaluation of for example the total pressure loss and the impact it would have.

12.3. Case Specific Settings: Cornering

The principle of the cornering case is the same as the straight line case. Still, there are a number of differences in preparing the case. Some basic, but therefore perhaps easy to forget, differences include:

- The wind tunnel domain must be doubled and the geometry positioned correctly
- The symmetry condition must be replaced by a free slip wall
- New boundaries must be defined and be giving their respective correct settings
- The number of cores to calculate on must be doubled to keep the efficiency

These basic difference are generally true for the difference between straight line and cornering cases. The main thing to keep in mind however, is the adjustment of the mesh. The method used currently at Porsche allows refinement boxes created to rotate with the yaw angle but not with the roll angle. For the RANS meshes used, the refinement boxes are often greatly oversized limiting the effect of this. For DES however, the boxes used follow the geometry more closely. This means that the roll angle can cause part of the geometry to not be fully encompassed by the desired refinement box. Three solutions for this are extending the boxes further, using non-symmetric boxes or also rotating the boxes with the roll angle. The first option is used in this report. It is easier to keep track of the boxes when the same boxes are used on both sides and when the roll angle is taken over the refinement with respect to the ground still needs to be taken into consideration. It is more difficult to predict where exactly the mesh will be refined and whether this still satisfies all the requirements.

13

Conclusion

Capturing the complex flow around motorsport geometries is and remains a challenge. The usage of Computational Fluid Dynamics is one of the ways to capture these flows, but success differs per method used and per application. Detached Eddy Simulation is one of these methods, where Large Eddy Simulation (LES) and the Reynolds-Averaged Navier-Stokes (RANS) equations are combined. In this thesis, two different application domains have been explored with this method, although both of them are tied closely to motorsport aerodynamics. The first is an airfoil model study, where a rear wing profile and a NACA 0012 airfoil are used to explore DES. The second application domain concerns full car simulations, which is the main topic of this master thesis. The purpose of the airfoil study is to explore the different parameters that can be adjusted in order to understand the abilities and restrictions of the method. The purpose of the full car simulations is to assess the results obtained and to improve these. This leads to a process in place that allows DES to be used as part of the design process.

The simulations in the airfoil study directly illustrate the ambiguous behaviour of the DES method. The airfoil study consists of simulations on a high downforce car rear wing and a NACA 0012 airfoil. The first is a valid motorsport application while the second is a commonly used test case for which experimental data is available. From the simulations on the airfoil models, a number of conflicting conclusions can be drawn. This includes the influence of the time step, the mesh and the spanwise extend. The most important conclusions about simulating an airfoil are therefore:

1. The mesh including the number of prism layers, wall cell thickness and the (spanwise) refinement near the airfoil has a big influence on the results. Mesh design should therefore be done carefully. For the number of prism layers, a stretch factor of 1.15 is preferred with a wall y+ below 1. The spanwise refinement can be ensured by using isotropic meshes and satisfying the length ratio condition around the airfoil.

2. The stability of the solution is very dependent on the mesh, the initialization, the time step and the geometry simulated. This means that monitoring the solution is important to determine the appropriate simulation and averaging time. Initialization with RANS or a solution at a lower angle of attack on a properly designed mesh helps to stabilize more quickly.

3. The DES shows promising results regarding the prediction of low angle of attack flow phenomena like laminar separation bubbles and a limited pressure side trailing edge separation.

4. The results for NACA 0012 airfoil are not fully in agreement with experimental data, especially regarding the separation point. This means that the recommended settings are a starting point from which further improvements need to be found in order to improve the process.

The actual application domain however, is the full car. The ability of the DES method to capture the flow around the car is therefore assessed for three different car configurations developed by Porsche Motorsport over the past years: the GTE19, the LMP1 S09 and the LMP1 S15. Comparing the DES results with other CFD methods and wind tunnel data leads to a number of interesting conclusions about the application of the DES method to full car simulations:

1. The big influence of the mesh refinement on the performance and the behaviour of the method is confirmed. A mesh that is finer in critical flow areas gives a much better prediction than a coarser mesh. The difficulty here is that the mesh size that is considered fine enough differs between the GTE19 and the LMP1 S09 car as illustrated by the separating rear wing in the latter case. Either the flow speed or the shape of the rear wing causes Grid Induced Separation. This might be solved by refining the mesh further although this has not been tested due to the costs involved. Instead, coarsening towards a RANS solution is used to solve the issue.

2. The DES method shows the ability to capture transition. With a fine mesh, transition phenomena can be captured improving the prediction of the flow structures underneath the wings. The illustrates the potential additional insight the DES method can provide compared to RANS methods, which can only predict transition with a costly transition model. DES is more costly than this transition model (rough estimate of 20% in the discussed cases) but also predicts transition with the turbulent structures resulting from it. The transition locations of the two methods do not fully agree, although this is hard to assess due to the very different transition behaviour. A laminar separation bubble with turbulent reattachment is predicted by the DES method, while the transition model transitions almost instantly.

3. Capturing vortices and their development downstream is not done well by the DES method. Comparisons with PIV data and other CFD methods show the tendency to overpredict the strength of the vortices. The DES on the fine mesh is often closer than the DES on the coarse mesh thus confirming earlier findings, but it is still quite far off especially further downstream from the vortex formation. A smaller time step or variations in the inflow conditions could potentially lead to improvements here. The smaller time step would reduce the Courant number, which is an indicator for how well the time evolution of the structures is captured. The inflow conditions influence the decay of the vortices greatly, which is one of the factors that is currently not captured well.

4. In terms of absolute downforce predictions the DES method is performing less well than the normally used RANS method. It generally predicts a lower static pressure underneath the floor of the car and hence a higher downforce. The rear downforce is overpredicted with 5-10% by RANS and around 17% by DES. The origin of this has not been found yet.

5. In terms of absolute drag predictions the DES method is performing better than the normally used RANS method. The Realizable $k-\epsilon$ RANS simulations underpredicts the drag compared to experimental data up to 16%. The DES simulations on a fine mesh get fairly close, the underprediction is maximum 5% but often closer to 1% only.

6. The balance is the percentage of the total downforce working at the front axle. The balance for the GTE19 car is spot on for the DES method, but the Realizable $k-\epsilon$ method performs well too here. The balance on the LMP1 car is underpredicted by the DES method around 8% and by the Realizable $k-\epsilon$ method 2-3%.

7. The deltas predicted by the DES method are very good. The deltas are the differences in forces due to geometry or ride height changes. Often, the deltas are preferred over the absolute values since also between wind tunnels the absolute values differ. The difference in delta prediction for the DES method stays within 3%, while the difference for the Realizable $k-\epsilon$ method goes up to 7%. The fact that the deltas are predicted well is therefore a promising result for the DES method as a design tool.

Overall, the DES method has a number of promising characteristics but needs more fine tuning to become a reliable tool in the aerodynamics team. Ambiguities like the Grid Induced Separation on the rear wing need to be preventable or identifiable. The costs are around three times higher than for the standard model used by the team, the Realizable $k-\epsilon$ RANS model. The results obtained show that transition can be captured and that the deltas between two different ride heights can be captured very well. The absolute downforce is still off compared to the wind tunnel data and the source of this should be investigated further to improve the usability of the DES method for motorsport aerodynamics.

A process and set of recommended settings have been put in place for the Porsche team to continue the work and as a starting point for the application of the Detached Eddy Simulation method in other domains. The method can enrich the knowledge of the team about different flow phenomena and aid in the design process. For now it can not replace other methods due to the sometimes unpredictable errors, but it can give more information leading to a better design and bringing Porsche one step closer to once more beating their competitors.

14

Recommendations

As discussed in the conclusion, the Detached Eddy Simulation method shows a lot of potential as a tool in aerodynamic design in motorsport. Compared to RANS more flow phenomena can be captured giving a richer insight into the flow. The costs of using this method are higher however, since a finer mesh is needed to capture these flow phenomena. The main disadvantage however, is the reliability of the method. The method should be further improved in order to act as a reliable tool in CFD design. A number of recommendations to continue with this method are:

1. The airfoil study could be improved by selecting an airfoil with easier stall behaviour. Consistent separation behaviour less sensitive to the experimental settings would be easier to compare CFD results with. After finding the best settings to capture the airfoil, the step back to the more ambiguous airfoil can be made.

2. In order to capture the vortices underneath the flow of the car better, the time step could be reduced. Some of the results are obtained with a 1 mm mesh, but the method is still not able to capture the vortices perfectly. The Courant number in this area is quite high due to the very refined mesh, which indicates that a smaller time step could improve the results.

3. Another suggestion to improve the correlation with the PIV data is to adjust the turbulent inflow settings. Neither the usage of the Synthetic Eddy Method, nor increasing the turbulent intensity has been tested. The differences with [14] indicate that different turbulence settings give different results supporting a step towards this direction.

4. The source of the lower pressure underneath the floor has not been identified. Pressure tap data here could help to identify the origin but this was not available for the configurations simulated. Also, experimenting with a finer mesh could be an option, going from a 2 mm mesh size to 1 mm for all configurations. The 1 mm mesh underneath the floor for the LMP1 S09 mesh gives results very close to the Realizable $k-\epsilon$ RANS, but without wind tunnel data a well-supported conclusion can not be drawn.

5. The rear wing of the LMP1 in the end could only be captured with the RANS solution. Using a finer mesh (refining up to 0.5 mm) could prevent the premature separation of the flow while allowing the region to default to LES close to the walls.

6. The difference with Large Eddy Simulation in terms of both accuracy and simulation costs has not been assessed. This could be useful to identify how much the DES method saves in terms of costs and what the difference in accuracy is.

7. The ability of the DES method to predict the influence of a design change should also be testing. The results for a change in ride height are promising and calls for taking it one step further.

Most of the recommendations have not been tested due to cost and time constraints. Apart from doing a full LES, all of the recommendations are quite achievable at this point in time already and could be done using the normal process. This full LES could be done for the airfoil study instead of the full car to limit the costs involved. The further explorations mentioned could lead to new insights and conclusions allowing for the improvement of the process used and of the results obtained with the Detached Eddy Simulation method.

A

Overview Full Car Set-Up Characteristics

This appendix provides an overview of all of the set-ups used for the different full car simulations. The characteristics are first given for the GTE19 car in Table A.1. This includes the set-ups for the straight line cases as well as the set-ups for the cornering cases. For the LMP1 car of 2015, two tables are given. The first is Table A.2 and contains the characteristics of the LMP1 S09. Table A.3, contains the set-up for the LMP1 S15.

All three tables can be split into two parts. On the left side of the table the characteristics for the mesh are given. These include a description that is used in the main text, the number of cells, the number of prism layers and which areas are refined up to 1 mm and up to 2 mm. These refinement areas can concern the front wing, rear wing, foot plate, front floor and rear floor. The tag *aniso* is used when the mesh is not refined in all directions evenly, where the smallest edge length is given in these tables. Anisotropic mesh refinement is used for the RANS meshes only, the DES mesh is always fully isotropic. Note that the number of prism layers refers to the critical parts of the car, which are the aforementioned front wing, rear wing and floor. On the remainder of the car 2 or 3 prism layers are used for all meshes.

On the right side of the table, the simulations that were run with a particular mesh are given. Here, the section in which the results can be found is given, as well as the turbulent inflow conditions. The number included in front of the section is used in Tables B.1 and B.2 to refer back to these settings. Tables B.1 and B.2 contain the CFD results obtained for the different simulations.

Mesh Set-Up					**Simulations Run**	
Description	**Cells** *Millions*	**Prism Layers**	**Boxes** *1 mm*	**Boxes** *2 mm*	**Results**	**Settings**
RANS Mesh	85	7 or 8	-	*aniso* Floor	1) Sec 10.1	$I = 1\%$, $\frac{\mu_t}{\mu} = 10$
Baseline DES Mesh	182	12	Front Wing Foot Plate	Front Wing Rear Wing Floor	2) Sec 10.1	$I = 1\%$, $\frac{\mu_t}{\mu} = 10$
Revised DES Mesh	192	16	Front Wing Foot Plate	Front Wing Rear Wing Floor	3) Sec 10.3 4) Sec 10.2	$I = 2.5\%$, $\frac{\mu_t}{\mu} = 10$ $I = 2.5\%$, $\frac{\mu_t}{\mu} = 20$
Revised DES RW Mesh	215	16	Front Wing Foot Plate Rear Wing	Front Wing Rear Wing Front Floor	5) Sec 10.3 6) Sec 10.4 7) Sec 10.5	$I = 2.5\%$, $\frac{\mu_t}{\mu} = 20$ SEM + $I = 2.5\%$, $\frac{\mu_t}{\mu} = 20$ $I = 2.5\%$, $\frac{\mu_t}{\mu} = 20$
RANS Mesh Cornering	178	7 or 8	-	*aniso* Floor	8) Sec 10.6	$I = 1\%$, $\frac{\mu_t}{\mu} = 10$
Revised DES RW Mesh Cornering	495	16	Front Wing Foot Plate Rear Wing	Front Wing Rear Wing Front Floor	9) Sec 10.6	$I = 1\%$, $\frac{\mu_t}{\mu} = 10$

Table A.1: GTE19 Straight Line and Cornering Mesh Set-Up and Simulations Run with that Set-Up.

Description	Mesh Set-Up: Cells *Millions*	Prism Layers	Boxes *1 mm*	Boxes *2 mm*	Simulations Run: Results	Settings
RANS Mesh	85	7 or 8	-	*aniso* Floor	10) Sec 11.2	$I = 1\%$, $\frac{\mu_t}{\mu} = 10$
Baseline DES Mesh	203	16	Front Wing Rear Wing Foot Plate	Front Wing Rear Wing Floor	11) Sec 11.2	$I = 1\%$, $\frac{\mu_t}{\mu} = 10$
RANS Mesh 16	106	16	-	*aniso* Floor	12) Sec 11.2	$I = 1\%$, $\frac{\mu_t}{\mu} = 10$
Revised DES Mesh	216	16	Front Wing Foot Plate Floor	Front Wing Rear Wing Floor	13) Sec 11.2	$I = 1\%$, $\frac{\mu_t}{\mu} = 10$
RANS Mesh Cornering	170	7 or 8	-	*aniso* Floor	14) Sec 11.3	$I = 1\%$, $\frac{\mu_t}{\mu} = 10$
RANS Mesh 16 Cornering	188	16	-	*aniso* Floor	15) Sec 11.3	$I = 1\%$, $\frac{\mu_t}{\mu} = 10$
Baseline DES Mesh Cornering	395	16	Front Wing Foot Plate	Front Wing Rear Wing Floor	16) Sec 11.3	$I = 1\%$, $\frac{\mu_t}{\mu} = 10$

Table A.2: LMP1 S09 Straight Line and Cornering Mesh Set-Up and Simulations Run with that Set-Up.

Description	Mesh Set-Up: Cells *Millions*	Prism Layers	Boxes *1 mm*	Boxes *2 mm*	Simulations Run: Results	Settings
RANS Mesh	85	7 or 8	-	*aniso* Floor	17) Sec 11.4	$I = 1\%$, $\frac{\mu_t}{\mu} = 10$
Baseline DES Mesh	171	16	Front Wing Foot Plate	Front Wing Rear Wing Floor	18) Sec 11.4	$I = 1\%$, $\frac{\mu_t}{\mu} = 10$

Table A.3: LMP1 S15 Straight Line Mesh Set-Up and Simulations Run with that Set-Up.

B

Full Car Simulations Detailed CFD Results

In this chapter, the resulting force data from the CFD simulations is given. This force data is given as a difference in percentage compared to results obtained with the Realizable $k-\epsilon$ RANS method. These differences in total downforce, total drag, front downforce, rear downforce and balance can all also be found in the main body of the thesis. In this appendix more information about the origin of the difference in downforce is given. This is done by showing the increase or decrease in downforce on the front wing, rear wing, front floor and rear floor in addition to the total front and rear downforce. The purpose of this is to further clarify the results obtained and explained in Chapter 10. In the main body, these results are often referred to.

The meshes and simulation settings used for the various simulations are indicated by *Result Nr.*, which refers to Tables A.1, A.2 and A.3 in Appendix A. The mesh and set-up for the various simulations shown there are used to obtain the results shown here. The straight line results and the cornering results for the GTE19 are both given in Table B.1. Table B.2 then gives similar information for the LMP1 car.

The difference in total downforce is given and split between front and rear downforce. This is the same as the divisions used and discussed in Part III of the report. These table are extended however, in order to show the contributions of the front wing, the rear wing, the front floor and the rear floor to this difference in downforce. Note that there are other components of the car that generate downforce as well, which means that the percentages do not add up completely. The contributions of the other parts of the car to the downforce differences are smaller and not explored in detail. They are therefore not further discussed in the report and not shown in the tables.

A final remark regarding the splitting is the way the front and rear downforce is computed. In the table, the front wing and front floor might seem to contribute to the front downforce and the rear wing and rear floor to the rear downforce. This is not entirely true however. The split between the front floor boundary and the rear floor boundary is approximately in the middle of the car. The downforce created by the front floor is based on this boundary and therefore from the front of the floor up to the middle of the car. The front and rear downforce are not computed through these separate boundaries. Instead, they are based on the total downforce, which is an addition of the downforce of all the boundaries, and the moment at the front and rear axle. This allows for a computation of the balance and therefore of the front and rear downforce. This means that, for example for the GTE car, the difference in downforce on the front floor also partially contributes to the difference in rear downforce. This explains why the numbers in the tables do not always seem to add up.

Result Nr.	Simulation	C_z	C_x	$C_{z,front}$			$C_{z,rear}$			Bal
				FW	Floor	Total	RW	Floor	Total	
1	**Realizable $k-\epsilon$ RANS**	-	-	-	-	-	-	-	-	-
1	$k-\omega$ **SST RANS**	-16.1%	-6.38%	-1.44%	-16.8%	-9.3%	-14.3%	-0.96%	-20.8%	7.98%
1	$k-\omega$ **SST-IDDES** RANS mesh	10.3%	9.74%	4.39%	-4.19%	6.42%	-4.48%	20.47%	12.9%	-3.48%
2	$k-\omega$ **SST-IDDES**, I=1.0% (μ_t/μ)=10, 12 prism	7.46%	12.0%	3.01%	-9.11%	-0.11%	-3.79%	18.8%	12.7%	-7.05%
3	$k-\omega$ **SST-IDDES**, I=2.5% (μ_t/μ)=10, 16 prism	10.7%	12.8%	6.75%	-5.96%	7.97%	-4.93%	20.5%	12.6%	-2.49%
4	$k-\omega$ **SST-IDDES**, I=2.5% (μ_t/μ)=20, 16 prism	10.4%	12.3%	6.36%	-5.77%	6.65%	-4.66%	20.1%	13.0%	-3.41%
5	$k-\omega$ **SST-IDDES**, RW refined	5.59%	12.3%	5.24%	-12.3%	-1.95%	-0.41%	14.4%	10.9%	-7.15%
6	$k-\omega$ **SST-IDDES**, RW refined, SEM	8.95%	12.8%	5.64%	-9.11%	2.40%	-1.19%	17.3%	13.5%	-6.02%
7	$k-\epsilon$ **EB-DDES**, RW refined	1.83%	10.3%	2.03%	-9.96%	-0.58%	-4.71%	11.83%	3.51%	-2.38%
8	**Realizable $k-\epsilon$ RANS [Cornering]**	-	-	-	-	-	-	-	-	-
8	$k-\omega$ **SST-IDDES [Cornering]**	8.47%	8.12%	3.65%	2.70%	9.67%	-3.08%	10.6%	7.67%	1.11%
9	$k-\omega$ **SST-IDDES [Cornering]**	12.4%	12.7%	6.79%	3.36%	11.6%	-1.78%	13.41%	12.8%	-0.65%

Table B.1: GTE19 Straight Line and Cornering Forces CFD Simulations Split Further

Result Nr.	Simulation	C_z	C_x	$C_{z,front}$			$C_{z,rear}$			Bal
				FW	Floor	Total	RW	Floor	Total	
10	**Realizable** $k-\epsilon$ **RANS**	-	-	-	-	-	-	-	-	-
12	**Elliptic Blending** $k-\epsilon$ **RANS**	-3.71%	0.64%	-0.79%	-5.46%	-4.73%	0.00%	-2.37%	-2.90%	-1.06%
10	$k-\omega$ **SST RANS**	-10.7%	-1.71%	-2.55%	-8.29%	-9.68%	-0.97%	-10.3%	-11.5%	1.11%
10	$k-\omega$ **SST-IDDES** RANS mesh	-5.75%	8.27%	-3.34%	-7.59%	-9.56%	-0.31%	-4.02%	-2.72%	-4.05%
11	$k-\omega$ **SST-IDDES** DES mesh	-2.57%	5.72%	4.68%	-4.95%	1.45%	-2.43%	-2.12%	-5.75%	4.12%
12	$k-\omega$ **SST-IDDES** RANS mesh 16 prism	-7.44%	7.27%	-4.40%	-8.06%	-12.6%	0.31%	-4.02%	-3.37%	-5.54%
13	$k-\omega$ **SST-IDDES** DES mesh refined PIV region	-0.48%	7.37%	4.54%	-4.32%	-0.26%	0.47%	-0.28%	-0.66%	0.22%
10	**Realizable** $k-\epsilon$ **RANS**	-	-	-	-	-	-	-	-	-
15	**Elliptic Blending** $k-\epsilon$ **RANS**	-6.63%	-0.54%	-1.55%	-3.19%	-5.65%	-0.68%	-6.25%	-7.40%	1.05%
14	$k-\omega$ **SST RANS**	-12.0%	-1.22%	-4.87%	-6.05%	-13.4%	-0.46%	-11.3%	-10.8%	-1.64%
14	$k-\omega$ **SST-IDDES** RANS mesh	-3.67%	8.13%	-5.19%	-7.65%	-12.0%	0.29%	2.41%	2.99%	-8.69%
16	$k-\omega$ **SST-IDDES** DES mesh	0.53%	6.78%	2.99%	-5.73%	0.09%	-2.05%	4.33%	0.88%	-0.44%
17	**Realizable** $k-\epsilon$ **RANS**	-	-	-	-	-	-	-	-	-
17	$k-\omega$ **SST-IDDES** RANS mesh	0.14%	9.12%	-5.00%	-5.36%	-7.63%	-1.02%	5.23%	7.09%	-7.75%
18	$k-\omega$ **SST-IDDES** DES mesh	-1.22%	6.78%	-2.53%	-5.12%	-7.40%	-0.77%	2.14%	4.31%	-6.25%
17	**Realizable** $k-\epsilon$ **RANS**	-	-	-	-	-	-	-	-	-
17	$k-\omega$ **SST-IDDES** RANS mesh	-8.10%	7.74%	-15.8%	-8.10%	-20.7%	-0.77%	-3.12%	5.20%	-13.7%
18	$k-\omega$ **SST-IDDES** DES mesh	3.02%	8.58%	-3.00%	-1.22%	-2.87%	-0.85%	1.56%	0.78%	-5.72%

Table B.2: LMP1 S09 Straight Line and Cornering and LMP1 S15 Straight Line Forces CFD Simulations Split Further

C

Simulation Settings

Category	Setting	Value
Physics Models	All y+ Wall Treatment	Iterative Ustar off
	Cell Quality Remediation	
	Constant Density	
	Detached Eddy Simulation	
	Exact Wall Distance	
	Gas - Air	Density=1.18415 kg/m^3
	Gas - Air	Dynamic Viscosity=1.85508E-5 Pa-s
	Gradients	Expert STAR-CCM+ v11.02 defaults
	Gradients - Gradient Method	Hybrid Gauss-LSQ
	Gradients - Limiter Method	Venkatakrishnan
	Gradients - Custom Accuracy Level Selector	2.0
	Gradients - Verbose	off
	Implicit Unsteady	
	Segregated Flow	Hybrid-BCD, Expert STAR-CCM+ v11.02 defaults
	Segregated Flow - Bounded Differencing	0.15
	SST (Menter) K-Omega Detached Eddy	Expert STAR-CCM+ v11.02 defaults
	SST .... - Curvature Correction Option	On
	SST .... - Realizability Option	Durbin Scale Limiter
	SST .... - Compressibility Correction	On
	SST .... - Low Re Damping Modification	Off
	SST .... - Convection	2nd-order
	SST .... - Formulation Option	IDDES
	SST .... - Compressibility Parameters	1.5
	SST .... - Realizability Coefficient	0.6
	SST .... - Curvature Correction Parameters	Cr1=0.04645, Cr2 = 0.25, Cct = 2.0, Upper Limit = 1.25
	SST .... - IDDES Coefficients	Ct = 1.87, Cl = 5.0, Cdt=20
	SST .... - Elevating Function	On
	Three Dimensional	
	Turbulent	
Physics Ref Values	Minimum Allowable Wall Distance	1.0E-6 m
	Maximum Number of Eddies	1000.0
	Reference Pressure	101325 Pa
Initial Conditions	Pressure	Constant, Value 0.0 Pa
	Synthetic Turbulence Specification	None
	Turbulence Intensity	Constant, 0.01
	Turbulence Specification	Intensity + Viscosity Ratio
	Turbulent Velocity Scale	Constant, 1.0 m/s
	Turbulent Viscosity Ratio	Constant, 10
	Velocity	Constant, [27.5,0,0] m/s
Boundaries	Physics Values - Blended Wall Function	E=9.0, Kappa=0.42
Solvers	Implicit Unsteady - Time Step	0.001 s (full car)
	Implicit Unsteady - Temporal Discretization	2nd-order (final part full car)
	Partitioning	
	Wall Distance	
	Segregated Flow	Velocity URF 0.8,
	Segregated Flow	Pressure URF 0.2
	K-Omega Turbulence	URF 0.8
	K-Omega Turbulent Viscosity	URF 0.7, Maximum Ratio 100000

Table C.1: Simulation Settings

Bibliography

[1] C.D. Argyropoulos and N.C. Markatos. Recent advances on the numerical modelling of turbulent flows. *Applied Mathematical Modelling*, 39(2):693–732, (2015). ISSN 0307-904X. doi: https://doi.org/10.1016/j.apm.2014.07.001.

[2] N. Ashton. Recalibrating Delayed Detached-Eddy Simulation to eliminate modelled-stress depletion. In *23rd AIAA Computational Fluid Dynamics Conference, AIAA AVIATION Forum*, (2017). doi: 10.2514/6.2017-4281.

[3] N. Ashton, A. West, S. Lardeau, and A. Revell. Assessment of RANS and DES methods for realistic automotive models. *Computers & Fluids*, 128:1–15, (2016). ISSN 0045-7930. doi: 10.1016/j.compfluid.2016.01.008.

[4] N. Ashton, A. West, and F. Mendonça. Flow dynamics past a 30P30N three-element airfoil using Improved Delayed Detached-Eddy Simulation. *AIAA Journal*, 54:3657–3667, (2016).

[5] CD-adapco. *STAR-CCM+ v.11.02 User Guide*, (2016).

[6] C.C. Critzos, H.H. Heyson, and Jr. R.W. Boswinkle. Aerodynamic characteristics of NACA 0012 airfoil section at angles of attack from 0 to 180, (1955).

[7] C.A. de Moura and C.S. Kubrusly. *The Courant-Friedrichs-Lewy (CFL) Condition*. Springer New York, (2013). doi: 10.1007/978-0-8176-8394-8.

[8] A.A. de Paula, V.G. Kleine, and F.M. Porto. *The Thickness Effect on Symmetrical Airfoil Flow Characteristics at low Reynolds number*, pages 1–20. doi: 10.2514/6.2017-1422.

[9] S. Deck. A one-equation turbulence model for aerodynamic flows. *30th Aerospace Sciences Meeting and Exhibit, Aerospace Sciences Meetings*, (1992). doi: 10.2514/6.1992-439.

[10] S. Deck. Zonal-Detached-Eddy Simulation of the flow around a high-lift configuration. *AIAA Journal*, 43 (11):2372–2384, (2005). doi: 10.2514/1.168106.

[11] S. Deck. Recent improvements in the Zonal Detached Eddy Simulation (ZDES) formulation. *Theoretical and Computational Fluid Dynamics*, 26:523–550, (2012). doi: 10.1007/s00162-011-0240-z.

[12] P.A. Durbin. Near-wall turbulence closure modeling without damping functions. *Theoretical Computational Fluid Dynamics*, 3:1–13, (1991).

[13] P.A. Durbin. Separated flow computations with the k-epsilon-v2 model. *AIAA Journal*, 33(4):659–664, (1995).

[14] G.K. Dutzler and C. Pashias. Simulating the aerodynamics of the 919 Hybrid LMP1 racing car. *Turbulence, Heat and Mass Transfer 9. Proceedings of the Ninth International Symposium on Turbulence, Heat and Mass Transfer*, pages 677–688, (2018).

[15] N. Gregory and C.L. O'Reilly. Low-speed aerodynamic characteristics of NACA 0012 aerofoil section, including the effects of upper-surface roughness simulating hoar frost. Technical Report 3726, Ministry of Defence, (1970).

[16] M.S. Gritskevich, A.V. Garbaruk, and F.R. Menter. A comprehensive study of Improved Delayed Detached Eddy Simulation with wall functions. *F.R. Flow Turbulence Combustion*, 98:461–479, (2017).

[17] F. Hamba. Log-Layer Mismatch and commutation error in hybrid RANS/LES simulation of channel flow. *International Journal of Heat and Fluid Flow*, 30(1):20–31, (2009). ISSN 0142-727X. doi: 10.1016/j.ijheatfluidflow.2008.10.002.

[18] M. Islam, F. Decker, E. de Villiers, A. Jackson, J. Gines, T. Grahs, A. Gitt-Gehrke, and J. Comas i Font. Application of Detached-Eddy Simulation for automotive aerodynamics development. In *SAE Technical Paper*. SAE International, (2009). doi: 10.4271/2009-01-0333.

[19] N. Jarrin, S. Benhamadouche, D. Laurence, and R. Prosser. A synthetic-eddy-method for generating inflow conditions for Large-Eddy Simulations. *International Journal of Heat and Fluid Flow*, 27:585–593, (2016). doi: 10.1016/j.ijheatfluidflow.2006.02.006.

[20] J. Katz. Aerodynamics of race cars. *Annual Review of Fluid Mechanics*, 38(1):27–63, (2006). doi: 10.1146/annurev.fluid.38.050304.092016.

[21] J. Larsson, S. Kawat, J. Bodart, and I. Bermejo-Moreno. Large Eddy Simulation with modelled wall-stress: Recent progress and future directions. *Mechanical Engineering Reviews*, 3, 11 (2015). doi: 10.1299/mer.15-00418.

[22] O. Lehmkuhl, I. Rodrígueza, A. Baeza, A. Olivaa, and C.D. Pérez-Segarra. On the large-eddy simulations for the flow around aerodynamic profiles using unstructured grids. *Computers & Fluids*, 84:176–189, (2013).

[23] H. Lei, D. Zhou, Y. Bao, Y. Li, and Z. Han. Three-dimensional Improved Delayed Detached Eddy Simulation of a two-bladed vertical axis wind turbine. *Energy Conversion and Management*, 133:235–248, (2016).

[24] R. Manceau and K. Hanjalic. Elliptic blending model: A new near-wall Reynolds-stress turbulence closure. *Physics of Fluids*, 14(2):744–754, (2002). doi: 10.1063/1.1432693.

[25] C.P. Mellen, J. Fröhlich, and W. Rodi. Lessons from LESFOIL project on large-eddy simulation of flow around an airfoil. *AIAA Journal*, 41(4):573–581, (2003). doi: 10.2514/2.2005.

[26] F.R. Menter. Two-equation eddy-viscosity turbulence models for engineering applications. *AIAA Journal*, 32(8):1598–1605, (1994). doi: 10.2514/3.12149.

[27] F.R. Menter. Review of the shear-stress transport turbulence model experience from an industrial perspective. *International Journal of Computational Fluid Dynamics*, 23(4):305–316, (2009). doi: 10.1080/10618560902773387.

[28] F.R. Menter and Y. Egorov. The Scale-Adaptive Simulation method for unsteady turbulent flow predictions. Part 1: Theory and model description. *Flow, Turbulence and Combustion*, 86(1):113–138, (2010). ISSN 1573-1987. doi: 10.1007/s10494-010-9264-52.

[29] F.R. Menter and M. Kuntz. Adaptation of Eddy-Viscosity turbulence models to unsteady separated flow behind vehicles. In *The Aerodynamics of Heavy Vehicles: Trucks, Buses, and Trains. Lecture Notes in Applied and Computational Mechanics*, volume 19, pages 339–352. Springer, Berlin, Heidelberg, (2004).

[30] N.V. Nikitin, F. Nicoud, B. Wasistho, K.D. Squires, and P.R. Spalart. Letter: An approach to wall modeling in Large-Eddy Simulations. *Physics of Fluids*, 12(7):1629–1632, (2000).

[31] S. Pope. *Turbulent Flows*. Cambridge University Press, Cambridge, U.K., (2000). doi: 10.1017/CBO9780511840531.

[32] P. Sagaut. *LES for incompressible flow*. Springer Berlin Heidelberg, (2006).

[33] P. Sagaut, S. Deck, and M. Terracol. *Multiscale and multiresolution approaches in turbulence. LES, DES and Hybrid RANS/LES Methods: Applications and Guidelines*. Imperial College Press, London, (2013).

[34] H. Shan, L. Jiang, and C. Liu. Direct numerical simulation of flow separation around a naca 0012 airfoil. *Computers & Fluids*, 34(9):1096 – 1114, 2005. ISSN 0045-7930. doi: https://doi.org/10.1016/j.compfluid.2004.09.003.

[35] R.E. Sheldahl and P.C. Klimas. Aerodynamic characteristics of seven symmetrical airfoil sections through 180-degree angle of attack for use in aerodynamic analysis of vertical axis wind turbines. Technical Report SAND80-2114, Sandia National Laboratories, (1981).

[36] T. Shih, W.W. Liou, A. Shabbir, Z. Yang, and J. Zhu. A new k-epsilon model for high Reynolds number turbulent flows. *Computers & Fluids*, 24(3):227–238, (1995). doi: 10.1016/0045-7930(94)00032-T.

[37] M. Shur, P.H. Spalart, M.K. Strelets, and A. Travin. Detached Eddy Simulation of an airfoil at high angle of attack. *Engineering Turbulence Modelling and Experiments*, 4:669–678, (1999). doi: 10.1016/B978-008043328-8/50064-3.

[38] M. Shur, P.R. Spalart, M.K. Strelets, and A. Travin. A hybrid RANS-LES approach with delayed-DES and wall-modelled LES capabilities. *International Journal of Heat and Fluid Flow*, 29(6):1638–1649, (2008). ISSN 0142-727X. doi: 10.1016/j.ijheatfluidflow.2008.07.001.

[39] Siemens PLM Software. *STAR-CCM+ v.14.02 User Guide*, (2019).

[40] P.H. Spalart. Detached Eddy Simulation. *Annual Review of Fluid Mechanics*, 41(1):181–202, (2009). doi: 10.1146/annurev.fluid.010908.165130.

[41] P.H. Spalart, W.H. Jou, M.K. Strelets, and S. Allmaras. Comments on the feasibility of LES for wings, and on a hybrid RANS/LES approach. pages 137–147. Greyden Press, Columbus, (1997).

[42] P.H. Spalart, S. Deck, M. Shur, K. Squires, M.K. Strelets, and A. Travin. A new version of Detached Eddy Simulation, resistant to ambiguous grid densities. *Theoretical and Computational Fluid Dynamics*, 20:181–195, (2006). doi: 10.1007/s00162-006-0015-0.

[43] P.R. Spalart. Young-person's guide to Detached Eddy Simulation grids. Technical report, NASA Langley Technical Report Server, (2001).

[44] M.K. Strelets. Detached Eddy Simulation of massively separated flows. *American Institute of Aeronautics and Astronautics Journal*, page 0879, (2001). doi: 10.2514/6.2001-879.

[45] H. Stumpf, P. Röser, T. Wiegand, B. Pfäfflin, J. Ocker, R. Müller, W. Eckert, and H.-U. Kroß. The new aerodynamic and aeroacoustic wind tunnel of the Porsche AG. In M. Bargende, H.-C. Reuss, and J. Wiedemann, editors, *15. Internationales Stuttgarter Symposium*, pages 811–826, Wiesbaden, (2015). Springer Fachmedien Wiesbaden. ISBN 978-3-658-08844-6.

[46] J. Tank, L. Smith, and G. R. Spedding. On the possibility (or lack thereof) of agreement between experiment and computation of flows over wings at moderate Reynolds number. *Interface Focus*, 7(1):20160076, (2017). doi: 10.1098/rsfs.2016.0076.

[47] K. Weinman, H. van der Ven, C. Mockett, J.C. Kok T. Knopp, R.T.E. Perrin, and F. Thiele. A study of grid convergence issues for the simulation of the massively separated flow around a stalled airfoil using DES and related methods. In *Proceedings of the European Conference on Computational Fluid Dynamics, ECCOMAS CFD*, (2006).

[48] F.M. White. *Viscous fluid flow*. McGraw-Hill New York, (2006).

[49] D.C. Wilcox. *Turbulence Modeling for CFD*. DCW Industries, (2006).

[50] J. Winslow, H. Otsuka, B. Govindarajan, and I. Chopra. Basic understanding of airfoil characteristics at low reynolds numbers (104–105). *Journal of Aircraft*, 55(3):1050–1061, (2018). doi: 10.2514/1.C034415.

[51] Ö. Yalçın, K. Cengiz, and Y. Özyörük. High-order Detached Eddy Simulation of unsteady flow around NREL S826 airfoil. *Journal of Wind Engineering and Industrial Aerodynamics*, 179:125–134, (2018). ISSN 0167-6105. doi: 10.1016/j.jweia.2018.05.017.

[52] Z. Yang. Assessment of unsteady-RANS approach against steady-RANS approach for predicting twin impinging jets in a cross-flow. *Cogent Engineering*, 1(1), (2014). doi: 10.1080/23311916.2014.936995.

[53] Z. Yin and P.A. Durbin. An adaptive DES model that allows wall-resolved eddy simulation. *International Journal of Heat and Fluid Flow*, 62 B(1):499–509, (2016). doi: 10.1016/j.ijheatfluidflow.2016.08.009.

[54] X. Zhang, W. Toet, and J. Zerihan. Ground effect aerodynamics of race cars. *Applied Mechanics Reviews*, 59(1):33–49, (2006). doi: 10.1115/1.2110263.